Author:
Ayat, Sabrina S

Title:
An Experiment-Informed Methodology for the Thermal Design of Permanent Magnet Electrical Machines

An Experiment-Informed Methodology for the Thermal Design of Permanent Magnet Electrical Machines

Sabrina S. Ayat

A thesis submitted to the University of Bristol in accordance with the requirements of the degree of Doctor of Philosophy in Electrical Engineering.

Department of Electrical and Electronic Engineering
University of Bristol

September 2019

To my parents

Abstract

The continuous drive towards more electric technologies and the subsequent need for high-performance electric machines calls for a more accurate and reliable thermal design-analysis, where various design, manufacture and assembly factors are accounted for at the initial stage of the design process. The wide ranges of built factors have a significant impact on the overall thermal behaviour of the machine, and frequently require empirical techniques to validate the initial design assumptions. The conventional approach employed in empirical validation of thermal models of electrical machines makes use of thermal testing on a complete machine prototype. This is usually performed at the end of the machine manufacturing process to assess the measured thermal characteristics against the design targets and theoretical predictions. Thermal model validation from a complete machine assembly is frequently effective for experienced-based designs, where a designer has confidence in the pre-existing machine thermal design. In such a case, the initial machine assembly should closely match the specifications. However, for novel machine topologies, a designer typically needs to evaluate several design variants to realise an optimal solution. The machine fabrication for all design iterations would not be feasible due to the cost and time constraints. For these reasons, a method providing reliable loss and thermal predictions would significantly reduce the number of prototype iterations required for the development of a new machine. Therefore, time and cost associated with the new design would be substantially reduced. This thesis presents an experimentally-informed methodology for the high-fidelity thermal design of electrical machines. The methodology focuses on the stator-winding region, which is frequently attributed with the dominant power loss component within the machine body. The developed approach accounts for a variety of permanent magnet machine designs, where the majority of the heat produced in the machine is evacuated by conduction into the machine periphery. Three machine sub-assemblies have been selected to form the foundation of the proposed methodology, based on their complementarity and their capability to incrementally inform the machine thermal design. Efficacy of the proposed methodology is illustrated on a number of machine demonstrators with different build attributes. The proposed methodology aims to be a systematic and reliable tool for machine designers, guiding empirical calibration depending on available hardware, required fidelity and machine design focus.

Acknowledgements

This work was supported by the European Commission (FP7 Marie Curie ITN Project 607361 ADEPT) and Motor Design Limited. In addition, I would like to express my gratitude towards the following people:

Dr. Rafal Wrobel for his technical expertise, enthusiasm and availability, which have surpassed all the expectations I had when I started my thesis. He has set an example of excellence as a researcher and a mentor.

Dr. David Drury for his guidance and for offering thorough feedback on this thesis. He also encouraged me to think independently about my work.

Dr. Dave Staton, Dr. James Goss and the team in Motor Design Limited for their technical expertise and the help and opportunities they provided me, especially my secondments at Jaguar Land Rover.

Prof. Phil Mellor and the members of the Electrical Energy Management Group (past and present) for creating a pleasant working environment. Particular thanks are due to Haipeng Liu for our numerous technical discussions.

The former members of the 0.25 Office, and my flatmates from the 203A Cheltenham road, who have provided friendship and enjoyment. A special thanks goes to Dr. Plamen Proynov for his steadfast support, kindness, and encouragements.

Finally, I am fortunate to have a family that has always encouraged and supported me. Each of its members, especially my parents and grandparents, are models and inspiration for me. Thank you.

Declaration

I declare that the work in this dissertation was carried out in accordance with the requirements of the University's Regulations and Code of Practice for Research Degree Programmes and that it has not been submitted for any other academic award. Except where indicated by specific reference in the text, the work is the candidate's own work. Work done in collaboration with, or with the assistance of, others, is indicated as such. Any views expressed in the dissertation are those of the author.

SIGNED: ..... DATE:.....

Memorandum

The accompanying thesis “An Experiment-Informed Methodology for the Thermal Design of PM Electrical Machines” is based on work carried out by the author as a member of the Electrical Energy Management Group (EEMG) in the Department of Electrical and Electronic Engineering of the University of Bristol, Bristol, United Kingdom between the dates of July 2014 and February 2018.

The main contributions claimed by the author are as follows:

1) The development of an experiment-informed methodology for the coupled thermal and power loss analysis of permanent magnet electrical machines
2) The development of two sets of formulae for the estimation of the equivalent thermal conductivity of winding formed with round and rectangular profiled conductors
3) The development of a technique for the estimation of the winding heat capacitance applicable to several hardware types, including stator-winding segments (motorette) and complete stator assembly.

Publications

Journal Publications

1. S. Ayat, R. Wrobel, J. Goss, D. Drury, “Estimation of Equivalent Thermal Conductivity for Impregnated Electrical Windings Formed from Profiled Rectangular Conductors”, *IET Electric Power Applications, (under review)*

2. R. Wrobel, S.J. Williamson, N. Simpson, S. Ayat, J. Yon, P.H. Mellor. "Impact of slot shape on loss and thermal behaviour of open-slot modular stator windings," *IET Electric Power Applications, (under review)*

Conference Publications

3. S. Ayat, L. Haipeng, F. Chauvicourt, R. Wrobel, “Experimental Derivation of Thermal Parameters of the Stator-Winding Region in Thermal Analysis of PM Electrical Machines”, *44th Annual Conference of the IEEE Industrial Electronics Society (IECON 2018),* Washington, 2018, *(in press).*

4. H. Liu, R. Wrobel, S. Ayat, C. Zhang, “Coupled Electromagnetic and Thermal Design-Optimization of a Traction IPM machine with High-Torque Overload Capability”, *23th International conference on electrical machines (ICEM 2018)*, Alexandroupoli, 2018, *(in press).*

5. H. Liu, S. Ayat, R. Wrobel, C. Zhang, “Comparative Study of Thermal Properties of Electrical Windings Impregnated with Alternative Varnish Materials”, *in 9th IET International Conference on Power Electronics, Machines and Drives (PEMD)*, Liverpool, April 2018.

6. P. Romanazzi, S. Ayat, R. Wrobel, D. Howey, “3D Homogenisation of concentrated windings with rectangular conductors”, *IEEE International Machines and Drives Conference (IEMDC)*, Miami, May 2017.

7. R. Wrobel, S. Ayat, J. Baker, “Analytical Methods for Estimating Equivalent Thermal Conductivity in Impregnated Electrical Windings Formed Using Litz Wire”, *IEEE International Machines and Drives Conference (IEMDC)*, Miami, May 2017.

8. R. Wrobel, S. Ayat, J. Godbehere, “A Systematic Experimental Approach Deriving Stator-Winding Heat Transfer”, *IEEE International Machines and Drives Conference (IEMDC)*, Miami, May 2017.

9. S. Ayat, R. Wrobel, J. Baker, D. Drury, “A Comparative Study Between Aluminium and Copper Windings for a Modular-Wound IPM Electric Machine”, *IEEE International Machines and Drives Conference (IEMDC)*, Miami, May 2017.

10. S. Ayat, R. Wrobel, J. Goss, D. Drury, “Experimental Calibration in Thermal Analysis of Electrical Machines”, *IEEE Energy Conversion Congress and Exposition (ECCE),* Milwaukee, September 2016.

11. S. Ayat, R. Wrobel, J. Goss, D. Drury, “Estimation of Equivalent Thermal Conductivity for Impregnated Electrical Windings Formed from Profiled Rectangular Conductors”, *in 8th IET International Conference on Power Electronics, Machines and Drives (PEMD)*, Glasgow, April 2016.

12. S. Ayat, R. Wrobel, J. Goss, D. Drury, “Experiment Informed Methodology for Thermal Design of PM Machines”, *Eleventh International Conference on Ecological Vehicles and Renewable Energies (EVER),* Monaco, *April 2016*.

13. R. Wrobel, S.J. Williamson, N. Simpson, S. Ayat, J. Yon, P.H. Mellor. "Impact of slot shape on loss and thermal behaviour of open-slot modular stator windings," *IEEE Energy Conversion Congress and Exposition (ECCE)*, pp. 4433-4440, Montreal, September 2015.

List of Abbreviations

AC	Alternating Current
ADEPT	ADvanced Electric Powertrain Technology
AL	Active Length
BI	Back Iron
CFD	Computational Fluid Dynamics
DC	Direct Current
EDM	Electric Discharge Machining
EMF	Electromotive Force
EU	European Union
EW	End Winding
FE	Finite Element
FEA	Finite Element Analysis
GA	Genetic Algorithm
HTC	High-Throughput Computing
IC	Internal Combustion
IEC	International Electrotechnical Commission
IM	Induction Motor
IPM	Interior Permanent Magnet
LCM	Least Common Multiple
M	Machine
ME	Motorette exemplar
MMF	Magneto motive force
MS	Material sample
NEMA	National Electrical Manufacturers Association
NVH	Noise Vibration and Harshness
OC	Open-circuit
PM	Permanent Magnet
PSO	Particle Swarm Optimisation
PWM	Pulse Width Modulation
RMS	Root Mean Squared
RPM	Revolutions Per Minute
S	Stator
SC	Short-circuit
SE	Stator exemplar
SMPM	Surface Mount Permanent Magnet
SST	Single Sheet Tester
T	Tooth
TEC	Thermal Equivalent Circuit
TEFC	Totally-Enclosed Fan-Cooled
TENV	Totally Enclosed, Non-Ventilated
W	Winding
WS	Winding sample
Y	Yoke
1D	One Dimensional
2D	Two Dimensional
3D	Three Dimensional

Nomenclature

Symbol	Quantity	Units
A	Cross-section area	m^2
A_{air}	Air equivalent cross-section area	m^2
A_{coat}	Lamination coating cross-section area	m^2
$A_{contact}$	Contact area	m^2
A_i	Impregnation cross-section area	m^2
A_L	Lamination material cross-section area	m^2
A_s	Complete lamination stack cross-section area	m^2
A_{sa}	Per slot active cross-section area	m^2
A_{w-s}	Theoretical winding-to-stator contact surface area	m^2
α	Temperature coefficient of the electrical resistivity	$°C^{-1}$
α_{B_r}	Temperature coefficient of remanence	$°C^{-1}$
α_{copper}	Temperature coefficient of the electrical resistivity of copper	$°C^{-1}$
α_{steel}	Temperature coefficient of the electrical resistivity of steel	$°C^{-1}$
$\alpha_{pm,rotor-induced}$	Temperature coefficients of the rotor induced magnet loss	$°C^{-1}$
$\alpha_{r,iron,rotor-induced}$	Temperature coefficients of the rotor induced rotor core loss	$°C^{-1}$
$\alpha_{s,iron,rotor-induced}$	Temperature coefficients of the rotor induced stator core loss	$°C^{-1}$
B	Magnetic flux density	T
$(BH)_{max}$	Maximum energy product	$kJ.m^{-3}$
B_r	Remanence	T
β	Temperature coefficient for the ac loss component due to the current excitation	-
β_{cubic}	Coefficient of cubic expansion	$°C^{-1}$
C	Heat capacitance	$J.K^{-1}$
C_r	Rotor core heat capacitance	$J.K^{-1}$
C_s	Stator core heat capacitance	$J.K^{-1}$
C_w	Winding heat capacitance	$J.K^{-1}$
C_Ω	Electrical capacitance	F
C_d	Skin friction coefficient	$kg.m^2.s$
c_s	Specific heat capacity	$J.K^{-1}.kg^{-1}$
$c_{s,c}$	Conductor specific heat capacity	$J.K^{-1}.kg^{-1}$
$c_{s,ci}$	Electrical insulation specific heat capacity	$J.K^{-1}.kg^{-1}$
$c_{s,f}$	Fluid specific heat capacity	$J.K^{-1}.kg^{-1}$
$c_{s,i}$	Impregnation specific heat capacity	$J.K^{-1}.kg^{-1}$
$c_{s,s}$	Stator core equivalent specific heat capacity	$J.K^{-1}.kg^{-1}$
$c_{s,sol}$	Solid specific heat capacity	$J.K^{-1}.kg^{-1}$
$c_{s,w}$	Winding equivalent specific heat capacity	$J.K^{-1}.kg^{-1}$
d	Depth	m
ΔB_i	Flux reversal associated with a given minor loop	T
ΔT	Temperature difference	°C
ΔT_f	Fluid temperature difference between time t_1 and t_2	°C
ΔT_s	Solid temperature difference between time t_1 and t_2	°C
ΔT_{w-s}	Winding-to-stator temperature difference	°C
ΔV	Electric potential difference	V
ε_e	Eddy-current loss coefficient (see (2.7))	$W.s^a.T^{-b}$
$\varepsilon_{friction}$	Friction loss coefficient	$W.m^{-1}.s$
ε_h	Hysteresis loss coefficient	$W.s^2.T^{-2}$
ε_{exc}	Excess loss coefficient	$W.s^{1.5}.T^{-1.5}$

ε_{surf}	Surface emissivity	-
$\varepsilon_{windage}$	Winding loss coefficient	$W.m^{-3}.s^{3}$
f	Excitation frequency	Hz
FF	Fill factor	-
FF_b	Litz wire bundle fill factor	-
FF_s	Litz wire strand fill factor	-
FF_x	Equivalent winding fill factor in the x-axis	-
FF_y	Equivalent winding fill factor in the y-axis	-
F_{1-2}	View factor for dissipating surface 1 to absorbing surface 2	-
g	Gravitational attraction force	$m.s^{-2}$
Gr	Grashof number	-
γ	Temperature coefficient for the ac loss component due to the rotation of the rotor PM array	-
γ_I	Current angle	-
h	Heat transfer coefficient	$W.m^{-2}.°C^{-1}$
$h_{e,s-h}$	Stator-to-housing thermal conductance	$W.m^{-2}.°C^{-1}$
$h_{e,w-s}$	Winding-to-stator thermal conductance	$W.m^{-2}.°C^{-1}$
h_{e12}	Winding-to-stator thermal conductance after applying shape and size correction functions	$W.m^{-2}.°C^{-1}$
h_{forced}	Forced convection heat transfer coefficient	$W.m^{-2}.°C^{-1}$
h_{h-a}	Heat transfer coefficient from the machine housing frame to ambient	$W.m^{-2}.°C^{-1}$
h_{mixed}	Heat transfer coefficient resulting from the association of the natural and forced convection	$W.m^{-2}.°C^{-1}$
$h_{natural}$	Natural convection heat transfer coefficient	$W.m^{-2}.°C^{-1}$
$h_{radiation}$	Radiation heat transfer coefficient	$W.m^{-2}.°C^{-1}$
H_{ci}	Intrinsic coercivity	$kA.m^{-1}$
I	Current amplitude	A
I_d	Magnitude of demagnetizing direct axis component	A
I_{dc}	Dc current	A
I_{pk}	Current amplitude	A
I_q	Magnitude of demagnetizing quadrature axis component	A
I_{RMS}	Root means square current	A
$\vec{J}$	Current density	$A.m^{-2}$
k	Thermal conductivity	$W.m^{-1}.°C^{-1}$
k_a	Equivalent thermal conductivity of the impregnation/electrical insulation amalgam	$W.m^{-1}.°C^{-1}$
k_c	Conductor thermal conductivity	$W.m^{-1}.°C^{-1}$
k_{ci}	Electrical insulation thermal conductivity	$W.m^{-1}.°C^{-1}$
k_{coat}	Lamination coating thermal conductivity	$W.m^{-1}.°C^{-1}$
k_L	Lamination material thermal conductivity	$W.m^{-1}.°C^{-1}$
k_i	Thermal conductivity of impregnation	$W.m^{-1}.°C^{-1}$
k_s	Equivalent thermal conductivity of the laminated core pack	$W.m^{-1}.°C^{-1}$
$k_{s,in-plane}$	In-plane thermal conductivity of the laminated core pack	$W.m^{-1}.°C^{-1}$
$k_{s,through-stack}$	Through stack laminated core pack thermal conductivity	$W.m^{-1}.°C^{-1}$
k_w	Equivalent winding thermal conductivity	$W.m^{-1}.°C^{-1}$
$k_{w,axial}$	Thermal conductivity in axial direction	$W.m^{-1}.°C^{-1}$
$k_{w,radial}$	Thermal conductivity in radial direction	$W.m^{-1}.°C^{-1}$
$k_{w,x}$	Winding thermal conductivity in x-axis	$W.m^{-1}.°C^{-1}$
$k_{w,y}$	Winding thermal conductivity in y-axis	$W.m^{-1}.°C^{-1}$
$k_{w,z}$	Winding thermal conductivity in z-axis	$W.m^{-1}.°C^{-1}$
k_{s-h}	Stator-to-housing t interface region thermal conductivity	$W.m^{-1}.°C^{-1}$
k_{w-s}	Winding-to-stator interface region thermal conductivity	$W.m^{-1}.°C^{-1}$
k_{w-T}	Winding-to-tooth interface region thermal conductivity	$W.m^{-1}.°C^{-1}$
k_{w-Y}	Winding-to-yoke equivalent interface region thermal conductivity	$W.m^{-1}.°C^{-1}$

k_1	End-space heat transfer coefficient - natural convection	$W.m^{-2}.°C^{-1}$
k_2, k_3	End-space heat transfer coefficient - forced convection	$m^{-1}.s$, -
K_{fb}	Frictional loss coefficient	$m.s^{-2}$
l	Length	m
l_a	Winding active length	m
l_e	End-winding length	m
l_r	Rotor active length	m
L	Heat path length	m
L_{surf}	Characteristic length of the surface	m
Λ_d	Direct axis flux linkage component	Wb.turn
Λ_q	Quadrature axis flux linkage component	Wb.turn
m	Mass	kg
m_c	Conductor mass	kg
m_{ci}	Electrical insulation mass	kg
m_f	Fluid mass	kg
m_i	Impregnation mass	kg
m_r	Rotor mass	kg
m_{sol}	Solid mass	kg
m_w	Winding mass	kg
n	Machine rotational speed	RPM
n_f	Fluid velocity	$m.s^{-1}$
N_m	Number of phases	-
Nu	Nusselt number	-
PF	Packing factor	-
Pr	Prandtl number	-
p	Number of pole pairs	-
P_{ac}	Total winding power loss at ac operation	W
$P_{ac,e}$	Winding power loss from the winding ac excitation	W
$P_{ac,r}$	Winding power loss from rotational effects of the PM array	W
P_{dc}	Winding power loss at dc operation	W
P_{eddy}	Eddy current power loss	W
P_{exc}	Excess or anomalous power loss	W
$P_{friction}$	Friction loss	W
P_{hyst}	Hysteresis power loss	W
P_{iron}	Total iron power loss	W
$P_{mechanical}$	Total mechanical loss	W
P_{mes}	Total measured power loss	W
P_{pm}	Magnet loss	W
$P_{pm,iron,rotor-induced}$	Rotor induced magnet loss	W
$P_{r,iron,rotor-induced}$	Rotor induced rotor core loss	W
$P_{s,iron,rotor-induced}$	Rotor induced stator core loss	W
$P_{slotting}$	Magnet loss due to slotting effect	W
$P_{stator\ interaction}$	Magnet loss from stator field interaction	W
$P_{v,dc}$	Volumetric winding power loss at dc excitation	W
P_w	Winding power loss	W
$P_{windage}$	Windage loss	W
q	Number of slots	-
Q	Heat flow	$W.m^{-2}$
$\dot{Q}$	Heat transfer rate	$W.m^{-2}.s^{-1}$
$\dot{Q}_{v,hp}$	Volumetric hot plate heat generation	$W.m^{-2}.s^{-1}$
r	Outer radius	m
r_c	Conductor outer radius	m
r_{ci}	Electrical insulation outer radius	m
r_i	Equivalent impregnation outer radius	m
r_r	Rotor outer radius	m
r_s	Stator outer radius	m

R	Thermal resistance	°C.W^{-1}
R_c	Conductor thermal resistance	°C.W^{-1}
R_{ci}	Electrical insulation thermal resistance	°C.W^{-1}
R_{coat}	Lamination coating thermal resistance	°C.W^{-1}
R_e	Equivalent winding thermal resistance	°C.W^{-1}
R_i	Impregnation thermal resistance	°C.W^{-1}
R_L	Single lamination thermal resistance	°C.W^{-1}
R_{h-a}	Housing-to-ambient thermal resistance	°C.W^{-1}
R_{s-h}	Stator-to-housing thermal resistance	°C.W^{-1}
R_{r-sh}	Rotor-to-shaft thermal resistance	°C.W^{-1}
R_{w-s}	Winding-to-stator thermal resistance	°C.W^{-1}
R_{w-T}	Winding-to-tooth thermal resistance	°C.W^{-1}
R_{w-Y}	Winding-to-yoke thermal resistance	°C.W^{-1}
R_{ac}/R_{dc}	Ratio of equivalent ac to dc resistances	-
$(R_{ac}/R_{dc})\vert_e$	Average winding power loss due to excitation at ac operation	-
$(R_{ac}/R_{dc})\vert_{e,EW}$	Average end-winding power loss due to excitation at ac operation	-
R_Ω	Electrical resistance	Ω
Re	Reynolds number	-
ρ	Electrical resistivity	Ω.m
ρ_{pm}	Magnet electrical resistivity	Ω.m
ρ_d	Density	kg.m^{-3}
$\rho_{d,air}$	Air density	kg.m^{-3}
$\rho_{d,c}$	Conductor density	kg.m^{-3}
$\rho_{d,i}$	Impregnation density	kg.m^{-3}
σ	Electrical conductivity	S.m^{-1}
t	Thickness	m
$t_{air,w-s}$	Equivalent winding-to-stator interface air cavity thickness	m
$t_{air,s-h}$	Equivalent stator-to-housing interface air cavity thickness	m
t_{ci}	Electrical insulation thickness	m
t_L	Thickness of a single lamination	m
t_g	Air gap radial thickness	m
T	Temperature	°C
Ta	Taylor number	-
T_{cp}	Averaged cold plate temperature	°C
T_h	Averaged housing temperature	°C
$T_{hotspot}$	Hotspot temperature	°C
T_s	Averaged stator core temperature	°C
T_w	Averaged winding temperature	°C
$\bar{T}$	Averaged node temperature	°C
U	Voltage	V
U_{dclink}	Dc link voltage	V
U_{lim}	Maximum inverter output voltage	V
μ	Dynamic viscosity	kg.s^{-1}.m^{-1}
v	Volume ratio	-
v_c	Conductor volume ratio	-
v_{ci}	Electrical insulation volume ratio	-
v_i	Impregnation volume ratio	-
V	Volume	m^3
V_{hp}	Hot plate volume	m^3
V_{pm}	Magnet volume	m^3
w	Width	m
w/h	Averaged slot width over height ratio	-
w_{pm}	Magnet width	m
W	Thermal energy	J
ω_s	Angular frequency	rad.s^{-1}

x	Length in the x-axis	m
x_b	Litz wire bundle length in the x-axis	m
x_{bs}	Litz wire bundle spacing in the x-axis	m
x_c	Conductor length in the x-axis	m
x_{ci}	Electrical insulation length in the x-axis	m
y_e	Equivalent length of an individual conductor with electrical insulation and impregnation in the x-axis	m
x_i	Impregnation length in the x-axis	m
y	Length in the y-axis	m
y_b	Litz wire bundle length in the y-axis	m
y_{bs}	Litz wire bundle spacing in the y-axis	m
y_c	Conductor length in the y-axis	m
y_{ci}	Electrical insulation length in the y-axis	m
y_e	Equivalent length of an individual conductor with electrical insulation and impregnation in the y-axis	m
y_i	Impregnation length in the y-axis	m
z	Length in the z-axis	m
z_e	Equivalent length of an individual conductor with electrical insulation and impregnation in the z-axis	m

Table of Contents

Chapter 1 Introduction

1.1 Introduction

The increasing energy needs of the world, growing concerns toward climate change, and scarcity of fossil fuel resources make electrical energy management an important societal and technological issue [1]-[3]. Electric machine technologies have a significant role to play in the future, as electric motor systems currently constitute around 45% of global electricity consumption [4]. Two of the main objectives of Europe 2020 - the European Union (EU) growth strategy - are to cut greenhouse gas emissions by at least 20% from 1990 levels, and increase the share of renewable energy in final energy consumption to 20% [1]. About 20% of worldwide CO_2 emissions are attributed to transportation [2], so electric machines and power electronic energy conversion are seeing increased attention in automotive, aviation, railway and shipping industries [4]-[11]. This is the context of establishing the Advanced Electric Powertrain Technology (ADEPT) consortium funded by the EU's Horizon 2020 programme. This PhD work on the thermal design of Permanent Magnet (PM) electrical machines is one of the research activities within ADEPT. One of the consortium's underpinning objectives was to qualify 12 early stage researchers in specific disciplines related to electric-propulsion, such as control, electrical engineering or safety [13]. By providing a structured way for these disciplines to be collaborated on, the program aims to facilitate the development of the European research community focused on electric propulsion. Fig. 1.1 presents an overview of ADEPT partner institutions with geographic location.

Fig. 1.1 Overview of ADEPT partner institutions

The automotive industry is primarily concerned by the move towards electric propulsion alternatives, as several countries, including the United Kingdom and France, have committed to outlaw the sale of internal combustion (IC) based vehicles by 2040 [14]. Cost is a specific driver for the automotive industry in a different manner than for other transportation sectors, as it needs to be made affordable for individual customers. Other sectors that require low-cost machine design for high volume production include household appliances. In this case, most companies use low-tech solutions, such as asynchronous single-phase motors. However, getting the cost of an electric machine for automotive applications down to acceptable levels, while ensuring that it is as powerful as its IC engine equivalent can only be achieved via a more accurate and comprehensive design procedure, where electromagnetic, mechanical and thermal behaviours are concurrently accounted for.

The focus of this thesis is the development of a multi-physics methodology for the concurrent thermal and electromagnetic design of PM electrical machines, with emphasis placed on selected thermal aspects of the machine design. The existing design practice makes use of thermal analysis at a later stage of the design process, which can be subject to uncertainties due to a lack of appropriate data associated with processes used in construction and assembly of electrical machines. The thermal data is typically acquired from tests on a complete machine prototype, and several iterations are usually required to satisfy all the design requirements. The proposed methodology, which is the subject of this PhD, attempts to provide a more informed design process, where the initial power loss and thermal data is experimentally validated and made available to a machine designer. Such an approach ensures that each of the thermal and electromagnetic analyses provides a more reliable and accurate prediction of the machine's behaviour, before prototyping a complete machine. An overview of the existing design methodologies and approaches adopted in thermal analysis of electric machines is provided in the next section.

1.2 Design of electrical machines

1.2.1 Machine design methodologies

When designing electric machines, the large number of parameters to evaluate, the demanding and sometimes conflicting requirements, and the limited time and resources available, mean the design process is far from being standardised. A common first step in the machine design process is to choose an appropriate machine topology. There may be several topologies which would meet a set of design targets for a machine's particular application. This initial choice might be made on the basis of designer's experience or

preferences, and review of available machine types with similar characteristics. Once the choice of machine topology is made, a thorough design-analysis needs to be performed. When reviewing existing literature in the field, three main approaches for detailed machine design process can be identified.

The first design technique is an experience-based approach, where the machine design is completed analytically and informed from previous machine developments or design iterations [15]-[21]. The successful validation of a previous design means that the engineer will have confidence in the machine analysis and analytical approach associated with that previous machine. The experience-based approach usually neglects or simply assesses the thermal aspect at an early design stage, for example by limiting the magnetic loading or the current density [22]-[27]. This approach is well-suited for mature technologies supported by an abundance of available data. However, this approach has limited use in the development of less common machines, particularly where no previous experience or hardware exists. In such cases, high safety margins would typically be applied to compensate for the approach uncertainty.

The second design technique is referred to as assumption-based or 'textbook' method and consists of several consecutive steps, where the machine design is derived using a combination of analytical methods and optimisation routines [28]-[36]. Here, the more challenging design aspects are frequently analysed at a later stage of the design process using numerical methods. Such an approach became very popular in the early nineties, with the practical implementation of numerical methods such as Finite Element Analysis (FEA). This was made possible thanks to the development of modern computers. Fig. 1.2 presents a flowchart schematically illustrating a machine design practice. In this case, the thermal behaviour is verified at the end of the design process, during tests on a complete machine assembly [27], [37]-[39]. Analytical methods, such as lumped-parameter thermal equivalent circuit (TEC), may be used to predict machine temperature at an earlier stage of the design [39]-[48]. For less common machine designs, the simplifying assumptions used for the initial analytical electromagnetic sizing-optimisation routine may no longer be satisfied, and consequently, invalid machine designs may be generated. Many alterations are then required during the design validation using numerical tools, which may be a time demanding process. In such cases, the use of numerical methods or tools may be more appropriate from the onset of the design process.

The third design technique is based on a multi-physics analysis, where various design aspects are considered simultaneously to satisfy the application design requirements [26],

[27], [39]-[41], [45]-[50]. This approach has been gaining increased interest due to the standardisation of many software toolsets, the availability of high-performance computation systems, and the low cost of computation with respect to prototype manufacture. Ideally, the method uses detailed electromagnetic and thermal models iterating and exchanging information with each other, to converge to accurate predictions of machine performance. Several design aspects, such as the individual analyses of particular loss components, may also constitute building blocks for multi-physics optimisations methods. At this level of detail, a change in geometry or material of a particular component will affect all three aspects (electromagnetic, thermal and mechanical) simultaneously and in a different manner. For instance, moving from Litz wires to solid conductors makes a machine potentially better regarding thermal conduction within the slot but might also yield higher losses in that slot. In this context, the thermal analysis has to start at an early stage of the machine design process.

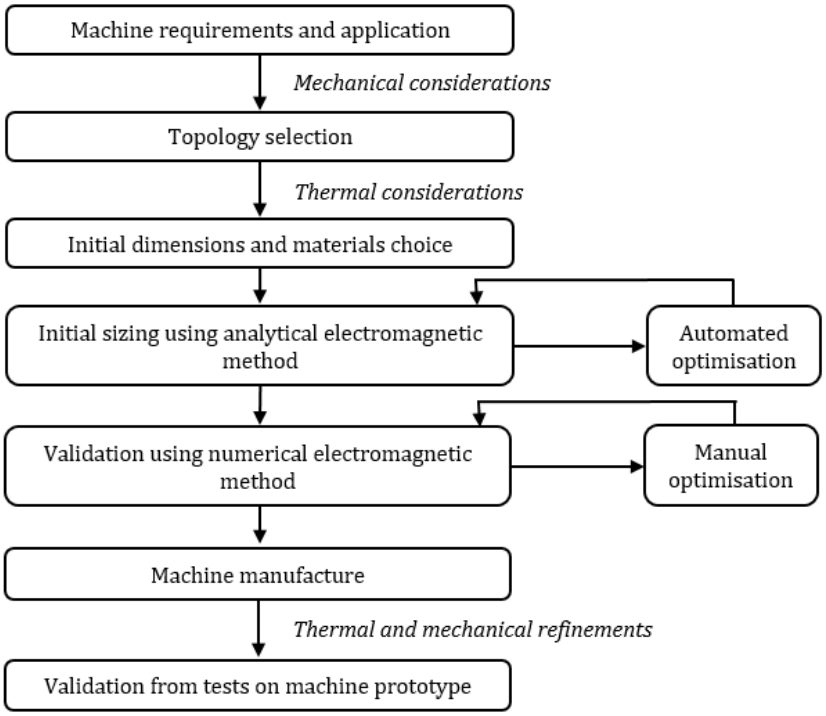

Fig. 1.2 A schematic flow chart of a selected machine design practice, where design focus is put on the electromagnetic analysis, as presented in [28]-[37].

The need for thermal modelling of electric machines emerged in the late nineties, due to the increased requirements regarding machine miniaturisation, efficiency, and high-power density. Also, at that time machines started to be operated on complex duty cycles with variable loads and speeds, and appropriate tools were required to correctly evaluate the machine thermal behaviour at steady-state and transient operations.

There are currently three main classes of mathematical approaches available for the thermal analysis of electrical machines: numerical methods including FEA, analytical methods including lumped-parameter TEC, and hybrid techniques that use a combination of both the options [51], [52].

Regardless of the design approach adopted, the thermal input data has a strong impact on the accuracy of the temperature predictions. The choice or derivation of these input parameters is usually a challenging exercise, as some of the physical phenomena are difficult to be accounted for or derived mathematically in a simple and reliable manner. At an early design stage, machine designers typically use a combination of their own experience, similar machine studies, and existing libraries of data to calibrate their models. However, this is no longer an option when considering novel machine designs. In such cases, limited published data exist, and empirical analyses are required to obtain a reliable machine thermal model.

1.2.2 Empirical approaches employed in thermal analysis

Empirical data are required in thermal analysis of electric machines, as some thermal and power loss phenomena are difficult to theoretically predict, making the estimation of thermal and loss parameters a challenging task. This is particularly true in the case of solid heat transfer because the thermal parameters influencing heat conduction highly depend on manufacturing and assembly techniques. For instance, the winding region is prone to numerous manufacturing imperfections like air cavities resulting from the winding arrangement, impregnating material, and the manufacture process used [53]. These manufacture and assembly nuances clearly make the accurate estimation of the winding thermal properties challenging for machine designers. Empirical measurements also give an insight into the power loss generated within the machine assembly. This is particularly important in the context of electric drivetrains with a relatively high operating fundamental frequency, e.g. for the traction machines frequently meeting or exceeding 1 kHz [54]. The ac effects for the PM, and winding and core pack assemblies need to be carefully considered for such applications to provide a feasible low-loss and cost-effective design solution.

The typical approach employed in empirical validation of thermal models for electrical machines makes use of thermal testing. This is usually performed at the end of the machine manufacturing process, to assess the measured thermal characteristics against the design targets and theoretical predictions. Thermal model validation from a complete machine prototype is frequently effective for experienced-based designs, where a designer has

confidence in the pre-existing machine thermal design. In such cases, as discussed earlier, the initial machine assembly should closely match the specifications. However, for novel machine topologies, a designer typically needs to evaluate several design variants to realise an optimal solution. The machine fabrication for all design iterations would not be feasible due to the cost and time constraints [55]. For these reasons, a method providing reliable loss and thermal predictions would significantly reduce the number of prototype iterations required when developing a new machine. Consequently, time and cost associated with the new design could be substantially reduced.

In this context, an empirical method employing special machine mock-ups and reduced-order sub-assemblies presents an attractive alternative, and has recently gained more interest [55]-[61]. The time and cost related to hardware manufacture for such experimental approaches are significantly reduced compared to prototyping of complete machines. This allows for numerous hardware samples to be constructed and tested to inform the machine design process. When testing a complete machine assembly, all the mechanical and electromagnetic loss components are measured together. As a result, the identification of the power loss sources is rather challenging. A clear benefit of custom-built experiments is their ability to provide a more detailed insight into various machine design aspects, e.g. segregation of power loss components or assessment of subsequent thermal effects [56]-[67].

A significant part of the recent work incorporating custom build mock-up and machine sub-assemblies focuses on the stator-winding region, which is frequently attributed with the dominant power loss component within the machine body [55]-[61]. Numerous manufacturing and assembly factors affect the stator-winding thermal behaviour and generated power loss, making them difficult to predict accurately. Stator-winding segments, so-called motorettes, allow for the experimental derivation of numerous thermal parameters associated with materials and processes used in machine construction, e.g. impact of various insulation systems on heat extraction from the winding body into the machine periphery [55]. Tests on motorette assemblies also provide vital information regarding the power loss effects generated within the stator-winding assembly. The motorette testing is limited to some of the loss effects present in the complete machine, e.g. the effects associated with rotation of the PM rotor are not accounted for. However, the measured loss data for such cases allow the identification of other effects associated with excitation and inform the design process of the stator-winding assembly [55]-[61].

The absence of some of the loss components present in the machine enables a simpler loss separation, and therefore provides a better understanding of the loss effects.

A good understanding of the link between the information extracted from a machine and its sub-assembly or mock-up experiments is required to handle the acquired data appropriately. Despite the increased interest in the machine custom-built mock-ups and sub-assembly testing, no generic experimental methodology has yet been defined. The research effort of this thesis is placed on formulating the basis for an experiment-informed machine design methodology, supplemented with machine mock-ups and sub-assemblies. This thesis focuses on PM electric machines, however, some of the techniques and findings are more generic and are applicable for other machine types. A detailed definition of the research objectives is provided in the following section.

1.3 Research objectives

The continuous drive towards 'more electric' technologies and the subsequent need for high-performance electric machines calls for a more accurate and reliable thermal design-analysis, where various design, manufacture and assembly factors are accounted for at the initial stage of the design process. The wide ranges of built factors have significant impact on the overall thermal behavior of the machine and frequently require empirical techniques to validate the initial design assumptions. In this context, testing methods that use the reduced-order machine subassemblies allow for a time and cost-effective derivation of various heat transfer coefficients and more in-depth analyses of power loss components are very desirable. The methods would also permit the reduction of the safety margins that are typically applied to compensate for the uncertainty associated with the thermal and power loss parameters.

The research objective of this PhD project is to validate a systematic and reliable experimentally-informed methodology for the high-fidelity thermal design of electrical machines. The developed approach should be sufficiently generic to account for a variety of PM machine designs, where the main heat source, associated with stator-winding assembly, is evacuated by conduction into the machine periphery. The methodology is not limited to the heat transfer analysis but also gives an insight into the loss generated in the stator-winding assembly. This is particularly important in the context of electric drive trains with a relatively high operating fundamental frequency, e.g. for the traction machines frequently meeting or exceeding 1 kHz. The ac effects, both for the winding and core pack assemblies need to be carefully considered for such applications to provide a feasible low-

loss design solution. Efficacy of the proposed methodology is to be validated on a number of machine demonstrators with different build attributes, which include machine topology and winding construction.

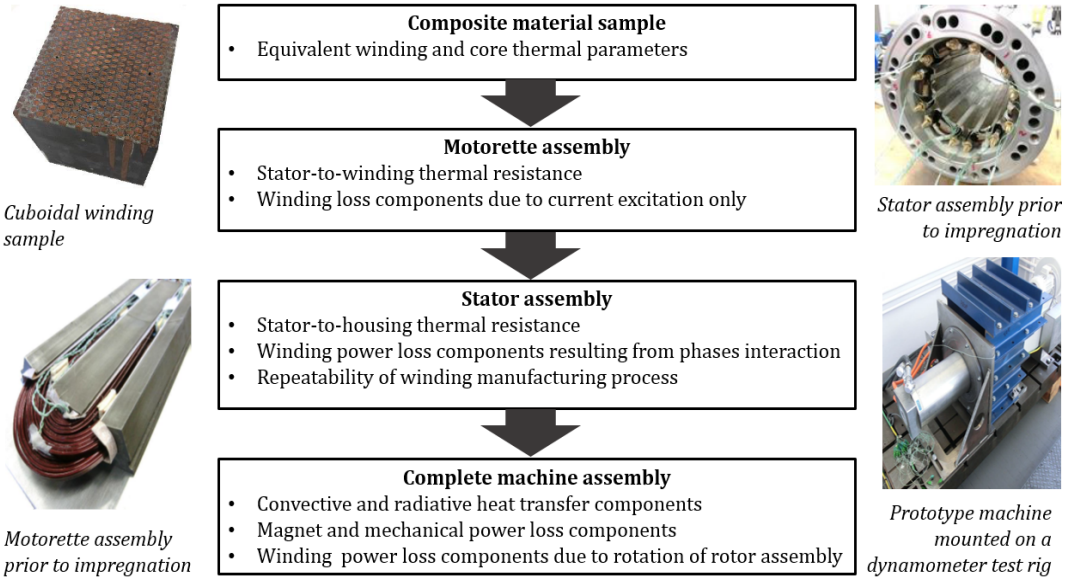

Fig. 1.3 Schematic flowchart of the proposed methodology

The first building block of the methodology (composite material sample) is used for the evaluation of the thermal characteristics for both homogeneous and composite materials For example, winding conductor, enamel and impregnation material, or laminated core packs with an insulating layer and adhesive, among others. The second building block of the methodology (motorette assembly) is used for the estimation of the dissipative heat transfer within a slot, and to extract some data regarding the power loss generated in the stator-winding assembly. The motorette approach offers significant reduction of manufacture cost and time in comparison to prototyping a complete machine. The third building block of the methodology (stator assembly) is used to evaluate the power loss from the interaction between neighbouring phases and repeatability of the winding manufacturing process. The fourth building block of the proposed methodology (complete machine assembly) is used for the estimation of convective and radiative heat transfer coefficients. The complete machine assembly also allows for the evaluation of the power loss effects resulting from the rotation of the rotor assembly, including PM and winding electromagnetic power loss components. The use of custom-built machine mock-ups and sub-assembly testing is intended to improve the design process and to provide a library of various build-factors for future development. Clearly, the final building block of the methodology (a complete machine assembly provides the most comprehensive source of information.

This includes temperature and loss effects due to the rotation of the rotor assembly, cooling set-up and convective and radiative heat transfer components, among others.

1.4 Thesis scope

This thesis is divided into eight chapters, as summarised below. The scope of the research intends to cover the importance of coupled electromagnetic and thermal analyses. For this reason, the author only refers to mechanical analysis when relevant.

A thorough literature review is conducted in Chapter 2. The main techniques of machine thermal management, from heat sources to heat sinks, are investigated. Available methods for the thermal modelling and testing of electrical machines are reviewed, including custom-built experiments and machine sub-assemblies. The review results in the definition of a set of focused research objectives covered in the remainder of the thesis.

A guided overview of the proposed methodology is presented in Chapter 3. The selected building blocks of the developed methodology are briefly examined, together with the machine exemplars selected for illustration. An emphasis is put on explaining build attributes of the selected machine exemplars, together with some considerations on how to improve the robustness of the methodology.

The first building block of the methodology, composite material properties, is investigated in Chapter 4. Methods used to determine the bulk thermal parameters of an electric machine's active elements are presented, together with suitable modelling approaches.

The methodology's second building block, motorette assembly, is presented in Chapter 5. The use of motorette assemblies for the estimation of dissipative heat transfer within a slot is investigated, in conjunction with power loss identification and characterisation. This includes a review of the most suitable testing and modelling approaches.

The third building block of the methodology, stator assembly, is investigated in Chapter 6. Methods used to evaluate the dissipative heat transfer are analysed along with the manufacture repeatability of the winding process. The power loss analysis is focused on interaction between the winding's phases.

Chapter 7 showcases the practical use of the methodology on selected machine demonstrators and case studies, including available hardware and data, and other general considerations regarding machine testing.

Chapter 8 concludes the presented research with a summary of the main contributions and suggestions for the future work, which could extend the applicability of the developed methodology.

Chapter 2
Literature Review

2.1 Introduction

The continuous drive towards 'more electric' technologies and the subsequent need for high-performance electric machines calls for a more accurate and reliable thermal design-analysis. An inaccurate assessment of thermal behaviour could lead to significant reduction of machine performance and reliability. For instance, underestimating the magnet temperature could result in an overestimation of the torque/power output capabilities, as the PM array remanence and coercivity decreases with temperature [68]. In the worst case, the elevated magnet temperatures might cause demagnetisation of the PM array and machine fault. Similarly, a lesser than expected heat transfer from the winding assembly could lead to machine derating in order to prevent damaging the electric insulation of winding conductors. However, despite of these important phenomena, thermal analysis of electric machines has only recently become a prominent issue. First records of thermal and power loss analysis in electric machines are found in the 1910s, when the limits of insulation [69], [70] and the importance of knowing the heat paths for identifying hot spots [71], [72], were presented. In [73], the need for cooling methods is highlighted for the first time. Nevertheless, the research into accurate tools for the thermal design and analysis of the electrical machines was only developed as recently as the early nineties. Before then, electrical engineers used to focus on the electromagnetic aspects of the machine design, as evidenced by the number of technical publications available on the subject. Designers' personal experience and elementary sizing approaches such as limiting the machine current density or magnetic load would be used to restrict machine hot spot [74], [75]. The approximative nature of such approaches frequently results in large design safety factors, which then might lead to an oversized machine design. Nowadays, the ever-increasing demand for compact, power dense and lightweight machine solutions enforces the use of a more holistic machine design approach, where thermal analysis is an important part of the process. The design tools used in thermal analysis need to accommodate for both the steady-state and transient operation to accurately evaluate the machine's performance for variable load or duty cycle.

This chapter presents a literature review of the topics relevant to the research carried out in this thesis. Firstly, a top-level overview of the main themes associated with thermal management is provided, including matters related to the heat source and heat paths. Secondly, the mathematical methods and tools for thermal analysis of electric machines are discussed. Thirdly, the available techniques for experimental calibration of the design process in application to PM machines are reviewed.

2.2 Heat sources

The power losses in electric machines are generated by two physical mechanisms: electromagnetic and mechanical. A common first step for the thermal analysis of electric machines is to identify the dominant power loss mechanism. The degree of detail with which the power loss is analysed is then adapted to the desired fidelity of the thermal modelling method. Two major trends can be identified when reviewing work on power loss analysis in electrical machines.

The first trend, which is the most recent, consists of a multi-physics design optimisation, where thermal and electromagnetic analyses are considered concurrently. Ideally, such method makes use of detailed electromagnetic and thermal models iterating and exchanging information with each other in order to converge to an accurate loss prediction. The computation time of such an approach is often prohibitive, especially when modelling transient operating conditions [76]-[78]. High-throughput computing (HTC) may be used to reduce computation time [76], [79]. However, this option is not always available and simplifying assumptions are typically chosen, which can diminish the accuracy of the models.

The second design trend includes separate individual analyses of particular loss components. This provides a precise overview of the power loss components at an early design stage, and allows the effective generation of accurate power loss data, e.g. the use of mapping techniques. The studied loss components then form the building blocks for multi-physics optimisation methods.

2.2.1 Electromagnetic Loss Components

In PM electric machines, the winding losses are typically the dominant power loss components within the machine assembly [80]-[88], and are associated with the stator assembly. A simplified expression for the winding power loss at ac operation includes three main components:

$$P_{ac}(I,f,T) = P_{dc}(I,T) + P_{ac,e}(I,f,T) + P_{ac,r}(f,T) \quad (2.1)$$

where P_{dc} is the dc winding power loss, $P_{ac,e}$ is the ac winding power loss resulting from the winding excitation, $P_{ac,r}$ is the ac winding power loss from rotational effects of the PM array and *I, f, T* are the current amplitude, frequency and temperature, respectively. P_{dc} is easily found from the dc winding resistance and dc current. $P_{ac,e}$ and $P_{ac,r}$ result from four loss effects: the skin effect, the circulating current effect, the proximity effect, and the rotational effect. The skin effect is the tendency for high-frequency current to flow on the surface of a conductor due to its own magnetic field, and can be quantified using the skin depth formula [81]. Circulating current effects result from different inductance per individual strand of conductors connected in parallel, which lead to uneven current sharing. The proximity effect is the tendency for high-frequency current to exhibit concentrated distribution due to the magnetic field generated by neighbouring conductors. The rotational effect results from the rotor magnetic field that varies spacially and leads to eddy-currents being generated in the winding. $P_{ac,r}$ is particularly significant in the case of open-slot stator topologies [83], [89]. Indeed, the absence of tooth tips results in the conductors at the top of the slot being more exposed to the rotor magnetic field.

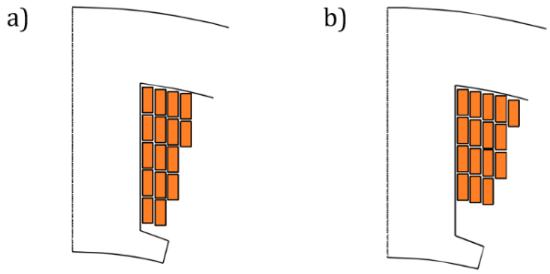

Fig. 2.1 Alternative winding layouts, a) conductors concentrated at top of the slot, b) conductors concentrated at the rear of the slot [83]

In [83], two winding configurations are compared as seen in Fig. 2.1: one with the conductors concentrated at the top of the slot, Fig. 2.1a), and the other with the conductors concentrated at the rear of the slot, Fig. 2.1b). A notable increase in ac winding power loss is observed in the first configuration. The presence of the tooth tip also contributes to elevated ac winding power loss, as the slot leakage flux increases when the slot opening is made narrower, resulting in higher proximity losses in the case of the first configuration [84].

A commonly used figure of merit, when characterising the ac winding loss, is the ratio of equivalent ac and dc resistances, (R_{ac}/R_{dc}). This ratio defines the average winding power loss at ac operation, and is usually obtained as follows:

$$\frac{P_{ac|f,I_{RMS},T_0}}{P_{dc|f,I_{dc},T_0}} = \left(\frac{R_{ac}}{R_{dc}}\right)_{|f,I_{RMS},T_0} \qquad (2.2)$$

where I_{RMS} and I_{dc} are the root means square (RMS) and dc current, respectively, and T_0 is the temperature at which the ac and dc winding power loss are calculated or measured. A variety of functional representations for the ac winding power loss components has been developed [80]-[84]. The underpinning work in the field is devoted to the design analysis of passive wound components and transformers with operating frequencies reaching hundreds of MHz. These frequencies are far beyond the range of fundamental frequencies for the electric machines (approximately 1kHz) [80]. Recent developments for functional representations of the ac winding power loss focus on electrical machines [81]-[84]. In [83], the winding power loss due to excitation $P_{ac,e}$, is expressed for windings formed with large section conductors. In [81] and [82], the total winding power loss, P_{ac}, is expressed for bundles of round conductors. The analytical expressions nonetheless suffer from a reduced applicability or accuracy due to the simplifying assumptions that were made for a specific application. The importance of knowing the position of the individual conductors within the slot for accurate winding power loss analysis has been also emphasised in the literature [81]-[86]. For instance, for a winding formed with a bundle of parallel strands, there may be more proximity loss when the parallel strands are wound one at a time than when all the strands are simultaneously wound, as in so called “grouped turns” [85].

Several research works focus on the development of methods for reducing the ac winding power loss components [83], [85]-[87], [89]. The common approach to reduce skin effects is to select the appropriate conductor cross-section based on the operating frequency and subsequent skin depth. This results in lower conductor cross-sections when the frequency is higher [81]. The proximity and circulating current effects can also be mitigated by a careful arrangement of the conductors [85]-[87]. As previously mentioned, the circulating currents in parallel connection of conductors are caused by the variation in inductance resulting in uneven current sharing per individual strand. If the conductors are arranged so that they are all exposed to the same quantity of magnetic field, then the circulating currents should be reduced. This can be achieved by twisting or transposing a bundle of conductors, at strand or bundle level. An analytical formula and optimal criterion have been defined to quantify these effects for various conductor types [86], [87]. Litz wires (a bundle consisting

of many thin individual strands, periodically transposed so that each strand occupies all positions within the conductor bundle) and Roebel bars (a large number of individual braided strands) are readily-available solutions [90]-[93]. Litz wires have been widely researched, where the requirement for minimum ac loss informs the conductor size and the way the strands are twisted [90], [91]. However, Litz wires, and windings with twisted bundles of conductors in general, have their own drawbacks in terms of copper fill factor, manufacturing cost and poor equivalent thermal conductivity. The insulation on the individual fine conductors is usually thin, and an additional layer of insulation paper might also be required to ensure a proper insulation between coils or turns, further worsening the heat transfer from the winding assembly. A comparison between windings with straight and twisted bundles of conductors is presented in [85] and highlights the benefits of twisting, Fig. 2.2a). The strand currents start to diverge from their uniform distribution at an early frequency of 80 Hz for the straight winding, as opposed to 1 kHz for the twisted coil, as seen in Fig. 2.2.b).

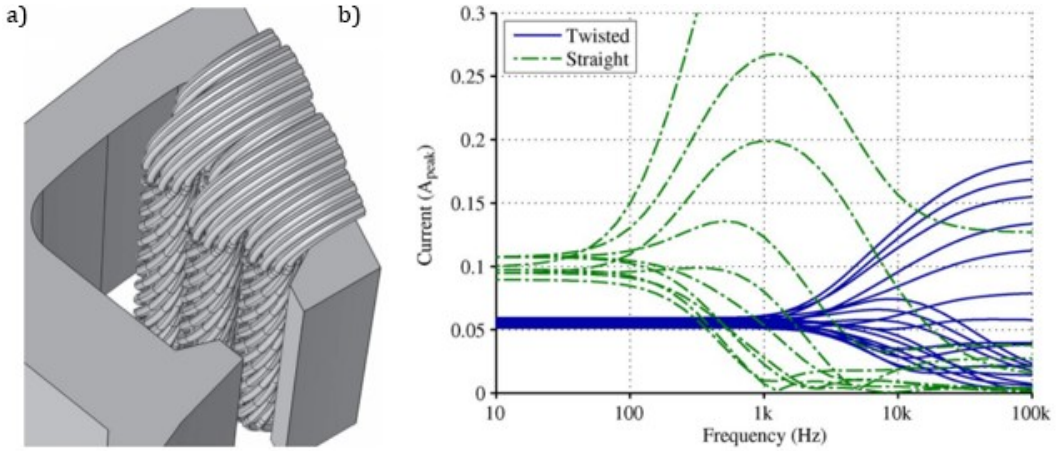

Fig. 2.2 a) Analysed twisted winding, b) Strand currents as functions of frequency for one straight and one twisted winding [85]

The temperature dependence of the winding power loss effects also needs to be accounted for. An important point to consider is the different dependence with temperature of the dc and ac winding power loss components. An increase in temperature implies a rise in resistivity, which leads to an increase in the dc power loss components. However, for the eddy-current related effects, a rise in resistivity implies a decrease in the induced voltage, so a reduction over the ac winding loss. This is however valid only for the resistance limited ac effects. The literature suggests that the ac winding loss becomes inductance limited for a high excitation frequency compared to the conductor skin depth [88], [96]. The change

in the electrical resistivity ρ of the conductor material due to the temperature is accounted for by using (2.3):

$$\rho = \rho_0(1 + \alpha(T - T_0)) \qquad (2.3)$$

where ρ_0 is the electrical resistivity of the conductor material at reference temperature T_0= 20ºC, and α is the temperature coefficient of the electrical resistivity, e.g. $\alpha = 3.93 \times 10^{-3}\mathrm{K}^{-1}$ for copper conductors. The winding power loss at ac operation varies with temperature in a more complex manner than that for dc excitation, and usually requires the derivation of the ratio of equivalent ac to dc resistance. Several methods are available for the derivation of the (R_{ac}/R_{dc}) ratio, including analytical formulas, FEAs, or experimental approaches [83]-[87], [92]-[95]. The analytical methods allow for a rapid derivation of the winding ac power loss, but are usually based on simplifying assumptions and consequently are only suitable for selected applications [84], [86], [87], [92], [97]. FEAs provide accurate ac loss data when the conductor positions within the slot are known and characterised. However, model alteration and solving for successive slot design iterations might be time-consuming. Experimental approaches provide an alternative to mathematical methods, where functional representations of the winding loss with frequency, temperature and magnitude are considered [94], [95]. However, measurements might not be feasible at an early design stage, due to the cost and time associated with hardware manufacturing.

The ac winding power loss has been discussed predominantly in the context of the winding active length, as the ac loss contribution associated with the end-winding region is usually less significant. Typically, only the dc loss component of the end-winding is accounted for [56], [89], [97]. However, the research focusing on concentrated winding has shown that at high-speed or high-frequency operation and for machines with short active lengths, the end-winding ac effects are not negligible [58], [89]. In this context, experimental measurements appear as a reliable alternative, as the derivation of the end-winding ac loss usually requires the use of complex 3D mathematical models. More research is required however to provide a clearer insight into the end-winding ac effects.

The functional representation of the ac winding power loss temperature dependence, proposed in [99], is provided in (2.4):

$$P_{ac|T_0} = P_{dc|T_0}\big(1 + \alpha(T - T_0)\big) + P_{dc|T_0}\frac{\left(\frac{R_{ac}}{R_{dc}}\right)_{|T_0}^{-1}}{\big(1+\alpha(T-T_0)\big)^{\beta}} \qquad (2.4)$$

where β is the temperature coefficient for the ac loss component and T_0 is the temperature at which P_{dc} has been calculated. The parameter β can be derived from a curve fit of (2.4) to the winding ac power loss data derived from FEAs or experiments at two reference temperatures. An updated version of (2.4) is presented in [89], where the temperature dependences of $P_{ac,r}$ and $P_{ac,e}$ are individually accounted for:

$$P_{ac|T_0} = P_{dc|T_0}\big(1+\alpha(T-T_0)\big) + P_{dc|T_0}\frac{\left(\frac{R_{ac}}{R_{dc}}\right)_{e|T_0}^{-1}}{\big(1+\alpha(T-T_0)\big)^{\beta}} + P_{ac,r|T_0}\frac{1}{(1+\alpha(T-T_0))^{\gamma}} \qquad (2.5)$$

Where $(R_{ac}/R_{dc})_e$ defines the average winding power loss due to excitation at ac operation,

$$\left(\frac{R_{ac}}{R_{dc}}\right)_{e|T_0} = \left(\frac{P_{ac}-P_{ac,r}}{P_{dc}}\right)_{e|T_0} \qquad (2.6)$$

and γ is the temperature coefficient for the ac loss component due to the rotation of the rotor PM array. Here, β is the temperature coefficient for the ac loss component due to excitation only. The parameter γ can be derived from a curve fit of (2.5) to the winding ac loss data derived from open-circuit FEAs or experiments at two different reference temperatures. The use of the $(R_{ac}/R_{dc})|_{T_0}$ ratio together with (2.4) or (2.5) can considerably reduce the number of required ac winding loss calculations. For instance, a map of the $\left(\frac{R_{ac}}{R_{dc}}\right)|_{T_0}$ ratio can be derived against the excitation current and/or frequency. The obtained values can then be supplied to the thermal model, with (2.4) or (2.5) appropriately accounting for the winding loss temperature dependence. This approach may form building blocks for a multi-physics optimisation procedure, and constitutes a computationally-efficient approach compared to coupled electromagnetic and thermal modelling. The impact that the change of current angle has on the $(R_{ac}/R_{dc})|_{T_0}$ ratio during field weakening operation has not yet been investigated in the literature.

The common approach in thermal modelling of electric machines is to average the total winding power loss over the winding region [56], [57], [98]. However, it has been outlined that this homogeneous power loss representation might not provide sufficient resolution, in particular when ac effects are expected to be significant [96], [97]. In this case, a decomposition of the winding assembly in appropriate sub-regions ensures a more-accurate identification of the winding hot-spot and averaged temperature predictions [89], [96].

More work is nonetheless required to provide a clearer understanding of the effects of inhomogeneous loss distribution on temperature prediction.

The core power loss is associated with both the stator and rotor cores, and depends on the machine topology, operating frequency, and flux density at which the core operates, among others. In PM machines, the core power loss component is typically second in terms of contribution to the overall power loss within the machine assembly. The core power loss is attributed to three mechanisms: the hysteresis loss component, P_{hyst}, caused by the reversal of magnetisation of the core due to its exposition to a time-varying magnetic field, the eddy current loss component, P_{eddy} due to the eddy-current induced in the core lamination due to Faraday's law of induction, and excess or anomalous loss component, P_{exc}, including any other material related loss effects [100]-[103]. The commonly-used approach of deriving the core loss in design analysis of electrical machines is based on the Steinmetz or Bertotti methods or even more comprehensive variations of these techniques [100]-105]. These methods provide accurate results if the appropriate loss coefficients are used [100]. These coefficients are usually provided by the manufacturer. However, the core manufacturing and assembly process might impact the coefficient values [100], [103]. In this case, a degree of experimental measurements is required to obtain accurate loss data. The Steinmetz and Bertotti equation in case of sinusoidal excitation is formulated in (2.7) [105]:

$$P_{iron}(f,B) = P_{hyst}(f,B) + P_{eddy}(f,B) + P_{exc}(f,B) = \varepsilon_h f^a B^b + \varepsilon_e f^2 B^2 + \varepsilon_{exc} f^{1.5} B^{1.5} \quad (2.7)$$

Where ε_h, ε_e and ε_x are the hysteresis, eddy-current and excess loss coefficients, respectively and B is the flux density. This expression can be adapted to account for the harmonic components [102]:

$$P_{iron}(f,B) = P_{hyst}(f,B) + P_{eddy}(f,B) + P_{exc}(f,B) = P_{hyst}\left(1 + \frac{k}{B}\sum_{i=1}^{N}\Delta B_i\right) + \varepsilon_e f^2 \sum_{h\geq 1}|hB_h|^2 + P_{exc}(f,B) \quad (2.8)$$

where k is a constant in a range of 0.6-0.7, N is the number of minor loops, ΔB_i is the flux reversal associated with a given minor loop, and B_h is the amplitude of the h^{th} flux density harmonic. The temperature dependence of the core loss is usually neglected in the context of laminated steel, as the temperature coefficient of steel, $\alpha_{steel} = 9.4 \times 10^{-4} K^{-1}$, is very small compared with the one for copper [100], [107]. However, this might be of interest

for high-speed applications or high-fidelity thermal modelling. Using (2.3), (2.8) can been adapted to account for the core loss thermal dependence as described in (2.9) [100]:

$$P_{iron} = P_{hyst} + \frac{P_{eddy}}{1+\alpha_{steel}(T-T_0)} + P_{exc} \qquad (2.9)$$

The temperature dependence of the core loss might be significant for materials other than steel, e.g. iron powder or ferrite cores. Nowadays, the Steinmetz and Bertotti equation is usually implemented in FE software packages, which allows the derivation of separate core loss components for the machine regions of interest. However, when completing transient analysis or evaluation on a complete duty cycle, many points need to be evaluated and carrying out FEA for each iteration may be prohibitive. The iron loss generated over the entire torque-speed envelope can be derived by coarsely mapping the loss as a function of the stator current magnitude, I_{pk}, and the current angle, γ_I. The resulting FE predictions are then interpolated to provide high-fidelity loss maps. The effect of operating frequency/rotational speed may be accommodated using the following formula,

$$P_{iron}(f, I_{pk}, \gamma_I) = P_{hyst|_{f0}}(I_{pk}, \gamma_I)\left(\frac{f}{f_0}\right)^a + P_{eddy|_{f0}}(I_{pk}, \gamma_I)\left(\frac{f}{f_0}\right)^2 + P_{exc|_{f0}}(I_{pk}, \gamma_I)\left(\frac{f}{f_0}\right)^{1.5} \qquad (2.10)$$

Where $P_{hyst|_{f0}}$, $P_{eddy|_{f0}}$ and $P_{exc|_{f0}}$ are respectively the hysteresis, eddy currents and excess iron loss components calculated at a frequency f_0. This method allows for a significant reduction of the computational effort associated with the calculation of the core power loss, when compared to calculating core power loss at many operating points over an entire duty cycle or torque/speed envelope. Alternatively, functional representations of the core loss have been developed to allow the derivation of the core loss data for the entire torque-speed envelope in a time-efficient manner [103], [104], [106]. The methods make use of a reduced number of FEAs to define the developed core loss functions. The first method requires two FEAs at open-circuit (OC) and one at short-circuit (SC) operations [103], while the second uses a least square fitting method on fifteen FEAs to obtain the direct, quadrature and PM flux linkages and to estimate the core loss components [104], [106]. The method also enables the evaluation of the machine torque and output voltage. Methods available for the experimental derivation of the core power loss are described at section 2.5.

High magnet temperature may lead to a reduction of the machine torque output capability and possible machine breakdown. In this context, it is crucial to maintain the PM loss at a

reasonable level, in particular in the absence of the specific rotor heat extraction system. Therefore, the PM power loss, if appropriately designed, is typically the lowest component in terms of contribution to the overall power loss within the machine assembly. Intensive research effort has been carried out to analytically estimate the magnet loss, focusing in particular on rare-earth PMs due to their relatively high electrical conductivity [107]-[113]. Comparatively, the PM loss is frequently neglected when ferrite PMs are adopted, due to their relatively low electrical conductivity. The loss component from rare-earth PMs mainly results from eddy-current effects, as hysteresis effects are often shown to be insignificant [107]. For instance, a simplified expression, neglecting skin effect and assuming the flux density across the magnet is uniform, can be used to get a first estimation of the magnet loss as described in (2.11) [110]:

$$P_{pm} \approx \frac{V_{pm} w_{pm}^2}{24 \rho_{pm}} \sum_i B_i^2 f^2 i^2 \qquad (2.11)$$

Where V_{pm}, $w_{pm}$and ρ_{pm} are the magnet volume, width and resistivity, respectively and i is the harmonic index. The analytical expressions nonetheless suffer from a reduced accuracy due to their simplifying assumptions or specific applications. For novel designs or high-fidelity modelling, FEA methods can be used to calculate the induced eddy-currents in the magnet segments and determine the corresponding loss components. When segmented magnets are used, it is crucial to employ 3D models to account for the boundary effects, including fringing [114]. The use of 3D numerical models allows accurate solutions, but with a high computational effort. As for the core loss compound, FEA evaluation of each intended machine operating point would be prohibitively long. In [108], a method is provided to derive an accurate mapping of the PM loss across the full operating envelope using a reduced number of FEAs. The method is based on a functional representation of PM loss with a set of coefficients *a*, *b*, *c* and *d* derived from a reduced number of FEAs as described in (2.12) [108]:

$$P_{pm} = (aI_q^2 + bI_d^2 + cI_d + d)\left(\frac{n}{n_0}\right)^2 \qquad (2.12)$$

where I_d and I_q are the magnitudes of the demagnetising direct and quadrature axis components of the stator phase current, respectively, n is the rotational speed, and n_0 is the speed at which all the parameters are derived. The coefficients *a* and *b* account for the PM loss from the armature reaction, whereas *c* and *d* are attributed with the PM loss associated with the stator slotting harmonics.

A typical solution to reduce the PM loss components is to axially segment the magnets. The number of PM segments is typically carefully optimised: a high number of segments reduces the PM loss component, but with drawbacks such as the reduction of mechanical stability and the increase of manufacturing price [110]-[113]. The temperature dependence of PM loss components is often overlooked until it is shown to be significant [109]. If so, it has been shown in [109] that the temperature dependence of the resistivity is quadratic for Neodymium Iron Boron (*NdFeB*) magnets and linear for other magnet types, such as Samarium cobalt (*SmCo*). Experimental techniques available for derivation of the magnet power loss are describe in section 2.5.

2.2.2 Mechanical Loss Components

The mechanical loss is a consequence of friction and windage/drag effects [115]-[119]. These loss components have not been widely discussed in the literature, and are usually neglected at an early design stage [113]. Empirical measurements typically provide a first insight into the friction and windage loss mechanisms. Friction losses are mainly caused by bearing friction, and depend on shaft speed, bearing type, and load, among other factors [115]. The common approach adopted by machine designers to estimate friction losses is to use the manufacturer bearing data loss at the bearing nominal operating conditions [116]. Windage/drag losses are a consequence of aerodynamic drag between the rotating surfaces and the surrounding gas or fluid, usually air or oil. Most of the work in the field concerns high-speed or forced air-cooled machines, where the windage loss effects are expected to be significant. Empirical formulas using simplifying assumptions are available for estimating the mechanical loss components [115], [116], [119]. For instance, a general expression for the mechanical loss for 'small' machines with natural air cooling was introduced in [115]:

$$P_{mechanical} = P_{windage} + P_{friction} = \pi \rho_{d,air} C_d \, r_r^4 l_r \, n^3 + \, K_{fb} m_r n \qquad (2.13)$$

Where r_r, l_r, m_r are the rotor outer radius, length and weight, respectively, $\rho_{d,air}$ is the air density, n is the machine rotational speed, C_d is the skin friction coefficient and K_{fb} is the frictional loss coefficient. Clearly, these generic, empirically derived formulas do not account for operating conditions, like temperature, which can lead to inaccurate results. Numerical methods, such as computational fluid dynamics (CFD), are commonly used to obtain more comprehensive estimations. Some correlations obtained from hardware tests are nonetheless required to provide more generic solutions [117]-[119]. The temperature dependence of the mechanical loss has not yet been investigated in the literature. However,

the thermal effects of the mechanical loss have been highlighted in a number of publications [62]-[65]. This includes the impact of the dissipation of the mechanical loss in the surrounding area, and the accelerated degradation of the bearing lubricants in the case of elevated bearings temperature [117], [120].

A large number of procedures available for the power loss analysis of electrical machines has been presented in this section. It has been shown that high-fidelity numerical methods provide a detailed insight into several loss mechanisms, but are computationally-intensive, while analytical methods are usually limited to a certain class of problems and the associated simplifying assumptions reduce their accuracy. The effective generation of accurate power loss data, using for instance mapping techniques, appears as a computationally-efficient solution in the context of thermal analysis. These power loss data can indeed be used as building blocks for multi-physics optimisation methods. A first sense of the importance of the experimental data for machine power loss analysis has been demonstrated, with two main purposes. On one hand, a degree of experimental analysis is required to estimate the impact on the power loss effects of manufacturing and assembly techniques and inform the numerical models. On the other hand, empirical analyses provide an alternative to the numerical methods in the context of challenging model representation, e.g. evaluation of the winding loss when the precise location of the individual conductors in the slot is unknown. Functional representations of the power loss, accounting for temperature, frequency and magnitude of excitation current, among others, may be derived using the empirically derived data.

2.3 Heat extraction systems

Methods for the heat extraction of electric machines vary according to the machine topology. In synchronous reluctance machines, the rotor is magnet-free, so the cooling focuses on the stator assembly. In induction machines, the important amount of heat produced within the rotor assembly due to the ac effects in the rotor winding or squirrel cage needs to be carefully monitored. In PM machines, it is essential to prevent magnet demagnetisation, so a part of the thermal analysis focuses on the rotor assembly and its neighbouring regions. For this machine type, the dominant source of loss is usually within the winding assembly, so efficient heat extraction from this region is required. Modern applications, where electrical machines are employed frequently rely on forced convection cooling systems that use a fluid to remove heat from the machine and transfer it to another location [121]-[136]. Other cooling techniques make use of heat transfer by radiation or

conduction [136]-[141]. Table 2.1 presents typical rules of thumb for cooling techniques and associated heat transfer coefficients [68], where h_{h-a} refers to the heat transfer coefficient from the machine housing frame to ambient. It is evident that a high heat transfer coefficient, i.e. good dissipative heat transfer, allows for high current density, which in turn results in higher machine output torque capability. However, high cooling efficiency is typically achieved using a high complexity system. Depending on the system requirements, thermal designers need to find the right compromise between cost, manufacturability and performance. This section reviews the techniques available for machine cooling, starting with convective heat transfer.

Table 2.1. Rules of thumb for cooling types and heat transfer coefficients [68]

Cooling type	Fluid employed	h_{h-a} [W/m^2/ºC]	Current density [A/mm^2]	Cooling system complexity
Natural	Air	5 – 10	1 – 5	Low
Forced	Air	10 - 300	5 – 10	Medium
Forced	Liquid	50 - 2000	10 – 30	High

2.3.1 Convective heat transfer

Undoubtedly, the simplest cooling method consists in dissipating heat to the ambient via natural convection. In natural air cooling, the fluid movement results from buoyancy forces, emerging from the variation of density within the fluid. A typical formula for the natural convection dimentionless parameters is defined in (2.14), (2.15) and (2.16) [121]:

$$h_{natural} = k.\frac{Nu}{L_{surf}} = k.\frac{a.(Gr.Pr)^b}{L_{surf}} \quad (2.14)$$

$$Gr = \beta_{cubic}.g.\Delta T.\rho_d^2.L_{surf}^3/\mu^2 \quad (2.15)$$

$$Pr = c_s.\mu/k \quad (2.16)$$

where *Nu* is the Nusselt number, *Gr* is the Grashof number, *Pr* is the Prandtl number, $h_{natural}$ is the natural convection heat transfer coefficient, L_{surf} is the characteristic length of the surface, g is the gravitational attraction force, β_{cubic} is the coefficient of cubical expansion, k, ρ_d, μ and c_s are the fluid thermal conductivity, density, dynamic viscosity and specific heat capacity, respectively, and a and b are constants, given in the correlation. In Totally Enclosed, Non-Ventilated (TENV) machines, the outer surfaces of the housing frame dissipate heat by natural convection and radiation. The external surfaces of a TENV machine housing can be smooth, however fins are frequently included to

increase the convection surface [121], [125]. Fig. 2.3 presents examples of housing types that are suitable for TENV electric machines.

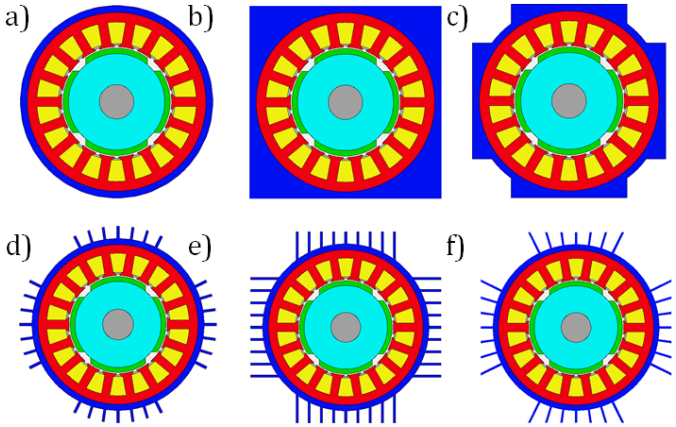

Fig. 2.3 Housing types suitable for TENV electric machines a) Round, b) Square, c) Servo, d) Round with fins, e) Square with fins, f) Servo with fins [130]

In forced cooling, the fluid motion is due to an external force, e.g. fan and pump, among others [122]. Fig. 2.4 presents some available methods for forced-convection cooling [130]. The fluid velocity will influence the flow regime, from laminar to turbulent. This will influence the heat extraction, e.g. turbulent heat flow will result in an increased heat transfer but with a larger pressure drop, hence a reduced flow rate. A typical formula for the forced air convection dimensionless parameters is defined in (2.17) and (2.18) [121]:

$$Nu = a.Re^{b}.Pr^{c}=h_{forced}.L_{surf}/k \qquad (2.17)$$

$$Re = \rho_{d}.n_{f}.L_{surf}/\mu \qquad (2.18)$$

where *Re* is the Reynolds number and n_f is the fluid velocity. A comparison between (2.14) and (2.17) highlights that natural convection is a function of the fluid properties and temperature difference between solid and fluid, while forced convection is a function of the fluid velocity and fluid properties. Some fluid properties are temperature dependent, so the fluid and solid temperatures also have an impact on forced convection. Forced-air cooling methods include totally enclosed, fan-cooled (TEFC) electric machines and 'through' machine ventilation. In TEFC machines, the heat dissipation from the machine housing frame is improved using forced-air cooling, with housing fins typically carefully designed to optimise the heat dissipation [121], [123], [141]. For stator or rotor 'through' cooling, air is ventilated through the stator or rotor via cooling ducts [122], Fig. 2.4a). Commonly used forced-liquid cooling techniques include water jackets, spray cooling and direct conductor cooling, among others [120], [122], [125], [131], [132].

Water jacket stator cooling is one of the most commonly used liquid-cooling methods, Fig. 2.4b). The technique uses a machine housing with a liquid-filled casing equipped with inlet and outlet apertures to allow the liquid to be pumped through and circulated. The liquid flow might be regulated, which allows for an accurate control of the temperature. This is well-suited for power dense machines used in traction applications, where the same cooling circuit might be used for the electric machine and the drive units [120], [122], [132]. Another liquid-cooling technique, sometimes referred to as shaft spiral groove, consists in passing a fluid down ducts in the shaft, Fig. 2.4c), enhancing the heat extraction from the rotor [131] or winding stator in the case of an outer-rotor topology [89]. Advantages of housing water jackets and shaft spiral grooves include low levels of noise and a completely enclosed setting. Disadvantages include high manufacturing costs, with the requirement for an auxiliary pumping system and risk of leakage, among others [89], [120], [122], [131].

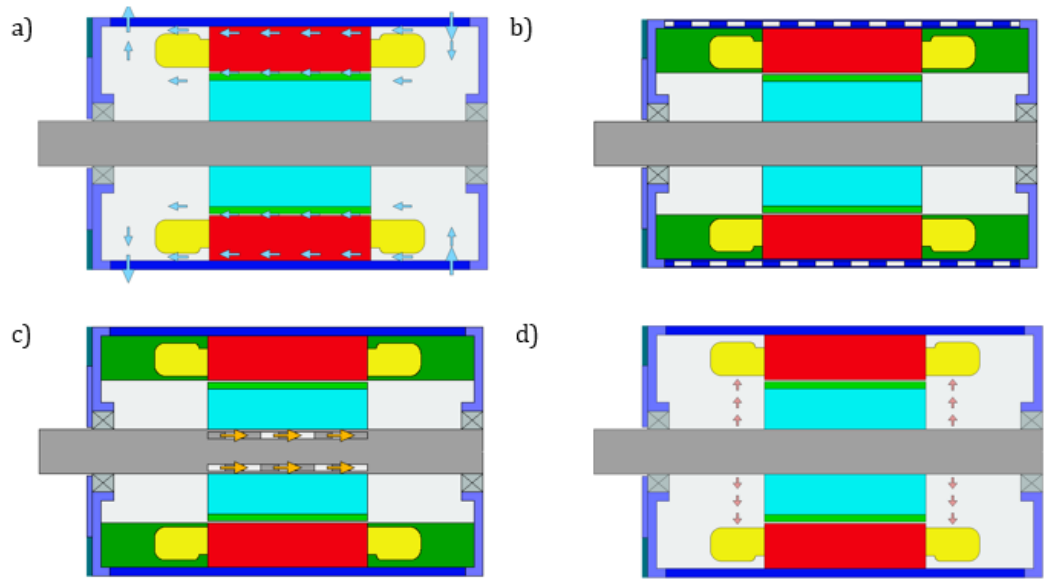

Fig. 2.4 Forced-convection cooling techniques, a) Through ventilated with stator ducts, b) Stator water jacket, c) Shaft liquid-cooling, d) Spray cooling [130]

Another prominent forced liquid-cooling method is oil spray cooling, making use of nozzles to spray oil on the rotor or end-windings [120], [125], [136], [137]. Spray cooling might also be completed without nozzles. In this case, a fluid is passed down a duct in the shaft and then is sprayed at the end-winding or rotor thanks to centrifugal effects, Fig. 2.4d). For both techniques, a controlled amount of oil is left in the air gap, which is splashed around by the rotor rotation, further increasing the cooling effect. The oil level needs to be carefully controlled, as a low level would reduce the amount of cooling, while a high level would result in increased drag losses [136]. Disadvantages of spray cooling include the possibility of contamination of the fluid with time, together with the complex fluid handling

and reconditioning (condensation, etc.) [120], [137]. Finally, direct conductor forced liquid-cooling, such as slot water jackets, is usually applied when water jacket cooling would be insufficient, e.g. if there is an important temperature gradient between the outer stator core and the winding region. In this case, cooling channels are placed directly within the slot, or inside the stator back iron to form a direct contact between the hot area and the coolant. The advantages and disadvantages of this method are similar to the ones of water jacket cooling, however, the reduced channel size for direct cooling lead to a reduced pressure drop, hence lower temperature for a similar fluid flow [125].

2.3.2 Radiative and conductive heat transfer

Heat transfer by radiation from a surface is due to the energy transfer of electromagnetic waves. Heat transfer happens by radiation inside and outside the electric machine, in parallel with conduction transfer and convection transfer. A typical formula for the heat transfer coefficient by radiation is defined in (2.19) [126]:

$$h_{radiation} = \sigma_{rad}\varepsilon_{surf}F_{1-2}\frac{(T_1^4-T_2^4)}{(T_1-T_2)} \qquad (2.19)$$

Where σ_{rad}=5.669×10^{-8} W/(m^2.K^4), ε_{surf}, F_{1-2}, T_1 and T_2 are the surface emissivity, view factor for dissipating surface 1 to absorbing surface 2, and the temperatures of surfaces 1 and 2, respectively. Methods to improve radiative machine cooling include the use of paint to improve the machine emissivity or the reduction of the surrounding temperatures. However, radiative heat transfer is usually negligible compared to forced convective cooling. Therefore, it is typically disregarded by thermal designers and only considered when shown to be significant or in the context of high-fidelity thermal analysis [99], [139].

Heat transfer by conduction is created by the molecule vibration in a certain solid material. The way the heat is transferred by conduction through a material is expressed via the Fourier's law,

$$\vec{q} = -k\nabla T \qquad (2.20)$$

where $\vec{q}$ is the vector of local heat flux density, k is the material thermal conductivity and ∇T is the temperature gradient. The thermal conductivity k typically varies with temperature, but may be considered as a constant when the variation is small over the range of temperatures. In anisotropic materials, the thermal conductivity varies with orientation,

and can therefore be expressed as a tensor. In the case of a unidirectional heat transfer, Fourier's law is used in its one-dimensional form. In the x-direction,

$$q_x = -k\frac{dT}{dx} \qquad (2.21)$$

Conductive heat transfer can be used to transport the heat from the machine assembly to reach an eventual heat sink, such as the ambient environment, a large platform or a heat exchanger. A popular solution is the heat pipe technology, which makes use of both the thermal conductivity and the phase transition of the working fluid to transfer heat between two solid regions.

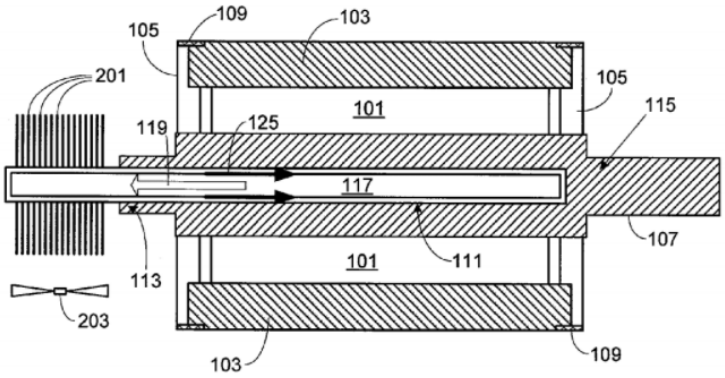

Fig. 2.5 Rotor cooling set-up including heat pipes [129]

Heat pipes can be located on the stator or rotor assembly, and a heat exchanger is typically used to dissipate the extracted heat [128], [129], [142]. Fig. 2.5 presents a rotor cooling set-up, where one heat pipe goes through the machine axle [129]. A heat exchanger formed by metallic plates is placed at the end of the heat pipe. An advantage of heat pipes include low system complexity, but the achieved cooling effectiveness is worse than the effectiveness of active liquid-cooling.

Thermal designers can use a combination of several cooling techniques [129], [140], [141]. The combination of heat transfer techniques is not a simple addition and is typically derived from experimental and/or numerical analysis. For instance, the heat transfer coefficient resulting from the association of the natural and forced types of convection is evaluated in (2.22) [121],

$$h_{mixed}^3 = \pm\, h_{natural}^3 + h_{forced}^3 \qquad (2.22)$$

where the sign used depends on whether the natural flow assists or opposes the forced convection [126].

This section has reviewed the most popular cooling techniques, and has shown that the machine topology and intended application play a major role into the adopted cooling solutions. For electric powertrain applications, which are the focus of the ADEPT project, liquid-cooling is frequently used, which provides good balance between system complexity and power density. Independently of the adopted cooling technique (if not direct stator slot or core cooling), the electric machine performance will also depend on the ability to dissipate heat from the active components within the machine assembly.

2.4 Winding-to-housing frame heat extraction path

The research presented in this thesis focuses on machines where the heat is extracted from the housing periphery. For this category of machines, a good knowledge of the path linking the heat source and the heat extraction system is crucial for a proper estimation of the machine thermal behaviour. Two factors are typically used to quantify the machine heat extraction path: the material thermal parameters, including thermal conductivity and specific heat capacitance, and the thermal contact resistances, which characterise the interfaces between two solids. This section presents the parameters of interest on the heat extraction path, together with available methods for their representation and analysis.

2.4.1 Material parameters

The winding region is frequently attributed with the dominant power loss source within a PM electrical machine. A good knowledge of the thermal parameters of this region is therefore decisive, in particular for compact, high-power-density or high-efficiency machine solutions. A typical electrical winding designed for low-voltage applications is a composite structure formed from conductors coated with an appropriate grade of electrical insulation commonly referred to as enamel. The choice of conductor shape and material typically depends on the operating, temperature, cost and availability, among others. In electric machines, conductor materials commonly include copper (*Cu*) and Aluminium (*Al*). Table 2.2 lists selected properties for copper and aluminium materials [60], [143]. Due to its lower resistivity, copper is the most commonly used material in high-performance electric machines [60], [143]. Aluminium has been favoured in low-weight and cost-effective applications [60], [143]-[147]. The raw material price of aluminium and copper, listed in Table 2.2, nonetheless does not include manufacturing cost (aluminium conductors require a specific anti-corrosion treatment [143]). Recent work suggests that replacing copper conductors with aluminium might be beneficial in the context of high-speed or high-frequency machines, as the high resistivity of aluminium results in lower winding ac loss

components. In case where ac winding loss is dominant, this could compensate for the elevated dc loss components in aluminium conductors [60], [143]. Existing work focuses on the comparison of wound components, such as coil exemplars with multi-stranded coils [60]. This allows for contrasting specific ac winding loss effects due to excitation for aluminium and copper, yet more work is required on complete machine comparison.

Table 2.2 Selected properties for copper and aluminium conductor materials

	Copper	Aluminium
Electric resistivity [Ω.m]	1.68×10^{-8} @20°C	2.82×10^{-8} @20°C
Temperature coefficient [$°C^{-1}$]	0.003862	0.00393
Thermal conductivity [W/(m.°C)]	385	205
Volumetric coefficient of thermal expansion [$°C^{-1}$]	51×10^{-6} @20°C	69×10^{-6} @20°C
Specific heat capacity [J/(kg.°C)]	385	835
Density	8890	2700
Price per tonne [152] [$]	5858	1904

Electrical insulation is used to coat electrical conductors, preventing from any short-circuits due to contact between wires. This material typically has a lower thermal class and mechanical strength than the conductor material. Therefore, the winding lifetime is usually limited by the choice of electrical insulation material [153]. A rule of thumb is that 10°C temperature rise for the winding electrical insulation material halves the life expectancy of the electric machine [68]. Table 2.4 lists some standard insulation classes, defined by the National Electrical Manufacturers Association (NEMA) and the International Electrotechnical Commission (IEC), [148], [149]. The recently developed NeoTem material is not yet part of the standard [150]. The cost of the material increases with its thermal class, and therefore there is a classic trade-off between cost and performance, depending on the primary design objective. The choice of insulation material also depends on various parameters such as the machine overload capability, operating temperature, winding process, solderability, resistance to moisture, etc.

Table 2.3 Selected standard insulation classes

NEMA letter class (maximum hot spot temperature allowed)	Typical materials
A (105 °C)	Organic materials (cotton, silk, paper, etc.)
B (130 °C)	Inorganic materials (mica, glass fibres, asbestos, etc.)
F (155 °C)	As for NEMA class B
H (180 °C)	Inorganic materials (mica, glass fibres, asbestos, silicon elastomers, etc.)
N (200 °C)	Inorganic materials (mica, glass fibres, asbestos, Teflon, etc.)
R (220 °C)	As for NEMA class N
S (240 °C)	Polyimide enamel (Pyre-ML [150]) or films (Kapton [151], etc.)
- (300 °C)	Newly developed polymer NeoTem [150]

The complete winding assembly is usually impregnated with varnish or epoxy resin to further improve the electrical insulation and provide 'good' heat transfer from the winding body into the machine periphery [55], [98]. Impregnation also ensures mechanical rigidity and robustness. Epoxy resin usually provides better heat transfer and environmental protection than varnish impregnation, but drawbacks include a higher overall weight, a more complex manufacturing process, and a lower transient overload capability [113].

The epoxy resin potting process requires an appropriate mandrel or former to ensure required shapes for the impregnated assembly. The process is typically completed under vacuum to improve the impregnation quality, as the winding assembly is prone to numerous air pockets and cavities resulting from the winding arrangement, impregnating material and manufacture process used, among others. The assembly is then cured at an appropriate temperature. Varnish impregnation appears as a cost-effective fabrication process, as no former is required. This process includes dipping, flooding or trickle impregnation of the complete stator winding assembly, and is usually completed under vacuum [55]. The machine is then cured at an appropriate temperature.

Table 2.4: Thermal parameters of selected winding amalgams [61]

Fill factor [%]	Wire diameter [mm]	$k_{w,radial}$ [W/(m.°C)]	$k_{w,axial}$ [W/(m.°C)]
74	1	1.47	290
82	1	2.1	320
66	0.3	1.03	250
74	0.3	1.34	278

The manufacture and assembly nuances have been shown to have a significant influence on the winding equivalent thermal conductivity, making the accurate estimation of the winding thermal properties challenging for a machine designer [99], [132]. Table 2.4 lists selected properties of windings formed with round conductors available from the literature, where $k_{w,radial}$ and $k_{w,axial}$ represent the winding equivalent thermal conductivity in radial/circumferential and axial direction, respectively [61]. All listed windings are formed with copper conductors coated with Polyamide-imide electrical insulation and epoxy impregnated.

From Table 2.4, it is clear that $k_{w,axial}$ is significantly larger than $k_{w,radial}$. However, in most cases, the heat extraction path from the winding body is realised via the stator core-pack to the machine housing, therefore $k_{w,radial}$ is particularly important. The equivalent thermal conductivity across the conductors is usually isotropic for windings made up of round conductors. However, this approximation is not valid for the windings built with rectangular conductors or Litz wires, where the winding individual materials are distributed

non-uniformly within the stator slot [17]-[22]. Analytical methods have been developed for the theoretical estimation of $k_{w,radial}$ for impregnated windings formed with round conductors, however more work is required to develop similar techniques for windings formed with other conductor types.

Another material of interest is associated with the stator core pack, as it typically represents an important portion of the heat extraction path. This region is generally made up of laminated steel to minimise the eddy currents, with a typical lamination width of 0.15-0.35 mm [154]. The laminated steel core is a composite made up of steel, interlamination insulation material, among others [155]. As for the winding amalgam, an accurate physical representation of the lamination is rather impractical, thus this region is frequently homogenised. The thermal parameters associated with laminated core regions are notoriously challenging to derive analytically, and are directly measured 'in situ' or from bulk material sample. Details about thermal parameters measurements are discussed in section 2.5.

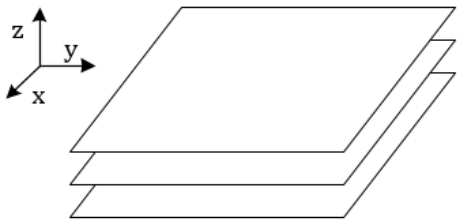

Fig. 2.6 Schematic view of laminated steel

The thermal conductivity of the laminated steel is a function of clamping pressure, lamination thickness, stacking factor, lamination surface finish, and interlamination insulation material, among others [89], [155]. The thermal conductivity of the laminated steel is orthotropic: the thermal conductivity along laminations, so called 'in-plane' thermal conductivity, see plane x-y on Fig. 2.6, and across the laminations, so called 'through-stack' thermal conductivity, see z-axis on Fig. 2.6, should be distinctly derived. The equivalent specific heat capacity of the stator core pack is typically assumed to be equal to the one of the lamination material, or is experimentally derived. Table 2.4 lists selected properties of the lamination available from the literature [155]. All listed laminated steels have a C-5 coating and a 99% stacking factor. Table 2.4 confirms the anisotropy of the laminated steel thermal conductivity and the subsequent need for adapted formulas.

Table 2.4: Thermal parameters of selected laminated steels [155]

Type	Thickness [mm]	$k_{s,through-stack}$ [W/(m.°C)]	$k_{s,in-plane}$ [W/(m.°C)]	$c_{s,s}$ [J/(kg.°C)]
M19	26-Gauge	1.6-2.1	23.0	451
M19	29-Gauge	1.6-2.0	21.9	463
HF10	0.254 mm	1.2-1.4	20.6	456
Arnon 7	0.178 mm	0.6-0.9	22.4	504

Another material of importance is associated with the PM array. This material is not on the heat extraction path from the winding to the housing frame, but is reviewed here due to its importance in thermal analysis of PM machines. This is due to the strong temperature dependence of the PM magnetic properties. Fig. 2.7 illustrates the temperature dependence of normal and intrinsic coercivity with the demagnetisation curves of a type of *NdFeB* magnet, Neo3525 [176]. Clearly, an increase in temperature decreases the intrinsic coercivity, and the load applied to the PM arrays requires careful control to avoid demagnetisation.

Table 2.5 presents selected properties of some permanent magnet materials: *AlNiCo,* anisotropic ferrite*, SmCo* and *NdFeB*, where $(BH)_{max}$ corresponds to the maximum energy product. From Table 2.5, there is an apparent trade-off between magnetic properties and temperature: *NdFeB* and *SmCo* have relatively elevated $(BH)_{max}$ parameters but relatively low resistance to temperature, while *Alnico* has a relatively high resistance to temperature, but relatively low $(BH)_{max}$.

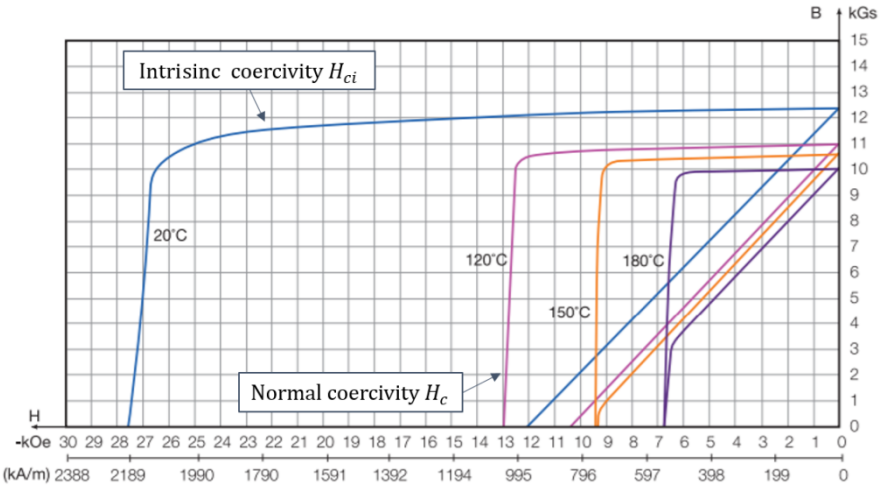

Fig. 2.7 Demagnetisation curve of Neo3525 permanent magnet [176]

Other parameters influencing the magnet choice include cost, resistance to corrosion, ease of manufacture and magnetic stability. From Table 2.5, it can also be noticed that anisotropic ferrite and *AlniCo* have negative temperature coefficients. When these types of

magnet are selected, a good knowledge of the PM temperature is required at both low and high temperatures. The thermal conductivity and specific heat capacity values used in thermal models are usually provided by PM manufacturers.

Table 2.5 Basic data for selected PM materials [68]

Physical property	*AlNiCo*	Anisotropic Ferrite	Sintered *SmCo*	Sintered *NdFeB*
Remanence B_r [T]	0.6-1.35	0.35-0.43	0.7-1.05	1.0-1.3
Intrinsic coercivity H_{ci} [kA/m]	40-130	180-400	800-1500	800-1900
$(BH)_{max}$ @20 °C [kJ/m^3]	20-100	24-36	140-220	180-320
Resistivity @20 °C [μΩ.cm]	47	>10^4	86	150
B_r temperature coefficient [%/°C]	-0.015	-0.2	-0.045 to -0.05	-0.08 to -0.15
H_{ci} temperature coefficient [%/°C]	-0.02	0.2-0.4	-0.2 to -0.25	-0.5 to -0.9
Thermal expansion [10^{-6}/℃]	11.3	13	9	3.4
Max. working temperature [°C]	500-550	250	250-350	80-200
Curie temperature [°C]	850	450	700-800	310-350
Density [kg/m^3]	7300	4900	8200	7400
Thermal conductivity [W/(m.°C)]	10-200	4	10-12	9
Specific heat capacity [J/(kg.°C)]	350-500	795-855	380	440

A supplementary reason to monitor magnets' temperatures is that their coefficients of thermal expansion is higher than that of silicon steel If not managed properly, the shear stress from the magnets could decrease machine performances and the rotor assembly could deteriorate.

Finally, the slot liner is a critical component for an electric machine, as it provides electrical insulation between the winding assembly and the stator core. Parameters influencing the choice of slot liner include dielectric breakdown voltage, tensile strength and thermal conductivity, absorptivity among others. Table 2.6 presents some basic properties for three slot liner materials typically used in low-voltage electric machines [55]. The thermal conductivity and specific heat capacity are greatly dependent on the materials and methods used in construction of the complete stator-winding assembly e.g. impregnation material and/or process. Therefore, the data provided by the manufacturer is generally insufficient to characterise the contact between winding assembly and stator core back. This is typically done ‘in situ’ and described in the context of thermal contact resistances.

Table 2.6 Basic properties for selected slot liner material data [55]

Property	Nomex 410 (Dupont)	ThermaVolt (3M)	CeQUIN I (3M)
Thickness [mm]	0.25	0.25	0.25
Density [g.m^{-2}]	249	366	270
Thermal conductivity [W/(m.°C)]	0.139 @ 180°C	0.230 @ 180°C	0.195 @ 180°C
Specific heat [J.°C^{-1}. kg^{-1}]	1200	N/A	N/A
Insulation class (see Table 2.3)	R	R	R

2.4.2 Thermal contact resistances

Intuitively, when analysing conductive heat transfer across layers of materials, one would assume a perfect contact between the solids. However, the contact surfaces are imperfect at the microscopic scale, and only a fraction of the initially assumed contacting area actually contributes to heat transfer by conduction [126]. The rest of the heat might be transferred by radiative or convective heat transfer, depending on the material present in the interstitial space, if any. To illustrate this point, Fig. 2.8 shows a schematic close-up of the interface between two contacting surfaces. Some parameters influencing the thermal contact resistance are the contact pressure, interstitial materials and surface roughness, flatness and cleanliness, among others. Interstitial material, such as thermal grease or paste, may be used to fill the voids and improve heat transfer [157], [158].

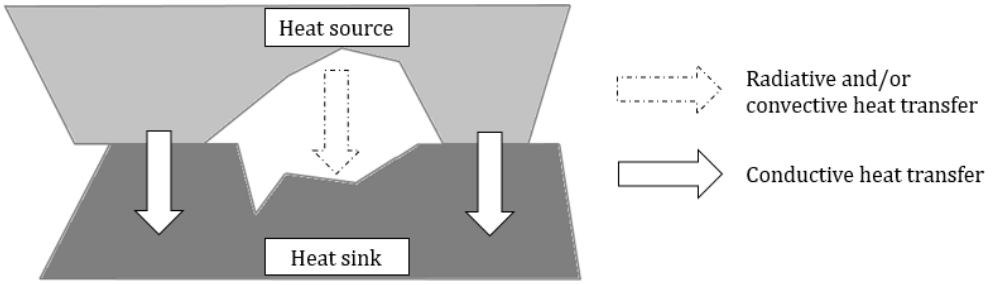

Fig. 2.8 Illustration of two contacting surfaces at microscopic level

The following formula can be used to calculate the thermal contact resistance R between two surfaces 1 and 2, [126]:

$$R = \frac{(T_1 - T_2)}{Q.A_{contact}} \qquad (2.23)$$

where Q is the heat flow between 1 and 2, $A_{contact}$ is the contact area and T_1 and T_2 are the temperatures of 1 and 2, respectively. From Fig. 2.9, it is clear that the analytical calculation of the thermal contact resistance might be challenging, due to the difficulty of estimating $A_{contact}$ without any empirical data. For machine configurations where a large portion of heat is extracted via the housing frame, two junctions have been shown to be crucial: the winding-to-stator core and stator core-to-housing frame interfaces [99], [127], [133]. Most of the heat produced by the winding and core assemblies crosses these two junctions.

The winding-to-stator core interface is a multi-material region comprising slot liner, impregnation material and some air cavities depending on the material and technique used for impregnation. The winding-to-stator core thermal contact resistance, R_{w-s}, is affected

by material properties and assembly processes, and by winding configurations; for instance, R_{w-s} is significantly reduced after one or two impregnations [55]. The contact pressure from the winding typically depends on selected winding procedures and conductor types. In [59], measured data suggest that dissimilar R_{w-s} might be derived for the contact between the winding and stator back iron, and winding and stator tooth due to different conductor lays, e.g. winding formed with rectangular profiled conductors. In [159], R_{w-s} values are measured for three Surface Mounted Permanent Magnet (SMPM) machines, with values ranging from 0.03 °C/W to 0.192 °C/W. The three machines were manufactured using the same materials, but with different overall geometries and winding configurations. This highlights the importance of in-situ evaluation of R_{w-s}. According to (2.27), R_{w-s} depends on the slot-cross section and machine axial length (parameter of Q in (2.27)), and therefore does not simply describe the quality of contact between the two solids. The different order of magnitude between the thermal resistances derived in [159] might be explained by their different geometries, and not by their difference in slot heat transfer capability. It is sometimes desirable to compare the contact quality of two stator-winding configurations regardless of their intrinsic geometries, focusing only on thermal parameters, such as surface roughness and contact pressure. A systematic approach in deriving the winding-to-stator heat transfer capability has not yet been presented in the literature, but would be valuable in this context.

The second interface of interest for machines with heat extracted from the housing frame is the one between the stator back iron and the housing frame. The stator-to-housing thermal contact resistance, R_{s-h}, depends on several parameters such as surface finish, interface contact pressure, use of thermal grease, among others. Initial work into thermal contact resistances between metallic interfaces focuses on flat joints, with various models based on empirical correlations, [160], [161]. The models were later adapted to curved joints, necessitating the coupling of the heat transfer analysis with thermo-elastic stress analyses [162], [164]. In [157], R_{s-h} values of nine silicon steel stators and mild steel housings with similar geometries but differing in terms of shrink fit pressure, surface finish and interfacing materials are compared. Table 2.7 presents the obtained values, demonstrating a decrease in R_{s-h} with increase of contact pressure, surface machining and use of interfacing material. However, no information is provided about the machine dimensions and surface finish, making it arduous to compare or replicate the results. In [158], several empirical correlations are derived for R_{s-h} for alternative contact pressures and surface finishes.

In the three previous references, [157], [162] and [164], the temperature dependency of the thermal contact resistance is overlooked. However, this effect has been shown significant as the linear coefficient of thermal expansion might be greater for the housing material than that of the core material, e.g. *Al* and *SiFe*, respectively [158], [165]. The impact of temperature on the stator-to-housing thermal contact resistance was first investigated in the context of concentric cylinders, and an iterative procedure has been presented to update the thermal contact resistance with temperatures [163]. Reference [165] adapts the work presented in [163] to account for the contact pressure, and confirms that the stator-to-housing thermal contact resistance should be a function of temperature. In [158], it is mentioned that the ambient temperature shrink-fit must be intended to operate at an interface pressure very superior to 2 MPa such that the interface pressure will remain higher than 2 MPa up to the maximum machine operating temperature and uphold good thermal and mechanical holding (torque transfer) performance. The temperature dependence of the winding-to-stator thermal contact resistance has not yet been investigated in the literature. The high-rate of winding copper conductor thermal expansion compared to the one of the laminated core might have some impact on the electrical insulation system, and thus on machine aging.

Table 2.7 thermal contact resistance of nine stator assemblies with different interface conditions

Stator	Surface machined	Shrink fit pressure [MPa]	Thermal paste	Thermal pad	Thermal resistance [°C/(kW.m^2)]
I	Y	13.3	N	N	0.141
II	Y	21	N	N	0.133
III	Y	39	N	N	0.098
IV	Y	17	Y	N	0.112
V	Y	21	N	N	0.157
VI	Y	21	N	Y	0.090
VII	N	17	N	N	0.196
VIII	N	14	Y	N	0.151
IX	N	10	N	Y	0.153

This section has provided some insights into various physical parameters, whose accurate estimation of is crucial in thermal analysis. It has been shown that as manufacturing and assembly techniques influence these parameters, a degree of experimental calibration for reliable parameters estimation is essential.

2.5 Thermal modelling of electrical machines

The need for thermal modelling of electric machines emerged in the late eighties, as a result of more challenging machine specifications and operations, e.g. duty cycles. At that time, lumped-parameter magnetic equivalent circuit and numerical methods, including FEA,

were already used for electromagnetic analyses by machine designers [166]-[168]. Consequently, mathematical analyses are mainly based on these techniques for heat transfer analyses. Pure analytical methods solving the heat equation and/or Fourier's law may sporadically be applied to simple 1D- and 2D- cases, but become increasingly complex for 3D geometries [126]. There are currently three main methods available for the thermal analysis of electrical machines: lumped-parameter TEC, numerical methods (FEA and CFD) and hybrid methods that combine both options [51], [52]. This section reviews these different approaches, starting with lumped-parameter TECs.

2.5.1 Lumped-parameter thermal equivalent circuits

Lumped-parameter TEC modelling is the most widely adopted approach in thermal analysis of electric machines [39]-[48], [58], [169]-[173]. TEC theory is based on the computation of equivalent resistances for the conductive, convective and radiative heat transfer across different parts of the machine, assuming independent heat transfer for each axis of the relevant coordinate system. Thermal resistances associated with conductive heat transfer can be calculated as follow [126]:

$$R = \frac{L}{kA} \quad (2.24)$$

where *L, A* and *k* are the heat path length, cross-section area and material thermal conductivity, respectively, while thermal resistances associated with convective and radiative heat transfer can be calculated using the following formula [126],

$$R = \frac{1}{hA} \quad (2.25)$$

where *h* is the heat transfer coefficient. Thermal capacitances, depending on the mass and specific heat capacity of the studied part, can be employed to take thermal transient into account. The system obtained is similar to an electrical circuit, with analogous variables presented in Table 2.8. A first intuition for this analogy appeared in [91]. However, the apparition of more complex TEC was made possible several decades later by the development of modern computers. The reference paper [164] marks the emergence of more complex TECs through the formulation of both steady-state and transient solutions to the temperatures within a TEFC machine, improving the stationary model presented in [174].

In TEC models, machines are divided into sub-domains with a simple geometry. Available shapes comprise cuboidal and arc-cylindrical elements [53], [175], allowing to represent nearly all machine parts. Fig 2.9a) shows a TEC representing heat transfer through the x-axis within the cuboidal element, Fig. 2.9b). $R_{x,a}$ and $R_{x,b}$ are derived using (2.24), such that the common node $\overline{T}$, representing the average temperature, is at the centre of the element.

Table 2.8 Thermal-Electrical analogy

Thermal property	Symbol	Electrical analogy	Symbol
Temperature	T	Potential	U
Heat transfer rate	$\dot{Q}$	Current	I
Heat flow	Q	Current density	$\vec{j}$
Thermal conductivity	k	Electrical conductivity	σ
Thermal resistance	R	Electrical resistance	R_Ω
Heat capacitance	C	Electrical capacitance	C_Ω
Newton's law	$\Delta T = \dot{Q}R$	Ohm's law	$\Delta V = IR_\Omega$

The TEC formulation as listed in Table 2.8 is based on assumption of zero heat generation. Such model formulation would clearly have an impact on overall accuracy of thermal modelling of electrical machines, where most of the regions generate power loss. To account for internal heat generation, a negative resistance $R_{x,c}$ approach was shown to greatly improve model predictions [53], [164], [177] with mathematical proof provided in [53]. Fig. 2.9c) pictures the complete 3D TEC for a cuboidal element. Each individual thermal circuit connected to $\overline{T}$ represents an axis of the Cartesian coordinate system.

Commercial software programs are available to derive TECs based on input machine geometry and material [130], Fig. 2.10. The number of nodes adopted in a TEC depends on the empirical thermal data resolution and required accuracy. Many references in the literature adopt reduced-order lumped-parameters TEC models, with a number of nodes ranging from around 2 to 15 [40]-[46], [58], [169]. These low-fidelity models are typically used when only the average temperatures of selected machine regions are of interest. However, the model parameters may not have physical meanings, which makes any alteration of the machine design parameters directly in the reduced-order model difficult. It is frequently desirable for designers to have more information about the heat distribution within a sub-assembly, e.g. estimation of the winding hot spot temperature. In such case, a higher resolution thermal data is usually obtained by means of a more detailed thermal modelling approach (high-fidelity thermal modelling): a machine part might be sub-divided in several elements to assure the required resolution of the thermal data.

Several procedures are available in the literature for optimising the region subdivision process, allowing the derivation of both hot spot and average temperatures [52], [178]-[179]. Discretisation has been shown to greatly improve model accuracy in the case of inhomogeneous loss distribution, e.g. elevated ac winding loss component, see section 2.1 [177]. As underlined in section 2.1, an important element to account for when predicting the winding thermal behaviour is the temperature and power loss interdependence. The commonly used technique of updating the dc winding power loss with temperature is based on (2.3), where the power loss is iteratively updated with averaged temperature of the winding region [159], [180]-[182]. For high-fidelity models, (2.4) or (2.5) may be used instead of (2.3) [89], [99]. The lumped-parameter TECs have the advantage of being very fast and easy to modify. Due to its low solving-time, the TEC method is usually preferred for initial machine sizing, transient duty analysis and design optimization. However, as shown in the previous paragraphs, setting up a model requires a good understanding of the main heat-transfer behaviour of the system and of the desired accuracy.

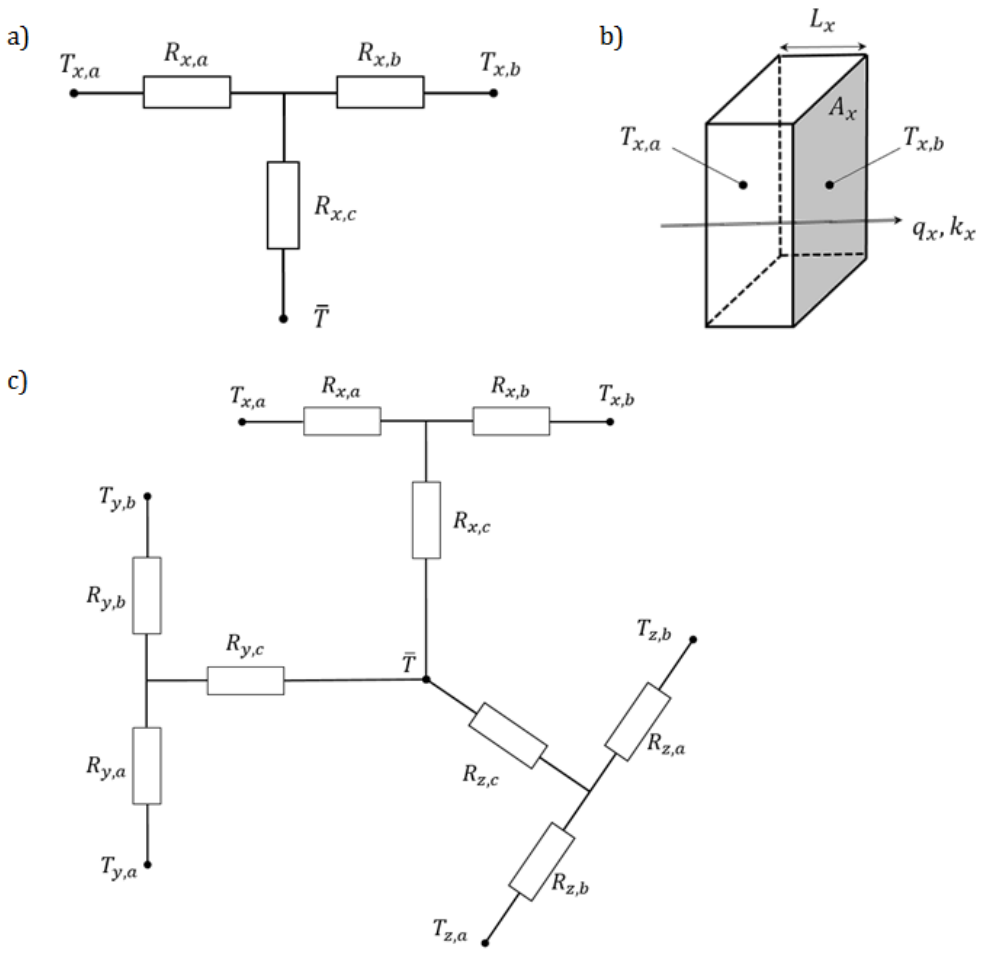

Fig 2.9 a) 1D TEC for x-axis of a cuboidal element, b) Outline of a cuboidal element, c) 3D TEC of a cuboidal element. $\bar{T}$ represents the average temperature

2.5.2 Numerical methods

The main numerical methods for thermal analysis of electric machines can be separated in two categories: CFD and FEA. These techniques discretise a 2D or 3D domain into a series of regular shaped elements forming a discretisation mesh, e.g. triangle or tetrahedrons. The appropriate differential equations describing heat and mass transfer are then solved for each of these elements, providing detailed temperature field solutions. A large number of elements provides high solution accuracy, but with the drawback of an increased computation-time. FEA allows the analysis of conduction heat transfer in solid components, while CFD accounts for convective heat transfer between solid and fluid domains. Fig. 2.11 presents the 3D FEA model of a stator-winding section, with active regions highlighted. Due to symmetry, only a quarter of the assembly is represented.

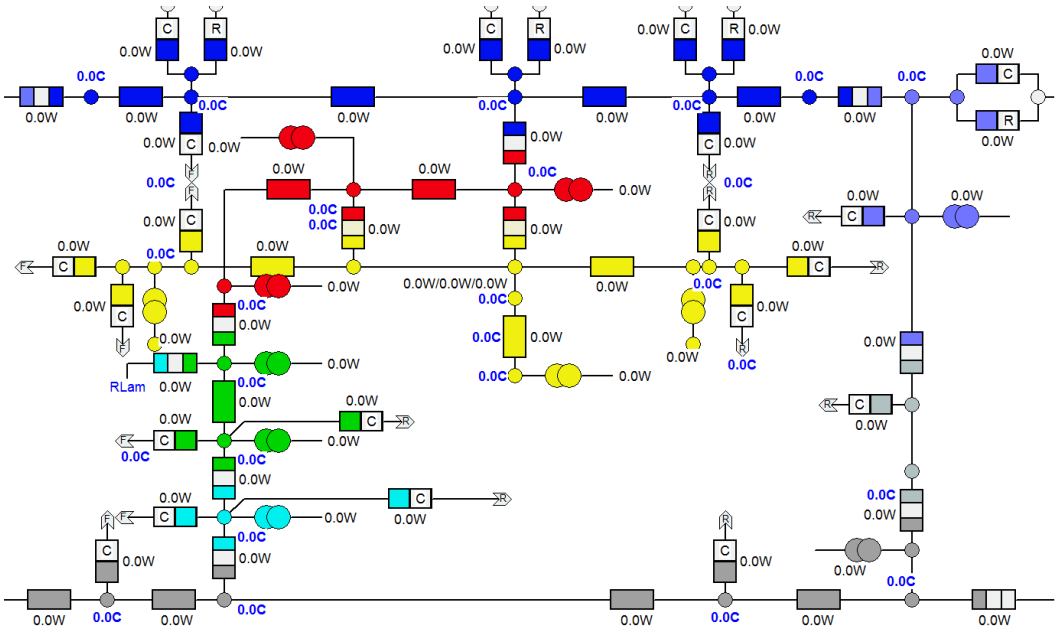

Fig. 2.10 Lumped-parameter TEC simulated using Motor-CAD [130]. Each colour corresponds to a machine region, e.g. the winding, stator core pack and housing assemblies are represented in yellow, red and blue, respectively. Thermal contact resistances are used to characterise the conductive, convective and radiative heat transfer between regions. The average temperature of each region is represented via a central node, as previously shown in Fig. 2.9c).

Unlike the magnetic flux, which is usually confined in high magnetic permeability materials and purpose-built air gaps, the heat flux tends to diffuse into surrounding space through conductive, convective and radiative heat transfer. A detailed thermal analysis requires each heat transfer mechanism to be accounted for. However, in order to simplify the analysis thermal problems are usually reduced to a single heat mechanism; FEA models typically apply appropriate boundary conditions to their outer limits, representing convection and/or radiation [58], [77], [96], [144], [178], [183]. A fixed temperature or a

fixed heat flux boundary condition may also be used to represent a liquid-cooled arrangement [58], [96], [144], [183].

One of the main advantages of numerical methods is their capability to model complex geometries and provide a detailed solution of temperature distribution within a device. Examples in the literature make use FEAs to define the required discretisation level of TECs [51], [52].

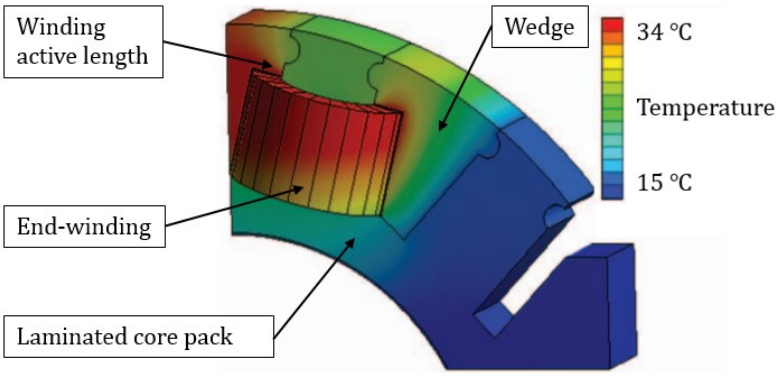

Fig. 2.11 3D FEA model of ¼ of a stator-winding section (motorette)

This may help to obtain a more realistic loss injection, for instance in case of inhomogeneous power loss distribution [51]. Depending on the model resolution, the use of numerical methods might be computationally expensive, with time intensive model set-up. Parametric approaches are often available to simplify model modifications; however, these do not reduce the computation-time. For these reasons, FEA and CFD techniques are usually chosen for investigations where a more detailed solution is required (final design).

2.6 Experimental calibration of electrical machines

The accurate prediction of thermal behaviour in design of electric machines is a challenging task. The machine's geometrical and material data is usually insufficient to provide reliable temperature estimates. The presence of thermal effects associated with a particular machine build, which cannot be solved by mathematical modelling makes derivation of the thermal parameters a difficult exercise. At a first design stage, designers typically use a combination of their previous experience, similar machine studies and existing libraries to calibrate their thermal models. The use of commercial software dedicated for thermal analysis of electric machines can be a valuable option in some cases, as years of experience allowed developers to get enough data to cover a wide range of machine designs [130]. In these software programs, users only need to input geometry, winding and materials, and the most appropriate analytical and/or empirical formulations for each of the lumped-parameter

components are automatically selected. However, this is no longer an option when considering innovative machine designs, where available data is limited. In such case, an appropriate experimental approach allowing for derivation of the unknown thermal parameters is used. This however, requires development of experimental methods, with focus on a particular thermal data or effect.

There are two main categories of approaches commonly used in the calibration of thermal models of electric machines. The first one involves tests on a complete machine prototype, where a series of experiments allow for the thermal and loss parameters of interest to be concurrently derived [99], [134] [184], [185]. This approach is the most commonly used, as thermal tests are a part of the comprehensive range of machine final testing and validation procedures. The second approach includes custom-designed experiments [53], [64], where geometries and/or material that are simpler to evaluate empirically are used, and the experiment targets a particular set of parameters. The tested hardware exemplars may be representative of the complete machine, e.g. stator-winding segments [55], [58], [170], [158], [186]. The custom-designed experiments allow the derivation of basic trends for the thermal and loss parameters [63]-[67]. This section reviews each method, highlighting their applicability and limitations.

2.6.1 Complete machine assembly

A range of test methods may be employed during the thermal and power loss analysis and calibration of electric machines. The most common tests include conventional dynamometer, static dc excitation, open-circuit and short-circuit evaluation of a complete machine assembly. Some of these experiments are used for the validation of machine specification requirements, whereas others inform and/or confirm the analyses developed during the design procedure.

Dynamometer tests are generally used to evaluate the machine performance and efficiency via input and output power loss measurements. Such testing is essential for a complete thermal characterisation of electric machines, as the machine runs closely to its intended operating conditions. On the one hand, every power loss and heat transfer phenomena are revealed during this test. On the other hand, the presence of all these effects might complicate the loss separation and not provide a good understanding of the individual effects. Moreover, the set-up for conventional dynamometer testing is complex and presents a risk of machine damages. Therefore, it is preferable to start evaluating the machine assembly with tests involving only a few heat transfer and power loss parameters,

with a reduced level of complexity and hazard. Should a failure occur, a useful amount of information would have already been gathered.

The dc testing process typically involves passing a dc current through the winding phases connected in series, with the temperature, current and voltage being recorded until steady-state is reached. This static test can be performed with simple laboratory apparatus and presents relatively low risk of damage for the machine compared to moving tests. Dc testing allows accurate characterisation of the winding dc power loss component, as it is the only loss component present during the test. Due to the well-defined power loss source, data from a dc test is a reliable tool in thermal model calibration. The analysis of steady-state data allows for calibration of thermal parameters, such as thermal contact resistances and material equivalent thermal conductivity, while data from transient tests may be used to estimate parameters impacting the machine dynamic performance, such as heat capacitances.

Open-circuit (OC) tests are typically completed to estimate the voltage induced by the winding and provide some insight into the mechanical and rotor induced power loss components (PM loss due to slotting, rotor induced ac winding loss, and main flux path iron loss components [106], [113], [187]). These tests require the use of a prime-mover operating in speed-control and a torque-transducer, and are therefore slightly more complex than dc ones. Short-circuit (SC) tests require the same test set-up as for open-circuit tests, and are usually used to identify the magnetic parameters, such as armature and synchronous reactance values, and characterise load-dependent winding and demagnetising flux path iron loss effects [106], [113], [187].

Table 2.9 Loss mechanisms associated with different test types [187]

Loss component		Static dc	OC	SC	Full load
Mechanical	$P_{friction}$		x	x	x
	$P_{windage}$		x	x	x
Iron	P_{hyst}		x	x	x
	P_{eddy}		x	x	x
	P_{exc}		x	x	x
Winding	P_{dc}	x		x	x
	$P_{ac,e}$			x	x
	$P_{ac,r}$		x	x	x
Magnet	P_{pm}		x	x	x

Table 2.9 recapitulates the different power loss components obtained from presented tests, highlighting how their completion might help the identification of individual loss effects. The individual contribution of some loss components remains impossible to derive using a

complete machine prototype, e.g. friction and windage loss. Experimental set-ups capable of isolating specific loss effects are highly desirable in this context.

A specificity of thermal analysis is that the number of thermal sensors used in measurements has a great impact on the obtained thermal data. The temperature is commonly recorded locally using thermocouples [169], [170], [184], [185]. Heat flux gauge and thermal imaging cameras are occasionally used to evaluate the radiative and convective heat transfer coefficients, and provide an overview of surface temperature distribution, respectively [125], [165], [185], [186]. Ideally, thermal designers would be able to use a sufficient number of thermal sensors, and the location of each of them would be well-known. In particular, the position of the thermal sensors would be adapted to the parameters to derive, e.g. temperature data from sensors located on both sides of an interface allow for the derivation of its associated thermal contact resistance. However, in practice, the exact location of the thermal sensor is often not well-known, e.g. thermal sensors placed between mushed-wound conductors during winding process and/or out-sourced machines. The overall number of sensors depends on various factors, e.g. cost per sensor, accessibility of the machine regions, measurement redundancy and accuracy. It is also technically difficult to instrument some regions, e.g. the analysis of rotating parts requires specific measurement apparatus. Likewise, the thermal sensors should not disturb the machine behaviour, e.g. insertion of thermal sensors directly in an interface gap between two solids could decrease quality of their intrinsic contact interface. When only a limited number of thermal sensors are used or the regions of interest are inaccessible, it is possible to use the change in resistivity to evaluate the material (winding) temperature. In [159], [180]-[182], such approach is used to derive the winding average temperature. The average winding temperature might also help to estimate the position of the thermal sensors [187].

The calibration method usually consists in the estimation of thermal parameters such that the difference between the measured and predicted temperatures is minimised. Depending on the model complexity and recorded thermal data resolution, tuning might be performed iteratively by hand, or using computational methods such as Genetic Algorithms (GA) and Particle Swarm Optimisation (PSO) [36], [184], [200]. Sensitivity analysis was also shown to be efficient at identifying crucial parameters of the thermal models, and may be used to accelerate the calibration process [201], [202].

The thermal calibration of models using data from tests on complete machines is well-suited for analysis where materials and processes are known. In such cases, the designers might have an idea for the range of values for each of the parameters. This allows one to predefine the process of estimating the parameters, and considerably accelerates the estimation time. For novel designs where no data is available, broad boundary limits for the range of parameters are set for the model calibration. Depending on the model complexity and number of thermal sensors used in measurements, there might be a number of parameter combinations, for which the estimation procedure converges to a solution. This is usually the case, when measured thermal data with insufficient resolution are used, i.e. the parameter estimation process is not well defined. The selection of a preferred set of parameters is then difficult, as the derived parameters may not yield physical meaning, i.e. the estimated values allow correct prediction of the output temperature for the investigated cases, but do not represent the intrinsic machine thermal properties. As already mentioned in section 2.4, a non-physical set of parameters might not be sufficient to capture the machine thermal behaviour for all design variants or in all operating conditions, and therefore the confidence of such thermal model is low.

In order to increase confidence in the derived data, several tests at various dc current excitations are typically required [188]. However, the duration of steady-state thermal tests is frequently prohibitively high. Alternatives to steady state thermal tests with dc excitation have been developed to reduce testing time [159], [180]-[182]. In [182], a technique making use of short-time transient dc tests is presented, focusing on the derivation of the winding thermal parameters. The technique assumes that no heat is transferred from the winding to the stator. In practice, the data are recorded until the temperature of the stator back iron of the tested machine increases by 1°C, independently from the machine volume. This approximation might not yield required reliability in the context of high-fidelity modelling, in particular for small machines with a short transient time, i.e. relatively low winding specific heat capacity.

Despite the use of dc tests at various current excitations and alternative testing methods focusing on the influence of some thermal effects, a degree of uncertainty might persist concerning some thermal parameters. It is sometimes necessary to have a high confidence into some thermal parameters, e.g. high-fidelity modelling. A solution to that issue is to isolate specific effects that are particularly complex to analyse within the machine assembly. This can be done using custom-designed experiments, making a set of simplified

experimental apparatus, where only one or few effects are occurring allowing for parameters of interest to be derived with confidence.

2.6.2 Custom-designed experiments

Custom designed experiments, where the experimental test rigs used in the research emulate the machine's sub-assembly of interest in a simplified manner, have been widely explored in the literature [58], [62]-[67], [188]-[199]. Traditionally, the heat transfer coefficients due to convection and radiation have been evaluated using dimensionless correlations obtained via tests on simplified geometric mock-ups [197]-[199]. In [198], first correlations of the heat transfer within the air gap of radial flux machine were developed using analysis on concentric cylinders. Recent works into forced-air cooling investigate the air gap heat transfer in the context of disc type axial-flux machines [63]-[67].

The use of the geometric mock-up is not limited to convective and radiative heat transfer [157], [158], [191]. In [191], a mock-up test setup with concentric cylinders has shown that R_{s-h} is affected by temperature related to the heat extraction technique from the machine housing. Once again, the use of geometric mock-up is shown to be an efficient option for analyses focused on a specific heat transfer effect. Some experimental set-ups substitute a machine region of interest with a simplified mock-up, and compare the difference in the machine thermal behaviour [157], [186], [188]. In [188], the natural convection and emissivity of a machine test bench base with a complex shape is evaluated by replacing it with an *Al* rectangular base. It is also possible to remove the machine part of interest and compare the difference in machine thermal behaviour with and without the part, without any replacement [188]. Simplified geometry might be used to ease hardware manufacturing process or for set-up control. In [186], a mock-up experimental setup is designed to provide some insight into heat extraction directly from the winding body by passing liquid. In order to simplify the hardware construction, heated pole pieces with identical shapes to the coils are used in some cases to replace the complete winding assembly. In [157], a complete stator core is used to evaluate the stator-to-housing thermal contact resistance, where the winding coils are replaced with heat cartridges to better control the temperature during tests.

Custom-designed experiments have also been investigated in the context of power loss estimation. It is typical to use material samples to evaluate the magnetic [100], [193], [203], mechanical [165], [191], [192] or thermal [58], [76], [183], [189] characteristics for both homogeneous and composite materials, which are then used in power loss analyses. In

particular, methods such as Epstein frame or single sheet tester (SST) are standardised measurements techniques for evaluating the magnetic properties of electrical steels [100], [203]. Some custom-built experiments adapt the machine geometry or material used in order to remove some effects, and focus on the parameters of interest. For instance, dummy rotor tests, where the rotor is magnetically inert, but mechanically representative, are typically used to assess the machine mechanical loss [117]-[119]. Dummy rotor geometry might be further simplified to estimate the isolate the contribution of various mechanical loss components. In [117], two dummy rotor assemblies are utilised in order to assess the mechanical loss and their associated heat transfer effects. One rotor is representative of the studied PM machine and comprise surface protrusions, while the second one is flat and illustrative of experimental studies described in the literature.

The stator-winding assembly is usually attributed to the dominant power loss component within the machine body. The most recent work in the field of custom-designed sub-assembly testing treats the stator-winding assembly in detail [60], [64], [67], [115], [125], [138], [186], [204]. Impregnated winding material samples have been used to identify the thermal parameters of winding amalgams (winding conductor, enamel and impregnation material) and laminated core packs with insulating layer and adhesive liner between individual sheets, [58], [183]. As seen in section 2.3, the thermal parameters of interest are typically the thermal conductivity and specific heat capacity.

In section 2.1, the challenges associated with ac winding loss derivation have been highlighted. This is particularly important in the context of electric drive trains with a relatively high operating fundamental frequency, e.g. for the traction machines frequently meeting or exceeding 1 kHz [194]. The ac effects, both for the winding and core pack assemblies, need to be carefully considered for such applications to provide a feasible low-loss design solution. A variety of geometric mock-ups is illustrated in the literature to estimate the effects of ac current excitation, from non-representative core-winding assemblies such as pot-core coils for the estimation of the proximity effects [60], [205], to the use of only two strands on a stator core to study the circulating current [206]. In [60], two air-cored solenoidal coils have been used to investigate the ac winding power loss of multi-stranded windings with aluminium and copper conductors, Fig. 2.12a). Even though the coil arrangements are not representative of typical machine windings, it is stated in [60] that the solenoidal coils were selected for a first analysis as they allow for simple manufacture and rapid analysis.

A number of studies also measure the ac winding loss on a full stator core-pack, wound with a single tooth, Fig. 2.12b), [85], [89], [206]. This option is particularly interesting when the core pack design is already defined, but the winding configuration is still to be designated. Experimental techniques used when analysing the ac winding power loss effects include direct power measurements and impedance analysis [89], [207]. In both cases, the studied hardware exemplar might be pre-heated at a selected temperature to account for the winding power loss and temperature interdependency. When evaluating the ac winding power loss, the separation of the iron loss from the total measured power loss is required. An FE model of the analysed hardware exemplar is typically utilised to derive the iron power loss component, which is subtracted from the total measured loss. The remaining power loss component is then assumed to be exclusively due to copper loss which allows for an accurate derivation of the winding ac power loss [94], [97], [183]. A scaling 'build factor' accounting for the core manufacture and assembly nuances, obtained for example from tests on a toroidal core material sample, [100], [102], or on a simplified stator sub-assembly with a known winding arrangement [60] can be used.

The degree of representability of the tested assembly depends on the desired parameters. Ferrite material can, for example, replace laminated steel in order to ensure very low core losses in the considered frequency range so only the winding power loss is measured [191].

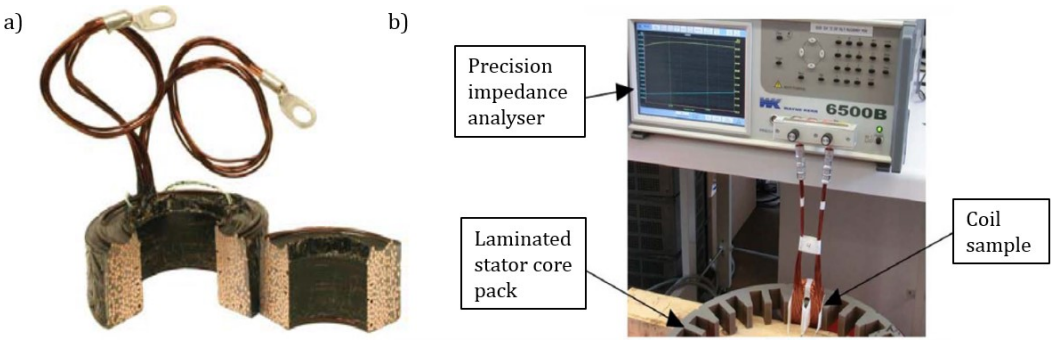

Fig. 2.12 Experimental setup used to evaluate ac excitation loss and winding inductance, a) Coil exemplar with multi-stranded copper conductors, b) Coil tested on a complete core [89]

The use of simplified core-winding assemblies has been shown to be useful at an initial stage of an analysis, e.g. for the comparison of various conductor materials [60]. However, it is sometimes necessary to proceed to ‘in situ’ power loss investigations, e.g. influence of conductors’ locations within a slot, and this can be done only by using representative machine sub-assemblies. A category of custom-built experiments makes use of tests on representative stator-winding segments, so called motorettes. The use of motorettes was initially developed for investigation regarding ageing of the complete winding insulation systems, and has been widely explored in the literature in this context [195], [208].

Motorette assemblies are also beneficial for thermal analysis, e.g. winding-to-stator thermal contact resistance or winding amalgam. Indeed, some of thermal properties are strongly dependent on the interaction of components, and processes employed in construction of the complete machine assembly. However, the use of motorette for thermal analysis is relatively novel.

A motorette exemplar is usually constructed using representative materials and processes, i.e. conductor type, gauge and arrangement together with representative core pack, and electrical insulation system identical to the complete machine assembly. Fig. 2.13 presents examples of motorettes used in the literature. The motorette approach allows for experimental derivation of numerous thermal parameters associated with materials and processes used in machine construction, e.g. impact of various insulation systems on heat extraction from the winding body into the machine periphery [55], [183], and influence of the winding arrangement on the power loss generated [56]-[60], [83], [89], [94], [97]. Also, a number of heat extraction techniques are initially evaluated using the motorette assemblies, e.g. natural convection, liquid cooling of the motor housing and direct oil cooling of the winding body has been shown in the literature [64], [67], [115], [125], [138], [186], [204]. A common experimental method used in derivation of contact thermal resistances involves thermal testing with dc excitation and is applicable for all the stator-winding assemblies from the motorette to the complete machine. In addition to a shorter manufacturing and testing time, the motorette approach allows for a well-defined experimental set-up with a reduced number of unknown thermal parameters to adjust, hence a very precise calibration process, when compared with prototyping the complete machine.

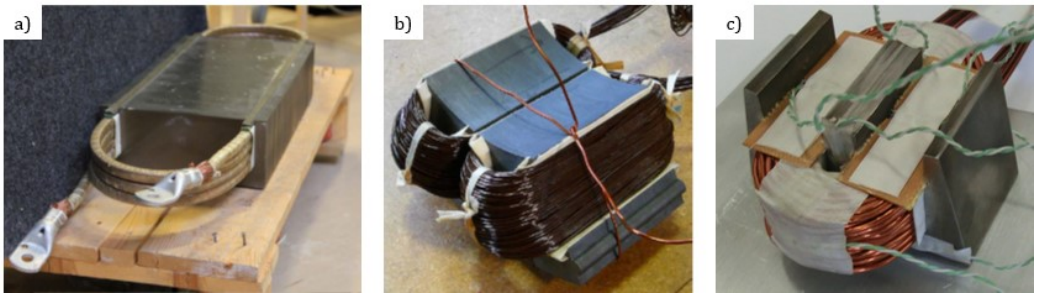

Fig. 2.13 Motorette hardware exemplars, a) Laminated test stack for Litz wire resistance factor measurement [214], b) Two segmented stator teeth with double-layer concentrated winding coils [215], c) Instrumented motorette prior to impregnation [216]

There are several examples in the literature of stator testing for the calibration of thermal models of electric machines [67], [95], [204]-[214].

These tests are typically completed prior to final machine assembly and allow the estimation of power loss from interaction between neighbouring phases and repeatability of the manufacturing process used are of particular interest [95], [208]-[214]. Some of the work reported in the literature refers here to insulation fault detection [208], [213] and heat transfer from the stator-winding into the machine housing [67], [125], [138], [186], [204]. The stator assembly dc testing process is similar to the complete machine one, and includes the connection of the winding phases in series with the temperature, current and voltage being recorded until steady-state is reached. Tests on a stator assembly allows for the interaction between phases to be accounted for. Experimental approaches commonly involve ac tests with three-phase current excitation. The mean winding temperature is often manually controlled by applying an additional excitation current or placing the sample in a thermal chamber in-between test points, in order to get some insight into the temperature/loss interdependence [95], [209]. An insight into the ac power loss is obtained, and a comparison with FE results allows for an accurate calibration of the thermal and electromagnetic models. Ac tests with one-phase excitation may be used in parallel, and the comparison between the results obtained from the three-phase analysis allows one to separate the bundle induced proximity loss from the strand-induced ones. Despite the continuous research in the domain of representative sub-assembly testing, further work is required to provide more definitive solutions concerning the motorette power loss analysis.

Table 2.10 Loss mechanisms associated with different test types [187]. Motorette refers here to a segment of stator-winding assembly

Loss component		Motorette/ Stator dc	Motorette/ Stator ac	Dummy rotor	Rotor, no windings	OC	SC	Full load
Mechanical	$P_{friction}$			x	x	x	x	x
	$P_{windage}$			x	x	x	x	x
Iron	P_{hyst}		x		x	x	x	x
	P_{eddy}		x		x	x	x	x
	P_{exc}		x		x	x	x	x
Winding	P_{dc}	x	x				x	x
	$P_{ac,e}$		x				x	x
	$P_{ac,r}$					x	x	x
Magnet	P_{pm}				x	x	x	x

Machine sub-assembly testing is not limited to the stator-winding region. A large part of the work focuses on testing sub-assembly hardware exemplars before complete machine assembly. In [117], the rotor assembly is evaluated in isolation to characterise the bearing loss before the machine assembly. Likewise, in [187], tests are conducted by rotating the

rotor assembly inside a stator core with no windings in order to get some insight into the mechanical, and some iron and PM loss effects.

In light of what was presented in Table 2.9, Table 2.10 introduces tests on machine sub-assembly. It is clear that custom-designed experiments, including both geometric mock-ups and representative machine sub-assembly, can contribute to an easier machine loss separation and identification. Tests on the complete machine hardware still provide a vital source of information used in the machine development, where numerous designs variants are considered. The use of the subassembly testing is intended to supplement the design process, shortening the time from the initial design to the final hardware implementation, and providing a database for various built-factors.

2.7 Summary

In this Chapter, a literature review was conducted, forming a base for the novel work presented in this thesis. The main procedures available for the power loss analysis of electrical machines have been presented in section 2.1, with focus on effective generation of accurate power loss data. The importance of experimental data for machine power loss analysis has been demonstrated. Section 2.2 has reviewed the most popular cooling techniques. This thesis focuses on electric machines where the heat is extracted via conduction from the stator to the housing periphery. This is indeed a widespread approach for electric machines used in automotive applications. For this configuration, a good knowledge of the path linking the heat source and the heat extraction system is crucial for a proper estimation of the machine thermal behaviour. Section 2.3 has provided some insights into the challenges linked with the evaluation of homogeneous and composite material properties, and thermal contact resistances. In particular, the influence of manufacturing and assembly techniques makes crucial a degree of 'in situ' experimental calibration for reliable material parameters and thermal contact resistances evaluation. The difficulty of physically representing some composite regions and multi-material interfaces has emphasised the importance of deriving appropriate thermal models. The mathematical tools for thermal modelling were introduced in section 2.4 in the context of required model accuracy and thermal sensor resolution. Finally, a wide selection of experimental techniques used to supplement thermal design of electrical machines has been reviewed at section 2.5. The need for tools for power loss separation and precise thermal parameters derivation has been highlighted. Testing methods making use of custom-built experiment have been presented in this context. In particular, approaches using representative reduced-order machine sub-assemblies are capable to provide accurate and reliable thermal and

power loss data in a time- and cost- efficient manner. Despite the recent findings in the domain of custom-built experiment and sub-assembly testing, further effort is required to provide more definitive solutions concerning the analysis of these assemblies, and the relation between sub-assembly and complete machine data. This thesis aims to validate an approach for the thermal and power loss analysis of electric machine, allowing for the machine development effort to be reduced.

The main objective of this thesis is the development and validation of a systematic and reliable experiment-informed methodology for high-fidelity thermal design of electrical machines. Three machine sub-assemblies have been selected to form basis for the proposed methodology: material samples, motorettes and stator assemblies, based on their complementarity and their capability to incrementally inform the machine thermal design. The selected building blocks will be investigated in comparison with the traditional machine testing methods, which will highlight both their respective limitations and applicability. The methodology will be demonstrated on several machine case studies to illustrate its potential. The following Chapter reviews the specificity of each building block in the methodology and presents selected machines for the methodology illustration.

Chapter 3
Experiment-informed methodology

3.1 Introduction

The commonly-used experimental method adopted for the thermal analysis of electric machines makes use of a complete machine assembly. This provides insight into the heat transfer and power loss effects with all the electromagnetic and mechanical loss components accounted for. However, this approach might not yield enough information regarding the loss share associated with individual machine regions, which is essential for high-fidelity design approaches. Testing on representative, reduced-order machine sub-assemblies can provide accurate and reliable thermal and power loss data for individual components in a time- and cost- efficient manner. This thesis establishes the basis of an experiment-informed methodology using reduced-order machine sub-assemblies to provide a systematic, comprehensive and reliable process for thermal design and analysis of PM machines. Firstly, this Chapter reviews the building blocks of the methodology with emphasis placed on the selected thermal or power loss parameters, which can be derived from the reduced order hardware tests. Secondly, the machine exemplars selected for the illustration and validation of the methodology are presented.

3.2 Methodology's building blocks

There are a number of mechanisms that require a degree of hardware calibration in thermal and power loss analysis of electric machines. In light of the observations made in Chapter 2, Fig. 3.1 presents a flowchart of the main parameters influencing a machine's thermal behaviour and generated power loss, along with the associated building blocks available for their derivation. The methodology aims at providing guidance for machine designers in various situations, including cases where only limited types of hardware exemplars are available to inform the design process. Therefore, the schematic flowchart presents first the recommended hardware exemplars to be used for the determination of each parameter, and then the existing alternatives. For instance, the recommended hardware exemplar for the derivation of the thermal conductivity parameters k_w and k_s is the material sample. However, tests on motorette, stator and complete machine assemblies may provide useful data for estimating these parameters if no material sample is available. The proposed

alternatives can also be used to verify the data obtained from the recommended hardware. A dashed-line indicates parameters that are outside the methodology's focus. Nonetheless, these parameters will be discussed in the context of the complete machine analysis. As mentioned in Chapter 2, the core and PM losses can be derived from tests on material samples, e.g. characterisation of laminated steel materials, and some mechanical loss components can be inferred from tests on custom-built experiments, e. g. dummy rotor tests. However, specific test rigs and hardware exemplars would need to be built and used to adequately measure these losses. These techniques are discussed in this thesis but not directly included in the proposed methodology.

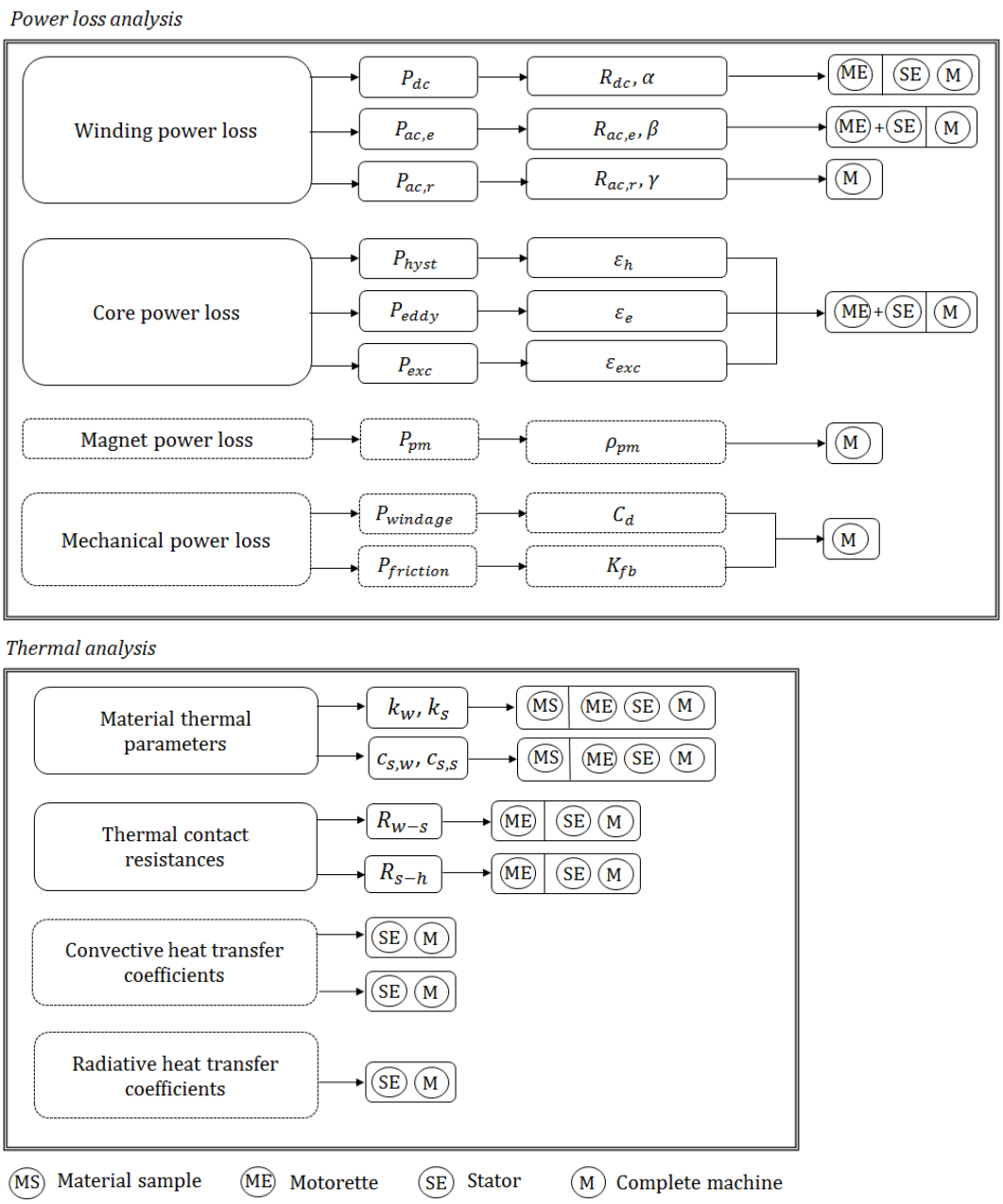

Fig. 3.1 Schematic flowchart of the proposed methodology, with suggested hardware exemplars

3.2.1 Composite material samples

The first building step of the proposed methodology utilises tests on composite material samples for the machine regions formed with multiple materials, e.g. impregnated winding [61],[183] or laminated core pack assemblies [133], [155], [183]. In addition to providing accurate material thermal data, the material samples simplify and accelerate the thermal analysis through the use of homogenisation [61], [156].

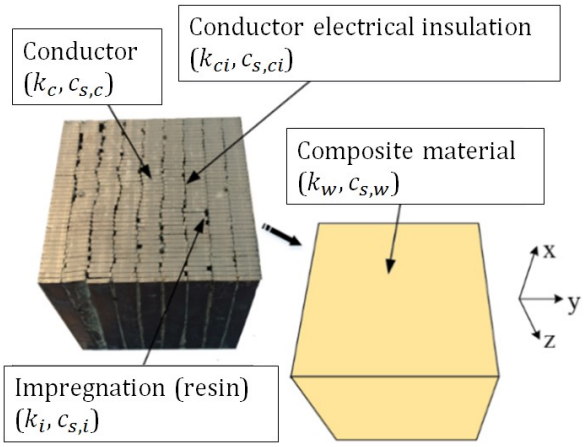

Fig. 3.2 Winding sample and equivalent homogenised region (k and c_s represent the thermal conductivity and the specific heat capacity, while the subscripts *c, ci, i* and *w* correspond to the conductor, conductor insulation, impregnation and winding, respectively) [53]

The principle of the homogenisation technique applied to the winding region is schematically shown in Fig. 3.2. The equivalent thermal material data include both the thermal conductivity and the specific heat capacitance. The testing of winding material samples is particularly useful in high fidelity thermal design analysis, where the material thermal anisotropy or inhomogeneous power loss distribution is accounted for [76], [89]. These are particularly important in identifying the winding hot-spot. The thermal anisotropy is frequently neglected in thermal analysis of electrical machines where a lower resolution or coarse modelling approach is employed [99], [127], [128], [180]-[182]. However, as highlighted in Chapter 2, existing empirically derived data highlights the importance of accounting for winding thermal anisotropy [53]-[59]. Building a large number of material samples might not be feasible due to cost and time constraints. Moreover, alternative approaches making use of theoretical methods have been proposed in the literature [155], [156], [190]. For instance, the analytical expressions used for estimating the winding thermal conductivity for various conductor fill factors and material design permutations have been developed for windings constructed with round conductors. These theoretical methods require calibration, with experimental data derived from tests

done using the material samples [156]. Once the individual material properties are derived, the global behaviour of the slot region may be investigated.

3.2.2 Motorette assembly

Testing on the motorette samples was selected as a second building block for the proposed methodology. Motorette testing is used for in-situ analysis of thermal behaviour accounting for interactions between various materials and sub-assemblies, e.g. the slot liner's capability for absorbing impregnation material and its influence on the contact thermal resistance from the winding body to the stator core pack. The methodology mainly focuses on the use of motorette testing for the derivation of the winding to stator thermal contact resistance R_{w-s}. Fig. 3.3 presents an outline of a motorette assembly cross-section, where the interface between the winding body and the core pack is represented as an equivalent composite 'gap' region comprising the slot liner, the impregnation and the air cavities amalgam. Such an approach simplifies the model definition and reduces the solving time. Due to different conductor lay in the radial and circumferential directions, separate adjustments for both heat transfer paths are frequently required [113]. It should be noted that, the contact interface between the motorette's back iron and the interfacing plate is not representative of that present in the complete machine assembly. This is related to the manufacturing and assembly processes used in housing the laminated stator core pack, e.g. a heat shrunk stator into an aluminium casing is used to provide 'good' heat transfer from the stator to the machine's housing. These conditions are difficult to replicate in a simple manner using the motorette assembly.

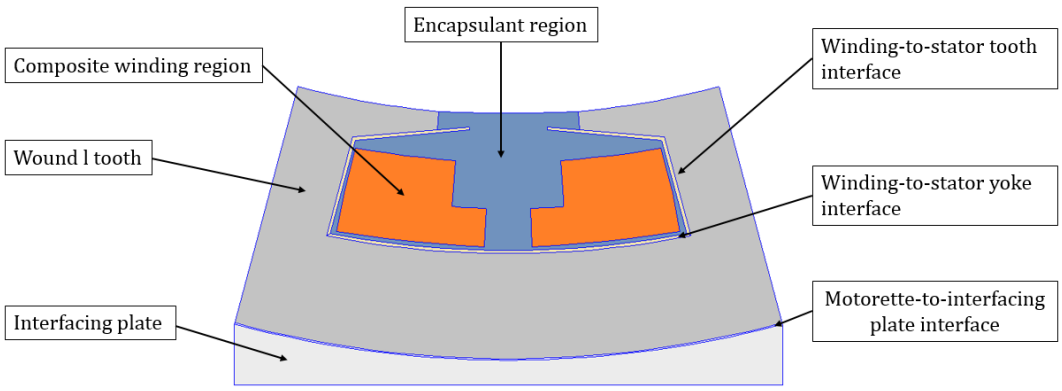

Fig. 3.3 Outline of a motorette assembly

The impact of different winding arrangements and stator slot shapes on the heat transfer might also be investigated. However, some of the design alterations used to improve the heat transfer from the machine's body also influence the machine electromagnetic

behaviour, in particular the generated power loss. Therefore, the loss analysis is vital in the thermal design of electrical machines. Furthermore, both the thermal and the loss effects need to be evaluated concurrently due to their interdependence. Tests on motorette assemblies provide an insight into the power loss effects suitable for loss separation and inform the loss temperature dependence. On the one hand, the motorette testing is only representative of some of the losses present in the complete machine, e.g. the effects associated with the rotation of the PM rotor and/or the interaction between the winding phases are not accounted for. However, the measured loss data for such cases allows identification of the most promising design variants and informs the design process of the stator-winding assembly [20]-[32]. On the other hand, the absence of some of the loss components present in the full machine allows for a simpler loss separation and provides better understanding of the loss effects. This is particularly important in the context of the ac loss effects, which require careful considerations for identifying the dominant ac effects.

Despite developments made in the field of computational electromagnetics, the prediction of ac winding losses remains a challenging and time-consuming task. This results from the need for detailed loss data related with individual winding conductors, and is further exacerbated by the fact that for some of the winding arrangements the precise location of the individual conductors in the slot is unknown, e.g. multi-stranded mush winding [94]. In this context, tests on motorettes provide an alternative to the ac loss estimation, where functional representations of the winding and iron loss variations with frequency, temperature and magnitude of the excitation current are accounted for [94], [95]. Motorettes can also be used for the estimation of the end-winding's contribution to the ac losses [56]. The derivation of the end-winding ac losses usually requires the use of a 3D FE model, and experimental measurements appear as a fast and reliable alternative. Once the power loss has been derived for a single stator-winding section, the global behaviour of the stator assembly may be investigated.

3.2.3 Stator assembly

The stator assembly is the third building step of the methodology. At first glance, building a full stator for the evaluation of some thermal parameters might seem both time-consuming and costly as compared with building a single-coil motorette assembly. However, tests on a stator assembly can be completed before testing of a complete machine. Manufacture of the complete stator-winding assembly is one of the stages of the machine development process. Tests on the stator-winding provide first insight into the machine actual performance. In particular, stator-winding testing is significantly simpler than

characterisation of the complete machine. A further advantage of the use of a stator assembly instead of a motorette is that it provides insight into the repeatability of the manufacturing process employed. The stator assembly might be analysed before or after inserting it in to the housing, depending on hardware availability and manufacturing or assembly processes used. The presence of the housing allows estimation of additional thermal parameters, such as the stator-to-housing thermal contact resistance R_{s-h} [211]-[213].

Stator tests are not limited to the heat transfer analysis and also give an insight into the loss generated within the stator-winding assembly taking into account the interaction between the winding phases. Experimental approaches commonly involve ac tests with three-phase current excitation. The mean winding temperature is often manually controlled by applying an additional excitation current or placing the sample in a thermal chamber in-between test points in order to derive the temperature and power loss interdependence. This is specifically done for ac operation [95], [209]. The measured ac power loss allows for a comparison with the FE results and an accurate calibration of the thermal and electromagnetic models. Ac tests with one-phase excitation may be used in parallel. The comparison between the results obtained from the three-phase analysis allows one to separate the proximity effects induced from a single phase from the ones induced from its neighbouring phases. This is very important in the context of winding loss reduction as the proximity losses due to neighbouring phases have been shown to be a significant part of the winding losses [95]. It is frequently assumed that the end-winding power loss contribution is not affected by the rotor induced proximity losses. Consequently, the stator-winding assembly is generally sufficient to estimate the machine overall end-winding loss component. At the end of the design process, it is necessary to provide further information regarding the machine's overall electromagnetic and mechanical losses, such as the ac effects due to the rotor rotation or the PM power losses. In this case, the complete machine assembly needs to be analysed.

3.2.4 Complete machine assembly

The final building block of the proposed methodology is the complete machine assembly. Tests on a complete machine allow evaluation of the power loss effects associated with the rotation of the rotor assembly, e.g. rotor-induced winding losses and mechanical losses, among others. The tests described in Chapter 2, including open- and short- circuit tests, can be used to infer the core, the winding and the mechanical loss components. Static dc tests are also useful for identifying thermal parameters during complete machine tests. The use

beforehand of the three first building blocks greatly simplifies the thermal model validation and loss separation process, as only a few parameters are left to be identified. A complete machine prototype designed with a truly coupled electromagnetic and thermal design, where thermal and electromagnetic models have been informed from the three first building blocks of the methodology, should be close to a final product.

3.3 Selected machines for illustration

Four exemplar PM machines have been selected to illustrate the use of the developed approach and showcase its potential. These machines were available in the laboratory and have been reverse-engineered in this thesis. Fig. 3.4 shows the cross-sections of each machine's geometry and indicates the active regions. Table 3.1 lists basic data for the four machines, and Table 3.2 provides information about each machine's cooling set-up. Tables 3.3 and 3.4 list data for the winding and rotor regions of each machine, respectively. Finally, Table 3.5 lists material data for each machine.

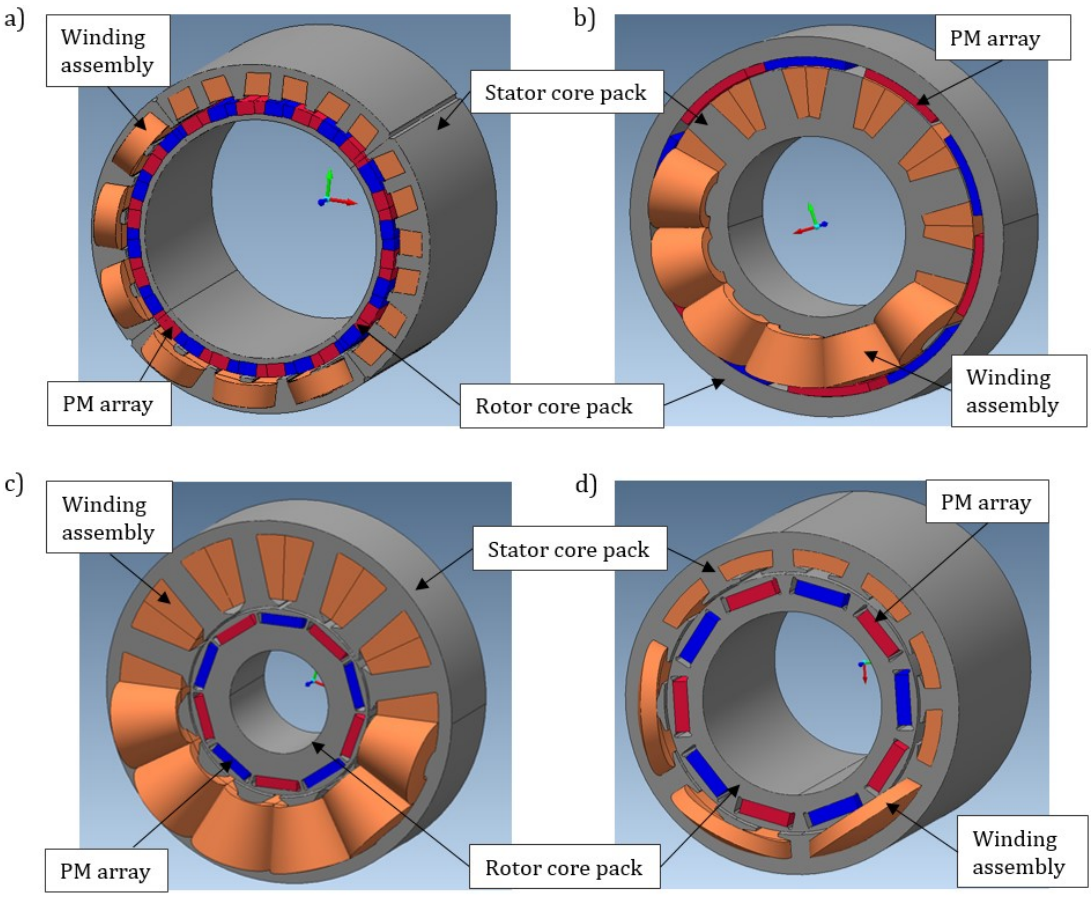

Fig. 3.4 Cross-section of the machines' geometries with the active regions indicated, a) M-I, b) M-II, c) M-III, d) M-IV

Table 3.1 Basic data of the selected machines

	M-I	M-II	M-III	M-IV
Number of poles/slots	28/24	10/12	10/12	10/12
Rated speed (max. speed) [RPM]	1700	4000	4200 (10 000)	4770 (12 000)
Rated fundamental frequency [Hz]	400	333	350 (833)	397 (1000)
Rated output power [kW]	180	30	12	60
Rated torque [N]	1000	72	30	150
Rated current [A_{rms}]	~400	141	77	71
Active length [mm]	209	51	90	277
Outer diameter [mm]	~330	250	175	162.6
Dc link [V_{dc}]	270	110	225	600

Table 3.2 Details of the cooling set-ups of the selected machines

	M-I	M-II	M-III	M-IV
Heat extraction region	Housing	Shaft	Housing	Housing
Form of convective heat transfer	'Forced'	Forced	Natural	Forced
Fluid type	Air	Liquid	Air	Liquid
Heat extraction set-up	Fins	Water jacket	Fins	Water jacket

Table 3.3 Winding data of the selected machines

	M-I	M-II	M-III	M-IV
Winding configuration	Concentrated	Concentrated	Concentrated	Concentrated
Number of layers	Single	Double	Double	Single
Slot structure	Open	Open	Quasi-closed	Quasi-closed
Number of turns	14	7	7	24
Number of parallel paths	4	1	44	1
Conductor type	Type-8 Litz wire	Rectangular	Round	Rectangular
Conductor size	10 Ø1.3 mm	1.4 × 7 mm^2	Ø 0.8 mm	1.5 ×3 mm^2
Impregnation type	Varnish	Varnish	Varnish	Epoxy
Winding process	Pre-built	Pre-built	On-slot	On-slot
Fill factor	60%	77%	55%	73%

Table 3.4 Description of the materials used for the selected machines

	M-I	M-II	M-III	M-IV
Conductor	*Cu*	*Cu*	*Cu*	*Cu*
Slot liner	Nomex 410	Nomex 410	Nomex 410	Nomex 410
Impregnation	Varnish[1]	Varnish[1]	Varnish[2]	Epoxy[3]
PM	*SmCO* (Recoma 33)	*NdFeB* (N42UH)	*NdFeB* (N38UH)	*SmCO* (Recoma 26)
Core (*SiFe*)	M250-35A	M250-35A	M270-35A	M270-35A

[1] Elmotherm 073-1010, [2]Ultimeg 2000/U380, [3]Aremco-Bond 231

Table 3.5 Rotor data of the selected machines

	M-I	M-II	M-III	M-IV
Rotor configuration	Inner	Outer	Inner	Inner
PM topology	Surface-mounted	Surface mounted	Interior	Interior
Axial PM segments	~20	10	8	36
Magnetisation	Halbach array	Parallel	Parallel	Parallel

3.3.1 Machine I (M-I)

M-I has been developed with the targeted application of a helicopter's electric tail rotor drive. One of the classic primary design criterions of the aeronautic industry is to ensure the machine reliability. M-I's fault tolerance is ensured by using electromagnetically insulated stator coils, assembled to form four autonomous three-phase modules around the stator circumference. This configuration is sometimes referred to as a machine-modular topology [187]. The intended application of M-I, at the tail of a helicopter, makes its cooling approach similar to a forced-air convection mechanism. An open-slot stator topology has been selected for M-I, which greatly simplifies the manufacturing, reliability and robustness of the winding assembly. However, this topology can lead to significant ac effects, due to 'high exposure' of the conductor to the magnetic field from the PM rotor. To mitigate these effects while still realising a relatively high conductor fill factor, a multi-stranded compacted rectangular profiled Type-8 Litz construction has been adopted here. Minimising the M-I's mass was a secondary design focus, also typical of the aeronautic industry. Here, M-I's targeted continuous specific torque exceeds 20 Nm/kg, and its volumetric envelop is also restricted.

3.3.2 Machine II (M-II)

M-II has been designed for an aircraft application, with the objective of replacing an existing mechanical brake used to decelerate a helicopter's main rotor and provide additional power source and control for the autorotation. M-II consists of an outer rotor and an open-slot stator topology with double-layer concentrated winding. The principal design requirements associated with M-II include mechanical robustness and manufacturability. Edge-wound preformed coils have been used, greatly simplifying the manufacturing process while improving the repeatability and robustness of the winding construction. Like M-I, M-II's open-slot topology makes the analysis of winding ac power loss crucial for an efficient design. Due to M-II's intended fixed-speed operation, the winding design has been finely tuned to minimize the ac and the dc winding power losses [89]. The heat from the stator-winding assembly is extracted via a liquid-cooled shaft arrangement [89].

3.3.3 Machine III (M-III)

M-III is a radial-flux brushless PM machine designed for an electrical vehicle propulsion application [104]. M-III's stator assembly comprises a double-layer concentrated winding configuration, made of 7 turns with 44 strands in hand. The theoretical analysis of the ac mush winding's losses is particularly challenging, since the exact positions of the

conductors within a bundle might be difficult to determine. Here, the developed methodology will allow for the investigation of the ac loss components using motorette, stator and complete machine assemblies. To improve heat extraction from the winding body to the machine's periphery, the complete stator-winding is impregnated with varnish and housed in a standard flange mounted aluminium finned frame.

3.3.4 Machine IV (M-IV)

M-IV is aimed at a steer-motor for a hybrid skid-steering transmission system [113]. One of the main design requirements focuses on machine reliability. As for M-I, M-IV's fault tolerance is ensured by using a machine-modular topology, making use of electromagnetically insulated stator coils assembled to form two autonomous three-phase modules around the stator ring. Each three-phase module is powered by a conventional inverter, simplifying the drive design compared to alternative fault-tolerant topologies, such as multi-phase machines [217]. M-IV consists of a segmented stator assembly with a single-layer concentrated modular winding. To provide 'good' heat extraction from the winding body to the machine periphery, the complete stator-winding is encapsulated with a high thermal conductive epoxy resin.

3.4 Discussion

This Chapter has outlined specifics related to each of the building blocks for the proposed methodology, and introduced the selected machine exemplars used to showcase the developed methodology. The methodology is specifically tailored for PM machines with concentrated windings, whose heat is extracted via the housing frame. Specific design characteristics have been presented for the selected four machines, which were shown to differ in terms of power output, operating speeds, and intended applications, among others. These differences should contribute to make the proposed methodology more robust, by allowing more general conclusions to be formed.

M-II, M-III and M-IV comprise a similar 12-slot 10-pole topology, which has been a popular choice in the literature due to its relatively 'high' fundamental winding factor and fairly high least common multiple between the number of slots and poles, resulting in a low cogging torque [58], [59], [113], [154]. The similarity in machine topologies should however not affect the generality of the proposed methodology, as the thermal parameters are sensitive to design aspects such as material, winding configuration, and slot geometry, but not to the number of stator slots per se. 12-slot 10-pole topologies might present high levels of rotor noise, vibration and harmonics due to sub-harmonic magneto motive force

(MMF) components generated by the stator winding [218]. A double layer has been adopted for M-II and M-III, as this winding configuration reduces MMF harmonic content, hence power loss and torque ripple, when compared to a single layer topology [219]. A single layer topology was adopted for M-I and M-IV, as double layer windings would not provide the thermal and magnetic insulation required for fault-tolerance operation. The single- and double- layer topologies are expected to influence the results obtained from motorette and stator testing, as the number of windings within the same slot will result in additional winding power losses and effects. Therefore, the selected machines featuring both winding constructions should broaden the view on the proposed methodology. Parallel studies of stator and motorette assemblies will be used to assess the thermal and magnetic separation between the phases, especially in the context of fault-tolerant machines.

Each of the selected machine exemplars has concentrated windings. This topology is undeniably well-suited for motorette testing, as a coil wound around a tooth represents an equivalent portion of the complete stator-winding assembly. A similar representation of distributed windings is however more challenging. In such case, the winding configuration must be adapted to represent as precisely as possible the dimensions and positions of the conductors in the complete stator assembly. For this reason, the methodology mainly focuses on machine with concentrated windings. Guidance will nonetheless be provided on the best approach to adopt when working with machines formed with distributed windings, based on the author's personal experience and existing literature [170].

The variety of operating speeds and output power embodied by the four baseline machines, from a rated speed of 1 700 rpm for M-I to a maximum speed of 12 000 rpm for M-IV, leads to a range of employed winding designs. The baseline machines comprise different conductor types, cross-sections and arrangements within the slot. This is very interesting in the context of the proposed methodology, as each conductor profile typically requires specific analysis, e.g. in terms of the manufacturing process and/or the sensitivity of ac loss effects, among others. The analysis of the three more prevalent conductor profiles for electric machine design, Litz wire, round- and rectangular-profiled conductors, should allow formation of general conclusions, as well as specific observations related to each conductor type. This also applies for the different materials adopted for the baseline machines, e.g. impregnation and slot liner constituents. The diversity of output powers and targeted applications for the baseline machines also results in different cooling approaches being adopted. Investigations for each cooling type shall contribute to making the proposed methodology more robust. Moreover, guidance will be provided on choosing the best

testing and modelling approaches for the thermal parameters' identification associated with different cooling set-ups.

The analysed hardware exemplars are not limited to the ones representative of the four baseline machines. In fact, the analysis of each building block of the developed methodology includes additional hardware exemplars different from the ones representative of the baseline machines. For instance, while studying the methodology's first building block, data from additional winding samples varying in terms of fill factor, conductor and impregnation materials enabled the derivation of generic correlations. The obtained values will also form a valuable data library, which may be used by thermal designers at an initial machine design stage.

Chapter 4
Material samples

4.1 Introduction

The first building step of the proposed methodology utilises tests on composite material samples (MSs) to evaluate the thermal parameters of selected machine regions. The determination of thermal parameters represents a significant challenge as they are influenced by many factors, including manufacturing and assembly methods [61], [183]. The composite regions include the impregnated windings and laminated core packs. In thermal analysis, such regions are frequently homogenised, as representing each component would lead to long set up and solving times and limit the applicability of the models in transient problems or iterative design and optimisation procedures. The winding material sample testing is particularly useful in high fidelity thermal design-analysis, where the material thermal anisotropy and inhomogeneous power loss distribution are accounted for.

This Chapter presents a repeatable procedure for the estimation of equivalent thermal properties of impregnated windings, making use of theoretical and experimental methods. The techniques allow for time effective and accurate derivation of thermal properties for composite materials, including the material thermal anisotropy. Efficacy of the methods is demonstrated on several hardware winding samples (WS) constructed using materials and processes commonly found in low-voltage machine designs. A comparative case study of the existing and proposed analytical methods for estimating the winding equivalent thermal conductivity is presented to showcase the importance of the input winding material data in thermal analysis of electrical machines and devices.

4.2 Composite material samples

4.2.1 Presentation of hardware exemplars

A variety of WSs and core samples have been analysed, Fig. 4.1. WSs I to IV correspond to the baseline machines, with each sample numbering matching its associated machine, i.e. WS-I is associated with M-I. The samples WS I to WS V, WS VII, WS VIII and WS XIX have been made as part of the research presented in this thesis, while the other samples

were already existing from previous university projects [53], [59], [89], [144], [156]. Table 4.1 presents basic data for the impregnated WSs associated with the baseline machines.

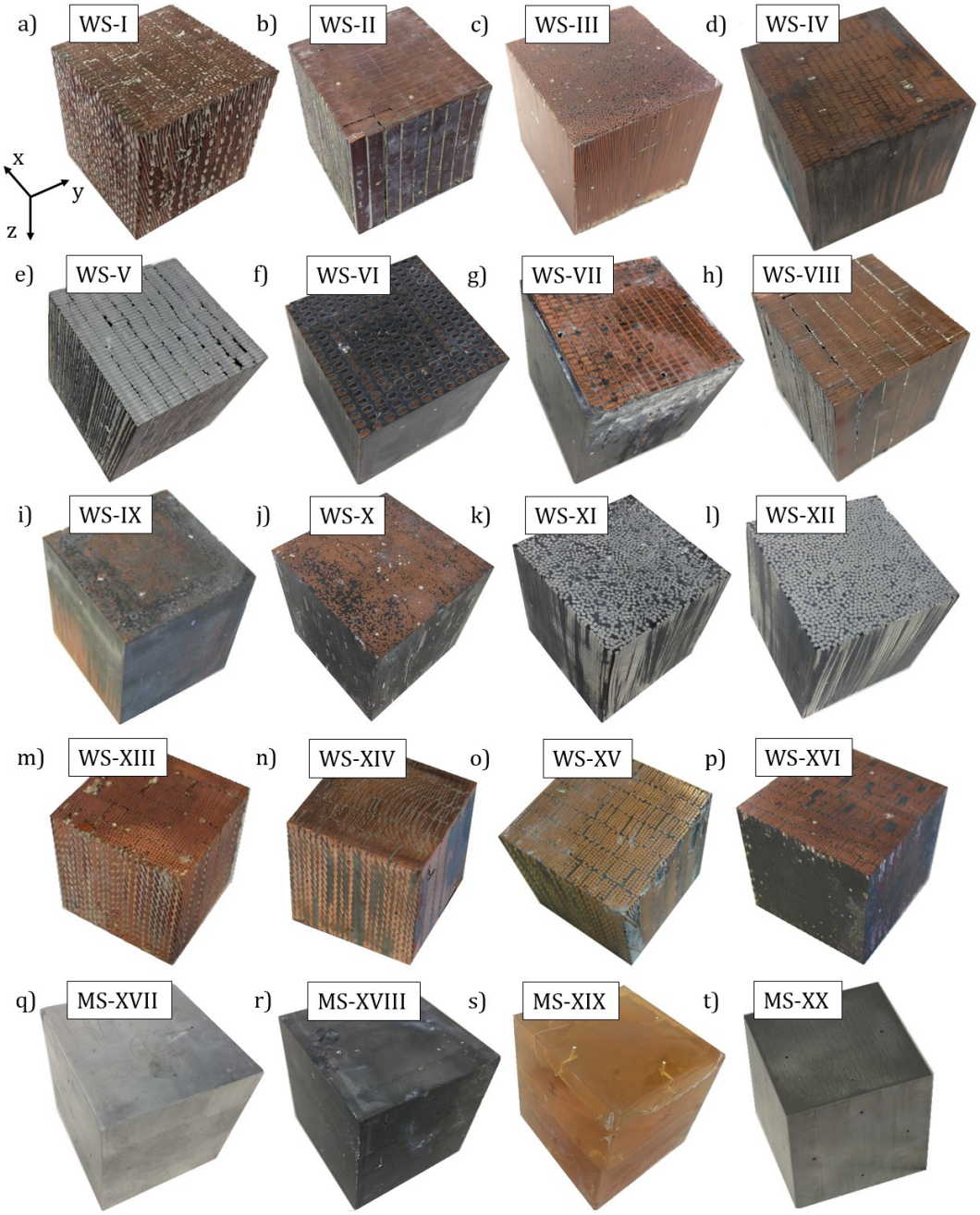

Fig. 4.1 Investigated material samples, including impregnated winding: baseline machine – WSs I to IV, rectangular conductors – WSs II, IV to VIII, round conductors – WSs III, IX to XII, Litz wires – WSs I, XIII to XVI, and selected materials present in the baseline machine – MSs XVII to XX

Tables 4.2, 4.3 and 4.4 list basic construction information for the impregnated WSs formed with rectangular conductors, round conductors and Litz wire, respectively. In Table 4.4, FF_b corresponds to the Litz bundle conductor fill factor, i.e. the ratio of the individual

strands of the Litz wire to complete Litz wire cross-section. The parameter FF_s is the complete WS conductor fill factor, as defined for other conductor types.

Windings formed with Litz wires have been studied throughout a collaborative work, and documented in the conference paper [217] listed in the publications associated with this thesis. Four cuboidal samples made of materials present in the baseline machines have also been investigated. The selected material includes: a cuboidal sample made of a particular *Al* alloy, used as means of calibration for empirical measurements, Fig. 4.1q), impregnation samples made of epoxy resin (Epoxylite EIP 4260), Fig. 4.1r), and varnish (ELAN-protect up 142), Fig. 4.1s), respectively, and a laminated steel cuboidal sample, made of 180 sheets of M300-35A with low viscosity cyanoacrylate (Loctite 493), Fig. 4.1t). The lamination thickness is 0.35 mm with 10 μm of insulation on each side, i.e. a total thickness of 0.37 mm.

Table 4.1 Basic data for the impregnated winding samples corresponding to baseline machines

Sample	Type	Conductor fill factor	Impregnating material	Conductor dimensions
WS-I *(Cu)*	Litz wire	60%	Varnish	8 ø 1.3mm strands
WS-II *(Cu)*	Rectangular	77%	Varnish	(1.4×7.0=9.8) mm^2
WS-III *(Cu)*	Round	55%	Varnish	Ø 0.8 mm
WS-IV *(Cu)*	Rectangular	73%	Epoxy	(1.5×3.0=4.5) mm^2

Table 4.2 Basic data for the impregnated winding samples formed with rectangular conductors

Winding sample	Conductor fill factor	Impregnating material	Conductor dimensions	Conductor aspect ratio
WS-V *(Al)*	77%	Varnish	(1.4×7.0=9.8) mm^2	5.0
WS-VI *(Cu)*	27%	Epoxy	(1.5×3.0=4.5) mm^2	2.0
WS-VII *(Cu)*	47%	Epoxy	(1.5×3.0=4.5) mm^2	2.0
WS-VIII *(Cu)*	77%	Varnish	(1.2×10.0=12.0) mm^2	8.3

Table 4.3 Basic data for the impregnated winding samples formed with round conductors

Winding sample	Conductor fill factor	Impregnating material	Conductor dimensions	Electrical insulation
WS-IX *(Cu)*	60%	Epoxy	ø 1.6 mm	Enamel
WS-X *(Cu)*	60%	Epoxy	ø 0.67 mm	Enamel
WS-XI *(Al)*	66%	Epoxy	ø 1.6 mm	Enamel
WS-XII *(Al)*	55%	Epoxy	ø 1.6 mm	Aluminium oxide

Table 4.4 Basic data for the impregnated winding samples formed with Litz wires

Winding sample	Number of strands	Strand gauge AWG	Nominal width and thickness [mm/mm]	Impregnating material	FF_b	FF_s
WS-XIII	15	16	10.74/2.46	Varnish	74%	64%
WS-XIV	15	16	10.74/2.46	Epoxy	74%	61%
WS-XV	8	16	6.10/2.46	Epoxy	70%	60%
WS-XVI	14	16	10.06/2.46	Epoxy	74%	60%

All the conductors used in WS-I to WS-XVI, except WS-XII, are coated with the same grade of polyamide-imide enamel (class N) with thermal conductivity equal to 0.26 W/(m·K) and measured thickness of 0.035 mm per conductor side. The WSs were carefully chosen here to differ in terms of conductor fill factor, conductor aspect ratio, and impregnating material. The comparison between these sets should provide a comprehensive insight into the problem in the context of model calibration with limited number of WSs. Fig. 4.2 recapitulates the relationship between different WSs. The connected WSs only differ in one or two parameters, indicated under the connection between the WSs. For instance, WS-II and WS-V have similar construction, apart from the conductor material used; copper for WS-II and aluminium for WS-V. The variety of the analysed samples enables a more generic insight into the composite winding thermal properties and their dependence on the geometrical, material and manufacture factors.

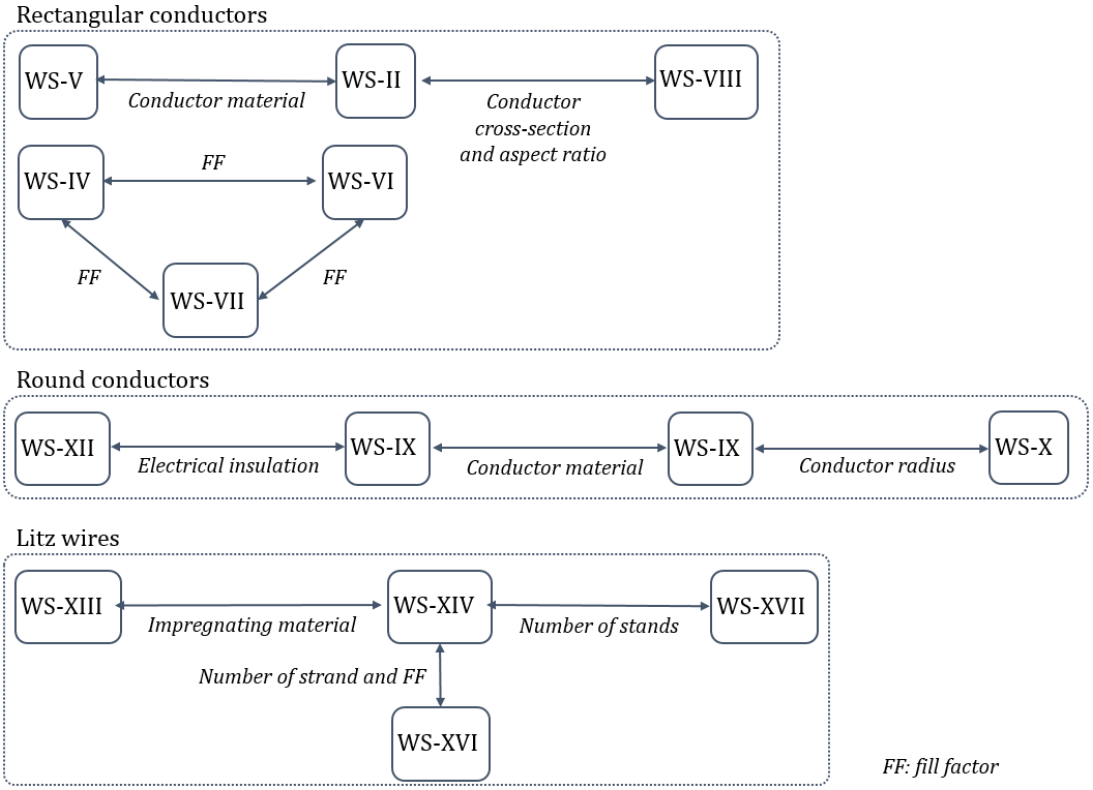

Fig. 4.2 Relation between WSs used in theoretical analysis

4.2.2 Winding and impregnation material sample construction

The winding sample manufacturing procedure involves stacking conductor segments of equal length in parallel inside an appropriate former, Fig. 4.3. The sample is then vacuum impregnated with a selected material (varnish or epoxy resin). After the impregnation is cured, the former is removed, and the winding sample is machined or sawn to provide a

'good' surface finish required in measurements of the composite material thermal conductivity. A Teflon non-sticky tape has been glued on the side of the former and bolts have been added to facilitate the sample extraction. The former has also been used for the impregnation material cuboidal samples. The samples are manufactured in a cuboidal shape, which ensures the same measuring conditions in all three axes of the sample, accounting for the potential anisotropy. The size of the cuboidal samples, ($66\times66\times66=2.87\times10^5$) mm^3, was initially chosen to fit six Type-8 Litz wires of a particular construction, and then became a 'standard' for fabricating further samples.

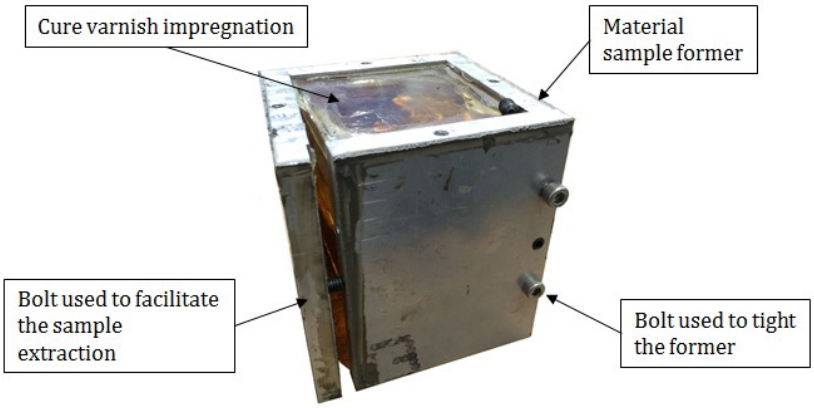

Fig. 4.3 Winding sample inside the former after impregnation. Bolts have been added to the former in order to facilitate the sample extraction

The adopted size of the winding sample is a compromise between manufacturing time (the larger the cuboidal sample, the longer it takes to construct it), and the desired data reliably. Indeed, it is desirable to ensure a large temperature gradient through the winding sample during test to minimise the impact of measurement errors. This can be straightforwardly achieved by testing a 'larger' hardware exemplar. This will be discussed in more detail in the following sections in the context of uncertainty analysis.

4.3 Winding and laminated core pack representations

4.3.1 Winding region

The computational methods employed in thermal analysis of electrical machines, transformers and wound passive components make use of various techniques for representing the winding region. The existing methods have been schematically shown in Fig. 4.4. The level of complexity for the winding model representation is usually chosen based on required fidelity for the temperature predictions within the machine assembly. This is driven by numerous factors, some of which include: the power loss sources and their mechanisms accounted for, e.g. inhomogeneous loss distribution due to ac effects in

the machine active regions [89], [96], [97]; higher resolution for the temperature predictions, e.g. accurate identification of the hot-spots [220]-[222]; reduced computational effort, e.g. thermal envelope mapping for a given operating envelope and/or cycle.

The physical representation of winding region with the individual winding conductors accounted for, Fig. 4.4a), is the most intuitive among the existing alternatives. However, the setting-up and solving time for such defined thermal model is frequently prohibitively high as all the individual material regions including conductor enamel and impregnation need to be represented in the model.

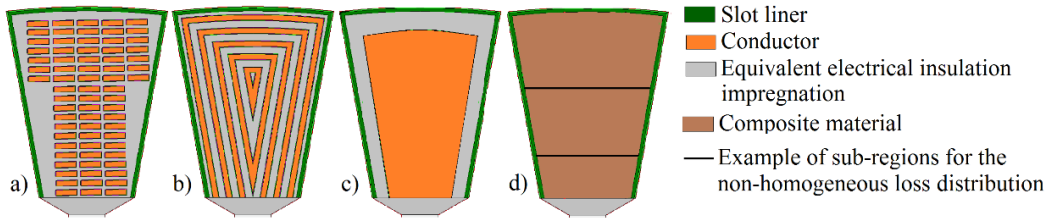

Fig. 4.4 Schematic cross-section of a stator slot with alternative winding representations used in thermal analysis of electrical machines: a) physical model, b) layered model, c) equivalent material model, d) homogenised model

The layered winding representation, Fig. 4.4b), was developed to accelerate the thermal model setting-up and solving time while maintaining accuracy of the temperature predictions including the hot-spot identification [133], [220]. In this approach, the physical winding representation is transformed into the layered equivalent, such that the volumetric contribution of each of the individual winding materials remains unchanged. The number of model layers is chosen using an analytical formula allowing for correct predictions for the hot-spot location [220]. The technique is well suited for the equivalent-circuit lumped-parameter thermal modelling approach with model complexity ranging from medium to high. The equivalent material method for the winding region approximation, Fig. 4.4c), is intended for reduced-order equivalent-circuit lumped-parameter thermal analysis, where temperature distribution within the winding body is of lesser importance [180], [183]. As for the previous approach, the volumetric contribution of each of the individual winding material is identical to that from the physical winding. However, the individual materials here form distinctive homogenous regions arranged by combining smaller discrete sub-regions present in the physical winding, Fig. 4.4c). The homogenised winding representation, Fig. 4.4d), requires thermal data for the winding amalgam to be known prior to machine thermal model definition. The complete winding is represented here by a single region defined with composite material data [183]. The approach allows for the inhomogeneous winding loss distribution to be accounted for by simply subdividing the

winding region into smaller sections, Fig. 4.4d), informed with appropriate winding loss share per section [89], [96], [97].

One of the thermal parameters required by the homogenised model is the equivalent winding thermal conductivity. The existing theoretical winding homogenisation methods were initially developed in the context of two-component composite materials for the electromagnetic or optic applications [224]-[227], later adapted in the thermal analysis [225]. The two-component formula neglects the conductor electrical insulation, which has been shown later essential for deriving accurate thermal material data [99]. A modified three-component formula has shown particularly suitable for the winding constructions impregnated with high thermal conductivity encapsulants, like epoxy resins [156]. Analytical expression for equivalent thermal conductivity, k_w, for three-component winding composite with round conductors is given:

$$k_w = k_a \frac{(1+v_c)k_c+(1-v_c)k_a}{(1-v_c)k_c+(1+v_c)k_a} \qquad (4.1)$$

where subscripts c and a refer to the conductor and impregnation/insulation amalgam, respectively. The conductor volume ratio v_c is taken to be equal to the conductor packing factor. To account for three-material winding composite, k_a is calculated with the following formula [156],

$$k_a = k_i \frac{v_i}{v_i + v_{ci}} + k_{ci} \frac{v_{ci}}{v_i + v_{ci}} \qquad (4.2)$$

where the subscripts *i* and *ci* refer to the impregnation material and electrical insulation, respectively. The existing analytical methods are focused on winding constructions utilising round conductors, where the equivalent thermal conductivity across the conductors is usually expected to be isotropic. This approximation however, is not valid for the windings formed with rectangular conductor or Litz wires, where the winding individual materials are distributed non-uniformly within the stator slot. As discussed in Chapter 2, the empirically derived data have highlighted the importance of accounting for the winding thermal anisotropy [53]-[59]. An effort is put in this Chapter on developing an appropriate analytical solution for deriving the orthotropic thermal conductivity of winding formed with rectangular-profiled or Litz conductors. The formulas developed for round conductor have also shown limited use for winding with packing factor higher than 40% [156]. Windings formed with high packing factor have recently gained more interest, e.g. development of pre-compressed windings with improved thermal conductivity [145], [191], [225], [226], and consequently novel approaches for the theoretical derivation of

equivalent winding thermal parameters have been researched in this thesis work. The homogenisation techniques discussed here refer to the equivalent thermal conductivity across the conductors only, as required for the model presented in Fig. 4.1d).

The winding equivalent thermal conductivity along the conductors may be calculated to evaluate the impact of the end-winding heat transfer on the winding active length, in particular for 'short' machines. The winding equivalent thermal conductivity along the conductors can be derived from the volumetric share and thermal properties of the individual materials [156]:

$$k_{w,axial} = k_i v_i + k_{ci} v_{ci} + k_c v_c \qquad (4.3)$$

By default, the parameter k_w refers to the radial or circumferential equivalent winding thermal conductivity in the next sections of this chapter. Finally, a formula describing the equivalent specific heat capacity for winding amalgam is given as follows,

$$c_{s,w} = \frac{PF(\rho_{d,c}c_c - \rho_{d,i}c_i) + \rho_{d,i}c_i}{PF(\rho_{d,c} - \rho_{d,i}) + \rho_{d,i}} \qquad (4.4)$$

where c_s, ρ_d and PF are the specific heat capacity, density and packing factor. It has been shown in [156] that the impact of the conductor electric insulation is usually negligible, as (4.4) is based exclusively on the volumetric contribution of each of the winding components, which is typically small for the enamel coating.

4.3.2 Laminated core region

The laminated steel equivalent thermal conductivity is a function of clamping pressure, lamination thickness, stacking factor, lamination surface finish, and interlamination insulation material, among others [89], [155]. In most cases, the heat extraction path is realised via the stator core pack to the machine housing; therefore the 'in-plane' thermal conductivity is of interest. The following formula is typically utilised to analytically evaluate the 'in-plane' thermal conductivity of the core [155]:

$$k_{s,in-plane} = k_L \frac{A_L}{A_s} + k_{coat} \frac{A_{coat}}{A_s} + k_{air} \frac{A_{air}}{A_s} \approx FF.k_L \qquad (4.5)$$

where the subscripts *s, L*, *coat* and *air* correspond respectively to the complete lamination stack, lamination material, lamination coating and interstitial space between the lamination. *A* is the equivalent cross-section area.

The 'through-stack' thermal conductivity might be of consideration if a less common orientation or topology is envisaged for the core assembly [144].

The following formula is typically utilised to analytically evaluate the 'through-stack' thermal conductivity of the core [155]:

$$k_{s,through-stack} = \frac{t_L}{R_{coat}+R_L} \qquad (4.6)$$

where t_L, R_{coat} and R_L correspond to, respectively, the thickness of a single lamination, and thermal resistance of the coating and lamination. It is worth noting than in [155], the area of contact is included in the definition of the thermal resistance, which is therefore expressed in mm^2.°C/W. As previously underlined, formulas (4.5) and (4.6) require a degree of experimental calibration, and are not intended for a 'stand-alone' use [144].

4.4 Experimental measurements

4.4.1 Thermal conductivity

There are several experimental methods applicable in measuring the equivalent thermal conductivity for the composite materials, e.g. the transient hot strip technique, the flash method or the heat flux meter approach [53], [156]. The heat flux meter approach with cuboidal MS has been selected as the recommended approach for this methodology, as the necessary equipment is commonly available in an electrical engineering laboratory. The method emulates a unidirectional conductive heat transfer through a given axis of a material sample, Fig. 4.5.

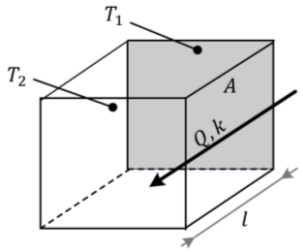

Fig. 4.5 Schematic of a one-dimensional conductive heat transfer across a cuboidal winding material sample

By applying a known heat transfer rate $\dot{Q}$ and measuring the temperature difference $\Delta T = T_1 - T_2$ along the sample length l and across the sample cross-section A, the thermal conductivity k in one-axis of the MS can be derived,

$$k = \frac{\dot{Q} l}{\Delta T \, A} \qquad (4.7)$$

During the test, a cuboidal sample is placed on a temperature controlled cold-plate and thermally insulated chamber to ensure a unidirectional heat transfer. A known heat transfer rate has been applied by dissipating a known power in a power resistor.

Fig. 4.6a) presents a schematic of the experimental heat flow meter shown in [156], while Fig. 4.6b) features a photograph of the experimental set-up before surrounding the winding sample with thermal insulating material. Thermocouples (located where T_1 and T_2 are shown, Fig. 4.5) are embedded into the sample on each face to allow an average temperature measurement to be taken. Thermally-conductive paste is applied to both interfaces to improve the heat transfer. T_1 and T_2 are measured when the steady-state is reached (approximated here when less than 1°C temperature change over 10 min is recorded), and the conductivity is derived from,

$$k = \frac{(R_\Omega I^2)l}{(T_1 - T_2)A} = \frac{P_\Omega . l}{(T_1 - T_2)A} = \frac{(UI).l}{(T_1 - T_2)A} \qquad (4.8)$$

where I and U represents the dc current excitation and tension applied to the resistor R_Ω. l represents the length between T_1 and T_2, and A describes the cross-section area. The applied current and voltage are both measured when the steady-state is reached in order to account for the effect of temperature on the ohmic resistance value.

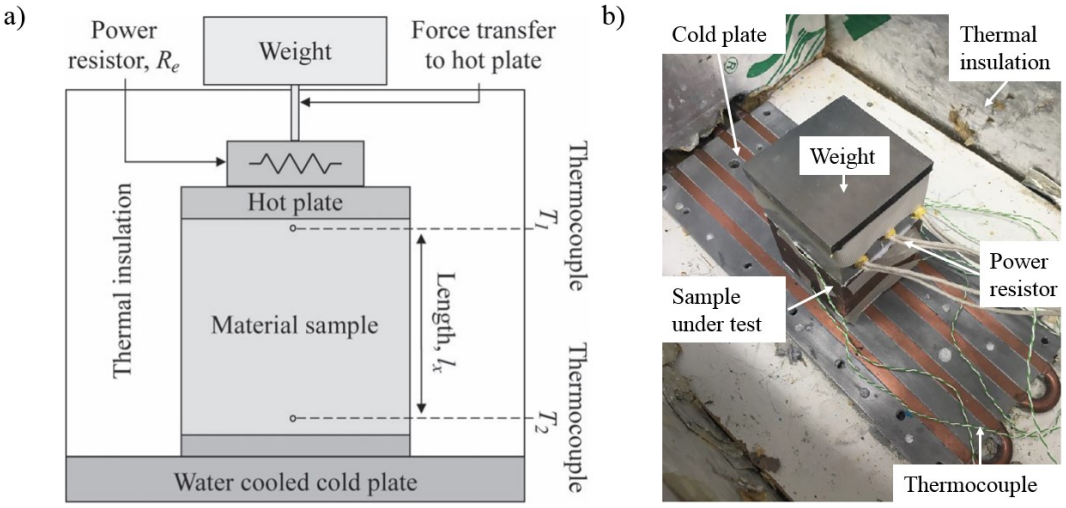

Fig. 4.6 a) Schematic of the experimental heat flow meter [156], b) Experimental set-up before surrounding the winding sample with thermal insulating material

4.4.2 Specific heat capacity

The specific heat capacity is typically derived using a calorimetric approach, such as heat flow or constant flux calorimeter [156]. A calorimetric method based on the energy balance

has been selected as the recommended technique. As for the selected heat flux approach, the required equipment shall be available in an electrical engineering laboratory.

The set-up involves the use of a known fluid residing in an insulated container that approximates adiabatic conditions to ensure that heat transfer only occurs between the tested MS and the fluid. Fig 4.7a) presents a schematic of the experimental heat flow meter [156], while Fig 4.7b) features a photograph of the experimental set-up before covering the fluid/winding sample container with thermal insulating material. The temperature of the fluid is measured until the steady state is reached.

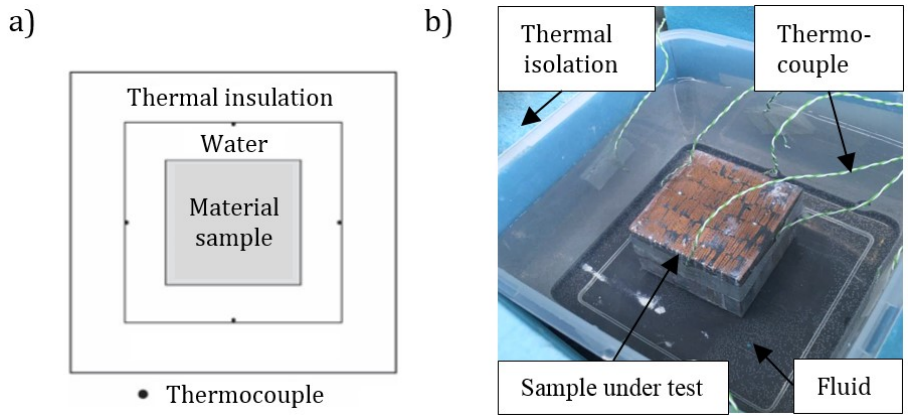

Fig. 4.7 a) Schematic of the experimental heat balance calorimeter [156], b) Experimental set-up before covering the fluid/winding sample container with thermal insulating material

The temperature changes of the sample and the fluid, along with the material properties and dimensions are employed to establish the specific heat capacity $c_{s,s}$ of the winding sample :

$$c_{s,s}=\frac{c_{s,f} m_f \Delta T_f}{m_s \Delta T_s} \qquad (4.9)$$

Where m and ΔT represent respectively the mass and temperature changes between times t_1 and t_2, and the subscripts s and f correspond to the solid and fluid, respectively.

4.4.3 Measured data

A necessary step when dealing with empirical data consists in evaluating the uncertainty u associated with the measured values. Mathematical proofs for the calculation of the uncertainty of the thermal conductivity and specific heat capacity measurements, $u(k)$ and $u(c_{s,s})$ are provided at Appendix B. The final expression obtained for the thermal conductivity uncertainty is presented below:

$$u(k) = \frac{k}{2}\sqrt{\left(\frac{u(l)}{l}\right)^2 + \left(\frac{u(A)}{A}\right)^2 + \left(\frac{u(U)}{U}\right)^2 + 2\left(\frac{u(T)}{(T_1 - T_2)}\right)^2} \quad (4.10)$$

where *u(l)*, *u(A), u(U) and u(T)* are the measurement uncertainties of the length, area, voltage and temperature, respectively.

The accuracy of the current is not considered, as a high-accuracy dc current source has been utilised for the tests with a measurement uncertainty of the current, *u(I)*, such that *u(I)* << 10^{-3} A. Table 4.5 presents the values of the uncertainties of the different parameters, together with the instrument and/or device used for measurement.

Table 4.5 Uncertainty of selected parameters with regards to measuring device accuracy

Uncertainty	Device used for measurement	Accuracy
u(l)	Electronic digital caliper	± 0.1 mm
u(A)	Electronic digital caliper	± 2.15 mm^2 (see Appendix B, B.9)
u(U)	Tenma 72-7725 digital multi meter	± 0.8% V
u(T)	Class 1 type-K thermocouples	± 1.5 °C

The uncertainty *u(k)* has been derived assuming a perfect thermal insulation of the cube under test. The heat flux meter is designed so that the heat flux goes from the heat source to the cold plate, ensuring a unidirectional heat transfer, and therefore most of the heat should cross the MS under test. However, there might still be a small degree of heat transferred to the thermal insulating material surrounding the winding sample. This is expected to be the case when the thermal conductivity of the insulating material is no longer negligible compared to the tested sample. A thermocouple has been placed inside the chamber to monitor the change in ambient temperature. Typically, less than 1 °C change has been observed when testing composite MSs, which suggests a good insulation of the sample. Completing the test in a vacuum chamber, where no convective heat transfer is possible, is a promising solution to ensure the absence of convective heat transfer from the sample under test.

The final expression obtained for the specific heat capacity uncertainty is presented below:

$$u\left(c_{s,sol}\right) = \frac{c_{s;s}}{2}\sqrt{\left(\frac{u(m_f)}{m_f}\right)^2 + 2\left(\frac{u(\Delta T_f)}{\Delta T_f}\right)^2 + \left(\frac{u(m_s)}{m_s}\right)^2 + 2\left(\frac{u(\Delta T_s)}{\Delta T_s}\right)^2} \quad (4.11)$$

Where $u(m_f)$, $u(\Delta T_f)$, $u(m_s)$ and $u(\Delta T_{sol})$ are the measurement uncertainties of the fluid mass, fluid temperature change, solid mass and solid temperature change, respectively. Table 4.6 presents the values of the uncertainties of the different parameters, together with the instrument and/or device used for measurement. The accuracy of mass of the fluid

measurement, m_f, has been set to 1 g instead of the 0.2 g accuracy to account for possible leftovers in the fluid container during fluid transportation to the calorimeter. The calorimeter is assumed to be perfectly insulated, with no heat transfer to the outer environment.

Table 4.6 Uncertainty of selected parameters with regards to measuring device accuracy

Uncertainty	Device used for measurement	Accuracy
$u(m_f)$	Jadever digital high precision scale	± 1 g (fluid transportation)
$u(\Delta T_f)$	Class 1 type-K thermocouples	$\pm \sqrt{2} \times 1.5$ °C
$u(m_{sol})$	Jadever digital high precision scale	± 0.2 g
$u(\Delta T_{sol})$	Class 1 type-K thermocouples	$\pm \sqrt{2} \times 1.5$ °C

Tests have been completed on an aluminium material cuboidal sample with known specific heat capacity, showing good correlation between known and measured results. However, if needed, it would be possible to place the calorimeter into a vacuum chamber, to ensure limited convective heat transfer to the outer environment.

Table 4.7 Measured set of thermal conductivities from tests on material samples (data presented between brackets have been calculated using (4.3) and (4.4))

Sample	$k_{w,x}$[W/(m.℃)]	$k_{w,y}$ [W/(m·℃)]	$k_{w,z}$ [W/(m.℃)]	$c_{s,w}$ [J/(kg.℃)]
WS-I	1.4±0.1	1.7±0.1	255±9	448±5
WS-II	2.0±0.1	2.2±0.1	331±12	385±4
WS-III	2.1±0.1	2.1±0.1	(232)	(427)
WS-IV	4.0±0.2	4.4±0.2	340±12	410±4
WS-V	1.9±0.1	2.0±0.1	235±6	904±7
WS-VI	2.0±0.1	2.3±0.1	121±4	(497)
WS-VII	2.4±0.1	3.0±0.1	(232)	(441)
WS-VIII	1.9±0.1	3.1±0.1	331±6	(385)
WS-IX	2.5±0.1	2.7±0.1	215±8	550±5
WS-X	2.0±0.1	2.5±0.1	166±6	(550)
WS-XI	2.4±0.1	2.3±0.1	151±5	1170±9
WS-XII	6.5±0.2	6.3±0.2	152±5	940±8
WS-XIII	1.2±0.1	1.6±0.1	167±6	(435)
WS-XIV	2.9±0.1	7.4±0.3	189±0.7	378±4
WS-XV	2.8±0.1	4.1±0.2	174±6	(378)
WS-XVI	2.2±0.1	5.1±0.2	253±9	(378)
MS-XVII	200±7	200±7	200±7	897±8
MS-XVIII	1.7±0.1	1.7±0.1	1.7±0.1	769±7
MS-XIX	-	-	-	1397±11
MS-XX	22.2±0.8	22.1±0.8	4.9±0.2	465±4

Table 4.7 includes a set of measured thermal conductivities and specific heat capacity for each of the selected MSs. As expected, the thermal conductivity in y-axis is larger than that in x-axis for WSs formed with rectangular profiled conductors or Litz wires. The use of aluminium conductor instead of copper has limited impact on the equivalent winding thermal conductivity, WSs II and V, and WSs IX and XI, but plays a significant role on the specific heat capacity. A significant improvement is shown for windings with 'high'

conductor fill factor as compared with counterparts with 'low' fill factor, e.g. WSs IV and VI. Furthermore, the use of epoxy resin impregnation has shown improved overall thermal properties of the impregnated WSs, e.g. WSs I and IV. This results from better material thermal properties and improved encapsulating properties for the epoxy impregnation as compared with the varnish impregnation, where fill of the air pockets and cavities between conductors is usually poorer. The limiting factors are the impregnation and electrical insulation materials. This is confirmed by the difference between WSs XI and XII; these samples only differ from their electrical insulation material, and the use of aluminium oxide instead of enamel results in a 170 % raise in the winding thermal conductivity. When comparing winding samples of similar fill factor and material, the conductor shape seems to be an additional limiting factor, WSs VII, IX and XIV, with slightly improved heat transfer in the case of rectangular profiled conductors. This will be studied in detail in the following sections of this Chapter.

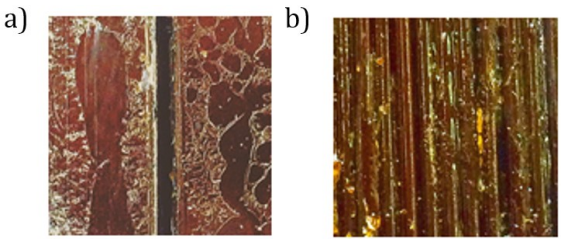

Fig. 4.8 Close-up on gaps between impregnated conductors for WS VI, a) x-axis, b) y-axis

Fig. 4.8 presents an example of close-up on gaps between the individual conductors for WS-II revealing different gaps in x- and y-axis, larger for y-axis than x-axis. This partially explains lesser than expected impact of the conductor aspect ratio on the degree of anisotropy observed from the measurements. Also, the measured data indicates impact of the conductor fill factor on the equivalent winding thermal conductivity.

4.5 Mathematical modelling techniques – round conductors

This section introduces the numerical and analytical methods used in the derivation of the equivalent thermal conductivity for windings constructed with round conductors. The numerical method, referred to as Method I, makes use of FE analysis. The first analytical method, referred to as Method II has been specifically developed for round conductors, but has shown limited applicability at high fill factor [156]. The second analytical method, which has been developed as part of this thesis, is referred to as Method III. This method makes use of the TEC lumped-parameter approach. For all methods, the calibration is completed by adjusting the thermal conductivity of the impregnation material k_i such that the measured and calculated equivalent winding thermal conductivity correlate well. The

thermal conductivities of conductor material and enamel remain constant. This approach has been adopted here as the impregnation quality has been shown extremely sensitive to manufacturing technique, e.g. variation of the impregnation goodness.

4.5.1 Numerical methods

Method I-round

Method I-round makes use of FEA to model a winding sample inside a heat flow meter. Fig. 4.9 presents 2D FE representation of an individual rectangular profiled conductor with all sub-regions highlighted. Previous work in the field indicates that the different conductor packing methods employed in FEA modelling, such as non-uniform or rhombus, only yield small changes in the thermal conductivity [156]. Here, the aligned conductor placement packing methods is adopted for the FEA model, Fig. 4.9. A fixed temperature boundary condition is used to represent the cold plate, while a fixed heat flux boundary condition is used to embody the known heat flow from the power resistor. The remaining sample surfaces are defined with adiabatic boundary condition emulating the adopted testing procedure. The model representation used in the FE analysis may be reduced to one individual conductor including the electrical insulation and impregnation regions. Initial analyses with complete WS and reduced-order one-conductor models have shown less than 1% discrepancy between the results, due to the structure periodicity, for all conductor types.

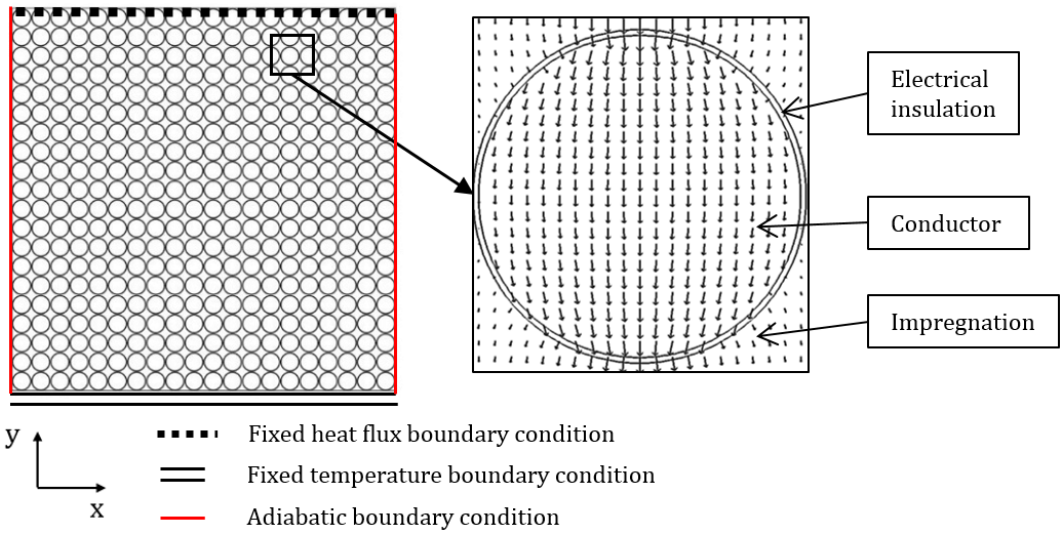

Fig. 4.9 2D thermal FEA model representation of a winding sample together with boundary conditions; a close-up view of an individual conductor with electrical insulation and impregnation is also shown with heat flux direction.

4.5.2 Analytical methods

Method II-round

Method II-round has been described in section 4.3.1 and is based on (4.1) and (4.2). The method does not allow the accurate estimation of the equivalent thermal conductivity of winding formed with round conductors with a high conductor packing factor (≥40%) [156], but is nonetheless used in this Chapter to highlight the merits of the proposed alternative analytical approach.

Method III-round

Method III-round makes use of the TEC theory to derive the equivalent thermal conductivity of a winding formed with round conductors. Fig. 4.10a) represents the physical representation of half of a conductor/electrical insulation/impregnation amalgam. The derivation of the equivalent thermal resistance for the impregnation region represented in Fig. 4.10a) is not trivial, due to the difficulty of setting-up adequate boundary conditions for this non-basic geometry. Method III-round proposes to find the equivalent thermal resistance of an equivalent half hollow cylinder with identical cross-section area A_i, Fig. 4.10b). Fig. 4.10c) presents the TEC associated with the cylindrical single conductor representation, together with the nomenclature used. Here, R_c, R_{ci}, R_i and R_e correspond to the thermal resistance of the conductor, electrical insulation, impregnation and equivalent homogenised materials, respectively. From Figs. 4.10a) and 4.10b), A_i can be expressed as follows:

$$A_i = \frac{\pi r_i^2}{2} \qquad (4.12)$$

where r_i is the radius of the impregnation hollow cylinder in the cylindrical winding model representa tion.

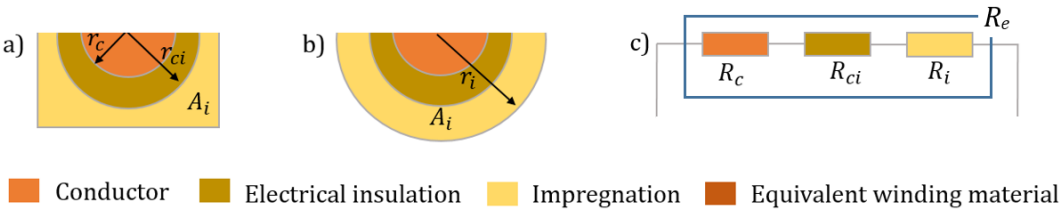

Fig. 4.10 Schematic model representation of the halve conductor/electric insulation/impregnation amalgam, a) physical representation, b) physical surrogate representation, c) lumped-parameter TEC and nomenclature used

The fill factor *FF* is defined as:

$$FF = \frac{\pi r_c^2}{2A_i} \qquad (4.13)$$

Where:

$$r_{ci} = r_c + t_{ci} \quad (4.14)$$

and r_c conductor radius and t_{ci} electrical insulation thickness. Hence, r_i can be expressed using the following expression:

$$r_i = \frac{r_c}{\sqrt{FF}} \quad (4.15)$$

The TEC model and associated choices in equivalent thermal resistance are based on observations from the heat flux behaviour on FEA models. According to observations made from Fig. 4.9, the heat fluxes across the electrical insulation and impregnation have a radial direction, while the heat flux across the conductor flows along y-axis. R_{ci} and R_i, are defined as radial thermal resistance.[2] Details of the mathematical derivation of k_w are provided in Appendix C, including derivation of R_c, R_{ci}, R_i and R_e. A closed-form equation is provided as follows:

$$k_w = \frac{1}{\frac{\ln\frac{r_c}{(r_c+t_{ci})\sqrt{FF}}}{k_i} + \frac{\ln\frac{r_c+t_{ci}}{r_c}}{k_{ci}} + \frac{1}{k_c}} \quad (4.16)$$

The assumptions made for the derivation of k_w, such as the radial heat transfer across the electrical insulation material, is only valid because $k_c >> k_{ci}$. This is generally the case for winding amalgam. However, if less-common materials were to be used, the formula might appear less-accurate.

4.5.3 Efficacy of the proposed method

In order to demonstrate applicability and limitations of the existing and proposed methods, k_w has been estimated for a number of winding topologies. Method I-round is used in this section as a reference when assessing the accuracy of the equivalent thermal conductivity estimation from Methods II-round and III-round. Fig. 4.11 presents variation of the equivalent thermal conductivity versus conductor fill factor *FF* assuming fixed cross-section of an individual conductor. Each plot corresponds to a specific value of the impregnation thermal conductivity k_i from 0.5 W/(m.°C) to 1.1 W/(m.°C). From Fig. 4.11, Method III-round shows a very good agreement with Method I-round while the limited applicability of Method II-round at high conductor *FF* is confirmed, in particular when k_i is relatively high. Method II-round has been originally developed for two-material composites [224]. An explanation for the discrepancy between Methods I-round and II-round is that if k_i is too different from k_{ci}, the initial assumption made in [224] might no longer be valid.

Fig. 4.12 presents variation of the equivalent thermal conductivity versus conductor radius assuming fixed fill factor of the winding assembly. On one hand, from Fig. 4.12, Method III-round shows again very good correlation with results from Method I-round. On one hand Method III-round shows again very good correlation with results from Method I-round. On the other hand, the applicability of Method II-round for conductor appears limited when the electrical insulation thickness t_{ci} is large compared to the conductor radius r_c. Again, when t_{ci}>>r_c, the configuration for which the initial two-material formula has been derived is less consistently represented.

Recent methods make use of pre-pressed winding or pre-compressed coils in order to increase the conductor fill factor [145], [191], [225], [226]. References in the literature indicate that the high-compression pressures tend to deform the conductors, typically from circular towards hexagonal-like shapes [191], [225], [226]. Further work is required to investigate the applicability of the proposed method to compressed coils. This is however beyond of the scope of this thesis and will be discussed later in the context of future work.

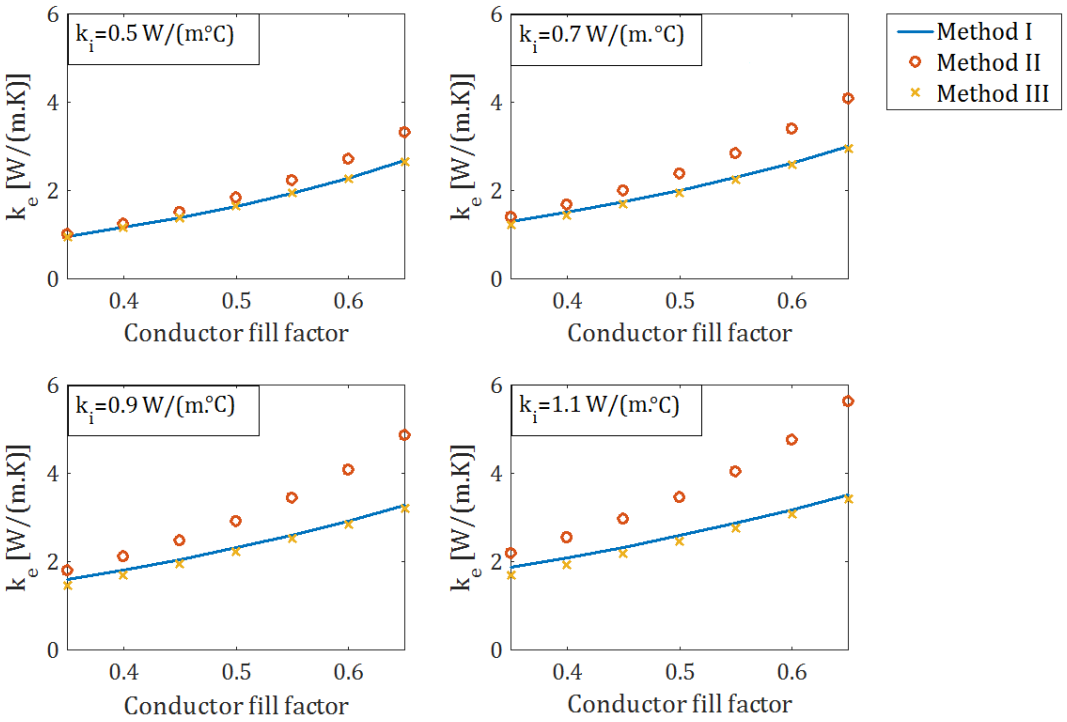

Fig. 4.11 Calculated thermal conductivity vs. conductor fill factor, a) k_i=0.5 W/(m.°C), b) k_i=0.7°C W/(m.°C), c), k_i=0.9 W/(m.°C), d) k_i=1.1 W/(m.°C)

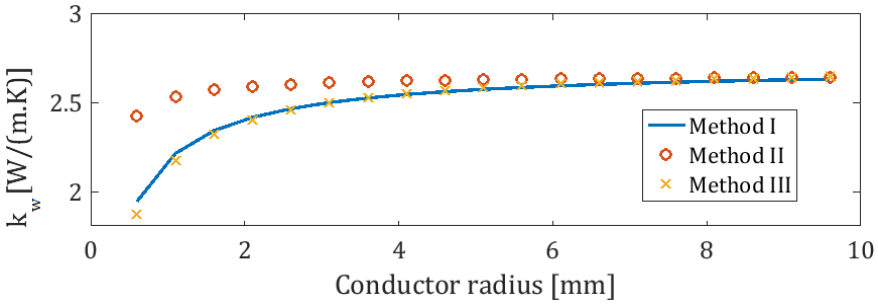

Fig. 4.12 Thermal conductivity vs. conductor radius

4.6 Mathematical modelling techniques – rectangular conductors

This section introduces the numerical and analytical methods used in derivation of the equivalent thermal conductivity across conductors k_w for impregnated windings constructed with profiled rectangular conductors. The numerical method, referred to as Method I-rectangular, makes use of FEA and is used as a reference when assessing the accuracy of the equivalent thermal conductivity estimation from the existing and proposed analytical methods. The first analytical method, referred to as Method II-rectangular, adapts Method II-round to account for the winding anisotropy. The second analytical method, referred to as Method III-rectangular, makes use of the TEC lumped-parameter approach to estimate the equivalent thermal conductivity of winding formed with rectangular conductors. For all methods, the calibration is completed by adjusting k_i such that measured and calculated k_w values correlate well, while k_c and k_{ci} remain constant. Due to the different conductors spacing in x- and y- axis, separate calibration is completed for the thermal conductivity of the impregnation material in x- and y-axis $k_{i,x}$ and $k_{i,y}$.

4.6.1 Numerical method

Method I-rectangular

Method I-rectangular makes use of FEA to model a winding sample inside a heat flow meter, with a model representation reduced to one individual conductor including the enamel and impregnation regions. The software Finite Element Method Magnetics (FEMM) has been employed for this investigation [166]. Fig. 4.13 presents 2D representation of an individual rectangular profiled conductor with all sub-regions highlighted. Unlike Method I-round, here the hot plate is represented in the model. This approach might be used as an alternative when setting up a fixed heat flux boundary condition in the FE model is difficult.

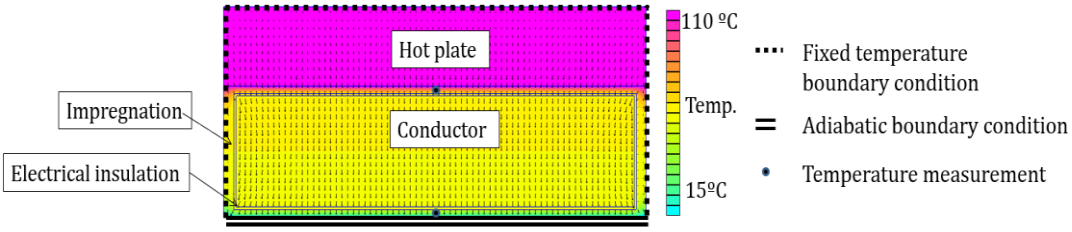

Fig. 4.13 2D thermal FEA model representation of an individual rectangular profiled conductor with electrical insulation and impregnation, together with boundary conditions

The hot plate is subjected to a volumetric heat generation, $\dot{Q}_{v,hp}$, such that,

$$\dot{Q}_{v,hp} = \frac{\dot{Q}}{V_{hp}} \qquad (4.17)$$

where V_{hp} is the hot plate volume. Equation (4.7) is then used to calculate the thermal conductivity.

4.6.2 Analytical methods

Method II-rectangular

Method II-rectangular alters (4.1) to account for the rectangular-profiled conductor anisotropy, by using individual *FFs* for each of the winding x- and y-axes,

$$FF_x = \frac{x_c}{l_{ex}} \qquad (4.18)$$

$$FF_y = \frac{y_c}{l_{ey}} \qquad (4.19)$$

where:

$$x_e = x_i + x_{ci} + x_c \qquad (4.20)$$

$$y_e = y_i + y_{ci} + y_c \qquad (4.21)$$

where x and y represents length in x- and y-axes, respectively. The conductor electrical insulation thickness is assumed here to be identical for x- and y-axis of the WS, $x_{ci} = y_{ci}$. The individual factors substitute FF in (4.1) when equivalent winding thermal conductivities k_x and k_y are estimated. The method does not necessarily require empirical data regarding impregnation gap thicknesses x_i and y_i. Indeed, it has been observed from the measurements that for the analysed WSs (WS-II and WS-IV to WS-VIII), in average,

$$x_i = 0.48\, y_i \qquad (4.22)$$

This difference in gap thickness agrees with the observation made in Fig. 4.8, and can be partly explained by the fact that it is easier to stack conductors together along their width

(x-axis) than along their heights (y-axis). Equation (4.22) can be used to estimate x_i and y_i when only the fill factor is known, further simplifying the proposed analytical method. The fill factor *FF* can be expressed as follows:

$$FF = \frac{x_c y_c}{x_e y_e} = \frac{x_c y_c}{(x_c + x_{ci} + x_i)(y_c + y_{ci} + y_i)} \qquad (4.23)$$

By replacing x_i by $0.48y_i$ in (4.23), a quadratic expression is obtained allowing for the derivation of y_i. Then x_i can be derived from (4.22), and both x_i and y_i can be used to derive FF_x and FF_y, following the proposed approach. The averaged ratio given by (4.22) has been derived from tests on a set of six WSs, and a larger number of samples would be required to obtain more general information.

Method III-rectangular

Method III-rectangular makes use of the TEC theory to emulate the experimental method with heat flux meter and derive the equivalent thermal conductivity. Fig. 4.14 presents a schematic representation of the winding sample together with the reduced-order TEC lumped-parameter network representation and the nomenclature used. The model representation used in the analysis has been reduced to one quarter of an individual conductor, including the enamel and impregnation regions. The initial investigation using the proposed approach and FEA with complete and reduced-order one-fourth models for the WSs has shown good correlation between the theoretical findings. Each of the winding material regions are represented by four thermal resistances aligned with x- and y- winding axes in the TEC lumped-parameter model. The common, central node for all the sets of resistors provides averaged temperature within the individual material regions. Such model definition stems from the fact of zero internal heat/power loss generation within the winding sample, i.e. heat is transferred across the winding sample only. The thermal conductivity for a particular winding axis is derived from (4.7) by setting the fixed heat source and temperature boundary conditions across the axis. The remaining peripheries of the model are assumed to be adiabatically insulated. The resulting TEC model has been solved using an electric circuit simulator (Simulink [167]), and the nodal voltages (temperatures) have been post-processed to estimate the thermal conductivity.

However, such an electric circuit-solver might not be readily available, and might be ineffective, e.g. estimation of the equivalent thermal conductivity embedded in an optimisation routine.

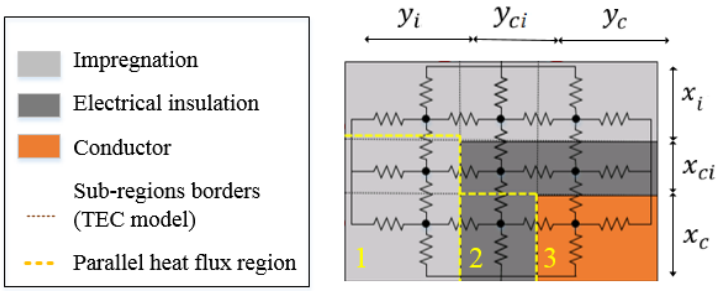

Fig. 4.14 Schematic representation of the one-fourth WS together with reduced-order equivalent-circuit lumped-parameter network representation and the nomenclature used

Here, a set of formulae leading to the derivation of equivalent thermal conductivity are provided to make the TEC method more accessible and practical. Details of the mathematical derivation of $k_{w,x}$ are provided in Appendix C. A closed-form equation is provided as follows:

$$k_{w,x} = \frac{x_e}{y_e}\left(\frac{k_{i,x}\, y_i}{x_{ci}+x_c} + \frac{k_{ci}\, y_{ci}}{x_c} + \frac{k_c\, k_{ci} k_{i,x} y_c (y_{ci}+y_c)\, y_e}{k_c k_{ci} x_i y_c (y_{ci}+y_c) + k_{ci} k_{i,x} x_c (y_{ci}+y_c) + k_c\, k_{i,x} x_{ci} y_c y_e}\right) \tag{4.24}$$

The equivalent thermal conductivity along y-axis, $k_{w,y}$, can be derived by replacing the subscript *x* with *y* and vice-versa in the previous set of formulas.

4.6.3 Efficacy of the proposed methods

To demonstrate applicability and limitations of the existing and proposed methods, the equivalent thermal conductivity for several winding topologies has been derived theoretically, numerically and experimentally. All the methods have been individually calibrated beforehand with experimental data from tests on the WSs. As previously, this has been done by tuning the thermal conductivity of the impregnation material. Method I-rectangular is used here as a reference when assessing the accuracy of k_w estimations from Methods II-rectangular and III-rectangular. Fig. 4.15a) presents variation of the equivalent thermal conductivity in x- and y-axis versus conductor aspect ratio, assuming fixed conductor cross-section and conductor *FF*. The different approaches are individually calibrated using empirical data from WS II-rectangular. The results from Methods II-rectangular and III-rectangular show an increase of $k_{w,y}$ and decrease of $k_{w,x}$ for the conductor profiles with 'high' aspect ratio. Methods II-rectangular and III-rectangular show similar trends with some discrepancies towards 'small' conductor aspect ratios. Here, maximum deviation of 8% has been observed for both methods.

This different spacing between conductors in x and y axes shifts the $k_{w,x} = k_{w,y}$ point towards higher conductor aspect ratios, here equal to approximately 5. The results comparison shown in Fig. 4.15a) assumes constant x- and y-axis fill factors respectively, which were informed from tests on the WSs formed with rectangular conductors. Fig. 4.15b) compares variation of k_w with conductor *FF*. The different approaches are individually calibrated using empirical data from WS VII. From Fig. 4.18b), it is evident that Method II-rectangular leads to less accurate equivalent thermal conductivity predictions, in particular at high conductor fill factor. The limitation for this method stems from simplified character of the approach. Unlike Method III-rectangular, which accounts for the conductors' shape and placement within the winding assembly, Method II-rectangular is based on volumetric assumptions only.

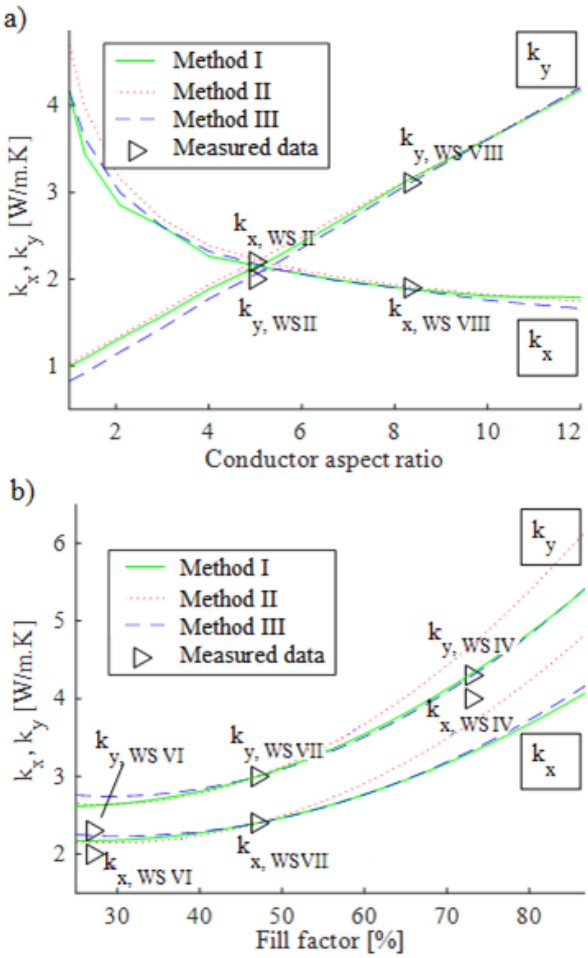

Fig. 4.15 Thermal conductivity of impregnated WSs with copper conductors, a) $k_{w,x}$ and $k_{w,y}$ vs. conductor aspect ratio, fixed *FF*=77%, b) $k_{w,x}$ and $k_{w,y}$ vs. conductor fill factor, fixed conductor aspect ratio equal to 2 [232]

From Fig. 4.15b), it is clear that the conductor shape and placement needs to be accounted for when deriving k_w. The theoretical findings and measured results confirm Method III-

rectangular to be the most reliable approach for estimating the equivalent thermal data among the analysed analytical methods.

The validity of the calibrated thermal conductivity of impregnation for alternative winding configurations is discussed in section 4.8 using the measured WS data presented in Fig. 4.15.

4.7 Mathematical modelling techniques – Litz wires

The proposed analytical method makes use of the TEC lumped-parameter approach for estimating k_w for windings formed with Litz wires. The method is based on a two-step homogenisation process, which is shown schematically at Fig. 4.16. The first homogenisation consists in deriving the equivalent thermal conductivity of a single bundle of Litz wire. This thermal data is then used in the second homogenisation, which derived the equivalent winding thermal conductivity of the winding.

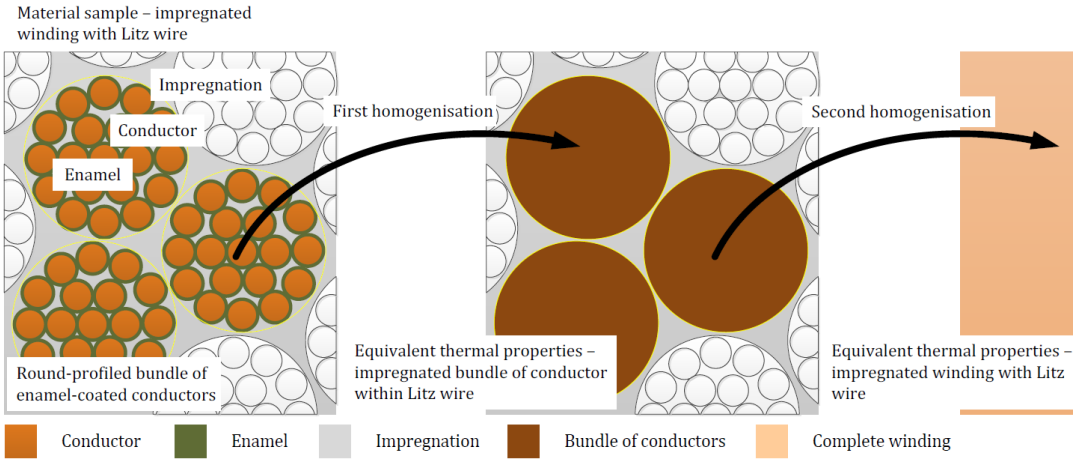

Fig. 4.16 Schematic representation of the equivalent thermal properties estimation process - a more conventional Litz wire construction with round-profiled conductors and bundle of conductors is illustrated [223].

The procedure illustrated at Fig 4.16 derives winding equivalent thermal conductivity based on assumptions that the conductors and/or bundles of conductors have circular profiles. Method III-round may be used for both homogenisation steps, and the equivalent thermal conductivity for such winding construction can be assumed to be isotropic [156]. For rectangular and compacted Litz wire, such as the type-8 Litz wires composing WS-I, this assumption is no longer valid. Consequently, a method, which accounts for a non-circular bundle or conductor profile, is required. The proposed method assumes that the individual conductors and bundles of conductors of type-8 Litz wires have an ideal square and rectangular profile, respectively. This assumption is based on the Litz wires'

manufacturing process, which results in the round conductors being compacted to form a semi-square profile. As previously, a set of formulae leading to the derivation of equivalent thermal conductivity are provided. Details of the mathematical derivation of $k_{w,x}$ are provided in Appendix C. A closed-form equation is provided as follows,

$$k_{w,x} = \frac{x_b + x_{bs}}{y_b + y_{bs}} \left(\frac{y_b k_{e,x} k_i (y_b + y_{bs})}{x_b k_i (y_b + y_{bs}) + y_b k_{e,x} x_{bs}} + \frac{k_i y_{bs}}{x_b} \right) \quad (4.25)$$

where $k_{e,x}$ represents the equivalent thermal conductivity of the Litz wire bundle, x_b and y_b are the Litz wire bundle length in the x- and y- axes, and x_{bs} and y_{bs} are the Litz wire bundle spacing in the x- and y- axes, respectively. Fig. 4.17 illustrates a sample of type-8 Litz wire, which confirms quasi-square conductor profiles. The square conductor dimension is defined by an equivalent round conductor radius, assuming the same conductor cross section area for both physical and represented conductor profiles.

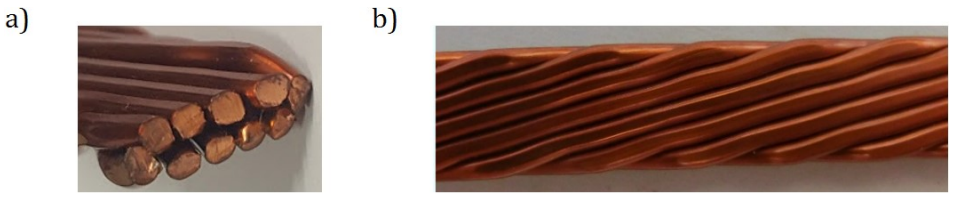

Fig. 4.17 A sample of type-8 Litz wire revealing a square-like conductor profile, a) Cross-section, b) Length

4.8 Validity of material sample empirical data

Building many material samples might not be feasible due to the cost and time constraints. Therefore, an important element of the proposed procedure is hardware calibration with a reduced number of required WSs. This section investigates the situations in which the data are transferrable from one WS to another.

4.8.1 Calibrated thermal conductivity of impregnation

The validity of the calibrated thermal conductivity of impregnation for alternative winding configurations is investigated here for the round and rectangular profiled conductors.

Round conductors

Firstly, the validity of calibrated k_i has been investigated in the context of a winding formed with round profiled conductors. The impregnation thermal conductivity obtained from WS-IX, k_i=0.92 W/(m.°C), has been used to predict k_w from WSs X, XI and XII using Method III-round. Table 4.8 presents the values used for calculation, together with the WSs estimated and measured thermal conductivity values. The difference between WS-

IX and the other WSs is emphasised in bold letters. The measured and calculated values show similar trends with a maximum deviation of 5% observed.

Table 4.8 Calculated and measured data for WSs IX to XII. The difference between WS-IX and the other WSs is emphasised in bold letters.

Winding sample	WS-IX	WS-X	WS-XI	WS-XII
r_c [mm]	1.6	**0.6**	1.6	1.6
FF	0.6	0.6	0.55	0.66
k_c [W/(m.°C)]	385	385	**234**	**234**
k_{ci} [W/(m.°C)]	0.25	0.25	0.25	**2**
$k_{w,measured}$ [W/(m.°C)]	2.6	2.25	2.35	6.4
$k_{w,calculated-\ Method\ III}$ [W/(m.°C)]	2.6	2.2	2.3	6.2

Rectangular profiled conductors

Secondly, the validity of the calibrated k_i has been investigated in the context of a winding formed with rectangular profiled conductors. In Fig. 4.15a), theoretical predictions from all models, which have been calibrated using WS II, are showing close correlation with measured data for WS VIII. Both WSs II and VIII are constructed using the same conductor and varnish materials and have approximately the same conductor fill factor. The only difference between the samples lies in the conductor aspect ratio and conductor cross-section area. This suggests that winding samples with similar constructions can be used to calibrate models with different conductor aspect ratios and conductor cross-section. Fig. 4.15b) illustrates the effect of model calibration with experimental data from tests on similar winding samples with different conductor fill factors, WSs IV (FF=73%), VI (FF=47%) and VII (FF=27%). The models have been calibrated from WS VII to predict the equivalent thermal conductivity for WSs IV and VI and vice versa, showing moderate agreement in thermal conductivity estimation. The thermal conductivity is over predicted for winding fill factor of 27%, and under predicted for winding fill factor of 73%. This outcome was predictable: for a low winding fill factor, i.e. larger spacing between conductors, air cavities are more prone to be formed, hence leading to a lower impregnation thermal conductivity than for a similar winding construction with higher fill factor, i.e. smaller spacing between conductors. For this reason, it is recommended to build a new winding sample when evaluating the equivalent thermal conductivity of various configurations with different winding fill factor.

4.8.2 Variation of equivalent winding thermal conductivity

The objective of this section is to establish, in which cases k_w is directly transferable, i.e. the measured data from a single hardware exemplar can be used to inform alternative winding configurations with no additional theoretical calculations or experimental work.

This differs from the approach adopted in sub-section 4.7.1, where the impregnation thermal conductivities k_i were derived using a WS, then these calibrated values were used to compute k_w for other WSs. Fig. 4.18 shows equivalent winding thermal conductivity predictions for various theoretical winding examples with the same materials and fill factor, but different conductor-cross sections and conductor aspect ratios. The conductors' shape is assumed here to be rectangular. Method III-rectangular is used for the equivalent winding thermal conductivity predictions, and has been calibrated using empirical data from WS VI, see measured points indicated in Figs. 4.18a) and 4.18b). Segments of winding configurations with equal equivalent thermal conductivity, referred to as isoconductivity lines, can be derived from Fig. 4.18, and used to evaluate the immediate transferability of the equivalent winding thermal conductivity. The theoretical findings suggest that the result transferability is limited and differs for $k_{w,x}$ and $k_{w,y}$ On the one hand, the results for thermal conductivity in y-axis can be used to calibrate windings with different conductor cross-sections only if the conductor aspect ratio is conserved, Fig. 4.18b). On the other hand, the transferability of thermal conductivity estimates in x-axis is more complicated, and requires derivation of the isoconductivity line, Fig. 4.18a). This confirms that the winding equivalent thermal conductivity depends on various parameters, including conductor aspect ratio and cross-section, which need to be carefully evaluated.

Figs. 4.19a) and 4.19b) show variation of the equivalent thermal conductivities $k_{w,x}$ and $k_{w,y}$, respectively, versus impregnation gap thicknesses x_i and y_i, assuming fixed cross-section and aspect ratio of an individual conductor. As previously, Method III-rectangular has been used to evaluate the equivalent winding thermal conductivity values and the conductors shape is assumed to be rectangular. The theoretical winding examples comprise same material and conductor cross-section as for WSs VIII, see measured points indicated in Figs. 4.19a) and 4.19b).

When deriving the isoconductivity lines for Fig. 4.19a) and Fig. 4.19b), it is clear the impregnation gap aligned with the heat flux, e.g. x_i for $k_{w,x}$, has an important impact on the equivalent thermal conductivity value, while the impregnation gap orthogonal to the heat flux, e.g. y_i for $k_{w,x}$, has insignificant impact on the thermal conductivity. According to the findings presented at sub-section 4.7.1, the transferability of the equivalent winding thermal conductivity data is effective only for winding configuration with comparable fill factors. When the conductor fill factors are significantly different, tests on a representative hardware sample are required for calibration.

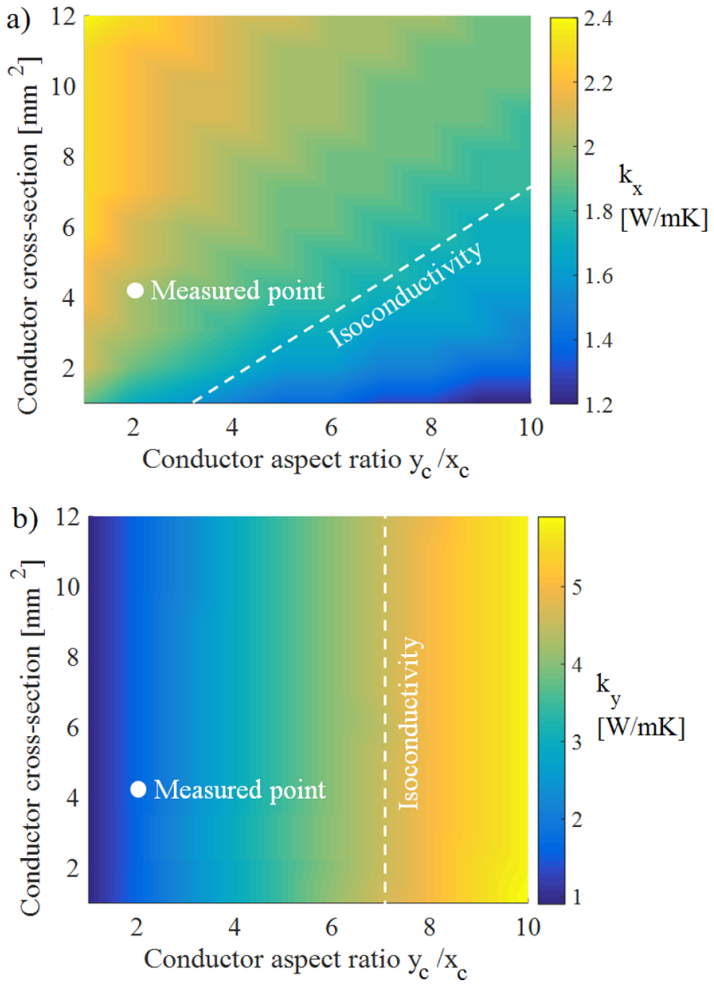

Fig. 4.18 Distribution of thermal conductivity vs. conductor aspect ratio and conductor cross-section for epoxy potted winding sample with rectangular copper conductors and *FF* = 27% – WS VI, a) thermal conductivity $k_{w,x}$, b) thermal conductivity $k_{w,y}$ [232]

4.9 Illustration

To highlight the effect of using a specific homogenisation method on the winding temperature predictions, four alternative 2D FE thermal models of a motorette have been built. Here, windings formed with rectangular profiled conductors are investigated. Each model is associated with one of the approaches of deriving a winding's equivalent thermal conductivity discussed in this Chapter, (Methods I-rectangular, II-round, II-rectangular and III-rectangular, respectively). As in the previous sections of this Chapter, Method I-rectangular is considered as a reference here. Method II-round is investigated here only to highlight the need to account for the thermal anisotropy of this type of winding configuration. Basic data for the theoretical winding assumed in this investigation are listed in Table 4.9. Fig. 4.20 presents the FE thermal model of a stator-winding assembly with the boundary conditions and model sub-regions highlighted. The software Finite Element Method Magnetics (FEMM) has been employed for this investigation [166].

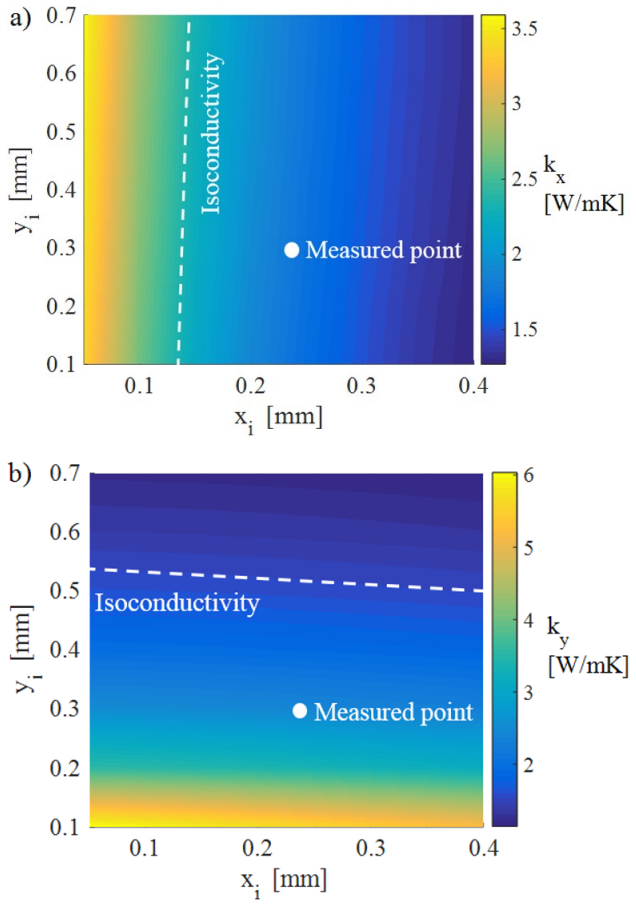

Fig. 4.19 Theoretically predicted distribution of thermal conductivity vs. impregnation gap for varnish impregnated winding sample with copper conductors – WS VIII, a) thermal conductivity $k_{w,x}$, b) thermal conductivity $k_{w,y}$ [232]

In the FE analysis, a fixed temperature boundary condition (25ºC) is used at the back iron, emulating machine heat extraction via liquid-cooled housing. The remaining external boundaries are assumed to be adiabatic, with no heat transfer across the air gap.

Table 4.9: Basic winding data

Conductor fill factor	77 %
Impregnating material	Varnish
Conductor dimension	(1.0×10.0=10.0) mm^2
Impregnation gaps x_i/y_i	0.225 mm / 0.45 mm

Table 4.10 Thermal conductivity data used in FE models

Model region	$k_{x,y}$ [W/(m.°C)]	Method	$k_{w,x}$ [W/(m.°C)]	$k_{w,y}$ [W/(m.°C)]
Copper conductor	330	I-rectangular	1.1	2.6
Impregnation	0.4	II -round	2.7	2.7
Electrical insulation	0.25	II-rectangular	1.8	3.7
Slot liner region	0.13	III-rectangular	1.1	2.4
Laminated core	20			
Wedge	0.3			

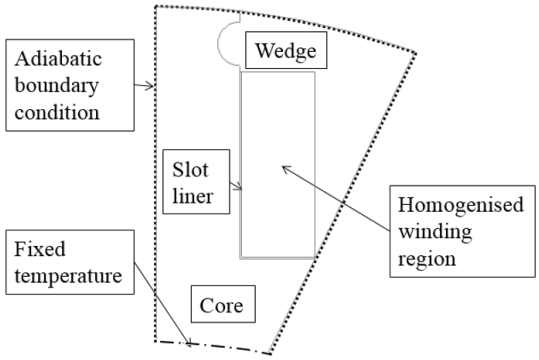

Fig. 4.20 2D FE thermal model representation of the stator winding assembly together with boundary conditions and model sub-regions indicated

The material thermal data, including the slot liner, wedge and core, have been extracted from the manufacturer datasheets and available literature [11], [12], [35], and is listed in Table 4.10. The analysed case study is purely theoretical, and the same basic material data is used to define all the FE models. Here, the only difference is the method used for the equivalent thermal conductivity estimation. As previously observed, Methods II-round and II-rectangular do not allow for reliable predictions of the thermal conductivity of winding with 'high' conductor fill factor, and therefore the estimations obtained from these methods differ from the ones obtained from Methods I-rectangular and III-rectangular. Fig. 4.21 shows the temperature distribution and hot spot prediction within the stator/winding section when the winding is excited with a dc current excitation of I=100 A. On one hand, the use of thermal data obtained from Methods II-round and II-rectangular leads to a large underestimation of the winding hotspot temperature, Figs. 4.21b) and 4.21c). On the other hand, the winding temperature distribution and hot spot temperature predictions correlate well for Methods I-rectangular and III-rectangular, Figs. 4.21a) and 4.21d), which is in line with the conclusions presented in previous sections of this Chapter. The winding hot spot temperature is frequently used in a multi-variant design and thermal analysis of electrical machines, where short setting-up and solving time are desirable. In this context, Method III-rectangular provides an accurate and computationally-efficient alternative to Model I-rectangular for the derivation of the equivalent winding thermal conductivity.

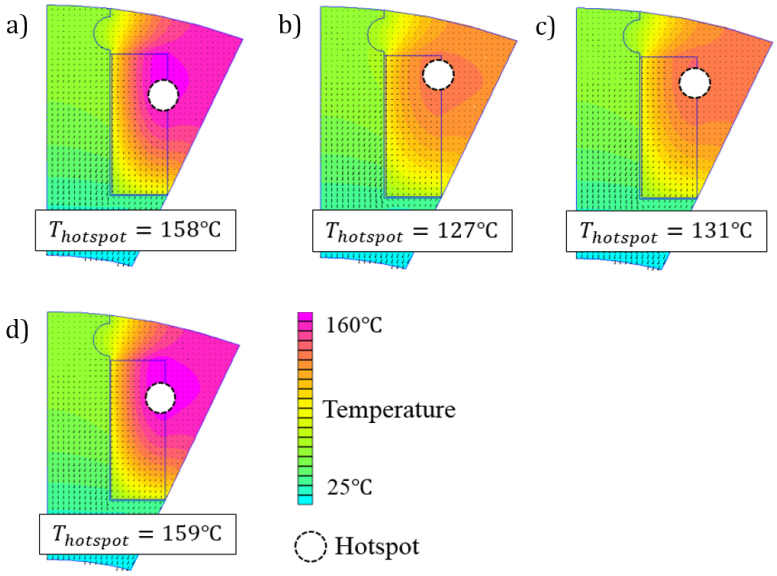

Fig. 4.21 An example of temperature distribution and hot spot location within the stator-winding assembly, a) Method I-rectangular, b) Method II-round, c) Method II-rectangular, d) Method III-rectangular

4.10 Summary

This Chapter has presented the first building step of the proposed methodology, which utilises tests on composite material samples to evaluate the thermal parameters of the core pack and winding region. A large number of samples have been investigated, establishing a library of thermal conductivity and specific heat capacity data for thermal designers. The measurement uncertainty has been discussed and accounted for. As highlighted in Chapter 2, the winding equivalent thermal conductivity is usually a highly sensitive parameter in thermal design of electrical machines. A repeatable procedure has been presented using both the analytical and experimental approaches for deriving the equivalent thermal conductivity for impregnated windings formed with round and rectangular conductors, and Litz wires, Fig. 4.22. The theoretical background and practical use of the proposed process have been discussed in detail and demonstrated on several hardware exemplars. Several theoretical approaches have been presented and compared, highlighting the merits of the TEC conductor/electrical insulation/impregnation representation for deriving the winding equivalent thermal conductivity, referred to as Method III in this Chapter.

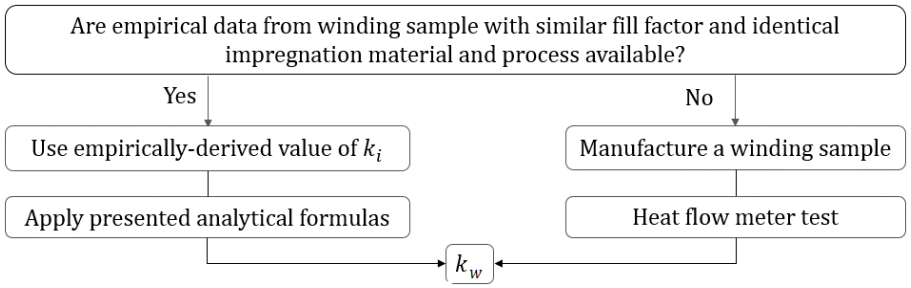

Fig. 4.22 Proposed equivalent thermal property estimation procedure

The approach accounts for the conductors' shape and placement within the winding assembly, which leads to more accurate predictions of the equivalent thermal conductivity when compared to existing techniques based on volumetric components. Three sets of formulae, associated with each studied conductor type and derived from TEC models, have been provided in order to improve the practical use and/or implementation of the proposed methods. Efficacy of the proposed approaches has also been demonstrated on several winding examples showing good correlation with the reference data. Finally, the effect of employing a specific homogenisation approach for estimating the winding equivalent thermal conductivity, on the stator-winding temperature predictions has been illustrated. A selected case study has showcased the importance of appropriate input thermal material data in the context of the proposed approach. The proposed procedure provides a building block for a more systematic approach in high-fidelity, computationally and resource effective thermal analysis. Depending on the availability of hardware exemplars, a motorette, a stator or full machine assembly analysis is an alternative to material samples, when estimating thermal parameters associated with heat transfer from the winding body to stator core pack. Here, the use of appropriate winding model representation, e.g. equivalent material or layered model is required in conjunction with experimental data. Such an approach is usually employed in thermal analysis using coarse and/or reduced order model definition. Testing on a motorette is well suited when deriving the contact thermal resistance between the winding and stator sub-assemblies. However, this approach is less suitable for derivation of in-situ equivalent thermal properties for the winding region when instrumented in a conventional manner, i.e. a limited number of temperature sensors are used across the tested machine sub-assembly. This aspect of thermal model definition is discussed in detail in the next Chapter, Motorette assembly

Chapter 5 Motorette assembly

5.1 Introduction

The second building block of the proposed methodology utilises tests on motorette exemplars (MEs) to evaluate various thermal parameters associated with the stator-winding regions, including winding-to-stator thermal contact resistances. These parameters are challenging to derive theoretically due to their strong dependence on manufacturing techniques [53]-[61]. By allowing machine designers to evaluate these parameters before building a complete machine prototype, motorette testing provides crucial information about the full machine heat extraction at an early stage of its design.

MEs are also used to inform power loss analysis to provide an insight into complex power loss mechanisms, such as ac winding loss effects. It should be noted that some effects present in the complete machine, e.g. rotor induced losses, are not present when testing the MEs analysed in this thesis. The absence of some of the loss components present in the full machine nonetheless allows for a simpler loss separation. A procedure is presented to simplify the comparison between stator-winding configurations and the estimation of power loss parameters.

The thermal and power loss theoretical analyses are supplemented with experimentally derived data from a number of MEs, showcasing the importance of empirically derived data for accurate predictions of a machine performance. In particular, the influence of the temperature sensor location and the thermal data resolution on the thermal parameter estimation is discussed.

5.2 Hardware exemplars

Motorette testing allows for in-situ analysis of the stator-winding thermal behaviour. In this context, the motorette assembly must include all components that could influence the thermal behaviour, e.g. slot liner and impregnation material, among others. The interaction between materials from the stator-winding region is of particular interest, e.g. slot liner capability for absorbing impregnation material and its influence on the winding-to-stator heat extraction capability.

The applicability of motorette testing depends on the winding topology of the investigated machine. Concentrated winding topology is undoubtedly well-suited for motorette testing,

as a coil wound around a tooth represents an equivalent portion of the complete stator-winding assembly [57]. A similar representation of the distributed windings would be more challenging, as the windings are spread over several slots. In such a case, the winding configuration of the ME must be adapted to represent as precisely as possible the dimensions and positions of the conductors in the complete stator assembly. In particular, distributed windings have significantly longer end-windings compared to concentrated topologies. In [170], the end-winding lengths have been calculated to be equal to the ones present in a complete machine. Therefore, the dc winding power losses in the four slots of the motorette were equal to the ones in four slots of a complete machine.

Slot wedges, or spacers, may be used to secure the coils within the stator slots. The wedges are expected to apply compressive forces to the conductors against the core tooth and back iron, which will impact the thermal contact resistance from the winding body to the stator core pack. The motorette configuration should be adapted to fully represent the situation, e.g. an entire slot may be more representative of the stator-winding assembly if the slot wedge is placed between two teeth.

Motorette hardware exemplars can also be used for ac power loss analysis. If a single tooth/coil motorette configuration is adopted, neighbouring tooth segments should be employed during power loss tests so that the flux path remains similar to the one of a complete machine. Depending on the investigated power loss effects, several alternative testing set-ups may be adopted, e.g. one wound tooth segment between two blank tooth segments, three wound tooth segments, etc. On the one hand, if a motorette comprises only one coil, this coil's own excitation effects may be analysed in detail. On the other hand, a first insight can be obtained on the neighbouring effects if two coils are placed in the motorette slot.

5.2.1 Analysed motorette exemplars

The analysed hardware comprises four MEs, each one representing a baseline machine, Fig. 5.1. The numbering of each ME follows the numbering of the corresponding complete machine, e.g. ME I is associated with M-I)). Table 5.1 lists basic data for the investigated MEs, where *w/h*, l_a, l_e, and A_{sa} represent the averaged slot width to height aspect ratio (w and h are the averaged slot width and height, respectively), winding active length, end-winding length and per slot active cross-section area. MEs II and III have been made as part of the research presented in this thesis, while the other samples were already existing from previous university projects [59], [89].

When motorette assemblies are used in aging analysis, an adequate number of motorette hardware exemplars is required to ensure statistically meaningful empirical data [232]. No well-defined procedure has yet been defined concerning the use of motorette exemplars in thermal analysis. A number of identical motorette exemplars have been manufactured for M-II (ME II-a and ME II-b) and M-III (ME III-a, ME III-b and ME III-c) to get first insight into the repeatability of their respective manufacturing process before complete stator analysis. Three variations of MEs I, II and IV have also been investigated and are indicated using an asterisk, e.g. the altered ME associated with ME I is referred to as ME I*. Fig. 5.2 summarises the links between baseline and supplementary MEs.

Table 5.1 Basic motorette hardware exemplars data

ME	I	II	III	IV
Number of coils	1	2	1	1
Active length	209 mm	51 mm	80 mm	185 mm
w/h	1.21	0.33	0.38	1.60
$l_a/(l_a + l_e)$	0.75	0.67	0.82	0.77
A_{sa}	412.7 mm^2	301.7 mm^2	524.7 mm^2	123.5. mm^2
Slot opening	Open	Open	Semi-closed	Semi-closed
Conductor type	Type-8 Litz wire	Rectangular	Round	Rectangular
Conductor material	*Cu*	*Cu*	*Cu*	*Cu*
Impregnating material	Varnish[1]	Varnish[1]	Varnish[2]	Epoxy[3]
Slot liner material	Nomex 410	Nomex 410	Nomex 410	Nomex 410
Winding process	Pre-built	Pre-built	On-slot	On-slot
Number of identical ME	1	2 (a and b)	3 (a, b and c)	1

[1] Elmotherm 073-1010, [2]Ultimeg 2000/U380, [3]Aremco-Bond 231

M-I comprises a parallel sided slot geometry, which should provide a superior conductor lay, Fig. 5.3a), and consequently improve the heat transfer from the winding to the stator core, but with the drawback of an increased stator core weight as compared with a conventional trapezoidal shape, Fig. 5.3b) [58]. The comparison of ME I and a motorette featuring a trapezoidal slot shape, referred to as ME I*, quantifies the benefit of using parallel sided slot geometry.

M-II's winding design has been finely tuned with the objective of minimising the ac and dc winding power losses for a fixed speed operation [89]. The results suggest that the common approach, where the highest manufacturable fill factor is considered, does not provide the optimal solution. This is due to the open-slot topology, which results in elevated ac effects due to the rotor rotation for the conductor at the top of the slot. The study of ME II and ME II*, which comprises copper and aluminium conductors, respectively, allows further investigation into the winding power loss optimisation.

Indeed, the high resistivity of aluminium will result in different ac and dc winding loss distributions for ME II and ME II*.

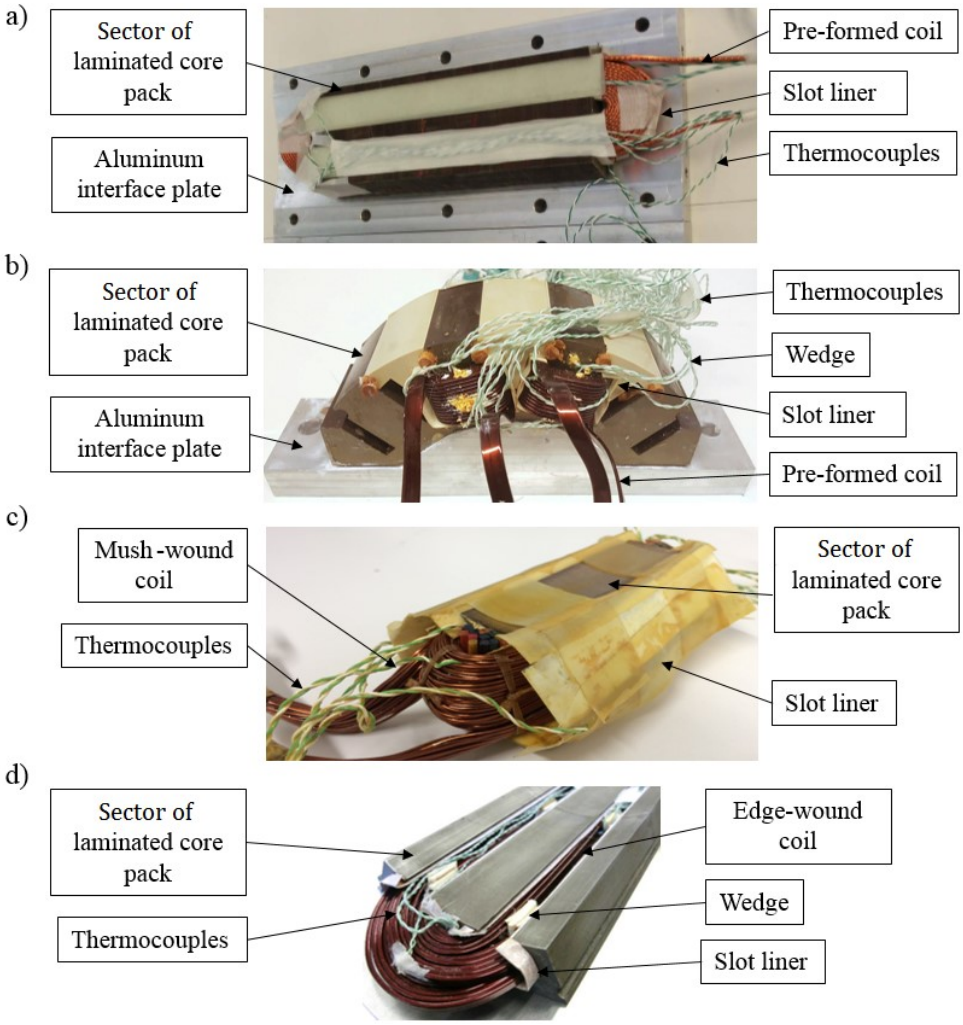

Fig. 5.1 Motorette hardware exemplars with sub-regions highlighted, a) ME I before impregnation b) ME II, c) ME III, d) ME IV before impregnation.

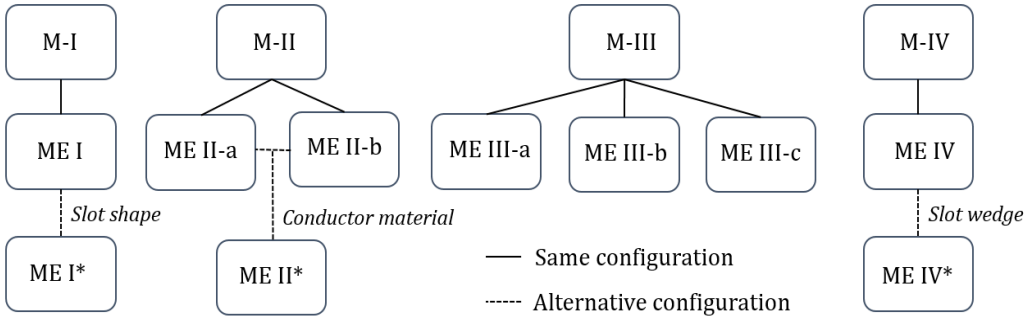

Fig. 5.2 Relationship between MEs used in theoretical analysis showing the difference between parameter changed in the alternative configurations.

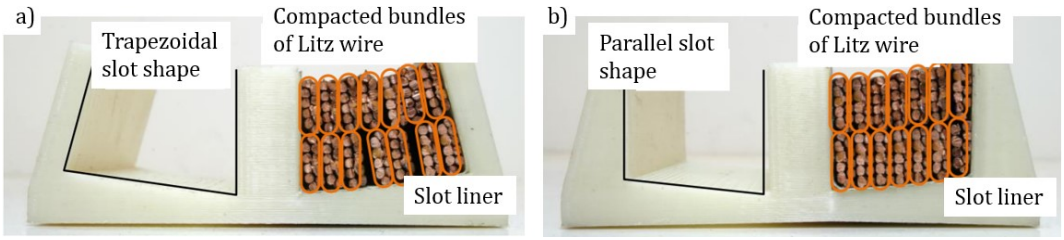

Fig. 5.3 Rapid-prototyped sectors of stator assembly with Litz wire winding, a) trapezoidal shaped slot geometry, b) parallel sided slot geometry [58]

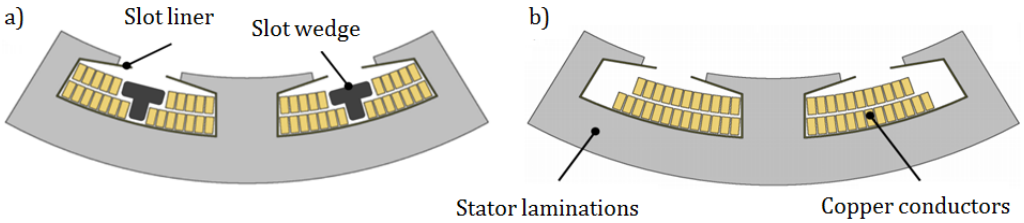

Fig. 5.4 Winding variants, a) Standard winding, b) Slot-wedge winding [59]

ME IV comprises a magnetically inert wedge, or spacer, to locate the individual conductors such that they are away from the stator slot region with high concentration of the magnetic flux leakage, i.e. around the slot-opening, Fig. 5.4a). The initial analysis of a winding arrangement with individual conductors tightly wound around the central tooth, Fig. 5.4b), confirmed that the ac effects were particularly high for the conductors located near the slot opening [59]. The slot wedge forces the conductors to the adjacent teeth, which also improves the winding to stator heat transfer. The comparison between ME IV and MEs IV* allows the evaluation of the advantages and limitations of using the slot wedge [59].

5.2.2 Motorette fabrication

The active iron parts of the studied MEs have been manufactured from M250-35A (MEs I and II) and M270-35A (MEs III and IV) silicon steel. Here, the lamination sheets have been pre-bonded to produce the initial lamination stack for machining. This method may not be ideal for mass-manufacture, but has been considered most suitable here for prototyping. The sheets were individually cut into a rectangular shape, degreased using acetone, assembled into an appropriate former, and placed into a hydraulic press under a weight of 50 tonnes at a temperature of 180 °C for a period of approximately 10 hours. The motorette core pack profile was then cut in a single operation using electrical-discharge machining (EDM). This method uses spark-eroding to cut a desired profile with very high tolerances (± 15 µm). The EDM process is conducted with the pre-bonded lamination stack submerged in cold water to avoid heat-damage of the lamination coating. The EDM machine available at the University of Bristol workshop is limited in terms of maximum

height of the parts it can accommodate. Consequently, core packs for MEs -I, -III and -IV have been manufactured in several segments, which then have been glued together. An assembly tooling has been manufactured to ensure a good radial and axial alignment of the individual core pack segments. Then, an appropriate slot liner material has been cut and placed into the core pack slots.

The winding types analysed here include single- and double-layer construction. The coils have been pre-formed (Ms I and II) or 'on tooth' wound (Ms III and IV). The edge-wound rectangular profiled conductors winding design adopted for M-II have been fabricated using custom built tooling. During the winding process, thermocouples have been placed in selected locations within the MEs. This includes the core, end-winding and winding active length regions, and the expected hot-spot location. For this reason, some thermal sensors have been placed on the conductors at the top of the slot as this region constitutes a potential hotspot location. Indeed, the heat produced within these conductors has the longest path to go through before reaching the cold plate. Thermocouples have also been placed at the bottom of the slot in order to observe the temperature gradient within the winding assembly. Concerning the instrumentation of the core pack, thermocouples have also been placed on the tooth, expected hot spot area of this assembly, and on the back iron. Thermocouples have been placed symmetrically on both sides of the motorette for redundancy. It is sometimes desirable to have some insight about the way the heat is transferred across an interface, e.g. the winding-to-core interface. However, placing a thermocouple between the winding and the core, i.e. within the slot liner region, might worsen the contact between the two regions. For this reason, it is preferable to avoid placing thermocouples in this region, and use other way to estimate the thermal contact between the two regions. For instance, the average temperatures of each of the interfacing region and the heat transferred within the interface can be used to calculate an equivalent thermal contact resistance.

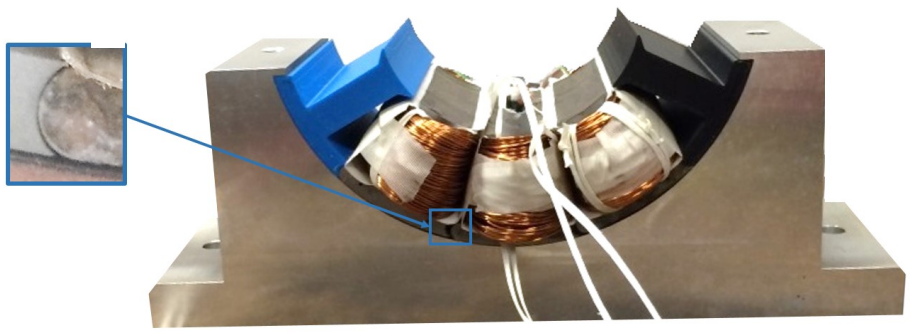

Fig. 5.5 a) MEs III-a, -b and -c on an aluminium arc-shape interfacing plate. A close-up view of the interface between two ME sectors is also shown

For each motorette exemplar, an aluminium interfacing plate with an arc shape coinciding with the stator outer radius has been manufactured. This enables good contact to the cold plate during experiments and ensures well defined testing conditions. Fig. 5.5 shows the three MEs corresponding to M-III on an aluminium interfacing plate. A close-up view of the interface between adjacent MEs is also provided, showing locating features. Electrical tests, consisting of measuring the electrical resistance between the laminations and the conductors, have been undertaken before impregnation to verify that each ME did not suffer any damage during manufacture and/or assembly. This is pertinent considering that a winding failure detected after impregnation would be very difficult to correct. All motorette exemplars have been impregnated or potted. The epoxy potting has been completed using a mould shell placed over the assembly, directly on the ME interfacing plates. The varnish impregnated motorettes have been dipped into a varnish-filled container. Independently of the impregnation material used, the motorettes have then been placed inside a vacuum chamber in order to be vacuum impregnated. Once most of the air has been evacuated, the motorette assembly has been cured in an oven, where the time and the temperature of the curing process depends on the material used.

5.3 Thermal analysis

5.3.1 Experimental set-up

A series of transient and steady-state thermal tests with dc excitation of the tested motorette assembly have been carried out for this investigation. The dc excitation provides well-defined testing conditions with a single source of power loss located in the winding. Fig. 5.6 presents the experimental setup used in this investigation. During motorette testing, the tested ME is mounted on an interfacing plate and placed in an insulated chamber. The heat generated within the winding body is conducted across the laminated core pack assembly through the interfacing plate to a liquid-cooled, temperature controlled plate, referred to here as a ‘cold plate’. This allows for a well-defined, unidirectional, heat path from the heat source to the heat sink. Such an arrangement is comparable to the heat extraction via a liquid-cooled housing jacket; however, it is applicable for a wide variety of machine topologies. To improve heat transfer, thermal paste has been applied between various interfaces of the experimental setup. These include the stator core pack to interfacing plate and interfacing plate to cold plate. The temperatures, current and voltage are acquired at a sampling frequency of 4 Hz until thermal equilibrium is reached. This frequency is assumed to be sufficient to gather a representative number of test data points for transient analysis. The thermal equilibrium is defined as temperature variations lower than 1ºC over 10

minutes. The temperature within various winding and stator sub-regions of the motorette is measured using type-K thermocouples.

In addition, the winding average temperature has been evaluated from the measured winding resistance. The change in the winding dc power loss due to the temperature is described at (5.1).

$$P_w = I^2 R_{\Omega,0}\left(1 + \alpha\left(T_w - T_{w,0}\right)\right) \qquad (5.1)$$

where $R_{\Omega,0}$ is the winding dc resistance at $T_{w,0}$ and α is the temperature coefficient of electrical resistivity of the conductor material used at reference temperature, e.g. 20ºC.

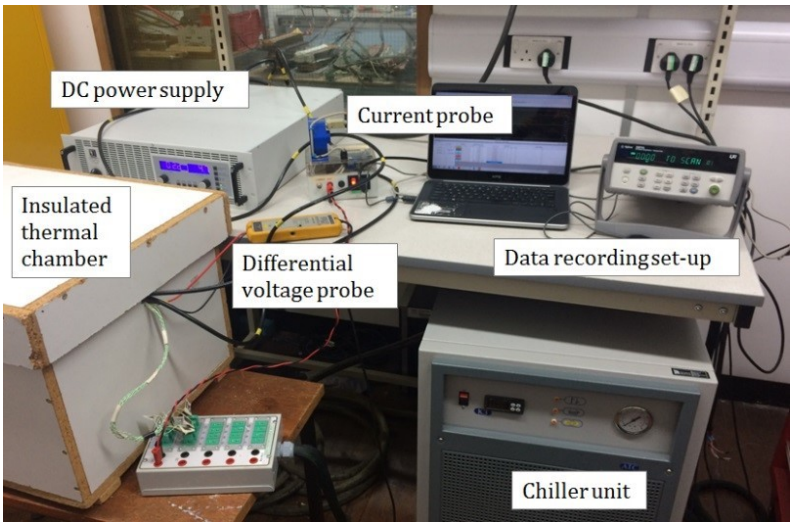

Fig. 5.6 Experimental set-up for DC power loss measurement

The averaged winding temperature T_w is then evaluated from (5.1) using the winding resistance measured for each level of dc excitation currents.

5.3.2 Mathematical models

The winding-to-stator core interface is a multi-material region affected by material properties and assembly processes, and by winding configurations. A description of the alternative representations for winding-to-stator interface is provided here, followed by a presentation of the adopted analytical and numerical thermal models.

Winding-to-stator interface representation

The physical representation of the winding-to-stator interface is acknowledged to be challenging by machine thermal designers, and homogenisation is often used to simplify

the model definition and reduce solving time. Fig. 5.7 presents alternative schematic representations of the stator-to-winding interface presented in [55].

Fig. 5.7a) shows the ideal situation, where the impregnated slot liner and the winding amalgam and stator core are in perfect contact between each other. According to (2.27), this representation would lead to an overestimation of the winding-to-stator core heat transfer capability, as the contact area A would be overestimated. Fig. 5.7b) illustrates the real-life like situation, where the contact between the slot liner and neighbouring bodies is subjected to air cavities and surface cracks. Building a representative and accurate model of such interface is nearly impossible.

Two methods have been developed to account for the contact interface imperfections in thermal analysis [55]. In Fig. 5.7c), an equivalent air cavity layer has been added, with equivalent air cavity thickness derived from empirical data [55]. Such a representation is also typically adopted for stator core-to-housing frame thermal contact resistances [133]. The method is well-suited for lumped-parameter TEC representations, but might be impractical in FE analysis: the layer is usually a few micrometres thick, and the different orders of magnitude between the air layer thickness and the other model regions might lead to computationally-expensive model formulation. Fig. 5.7d) presents a solution to overcome this issue by defining an equivalent slot liner region, where the thermal properties of the air cavities and slot liner are homogenised. This allows for an accurate and computationally efficient representation of the stator-to-winding interface [55]. The analytical and numerical approaches used for thermal modelling of motorette assemblies are presented in the following sub-sections, using the approaches presented at Figs. 5.7c) and 5.7d) for the representation of thermal contact resistances.

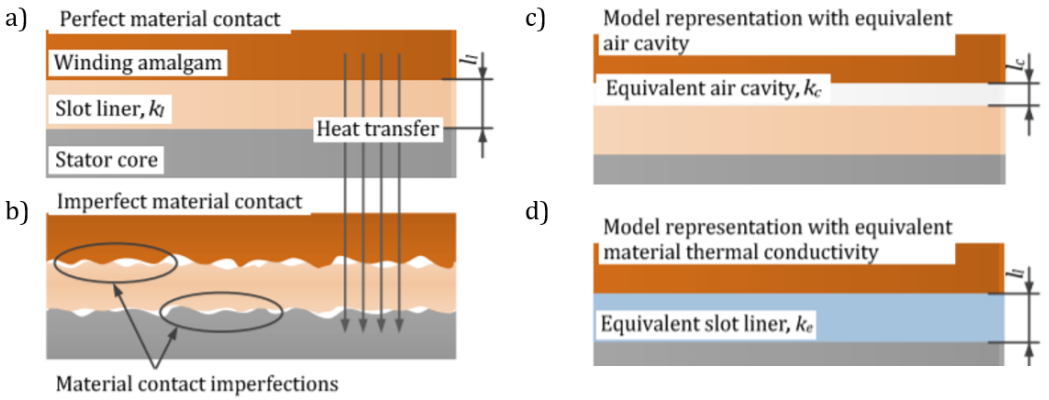

Fig. 5.7 Schematic explanation of material perfect and imperfect contact together with equivalent model representation [55], a) Ideal model, b) Physical model, c) 'Equivalent air cavity' model, d) 'Homogenised slot liner region' model

Analytical methods

The TEC approach is based on a lumped parameter network linking together temperature nodes in the main or selected heat paths. The method allows for the average or hot spot temperature derivation with model complexity altered to particular needs. One of the main advantages of low-resolution TECs is the ease of the circuit construction, as these models only comprise a limited number of nodes. However, setting-up a reliable low-order model also requires a good understanding of the assembly thermal behaviour in order to choose the adequate sub-region separation and a minimum number of nodes. Three different analytical models have been used for illustration, and are referred to as TEC-a, TEC-b and TEC-c in this Chapter. The models have been used to discuss the analytical model calibration in the context of model complexity, from low (TEC-a, 3 nodes), medium (TEC-b, 6 nodes) to high (TEC-c, 14 nodes). All the models analysed in this Chapter focus on temperature predictions at thermal equilibrium. The machine transient thermal behaviour is investigated in Chapter 6 in the context of winding heat capacitance estimation.

TEC-a is presented in Fig. 5.8a), together with the nomenclature used. Here, R, P, and T are the thermal contact resistance, power loss and temperature, respectively. The subscripts w and s correspond to the winding and stator core, respectively. TEC-b is created from TEC-a, where the node s is replaced by two nodes representing the stator tooth T and the stator yoke Y respectively, Fig. 5.8b). The other two nodes, representing the winding active length AL and end-winding region EW, respectively, substitute the node w. The power loss associated with the regions is injected directly in the appropriate nodes, e.g. winding dc power loss in active length AL and end-winding EW. The resulting TEC models have been solved using Simulink [167].

Unlike TEC-a and TEC-b, TEC-c has been automatically generated based on geometry and material using Motor-CAD, Fig. 5.8c), [130]. This software can produce the TEC of a complete machine, based on input machine geometry and material, but does not have a dedicated motorette module yet. An approach is adopted for the adaptation of a complete machine thermal model to a motorette analysis. To emulate the motorette test apparatus in TEC-c, the housing temperature has been set to the cold plate measured temperature. The stator and housing regions have been thermally isolated by introducing a large scaling factor to all thermal resistances connecting the stator to the rotor. These substantially large thermal resistances reproduce adiabatic conditions, emulating the experimental set-up.

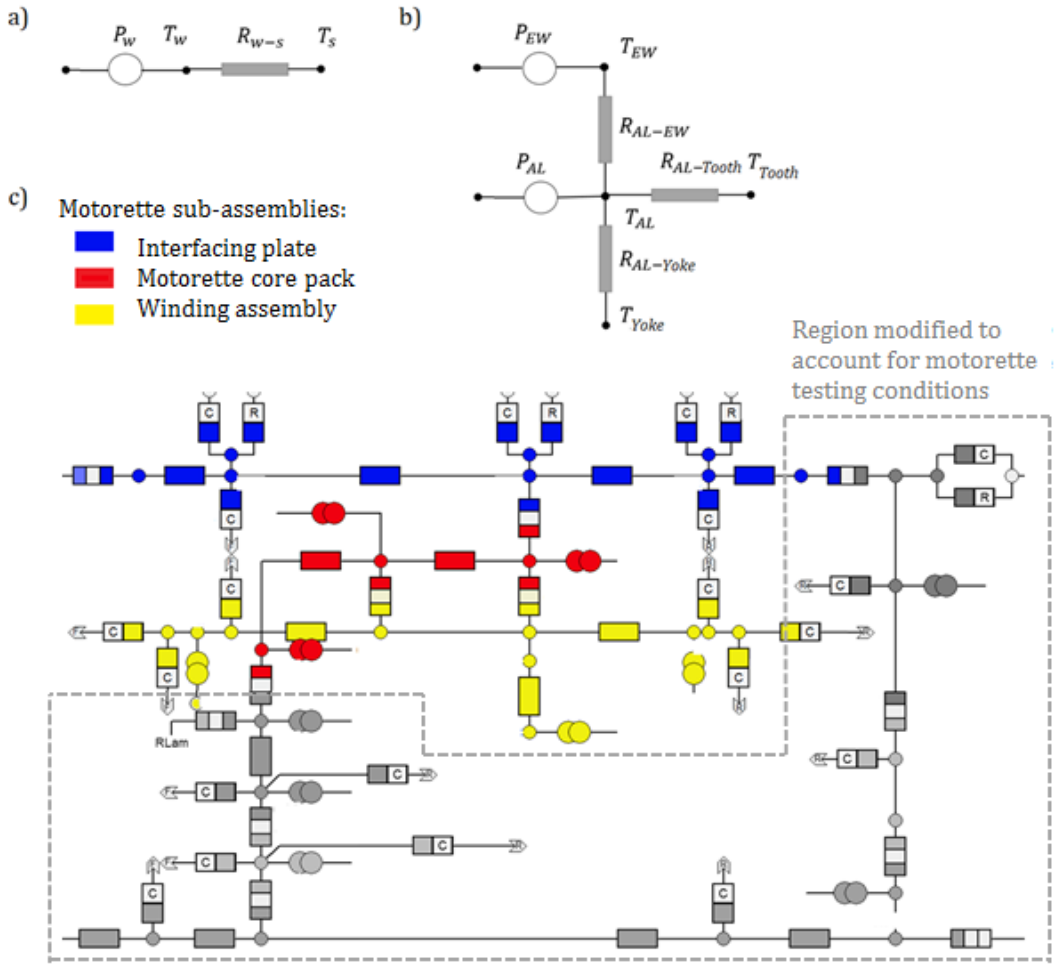

Fig. 5.8 Equivalent TECs of the motorette experiment apparatus a) TEC-a, b) TEC-b, c) TEC-c, the stator core pack, winding and housing regions are isolated [130].

The isolated regions are represented in TEC-c in grey colour, while the stator core pack, windings and housing assemblies are shown in red, yellow and blue, respectively. The other machine regions (grey) have been isolated and do not influence the stator-winding temperature prediction. The dc winding power loss within the complete machine model is calculated based upon the number of individual coils in the complete machine compared to the motorette. The winding-to-stator and stator-to-housing thermal contact resistances are represented in TEC-c using an equivalent airgap, as for the model representation shown on Fig. 5.7c). This representation will be compared to the 'equivalent slot liner' region one, as shown on Fig. 5.7d), adopted in the FEA models.

Numerical method

FEA numerical methods are able to model complex geometries and provide a detailed solution of temperature distribution within a device. Depending on the model resolution, the use of numerical methods might be computationally expensive. For these reasons, FEA techniques are usually chosen for investigations where a more detailed solution is required,

e.g. final design. The software ANSYS Mechanical has been employed for 2D and 3D FEA thermal analyses undertaken here [247]. The comparison between the calibration of 2D and 3D model will allow discussion of the use of 3D data, e.g. end-winding or winding active length, for the calibration of 2D thermal model.

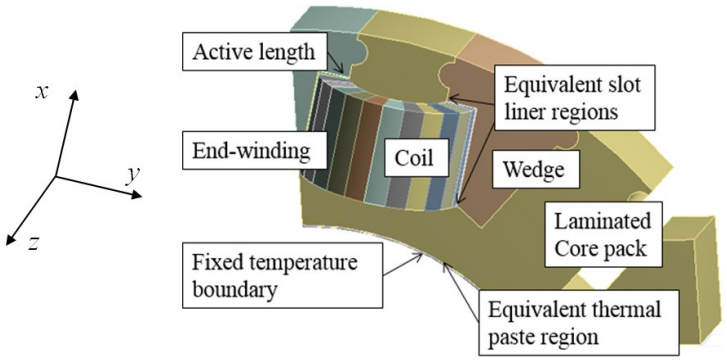

Fig. 5.9 3D FE model of 1/4 of ME II

Fig. 5.9 presents the 3D FE model representation of ME II with all sub-regions highlighted. Due to symmetry, only one quarter of the complete assembly has been modelled. A fixed temperature boundary condition is used to represent the interfacing plate, and the remaining motorette surfaces are defined with adiabatic boundary conditions, emulating the adopted testing procedure. Both the stator core pack and winding assembly have anisotropic thermal properties. The winding-to-stator interface is defined as an equivalent composite region referred here as equivalent winding-to-stator region, as the model representation shown on Fig. 5.7d). Similarly, the interface between interfacing plate and stator core pack, is defined here as an equivalent stator-to-housing region. A similar approach has been adopted for the 2D FE model representation.

5.3.3 Thermal model calibration

Estimation of the winding-to-stator thermal contact resistance

The theoretical method for the estimation of the winding-to-stator thermal contact resistance is based on the energy conservation law. Applying this law to TEC-a, Fig. 5.8a), the following equation is obtained for the winding dc power loss:

$$P_w = \frac{T_w - T_s}{R_{w-s}} = \frac{\Delta T_{w-s}}{R_{w-s}} \qquad (5.2)$$

Here, R_{w-s} is assumed to be a constant value, independent of temperature. R_{w-s} can easily be found from the following equation:

$$R_{w-s} = \frac{\Delta T_{w-s}}{P_w} \quad (5.3)$$

Usually, R_{w-s} is derived based on the results of a series of dc tests with various levels of DC current excitation. The rate $\frac{d\Delta T_{w-s}}{dP_w}$ is derived from these tests, corresponding of the average R_{w-s} value. Clearly, (5.3) is not limited to motorette testing, as the interfacing and cold plate temperature are not part of the investigated circuit, and could be derived in a similar manner for stator and complete machine analysis. The approach is also not restricted to the winding-to-stator thermal contact resistance, and can be applied to any adjoining regions of a machine assembly. For instance, the stator-to-housing thermal contact resistance can be derived using (5.3), by replacing the winding temperature T_w with the housing temperature T_h.

An essential step when analysing empirical data consists in estimating the uncertainty *u* associated with the measured values. The uncertainty $u(R_{w-s})$ associated with the derived thermal contact resistance value has been evaluated, using the following expression:

$$u(R_{w-s}) = \frac{R_{w-s}}{\sqrt{2}} \sqrt{2\left(\frac{u(T)}{(T_w - T_s)}\right)^2 + \left(\frac{u(U)}{U}\right)^2} \qquad (5.4)$$

where *u(U) and u(T)* are the measurement uncertainties of the voltage and temperature, respectively. The accuracy of the current is not considered, as a high-accuracy dc current source has been utilised for the tests with a measurement uncertainty of the current, *u(I)*, such that *u(I)* << 10^{-3}A. The values of uncertainties of the different parameters and the instrument or devices used for measurement are similar to the ones used in Chapter 4, listed in Table 4.5. Mathematical proof for the calculation of the uncertainty of the winding-to-stator thermal contact resistance is provided at Appendix B. Equation (5.4) can be adapted for the estimation of the uncertainty of the stator-to-housing thermal contact resistance, by replacing the winding temperature T_w with the housing temperature T_h.

The following sub-sections describe the procedures adopted for the analytical and numerical thermal model calibration using empirically-derived thermal contact resistance data. The issues of thermal model calibration are investigated in the context of available machine hardware and measured data resolution. ME II-a (copper) has been used for the illustration, and instrumented with multiple type-K thermocouples located in various sub-regions including the laminated core pack (tooth and yoke regions), winding (end-winding and active length regions) and liquid cooled heat sink. Two thermocouples were used respectively to measure the ambient temperature within the thermal chamber, and the

temperature of the aluminium interface plate used for the active heat extraction when testing the motorette assembly.

Reduced-order TEC models – TEC-a and TEC-b

Several approaches can be used to calibrate reduced-order TEC models. One of the techniques is based directly on measurements, e.g. the thermal resistance between the winding and the core pack region used in the TEC model is derived using (5.3) from averaged winding and core pack temperatures. The reduced number of nodes of these models enables quick computation if used in duty cycle analyses [164], [165]. However, these TEC models do not have an intrinsic mathematical basis, e.g. the exact influence of the core pack geometry is unknown, which makes their alteration difficult in case of design changes. Building and testing a new hardware exemplar is typically required in this situation. Considering that the machine hardware is usually instrumented with a few thermal sensors, it is important to locate them in the appropriate regions. These would include the parts with the main heat flux, e.g. winding active length and end regions, stator back iron and tooth, machine housing and others depending on the machine construction. For the averaged per region temperature measurements used in the dc model calibration, the temperature sensors located in the mid distance of the heat flux path or half region thickness and length seems adequate.

Fig. 5.10 shows the winding temperature rise above the stator back iron temperature, ΔT_{w-s}, versus winding power loss at thermal steady state with the slopes of individual plots, R_{w-s}, provided.

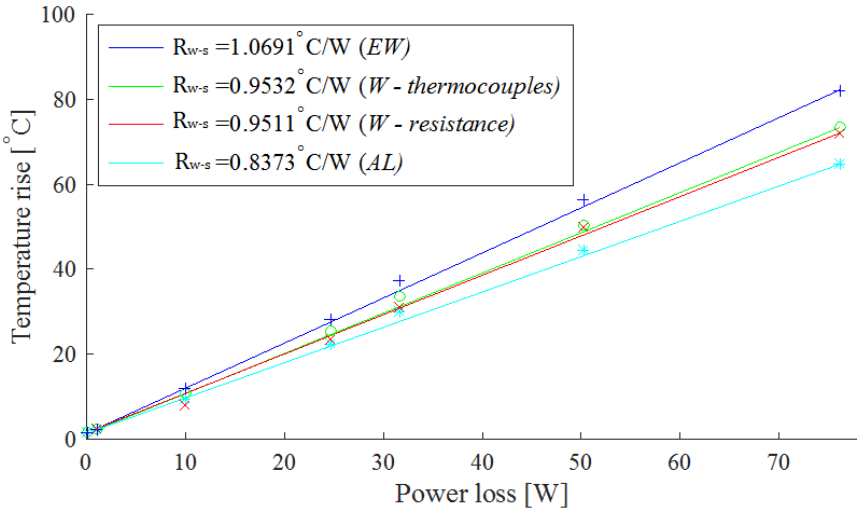

Fig. 5.10 Temperature rise above back iron ΔT_{w-s} vs. winding dc power loss P_w– ME II-a. The averaged back iron temperature used here as reference, while different temperature data from

winding active-length (*AL*), winding end region (*EW*) and combined active and end regions (*W*) have been used [230]

A set of plots shown in Fig. 5.10 corresponds to different temperature data from the winding region (winding active-length, winding end region, and combined active and end regions) used to average the overall winding temperature. The average back iron temperature used here as reference has been derived using the complete set of thermal sensors (tooth and yoke). The results indicate that the indirect temperature measurements using dc winding resistance provide 'good' alternative for the experimentations with limited number of temperature sensors. There is 25% discrepancy between R_{w-s} obtained using the temperature sensor data from the winding active length and end-winding region respectively. This suggests that the resolution used to calibrate a particular thermal model should match or exceed the model complexity, e.g. a reliable calibration of TEC models where the average and hot spot winding temperatures are of interest is only possible if both the end-winding and active length regions are appropriately instrumented with thermal sensors. The calibration of high-fidelity models using a limited set of thermal data can introduce some degree of uncertainty in the temperature predictions, as there might be a number of the thermal contact resistances combinations for which the estimation procedure converges to the measured data. The choice of a preferred set of parameters is then difficult, as the derived parameters may not yield physical meaning, i.e. the estimated values correctly predict the sub-assemblies temperature for the investigated cases, but do not represent the intrinsic machine thermal properties. A detailed study of the impact of the measured data from alternative sensor locations on the quality of the model calibration and consequently temperature predictions has been documented in the conference paper [230] listed in the publications associated with this thesis.

A second technique for TEC definition is making use of FE predictions to calculate the average temperature for each model sub-region and the heat flux across the sub-region boundaries [117]. The thermal resistances are then directly obtained from the temperature difference between the sub-regions divided by the heat flux across the boundaries multiplied by the area across which the heat is transferred. In particular, FE calculations provide detailed hot-spot temperature predictions in addition to the averaged one. The TEC can therefore be adapted to represent both average and hot spot temperatures [83]. The thermal resistances of the TEC previously defined in Figs. 5.8b) and 5.8c), TEC-a (2 nodes) and TEC-b (4 nodes), are derived from measurements and ideal FE 3D model. The measured and ideal thermal contact resistances, referred to as $R_{w-s,mes}$ and $R_{w-s,idealFE}$ respectively, are listed in Table 5.2 for both TECs. Thermal resistances obtained from

models informed from ideal FE are smaller as compared with the values directly derived from the experiments. This is attributed to the contact thermal resistance winding-to-stator case, which is not accounted for in the ideal FE model definition. Clearly, a calibrated FE model should be used to accurately estimate the thermal resistances of the reduced-order TEC models. The procedure for FE thermal model calibration is described in the next sub-section.

Table 5.2 Thermal resistances – TEC-a and TEC-b

Model	TEC-a (2 nodes)	TEC-b (4 nodes)			
Sub-regions	W-S	AL-Y	AL-T	Y-T	AL-EW
$R_{w-s,mes}$ [°C/W]	1.0	1.0	0.7	0.3	0.2
$R_{w-s,idealFE}$ [°C/W]	0.4	0.3	0.1	0.05	0.01

W: winding, S: core pack, AL: winding active length, Y: yoke, T: tooth, EW: end-windings

High-order model – TEC-c and FE models

The procedure for the calibration of the slot liner region of FE thermal models or high-order geometry-based TEC models depends on the adopted winding-to-stator interface representation. The calibration process for the 'homogenised slot liner region' representation, Fig. 5.7d), is based on the estimation of the thermal conductivity for the equivalent winding-to-stator, k_{w-s}, while the 'equivalent air cavity' representation, Fig. 5.7c), requires the calibration of the equivalent air cavity thickness, $l_{air,w-s}$, for the interface. The average temperatures for the winding and stator core pack are predicted using the analysed models for different levels of dc current excitation, allowing the calculation of winding-to-stator thermal contact resistance R_{w-s}. The temperature and power loss interdependence should be accounted for when calculating the winding temperature. The commonly used technique of updating the dc winding power loss with temperature is based on (5.1), where the power loss is iteratively updated with averaged temperature of the winding region. The calibration is completed by adjusting k_{w-s} or $l_{air,w-s}$ such that the measured and calculated thermal contact resistances $R_{w-s,mes}$ and $R_{w-s,cal}$ match.

A similar approach may be used for the calibration of the motorette core-to-cold plate interface (or stator core-to-housing in case of complete stator analysis). The average temperatures for the core and cold plate (or housing in case of stator analysis) are predicted using the analysed models for different levels of dc current excitation, allowing the calculation of core-to-cold plate (or core-to-housing) thermal contact resistance R_{s-h}. The thermal conductivity k_{s-h} or equivalent air cavity thickness $l_{air,s-h}$ of the core-to-cold plate region (or core-to-housing region) is then adjusted so that the measured and predicted thermal contact resistances $R_{s-h,mes}$ and $R_{s-h,cal}$ match.

The high-fidelity FE and TEC-c models used in this investigation have been informed with thermal conductivity data derived from tests on material samples for the composite sub-regions, including the winding and laminated core regions. If no material data were available, the material thermal parameters and the interfaces would have to be concurrently adjusted. As previously discussed in the context of reduced-order TEC model calibration, there might be a number of the parameter combinations for which the estimation procedure converges to the solution, depending on the model complexity and number of thermal sensors used in measurements. In order to increase confidence of the derived data, several tests at various dc current excitations are typically required. In [170], a particle swarm optimisation (PSO) routine has been adopted for the derivation of the material and interface parameters. Thermal data from the literature have been used to set the upper and lower boundary for each parameter, reducing the computation time of the PSO routine and preventing non-physical solutions.

The differences in calibration outcomes for 2D and 3D thermal models are investigated, including the impact of using '3D' data for the calibration of 2D models. 2D thermal model representations are frequently adopted, due to their lower computation-time as compared with their 3D counterparts. 2D models cannot represent 3D thermal effects happening in the stator-winding assemblies, e.g. heat transfer between end and active winding regions. Fig. 5.11a) presents the calibrated thermal conductivity of the equivalent winding-to-stator region data, k_{w-s}, from both 2D and 3D models versus R_{w-s}. The measured results show expected trends, where R_{w-s} is higher for the assembly regions further away from the heat sink. For instance, R_{w-s} derived values for the end-winding region with thermocouple location close to the stator back iron are higher than for the case where the temperature sensor is placed in the active length. Further to this, selecting the reference core temperature (tooth or back iron) impacts the R_{w-s} value. The factor is reduced for the reference core temperatures from the core regions away from the measured winding sub-regions.

a)

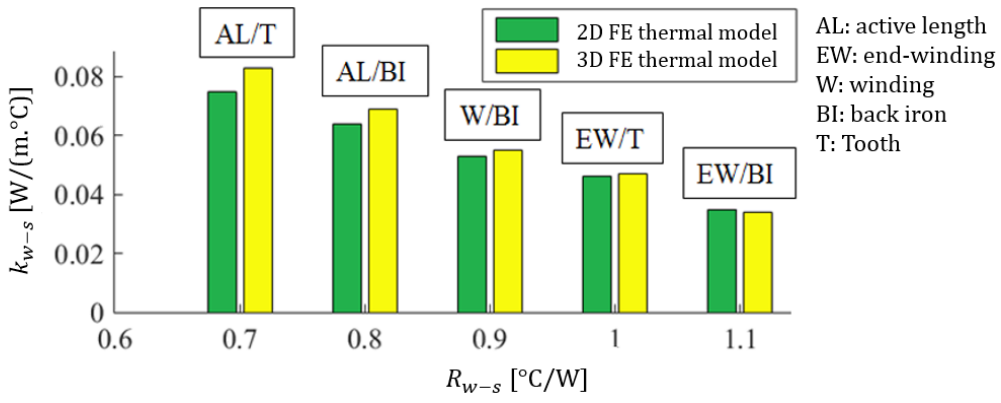

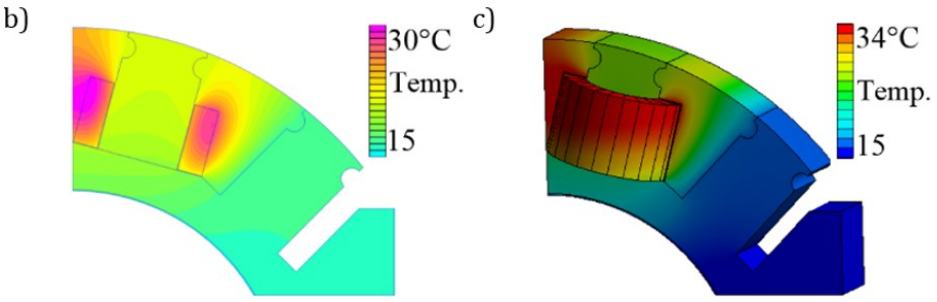

Fig. 5.11 a) Equivalent winding-to-stator thermal conductivity k_{w-s} vs. R_{w-s}, b) Thermal FEA model representations of the motorette assembly, ideal contact thermal resistance, 2D model, c) 3D model – ME II-a

The k_{w-s} data obtained using active length data sets are lower when using the 2D model, as compared with results obtained from 3D. Conversely, the k_{w-s} data derived using end-winding data sets are equal or slightly higher when comparing 2D to 3D results. This difference suggests an inherent ambiguity associated with the use of 3D end-winding or active length data for the calibration of 2D thermal models. During measurements, if the hot spot is located in the end winding, the temperature of the active length will increase due to the heat transfer from the end winding to the active length area, and vice-versa. This heat transfer and the subsequent increase of the temperature difference between the back iron and active length temperature cannot be captured by the 2D model, and is reflected in elevated thermal contact resistance. The 3D model can fully account for the end-winding and winding active length heat transfer effects and is therefore the recommended model when high fidelity is required. Figs. 5.11b) and 5.11c) presents an example of the temperature predictions from the ideal 2D and 3D FEA with a dc winding volumetric power loss $P_{v,dc}$ =14.0 W/cm^3 and a cold plate temperature T_{cp} =15 ºC. The temperature distribution is alike for both models; however, the presence of the end-winding in the 3D model results in an increase in the overall winding hot spot temperature. This corresponds with the measured data, where the hot spot is in the top end-winding.

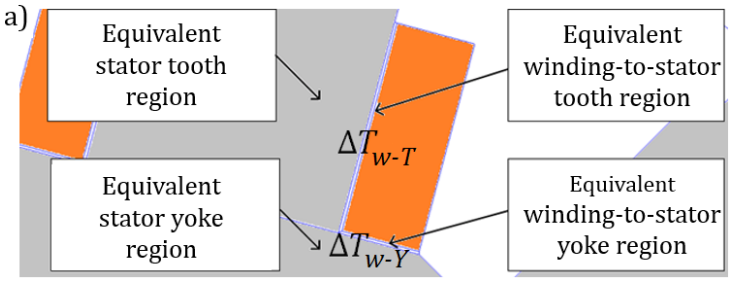

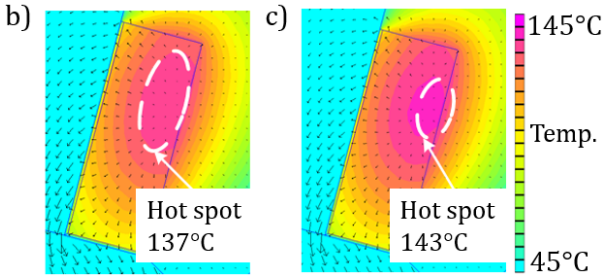

Fig. 5.12 2D thermal FEA model representation of the motorette assembly, a) sub-division of motorette regions, b) model calibrated using the same k_{w-s} for both winding-to-stator regions, c) model calibrated using adapted k_{w-T} and k_{w-Y} for winding to tooth and winding to yoke interfaces – ME II-a

Depending on the required model fidelity and analysed stator-winding configuration, a homogenised representation of the slot liner region might be too simplistic. A degree of discrepancy in hot-spot temperature predictions may be caused by the difference in the thermal contact resistance between winding and stator yoke, and winding and stator tooth, e.g. due to different conductor lay in the radial and circumferential directions [14], [20]. In this case, the equivalent winding-to-stator region has to be subdivided in two regions, winding-to-stator tooth and winding-to-stator yoke, with separate equivalent thermal conductivity values k_{w-T} and k_{w-Y}, respectively. Fig. 5.12a) presents a 2D thermal FEA model representation of ME II-a with updated sub-division of motorette regions. The calibration of the winding-to-stator tooth and winding-to-stator yoke regions allows for capturing the heat transfer effect related to the conductor lay. The presented procedure for the calibration of the thermal contact resistance is used here: the average temperatures for the winding and stator tooth regions are first calculated for different levels of dc current excitation, and the winding-to-stator tooth thermal conductivity k_{w-T} is adjusted using the calculated winding-to-stator tooth thermal contact resistance R_{w-T}. Then, the average temperatures for the winding and stator yoke regions are calculated for different levels of dc current excitation, and the winding-to-stator yoke thermal conductivity k_{w-Y} is adjusted using the calculated winding-to-stator yoke thermal contact resistance R_{w-Y}. The values obtained for k_{w-T} and k_{w-Y} are 0.050±0.002 W/(m.°C) and 0.055±0.003 (W/m.°C) respectively, while the previously estimated value for the single equivalent slot liner region k_{w-s} was 0.050±0.002 W/(m.°C). This difference may be partly explained by the fact that the contact between the bottom coil (along the conductor width) and the core back iron is better than between the side of the coil (conductors height) and the core tooth. This echoes the observations made in Chapter 4, where stacking conductors together along their heights was found more difficult than along their widths, enhancing the thermal conductivity in the latter direction.

Figs. 5.12b) and 5.12c) presents the temperature distribution within the motorette (ME II-a) for the calibration variants discussed earlier at thermal equilibrium and dc excitation current of 70 A. The temperature predictions indicate a discrepancy between the models with the alternative equivalent slot liner region definitions. The more detailed model suggests a higher hot spot temperature as compared with the counterpart with a single value equivalent contact thermal conductivity. This is particularly important as the impact of model calibration using adapted thermal conductivity values k_{w-T} and k_{w-Y} is expected to be more prominent in the complete machine assembly. Indeed, the presence of the ac power loss effects affect the heat distribution within the winding region, making the winding-to-tooth heat transfer capability crucial to accurately estimate.

5.3.4 Measured data

The complete set of results from tests on the motorette exemplars is discussed here, in particular with the comparison between 'baseline' and 'alternative' MEs. When comparing the thermal contact resistances of two different hardware exemplars the difference in slot numbers needs to be accounted for. This can be done using the following updated equations:

$$R_{w-s} = q\frac{\Delta T_{w-s}}{P_w} \qquad (5.5)$$

where q and P_w represent the number of slots and the total measured power loss, respectively. This will be particularly important in Chapter 6 when comparing sub-assembly hardware exemplars representative of the same machine assembly, e.g. complete stator and motorette assembly. The equivalent stator-to-winding thermal resistance R_{w-s} discussed in this section refer to the per slot conductive heat transfer.

Two slot geometrical factors, the slot shape *w/h* and cross-section area A_{sa}, need to be accounted for when comparing the heat extraction capability from the winding body into the stator core of different stator-winding assemblies. Ideally, both the shape and size of stator slots would need to be the same to make a valid comparison. Clearly, this requirement is difficult to satisfy in the majority of practical cases, including the selected MEs. Two correcting functions, the shape and size functions C_{f1} and C_{f2}, have been developed to enable an unconstrained comparison throughout a collaborative work, and documented in the conference paper [235] listed in the publications associated with this thesis. Further information about the derivation of the correcting functions C_{f1}, C_{f2} and C_{f3} is provided in

Appendix D. Both correcting functions have been individually obtained and were derived for the winding-to-stator thermal conductance h_e, defined as follows:

$$h_e = \frac{1}{R_{w-s}A_{w-s}} \qquad (5.6)$$

where A_{w-s} is the theoretical winding-to-stator contact surface area. By accounting for A_{w-s}, h_e already introduces a geometrical factor into the heat extraction capability evaluation. The value obtained after applying C_{f1} and C_{f2} is referred to as h_{e12}. A third parameter, the end-winding length, influences the comparison between different winding/slot configurations. The impact of the end-winding region is particularly prominent for short machines. Initial work has been presented in [235] for the definition of a correcting function C_{f3} accounting for 3D effects.

Tables 5.3 and 5.4 list a complete set of results from tests on the MEs. The table include R_{w-s} and h_e data obtained using (5.5) and (5.6), respectively, together with h_{e12} data obtained using the scaling functionsC_{f1} and C_{f2}, assuming that $w/h = 0.7$ and $\frac{A_{w-s}}{A_{w-s,0}}$=5, with $A_{w-s,0}$ equal to 10^3 mm^2. The results obtained for h_e suggest that ME I stator-winding heat transfer capability is significantly poorer than MEs II. However, when comparing the equivalent thermal conductance h_{e12}, ME I has a slightly better stator-to-winding conductive heat path and the difference between MEs I and II is less prominent. This confirms the need to use corrected data to account for the slot shape and size when comparing different stator-winding topologies. The winding-to-stator thermal contact resistance R_{w-s} can nonetheless be used directly to compare MEs with same configuration.

Table 5.3 Stator-to-winding thermal resistance and conductance data – MEs I and II

ME	I	I*	II-a	II-b	II*
R_{w-s} [°C/W]	0.43±0.02	0.56±0.03	1.32±0.07	1.43±0.07	2.2±0.1
h_e [W/(m^2.°C)]	93±5	64±3	253±13	234±12	151±8
h_{e12} [W/(m^2.°C)]	155±8	111±6	152±8	140±7	90±5

Table 5.4 Stator-to-winding thermal resistance and conductance data – MEs III and IV

ME	III-a	III-b	III-c	IV	IV*
R_{w-s} [°C/W]	2.2±0.1	1.79±0.09	2.06±0.1	0.23±0.01	0.3±0.02
h_e [W/(m^2.°C)]	67.6±3	82.7±4	71.9±4	902±45	571±29
h_{e12} [W/(m^2.°C)]	43±2	52±3	46±2	916±46	619±31

The repeatability of the stator-winding manufacturing process has been investigated. The values obtained for MEs II-a and II-b ('identical' edge-wound coils with copper

conductors) suggest a good repeatability of the process, with less than 8% difference between the measured data. This is within the range of measurement uncertainty. This result was predictable as the automated coil manufacturing allows the production of very similar exemplars. Slot wedges were also used to secure the coils within the slot, Fig. 5.1b), and should apply an equivalent contact pressure on each coil. The main uncertainty concerning the repeatability of the motorette manufacturing process was therefore associated with the impregnation procedure. According to the values obtained for MEs III-a, III-b and III-c, the random position of the round conductors within the slot has an impact on the winding-to-stator thermal contact resistance, with a maximum difference of 24% between the measured data of MEs III-a and III-b. It is important to note that the winding manufacturing process was identical for the three MEs, however the lay of individual conductors is not controlled. The potential variation of winding and core temperatures from one stator slot to another needs to be accounted for when testing a complete stator or machine assembly, especially if the tested exemplar is instrumented with a limited number of thermal sensors.

The analysis of data obtained from ME I (parallel slot) and ME I* (trapezoidal slot) shows that the winding-to-stator thermal contact is better for ME I. As noticeable in Fig. 5.3, the parallel slot allows for a better conductor lay and improves the contact between winding and tooth. Moreover, in case of parallel slot, the winding assembly is in contact with both teeth, which further improves the heat extraction.

ME II* (aluminium conductors) has significantly higher winding-to-stator equivalent thermal contact resistance than ME II (copper conductors). Such a difference cannot be entirely explained by the change of conductor material. This would rather be attributed to the different tooling used to manufacture the coils, resulting in different conductor lays, which impact the winding-to-stator heat extraction capability, Fig. 5.13. This information is useful to have at an early design stage, as the difference of heat extraction capability provided by both windings may influence the thermal designer in the coil manufacturing tooling to adopt in the final machine design.

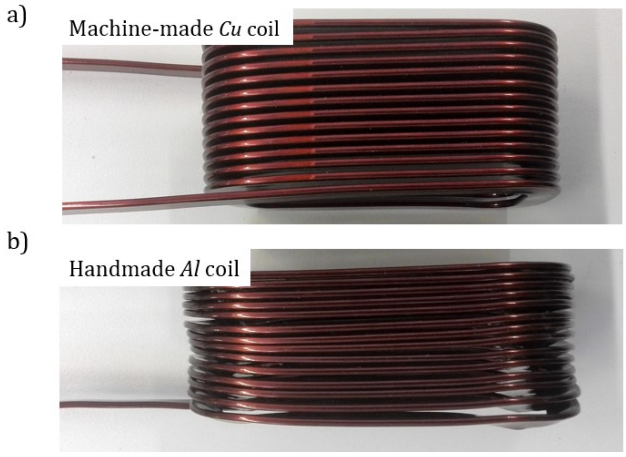

Fig 5.13 a) Machine-made copper coil used in ME II construction, b) handmade aluminium coil used in ME II* construction

The comparison between MEs IV (wedge) and IV* (no-wedge) shows that the presence of the slot wedge improves the slot heat extraction capability. By pushing the conductors towards both sides of the slot, the wedge allows for improved heat transfer from the winding body to the stator core pack. This is realised by ensuring larger winding to stator contact surface area. The use of Cf_1 and Cf_2 functions allows the evaluation of the benefits of the slot wedge in terms of winding-to- stator contact enhancement, independently of the winding to stator contact surface area. It appears that the slot wedge augments the contact pressure, which contributes to further increase ME IV winding to stator heat extraction capability. Moreover, ME IV has significantly higher stator-to-winding heat transfer capability compared to the other analysed MEs. This confirms the benefit of using epoxy potting in terms of winding heat transfer enhancement.

5.4 Power loss analysis

This section presents a methodology for the analysis of winding and core motorette power loss, including experimental set-up, mathematical models and loss parameters estimation depending of the intrinsic motorette configuration

5.4.1 Experimental set-up

There are several experimental methods applicable in measuring the winding and core power loss, e.g. calorimeter measurements (total power loss), Epstein frame or SST (core power loss), among others [100], [203]. The experimental approaches used here when deriving the ac winding and power loss includes the direct power measurements and impedance analysis, Figs 5.14a) and 5.14b), respectively. In both cases, the motorette under test is excited from a single-phase ac source with sinusoidal variation of current. The tested

motorette exemplar is placed in an environmental chamber and pre-heated to a selected temperature. This allows the derivation of the power loss and temperature interdependence. The direct power measurements have been conducted with different levels of excitation current magnitude and a set of discrete excitation frequencies. This frequency sweep was repeated for a range of average winding temperatures. The power measurements are taken 'instantaneously' at a pre-set winding temperature. The time required for a single measurement is relatively small, but sufficient for the averaged power analyser results to settle, and short enough to assume that the winding temperature remains unchanged during the tests. Unlike tests with dc current excitation, ac current excitation may generate eddy-current loss in the interfacing plate. Therefore, the aluminium interfacing plate is replaced with a non-magnetic wooden plate to strictly measure the ac power loss within the motorette assembly, Fig. 5.14c).

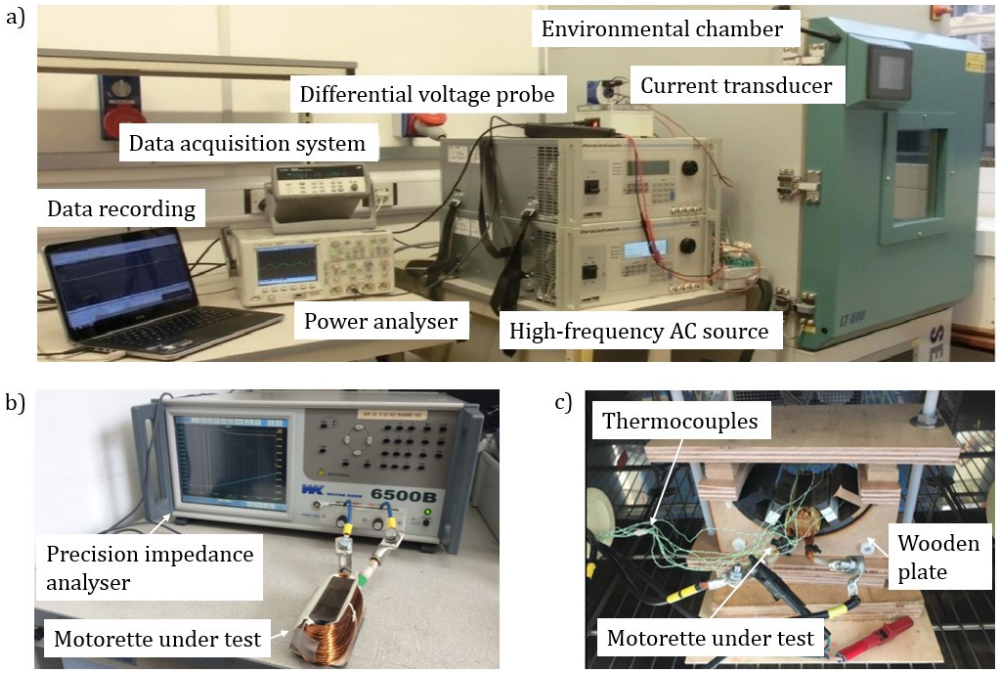

Fig. 5.14 Experimental set-up for AC power loss measurement, a) Direct power loss measurement – motorette under test in the environmental chamber, b) Impedance analyser, c) Complete set-up for direct power loss measurements

The precision impedance analysis can be used to access a broader frequency range when evaluating the ac power loss. The low excitation current (typically I<1 A_{RMS}) of impedance analyser tests is usually not representative of the machine excitation, and consequently provide limited insight into the magnetic saturation effects. An impedance analyser determines an equivalent circuit with series resistances for the coil being measured; using which the winding ac loss factor $(R_{ac}/R_{dc})_E$ is easily derived. Testing of a single tooth ME with two blank neighbouring stator segments, as shown

in Fig. 5.14c), provides a more-representative distribution of magnetic flux leakage as compared with a single-tooth alternative, Fig. 5.14b). Therefore, the multi-tooth configuration was adopted in this investigation, and the setup shown at Fig. 5.14b) is presented here for illustration only.

Fig. 5.15 presents a comparison of the total power loss measurements from direct power tests and impedance analyser tests on ME IV, for a fixed winding and core temperature of 20°C. Here, an equivalent ac resistance was obtained from the impedance analyser measurements, and was multiplied by the square of the excitation current of the direct power test, I=50 A_{RMS}, so that the measured power loss data obtained from both tests can be compared. The power losses obtained from the impedance analyser test are slightly lower than the ones from direct loss measurements, which suggests that the low excitation current of impedance analyser tests might not be able to capture all effects, in particular in ME IV core pack, present in the case of a more representative current excitation. This may also be attributed to measurement uncertainty, expected to be more important at low excitation current.

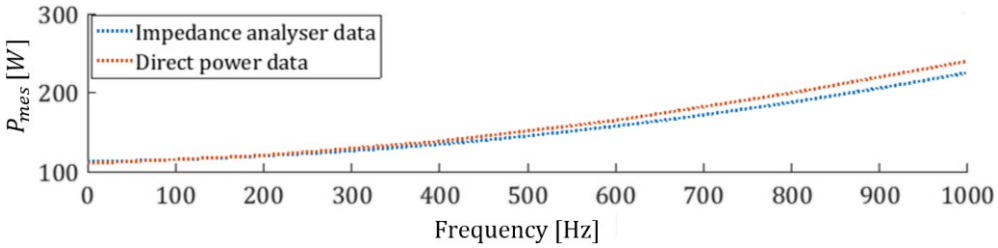

Fig. 5.15 Total winding power loss at 20 ºC and I =50 A_{RMS} for direct power loss and (scaled) impedance analyser measurements vs frequency – ME IV

5.4.2 Mathematical models

The loss contribution and thermal behaviour of the winding active length and end-windings often require separate analyses. The ratio $l_a/(l_a + l_e)$ can be used to separate the active length and end-windings dc winding loss; however, the ac winding loss mechanisms are dissimilar for the two regions. In this context, time-stepping 2D and 3D FE electromagnetic models have been employed to provide detailed power loss data [233], employing the software Infolytica Magnet [248]. The 2D and 3D analyses have been used to evaluate the active length and end-winding effects. These are particularly important for machines with short active length, as in this case the end-winding contribution to the overall winding loss cannot be neglected [89], [223].

Fig. 5.16 presents the 3D FE representation of MEs I to IV, with active regions highlighted. Due to symmetry, only one half of each ME has been represented, and a periodic boundary condition has been applied to the face located in the plan of symmetry. An air region has been drawn around the motorette, with a zero vector potential condition assigned to its outer boundary. The simulated MEs are driven by a one-phase sinusoidal waveform, reproducing the experimental set-up. The simulations are completed for a single electrical period, with one hundred calculation points. For example, for an excitation frequency of 100 Hz, the stop time has been set to 10 ms with a time step of 0.1 ms. In Fig. 5.16, the winding body of each ME model is represented as a homogenised region. However, various winding representations have been adopted depending on the studied ME. An accurate representation of each conductor of ME I's Type-8 Litz wire would be computationally challenging, due to the 3D nature of the conductor transposition. Here, an ideal conductor transposition, i.e. balanced current share for the individual strands of the Litz wire bundle, has been assumed to simplify the initial analysis. MEs II and IV's winding regions have been modelled as individual solid conductors with an appropriate external circuit representing the electrical connections between individual conductors and phases. This conductor representation allows the derivation of accurate $(R_{ac}/R_{dc})_e$ ratios. ME III's windings have been homogenised in a single region of copper material. The mush-wound round conductor bundles would be challenging to accurately model in a time-efficient manner, as the exact position of each conductor within the slot is unknown, but is needed to reliably predict the winding ac losses. Moreover, hundreds of conductor cross-sections should be represented in a single slot, which would lead to time-consuming model construction and solving procedures. In this case, measured data are crucial to inform FE models.

In a complete machine, the ac winding power losses are divided into two components, $P_{ac,e}$ and $P_{ac,r}$. In a motorette assembly, only the power loss component due to the current excitation $P_{ac,e}$, is present. The functional representation of the ac winding power loss temperature dependence for a complete machine presented in (2.4) can therefore be re-written for a motorette or stator assembly,

$$P_{ac|T} = P_{dc|T_0}\big(1 + \alpha(T - T_0)\big) + P_{dc|T_0}\frac{\left(\frac{R_{ac}}{R_{dc}}\right)_{e|T_0}{}^{-1}}{\big(1+\alpha(T-T_0)\big)^{\beta}} \qquad (5.7)$$

where $(R_{ac}/R_{dc})_e$ represents the ac-to-dc ratio for the analysed assembly. The complete machine slot arrangement and the number of coils present in the analysed hardware will

impact the representativeness of its $P_{ac,e}$ component. The 2D FE electromagnetic model has also been used to evaluate the core loss components. The adopted software makes use of the Steinmetz equation, [233],

$$P_{iron}(f,B) = \varepsilon_h f^a B^b + \varepsilon_e (fB)^2 \qquad (5.8)$$

Where B is the magnetic field, ε_h and ε_e represent the hysteresis and eddy-current loss coefficients. The Taylor series of the eddy-current power loss component includes the excess loss term. Therefore, (5.8) captures the excess loss component described in (2.7). First estimations of the core loss were obtained using manufacturer specific power loss data.

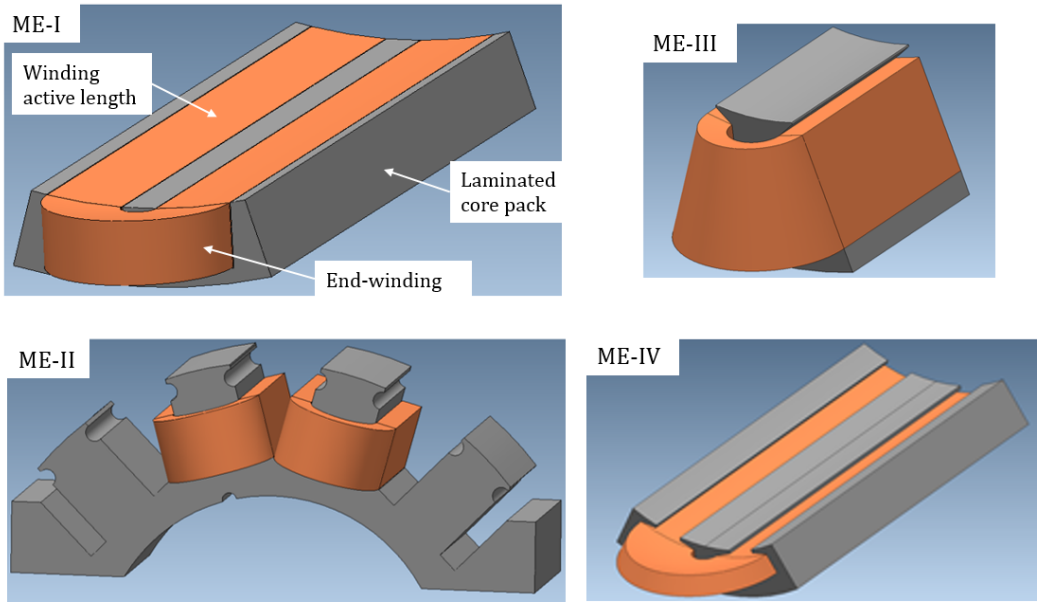

Fig. 5.16 Mathematical model representation of investigated MEs. ME-III requires neighbouring blank stator tooth segments for ac power loss analysis, as discussed in section 5.2.1.

5.4.3 Estimation of winding and core power loss parameters

Motorette testing can be used to evaluate various effects and material parameters associated with the winding and core power loss. Various approaches are presented for the estimation of these factors, depending on the confidence in the electromagnetic models and available data. For instance, both the winding and core power loss components may have been mathematically predicted prior to motorette testing, or on the contrary neither the winding nor the core power loss may have been estimated. The separation of the measured power loss at ac excitation into copper and iron loss components is discussed in this context. ME IV has been used to illustrate the proposed procedures for the derivation of the core and winding power loss parameters. Direct power loss tests have been conducted on ME IV

with a fixed winding current magnitude of 50 A_{RMS}, for an excitation frequency from 200 Hz to 1000 Hz and for temperatures from 20 ºC to 160 ºC. Furthermore, impedance analyser tests have been completed with a fixed winding current magnitude of 1 A_{RMS} at room temperature T_0 ~20 ºC.

Hysteresis and eddy-current core loss coefficients

In some cases, the confidence in the capability of the FE electromagnetic model to accurately predict the winding ac loss effects is relatively high compared to the one of the iron loss components. This is typically the case if the position of each conductor within the slot is well known, and the winding dc losses have been accurately predicted due to the calibration of the conductor conductivity using dc test data. The calculated ac and dc winding power losses can be subtracted from the total measured loss in order to identify the core loss components. The derived iron power loss data may then be compared to initial predictions from (5.8), and the hysteresis and eddy-current power loss coefficients ε_h and ε_e can be adjusted to provide a good match between the calculated and measured iron loss components.

Fig. 5.17 presents the measured, predicted and calibrated power loss data for all analysed frequencies for a winding and core temperature of 20°C, and at an ac current excitation of 50 A_{RMS}. The initial FE prediction shows more important measured core loss effects than calculated. The impact of manufacturing processes, such as the cutting of ME IV's core pack, may have caused some damages to the insulation coating and lamination material intrinsic properties.

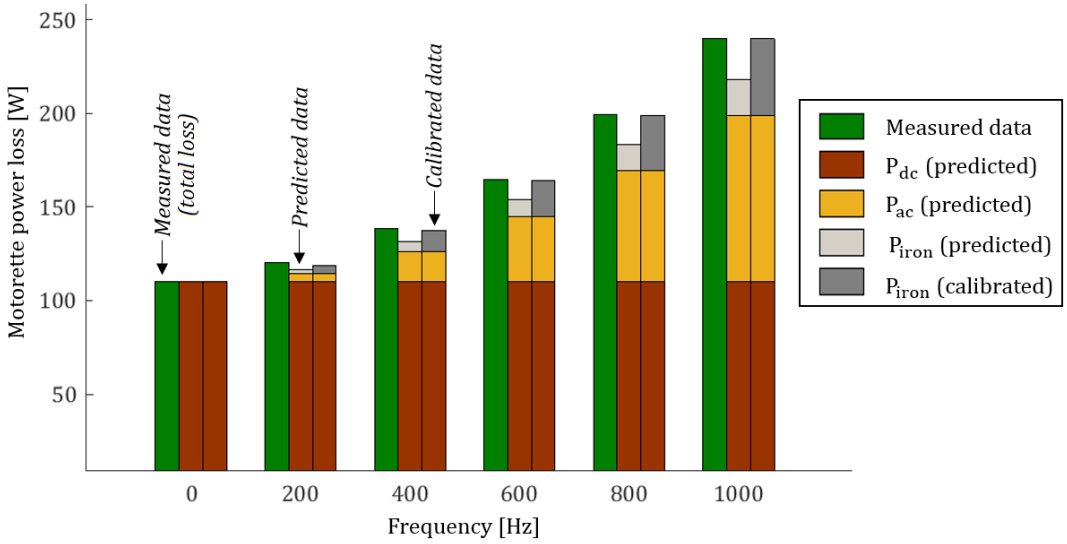

Fig. 5.17 Measured, predicted and calibrated data for winding and core temperature of 20°C and ac current excitation of 50 A_{RMS}

Eddy currents flow in closed loops, in planes perpendicular to the magnetic field, within conductors. By enabling contact between two laminations, damages on insulation coating would increase the effective loop area and would therefore lead to higher eddy-current loss. The hysteresis and eddy-current power loss coefficients ε_h and ε_e have been adjusted by comparing the measured data to (5.8). The original and calibrated iron loss coefficients are listed at Table 5.5, and the difference between the values emphasizes the need for some experimental estimation of the core loss components. The updated model predictions, Fig. 5.17, show a good match between the predicted and measured power loss data for all analysed frequencies. The software adopted for this analysis calculated the iron loss based on the Steinmetz equation, (5.8). For software where the iron losses are not directly calculated, (5.8) can be directly used for the derivation of ε_h and ε_e.

Table 5.5 Iron loss parameters estimation following ME test

Parameters	ε_h [$\times 10^{-4}$ W.Hz^{-a}.T^{-b}]	ε_e [$\times 10^{-5}$ W.Hz^{-2}.T^{-2}]
Model default parameters	90	3.24
Calibrated from ME measurement	178	7.14

For some stator-winding configurations, such as the randomly-wound round conductors used in M-III, the winding ac loss cannot be accurately predicted. Several possibilities exist for the derivation of the core power loss in this situation. The calibration of the ac winding and core loss components can be done simultaneously using the measured data from tests with ac excitation current. In this case, it is typically recommended to complete a series of tests at various excitation currents and frequencies to reduce the uncertainty associated with the estimation of several parameters in parallel. Alternatively, tests with ac excitation currents may be completed on a motorette core pack using a known winding arrangement, which is temporarily placed within the motorette slot [60]. Only the power losses are of interest in this context, and therefore the provisional ME does not have to be thermally representative of the complete machine assembly, e.g. presence of impregnation or slot liner. The temporary winding assembly has to be easily removed and replaced by the final winding arrangement once the tests have been completed. For these reasons, this test can be rapidly completed once the motorette core pack has been manufactured. The total measured power loss obtained from this test can be accurately separated using the method previously described. Depending on the machine excitation frequency range, windings formed with Litz wires may be a judicious choice of temporary winding arrangement. Indeed, if the Litz wires are appropriately selected, the ac winding power loss might be negligible, further simplifying the power loss separation. Likewise, a search coil could be used to derive the core power loss [229].

Manufacturing-related issues are generally identified from measurements, e.g. it is impossible to obtain a good match between measured data and (5.8) when tuning ε_h and ε_e. For instance, the results from MEs III impedance and direct power tests have shown significantly elevated power loss at ac operation. Additional tests with a coil formed with Litz wire were completed to identify the source of these high power losses. The ME core pack was found to be the origin of the abnormal losses. The manufacturing approach adopted in the University workshop for the lamination stack cutting is expected to have caused damages to the laminations. Indeed, a bead of weld was included down the length of the blank lamination stacks used to produce the other analysed MEs, but was not present on the stack used to produce ME III. This conduction path ensures the through-stack electrical conductivity, and is known to prevent lamination insulation damages. Therefore, its absence would have led to elevated iron losses. MEs III data unfortunately had limited use for the ac power loss analysis, and are therefore not provided here.

Estimation of ac-to-dc ratio

Motorette exemplars can also be used to evaluate the winding power loss at dc and ac operation. As previously discussed, the winding power at ac operation only includes P_{dc} and $P_{ac,e}$ for ME testing due to the absence of the rotor assembly. Thus, an ac excitation-to-dc ratio $(R_{ac}/R_{dc})_e$ can be derived from ME tests, by normalising the total winding power loss at ac excitation by P_{dc} obtained for $I_{dc} = I_{RMS}$. The comparison of $(R_{ac}/R_{dc})_e$ ratio obtained from tests on two different MEs provides first insight into the capability of both alternatives. The MEs configurations have to be identical in this case, e.g. same numbers of coils and slots. This will ensure that the same power loss effects are accounted for, e.g. impact of neighbouring coils. For example, ME II comprises two coils in series, so its measured $(R_{ac}/R_{dc})_e$ ratio accounts for some neighbouring effects, while the $(R_{ac}/R_{dc})_e$ ratio obtained for MEs I and IV should be similar to the ones of the complete machine M-I and M-IV, respectively, due to the magnetic isolation of each coil and slot for these two fault-tolerant designs. The representativeness of ME derived data compared to complete stator will be discussed in Chapter 6.

Fig. 5.18 presents the frequency variation of the winding ac loss obtained for impedance analyser tests using $(R_{ac}/R_{dc})_e$ ratio for a number of analysed MEs. The measurements were performed at a room temperature of ~20°C. Fig. 5.18a) shows that there is no significant difference between MEs I and I* in terms of winding power loss. Fig. 5.18b) shows the difference of $(R_{ac}/R_{dc})_e$ ratio between aluminium and copper, with the magnitude of the ac winding loss found to be approximately 15% lower in the case of the

windings formed with aluminium conductors for excitation frequencies higher than 500 Hz. Finally, ME IV shows more than 30% lower $(R_{ac}/R_{dc})_e$ ratio than ME IV* for excitation frequencies higher than 600 Hz, Fig. 5.18c). This confirms the initial FE results, which predicted that the presence of a slot wedge would lead to a valuable decrease of winding ac losses.

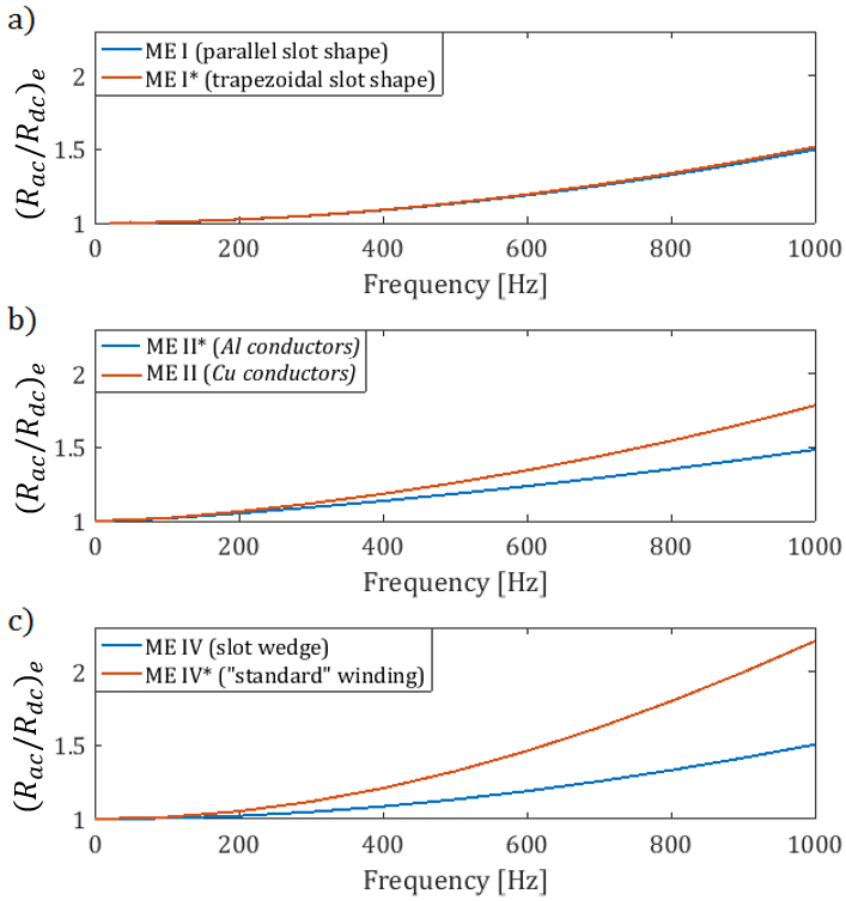

Fig 5.18 $(R_{ac}/R_{dc})_e$ratio vs. excitation frequency obtained from impedance analyser tests at T_0 ~20°C, a) MEs I and I*, b) MEs II and II*, c) MEs IV and IV*

A direct computation of the ac winding loss at a given temperature for consecutive iterations of thermal analysis would be computationally prohibitive. ME testing allows the evaluation of the thermal dependence of ac winding loss due to current excitation. The temperature coefficient for the ac loss component β can be derived from a curve fit of (5.7) to the winding ac loss data derived from electromagnetic FE analyses or measurements at two reference temperatures, e.g. 20ºC and 180ºC, which are the minimum and maximum winding temperatures, respectively, intended for a particular machine operation. Fig. 5.19 presents the $(R_{ac}/R_{dc})_e$ ratios at different temperatures for direct power loss excitation for ME IV. As expected, $(R_{ac}/R_{dc})_e$ decreases with temperature. Here, and in general, dc winding power losses are dominant, and therefore the overall winding loss components

typically increase with temperature. A value of β of 0.6 has been obtained from curve fitting (5.7) using ME IV's measured data. Here, it has been assumed that end-winding and active length temperature dependence is the same. However, if necessary, it is possible to obtain different β for the end-winding and active length regions.

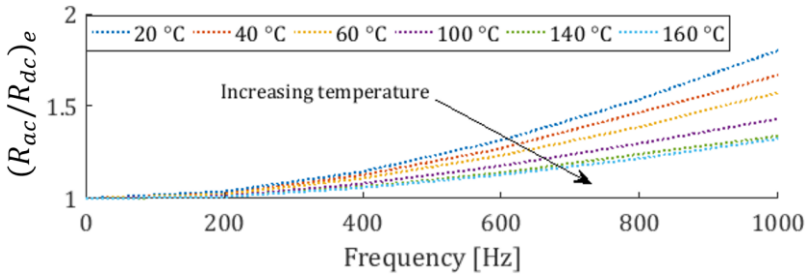

Fig. 5.19 Measured $(R_{ac}/R_{dc})_e$ ratios at different temperatures for direct power loss excitation, I_{RMS}=50 A vs frequency – ME-IV

Motorette testing allows the evaluation of the power loss effects associated with the end-windings. The numerical estimation of these effects would require the use of a 3D FE model and could lead to prohibitively long model setting-up and solving time, as each conductor should be represented for a reliable derivation. In particular, the end-winding ac power losses are expected to be very close to the one of a complete machine, as they are not exposed to the rotating magnetic flux from the air gap the same way as the winding active length. Two approaches are typically used in power loss analysis of electric machines: the end-winding ac losses are neglected, or the winding ac losses are homogenised for the entire winding region. In the latter, the ac winding power loss are underestimated for the active length, and overestimated for the end-winding. Fig. 5.20a) presents a separation between end-winding and active length $(R_{ac}/R_{dc})_e$, obtained from the 3D electromagnetic model of ME IV, together with the total winding ac power loss. For an excitation frequency of 1000 Hz, the end-winding power loss factor is equal to 1.2. Consequently, depending on the required model fidelity, neglecting this parameter may not be acceptable. The data shown in Fig. 5.20a) confirm that using the averaged complete winding power loss data would lead to an underestimation and an overestimation of the active length and end-winding ac effects, respectively.

A good understanding of the power loss repartition within the stator winding region is crucial to ensure the accuracy of the electromagnetic and thermal mathematical models. Calibrated numerical electromagnetic models can provide detailed power loss distribution solutions, which allow thermal designers to choose the appropriate level of complexity of their thermal or electromagnetic models, e.g. homogenised winding or representation of each conductor. Fig. 5.20b) presents the frequency variation of the winding ac loss,

calculated using FEA for the upper and lower layers of the Litz winding of ME I. The calculated data indicates that most of the ac losses are confined to the upper layer of the winding where the slot leakage fluxes are highest. The inhomogeneous repartition of the ac winding loss should be accentuated for the complete machine, as the PM rotor induced ac winding losses are expected to be confined to the upper regions of the windings. In this case, more accurate results can be obtained by representing the winding into two separate layers in the thermal and electromagnetic mathematical models.

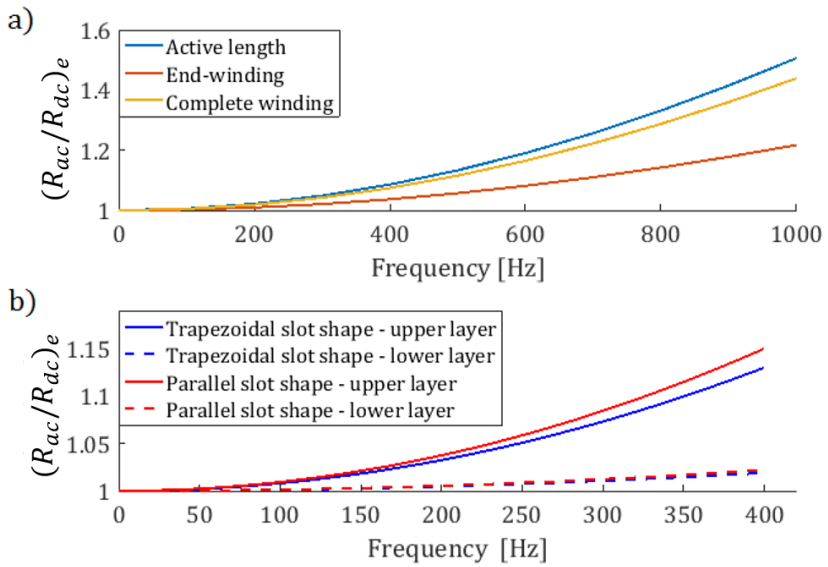

Fig. 5.20 a) Calculated active length and end-winding $(R_{ac}/R_{dc})_e$ ratios at 20 ºC and I_{RMS} =50 A for direct power loss vs frequency, b) Calculated $(R_{ac}/R_{dc})_e$ ratio vs. excitation frequency obtained from 3D FEA at T_0~20°C for MEs I and I*

5.5 Summary

This Chapter has presented the second building step of the proposed methodology, which utilises tests on motorette exemplars to evaluate selected thermal and power loss parameters of the stator-winding assembly. A systematic procedure has been presented for the estimation of the winding-to-stator thermal contact resistance. The impact of thermal sensor locations and quantity has been thoroughly analysed. Fig. 5.21 presents a schematic diagram summarising the proposed procedures for thermal analysis, together with the nomenclature used. A library of winding-to-stator thermal contact resistance data from all investigated MEs was also established. Furthermore, motorette testing has been used to evaluate various effects associated with the winding and core power loss. Various procedures have been introduced for the estimation of these effects, depending on previously available data and confidence in the electromagnetic models. Fig. 5.22 presents a schematic diagram summarising the proposed procedures for power loss analysis, together with the nomenclature used.

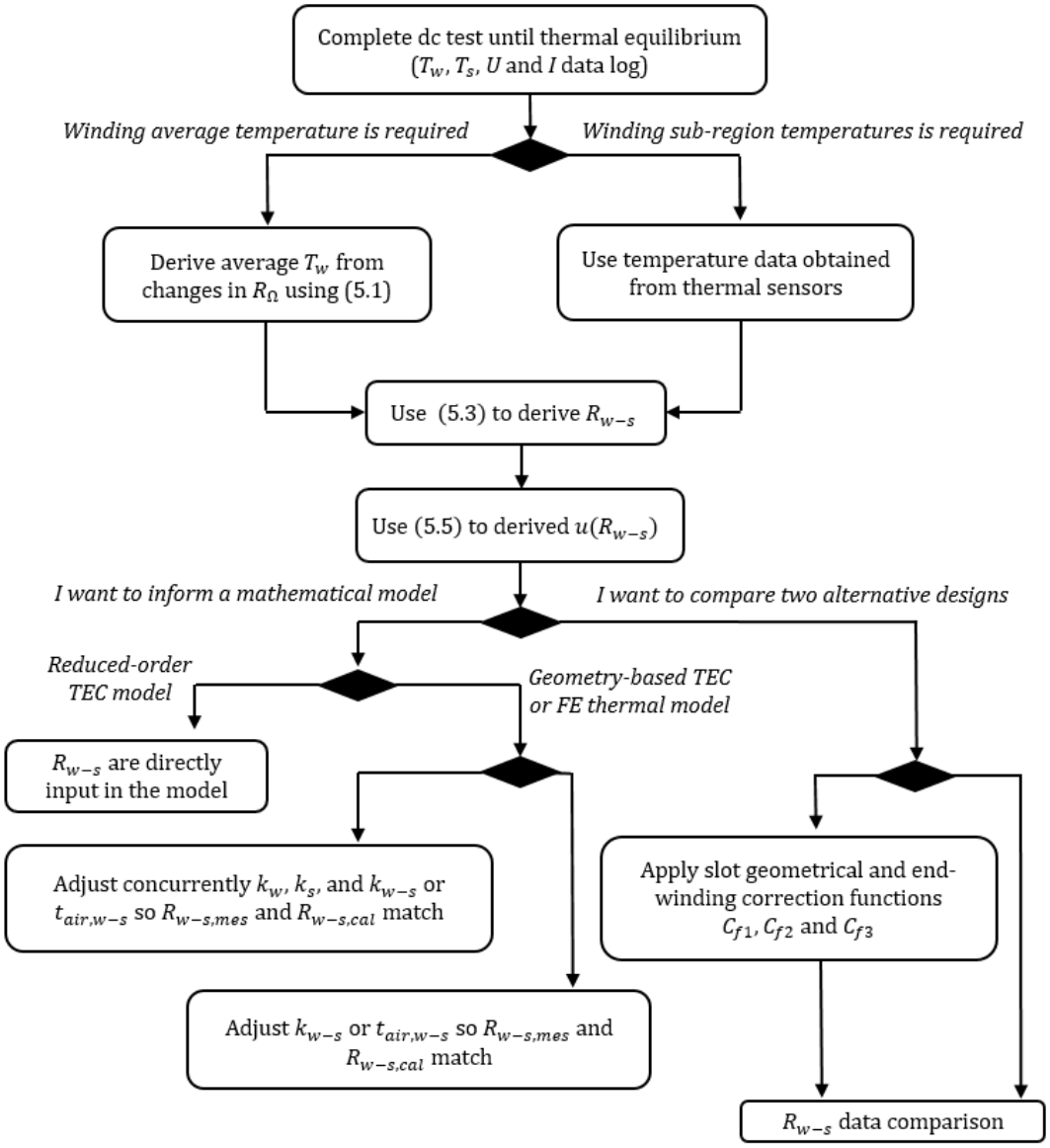

Fig. 5.21 Schematic diagram summarizing proposed systematic procedure for thermal analysis, T_w and T_s (winding and core temperatures), U (voltage), I (excitation current), R_Ω electrical resistance, R_{w-s} (winding-to-stator contact thermal resistance), k_w, k_s and k_{w-s} (winding core and slot liner region equivalent thermal conductivity), $t_{air,w-s}$ (equivalent slot liner air cavity thickness).

The separation between winding active length and end-winding ac power loss, and the impact of winding inhomogeneous loss distributions have also been discussed. The data derived in this section have been used to complete coupled thermal and loss analysis for the various MEs. The results of these analyses will be discussed in Chapter 7 as an illustration of the proposed methodology.

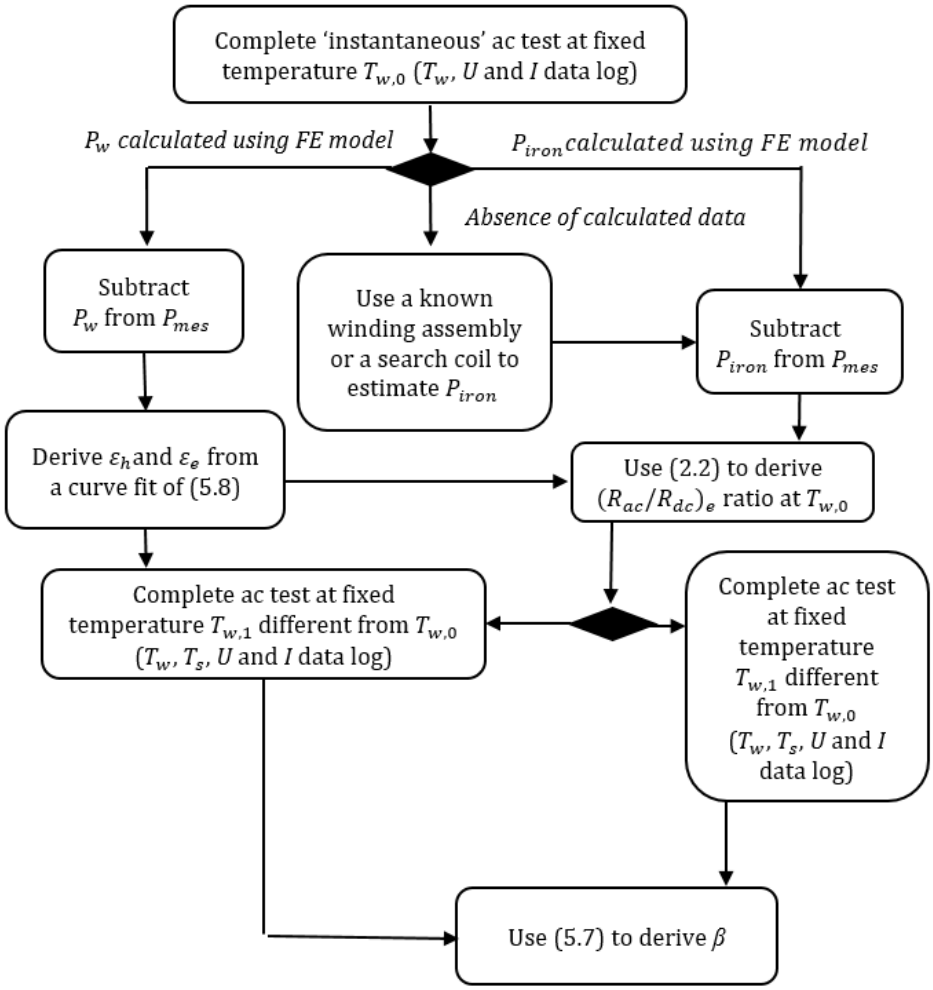

Fig. 5.22 Schematic diagram summarizing proposed systematic procedure for thermal analysis, T_w(winding temperature), U (voltage), I (excitation current), P_w and P_{iron} (winding and core power loss components), P_{mes} (total measured power loss), $(R_{ac}/R_{dc})_e$ (ac-to-dc ratio due to current excitation), ε_h and ε_e (hysteresis and eddy-current power loss components), β (winding ac loss temperature dependence para

Chapter 6 Stator assembly

6.1 Introduction

The third building block of the proposed methodology utilises tests on complete stator exemplars (SEs) for deriving thermal and power loss parameters. An advantage of testing stator assemblies is that it provides a good insight into the repeatability of the complete manufacturing and assembly process employed. As in the case of motorette hardware, dc thermal tests can be employed to derive thermal contact resistances and heat capacitances associated with the stator-winding region. The stator assembly can also be analysed after inserting it into the housing frame structure. The presence of the housing allows the estimation of additional thermal parameters, such as the stator-to-housing thermal contact resistances or convection heat transfer coefficients associated with the housing frame. In that respect, testing a housed stator is more beneficial than testing a stator core pack with the winding in place only.

A further advantage of tests on stator assemblies is that it allows for the interaction between phases to be accounted for. Unlike motorette testing, stator tests are more representative of a complete machine assembly when experimentally deriving ac winding power loss due to current excitation. Experimental approaches commonly involve ac tests with three-phase current excitation. Ac tests with one-phase excitation may be performed in parallel. The comparison between the results obtained from the three-phase analysis and one-phase analysis allows the proximity effects induced by a single phase to be separated from the one induced by its neighbouring phases. This provides a better understanding of the individual loss mechanism, which is valuable in the context of an overall winding loss reduction.

The theoretical thermal and power loss analyses discussed in this Chapter have been supplemented with experimentally derived data from several stator exemplars. Where appropriate, the data from experimentation on the complete stator assemblies has been correlated with results from the previous Chapters, i.e. material samples testing (MSs) and motorettes testing (MEs), Chapter 4 and Chapter 5, respectively.

6.2 Complete stator-winding hardware exemplars

6.2.1 Complete stator assemblies under analysis

The analysed hardware includes three stator exemplars representing machines M-I, M-III and M-IV. Machine M-II has been manufactured under stringent time limits, and consequently no experimental data could be collected at the prototyping stage for the stator-winding assembly. The power loss and thermal behaviours of SE-II are nonetheless investigated through FE analyses and data obtained from the first and second building block of the proposed methodology. All stator-windings analysed here were housed prior to the instrumentation of the complete assemblies with thermal sensors and impregnation of the windings. Having complete stators allows for the investigation of additional thermal parameters, such as the stator core-to-housing thermal contact resistance. All SEs are tested before machine assembly. The specifications of the SEs' assembly are provided in Tables 3.1 to 3.4. Fig. 6.1 shows the analysed SEs with the main assembly regions indicated. It should be noted that the numbering for the individual stator exemplars (SEs) and the motorettes (MEs) is identical.

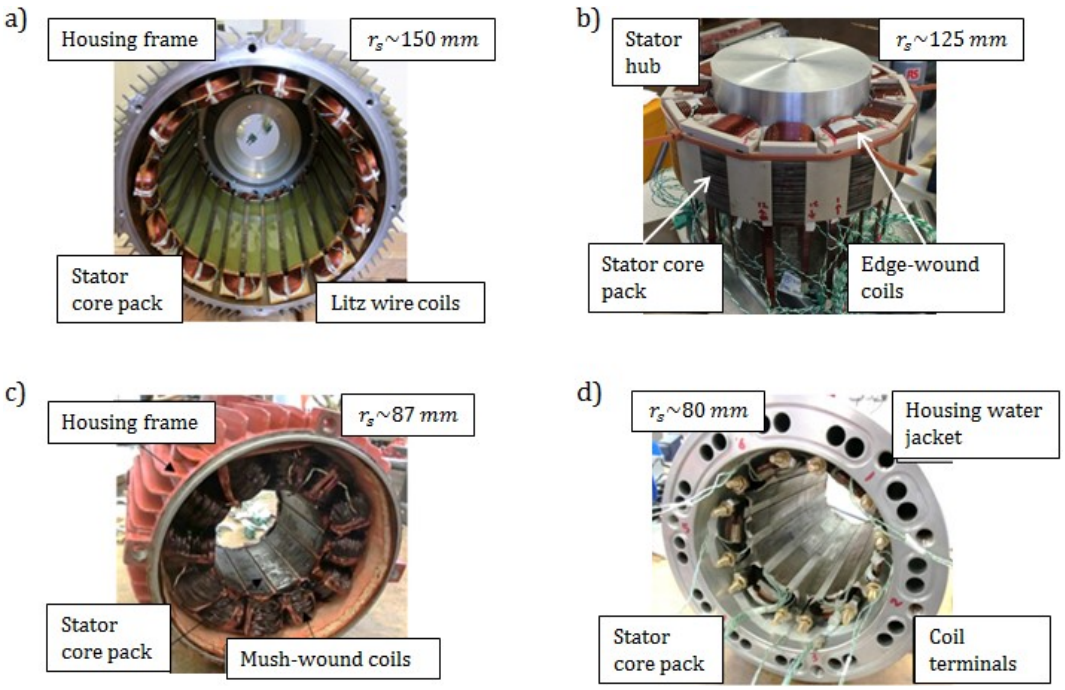

Fig. 6.1 Complete stator assembly after impregnation, with sub-assembly regions highlighted, a) stator exemplar I – (SE-I), b) stator exemplar II – (SE-III), c) stator exemplar III – (SE-III), d) stator exemplar IV (SE-IV)

6.2.2 Stator fabrication

The manufacturing process of the stator core pack and the winding assemblies is similar to the one described in Chapter 5, where the fabrication of the motorette hardware was discussed. However, the individual stator housing arrangements are specific to the intended application of each analysed machine. In general, the role of the housing frame is to provide a reaction torque through suitable anti-rotation features, protect the active components from the external environment, and ensure adequate cooling via fins or liquid cooling jacket. The technique used for all SEs when inserting the stator core pack into the housing was heat-shrinking. Such an approach involves preheating the housing in order to allow for a clearance between the stator outer diameters and the housing bore diameter, which are designed to have interference fit at ambient temperature. This provides sufficient pressure between the assembly parts to ensure adequate reaction torque and good heat transfer across. Several literature references investigated the optimum shrink-fit pressure with regards to the coefficient of friction or the thermal contact conductance [158], [228]. On the one hand, the pressure has to be high enough to maintain the required holding torque and ensure a good thermal contact between the stator core and the housing frame, as discussed in Chapter 2. On the other hand, an elevated pressure on the stator core pack might lead to a deterioration of the magnetic properties, e.g. reduction in magnetic saturation level, increase of core power loss or core pack mechanical deformation [158].

6.3 Thermal analysis

6.3.1 Experimental set-up

A series of short-transient and steady-state thermal tests with dc excitation of the stator-winding assembly have been carried out. In these tests, the stator windings are connected in series and excited with controlled levels of dc current. The measured power loss and winding and core temperatures are logged using a data acquisition system until thermal equilibrium is reached. Figs. 6.2a) and 6.2b) present the experimental setups used for forced liquid-cooled and natural air-cooled complete stator tests.

The testing procedure for the stators with liquid-cooling, Fig. 6.2a), is similar to motorette testing, since the heat generated within the winding body is conducted across the laminated core pack assembly through the housing frame. This allows for a well-defined, unidirectional, heat path from the heat source to the heat sink. The coolant is pumped through the stator jacket assembly to ensure an even temperature distribution around the core pack periphery.

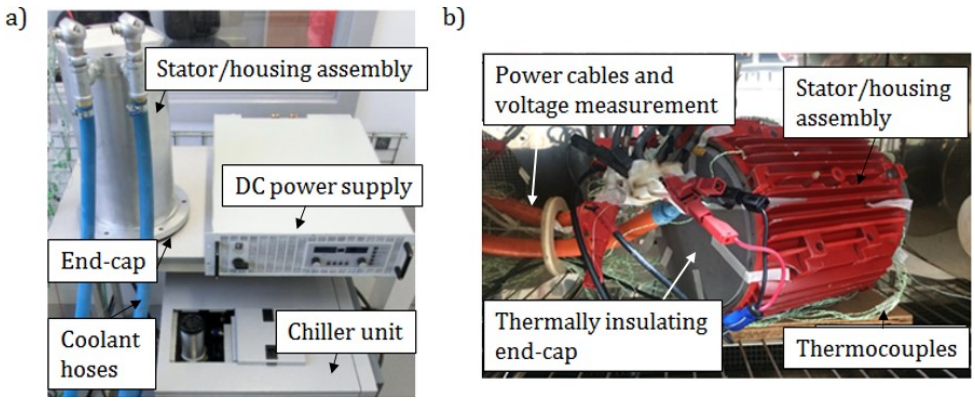

Fig. 6.2 Experimental set-ups for stator dc test, a) Forced-cooled assembly, SE-IV, b) Naturally-cooled assembly, SE-III.

Fig. 6.2b) presents an instrumented, naturally-cooled stator assembly placed in an environmental chamber with fixed temperature during a dc test. The use of the environmental chamber allows setting well-defined conditions for the ambient air. A plain cylinder and two end-caps made of thermally insulating material (Zotek N with a thermal conductivity k=0.045W/(m.°C) @130 °C [229]) have been built and placed inside the stator air gap and on the end-windings. This set-up has been adopted when deriving the winding-to-stator and stator-to-housing thermal contact resistances. By limiting convective heat extraction from the stator periphery other than the housing frame, such as the end-winding and stator air gap regions, the set-up ensures a well-defined heat path from the winding to the housing. The stator assembly is usually tested without thermally insulating material [159], [170], [184], [230]. A series of tests have been completed, where the thermally insulated materials have been removed. The test results will illustrate the impact of the various heat extraction paths on the estimation of the winding-to-stator thermal contact resistance, e.g. winding active length-to-housing frame and winding active length-to-end-windings.

6.3.2 Mathematical models and parameter derivation

The mathematical methods available for complete stator analysis include thermal equivalent circuit (TEC) and FEA. The model representation is similar to the one used for the motorette analysis, where the interfacing plate used for motorette testing is replaced with the stator housing frame. Convective heat transfer coefficients are used to model natural or forced air cooling, while fixed temperature boundary conditions are adopted to represent a water jacket cooling apparatus.

Appropriate estimation of the winding-to-stator thermal contact resistance R_{w-s} and the winding thermal capacitance C_w is crucial when evaluating the winding thermal behaviour.

In particular, C_w represents the heat storage within the winding assembly, and therefore impacts the transient temperature of the winding. In Chapter 5, a method for estimating R_{w-s} using motorette exemplars has been introduced. This Chapter further develops the subject and proposes an experimental method for deriving the winding thermal capacitance C_w.

The existing 'short-transient' method available for deriving the winding thermal capacitance C_w uses data recorded only for a couple of minutes at the beginning of the transient [159], [170], [230]. This is due to a number of assumptions, such as isothermal core pack, which reduces the method applicability and accuracy. The method introduced in this Chapter for the derivation of the winding capacitance C_w is based on data recorded until thermal equilibrium. To evaluate this 'steady-state' method, a comparison will be made with the existing 'short-transient' approach. Since the existing approach focuses exclusively on stator exemplars, the comparison will be performed using data from tests on stator exemplars. However it should be noted that the proposed approach is also applicable to motorette assemblies. The applicability of the proposed approach for motorette testing has been documented in the conference paper [231] listed in the publications associated with this thesis.

Fig. 6.3 presents the reduced-order TEC adopted for the method comparison, together with the nomenclature used. Here, *R, P, T,* and *C* are the thermal contact resistance, power loss, temperature and heat capacity, respectively. The subscripts *w, s, h,* and *a* correspond to the winding, stator core, housing, and ambient, respectively. As both the existing and proposed methods focus on deriving the equivalent winding thermal capacitance, C_w, and stator-to-winding thermal resistance, R_{w-s}, only a portion of the equivalent thermal network bordered by the red box is considered, Fig. 6.4. From Fig. 6.4, the equivalent thermal network highlighted with a red box can easily be used in the context of motorette analysis.

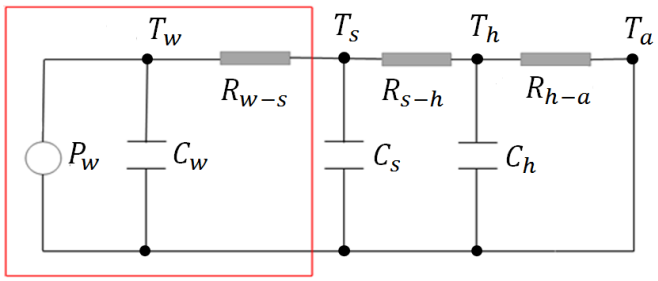

Fig. 6.3 Equivalent TEC of the naturally air-cooled stator assembly experiment apparatus. The circuit of interest is highlighted with a red box.

The winding dc power loss is expressed as follow,

$$P_w(t) = U(t)\, I_{dc} \qquad (6.1)$$

where *t* represents the time. Applying the Energy Conservation Law to the circuit in the red box in Fig. 6.3, the following equation is obtained:

$$P_w(t) = C_w \frac{dT_w}{dt} + \frac{T_w(t) - T_s(t)}{R_{w-s}} \qquad (6.2)$$

Here, C_w and R_{w-s} are assumed to be constant values, independent of temperature. Equation (6.2) is not limited to stator testing, as the housing is not part of the investigated circuit, and could be derived in a similar manner for motorette analysis. Solutions have been derived for (6.2), with the steps of the mathematical derivation provided in Appendix E. A discrete form of the solution of (6.2) is given as follows:

$$T_{w,k+1} = T_{w,k} + \frac{1}{1+\frac{R_{w-s}\, C_w}{t_{k+1}-t_k}} (T_{s,k} + R_{w-s} P_{w,k} - T_{w,k}) \qquad (6.3)$$

The existing 'short-transient' method uses a discrete formulation comprising the exponential function. If (6.4) is true, i.e. if the recording frequency is high enough so that $t_{k+1} - t_k \ll R_{w-s}C_w$, then the following solution is obtained from the power series of the exponential function, (6.5).

$$(t_{k+1} - t_k) = o(R_{w-s}C_w) \qquad (6.4)$$

$$T_{w,k+1} = T_{w,k} + (T_{s,k} + R_{w-s} P_{w,k} - T_{w,k})(1 - e^{-\frac{t_{k+1}-t_k}{R_{w-s}C_w}}) \qquad (6.5)$$

The existing and the proposed approaches are based on different assumptions and the uses of the (6.3) and (6.5). The existing 'short-transient' method is based on the assumption that the stator core pack is isothermal during dc tests, and thus only uses recorded data where the averaged stator lamination temperature rise is lesser than 1°C. Due to the isothermal assumption, the stator core temperature T_s is replaced by the initial temperature T_0 in (6.5) when deriving the thermal parameters. The 'short-transient' approach also requires the dc test to start when the experimental apparatus is at thermal steady-state, i.e. all hardware sub-regions are approximately at the same temperature T_0. In this case, T_w-$T_s = \Delta T_{w-s} \approx 0$, and (6.2) becomes:

$$P_w(t) = C_w \frac{dT_w}{dt} \qquad (6.6)$$

By combining (6.1) and (6.6), the following expression is obtained,

$$C_w = \frac{U(t).I_{dc}.dt}{dT_w} = \frac{dW}{dT_w} \quad (6.7)$$

In practice, C_w is derived from (6.7) using linear regressions between the thermal energy W and the averaged winding temperature T_w. Only a limited sample of the measured data is used for the derivation of C_w to ensure that $\Delta T_{w-s} \approx 0$. The existing work suggests performing the short-duty thermal tests with dc winding excitation, such that winding temperature rise does not exceed 1°C [159], [170], [230]. Once C_w is derived, R_{w-s} is obtained by curve-fitting (6.5) to the measured winding temperature.

The proposed steady-state approach makes use of the temperature and power measurements from tests completed until thermal equilibrium is reached. The method based on thermal data at thermal steady-state presented in Chapter 5 is used for the derivation of R_{w-s}. As described in section 6.3.1, the stator end-winding and inner regions should be thermally insulated to isolate the heat path from the winding to the housing frame. This thermal isolation would ensure accurate parameter derivation. Once R_{w-s} is estimated, C_w can be evaluated from curve-fitting (6.3) using the entire set of recorded data.

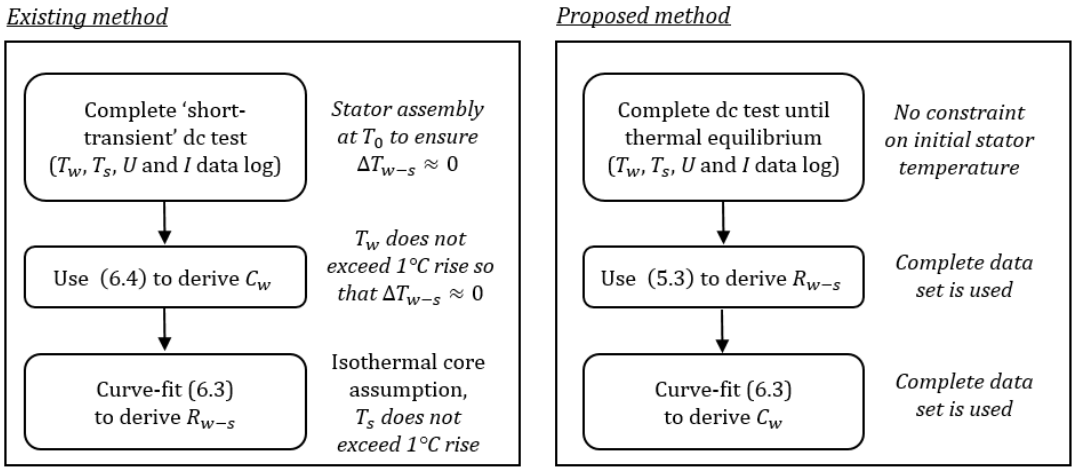

Fig. 6.4 Schematic diagram summarizing the existing and proposed methods for thermal parameter derivation, T_w and T_s (winding and core temperatures respectively), U (voltage), I (excitation current), R_{w-s} (winding-to-stator contact thermal resistance), C_w (winding thermal capacitance)

Fig. 6.4 presents a schematic diagram summarising the proposed procedures for thermal analysis, together with the nomenclature used. The existing 'short-transient' approach has been developed for fast testing, and is adequate when analysing a known machine assembly, e.g. inspection of mass-volume manufactured machines. However, when no information is available beforehand on the machine geometry or on the expected thermal

parameters, a series of thermal tests should be completed to gain confidence into the derived data. The requirement of the same temperature for the core pack and winding assemblies forces the designer to wait until the investigated assembly returns to thermal equilibrium before starting a new test. Therefore, the total testing time is only slightly shorter than the one of steady-state tests, but with the acquisition of a significantly lower amount of valuable data. The proposed 'steady-state' method does not require the core pack and winding regions to be at the same temperature when starting the test, and therefore a series of dc tests can be performed without the need to return to the initial temperature conditions. Moreover, the use of steady-state data should provide more insight into the stator thermal behaviour, in particular for the derivation of the winding-to-stator thermal contact resistance R_{w-s}.

Stator assembly testing also allows the estimation of the stator-to-housing thermal contact resistance. This parameter has a crucial influence on the machine hot-spot temperature, in particular for machines where the heat is extracted from the winding to the housing frame [158]-[164]. The derivation of the stator-to-housing and housing-to-ambient thermal resistances, R_{s-h} and R_{h-a}, has not been investigated in the existing 'short-transient' approach, and is therefore not discussed in the context of this comparison. The approach adopted for the derivation of R_{s-h} and R_{h-a} is similar to the one presented in Chapter 5 for the estimation of R_{w-s}, and makes use of steady-state thermal data obtained from dc tests.

6.3.3 Comparison of methods

This section explores the available approaches for the derivation of R_{w-s} and C_w. SE-III has been selected for the illustration and comparison of the investigated methods. SE-III's stator phases are referred to as phase-a, phase-b and phase-c, with each phase comprising four coils. The data derived from the tests on motorette assemblies are compared with the data from stator tests. For simplicity, ME III-a, ME III-b and ME III-c are referred to as ME-a, ME-b and ME-c, respectively. The experimental data from thermal tests on the motorette assemblies have been adjusted to account for any difference in active length between the motorette and the stator hardware, where appropriate. For instance, ME III's core packs are 10 mm shorter than SE-III's active length due to tooling restrictions. A scaling factor $R_{\Omega,scale}$ is applied when comparing motorette and complete stator data, allowing one to account for difference in active length Ohmic resistance R_Ω. Here, $R_{\Omega,scale}$=0.9474.

Winding-to-stator thermal contact resistance

Table 6.1 lists the per slot Ohmic resistance of the winding R_Ω, and winding-to-stator thermal contact resistance R_{w-s} obtained from (5.3) for the studied hardware exemplars. It shows a good correlation between data derived from tests on motorette and stator hardware. The stator coil resistances are slightly higher than the motorette ones, which may result from the leads used for the coil connection within the stator regions.

Table 6.1 Measured per slot electrical and thermal contact resistances – SE-III

	ME-a	ME-b	ME-c	phase-a	phase-b	phase-c
R_Ω @ 23°C [mΩ]	1.37	1.46	1.47	1.50	1.76	1.79
R_{w-s} [°C/W]	1.79	2.06	2.22	2.03	1.98	2.20

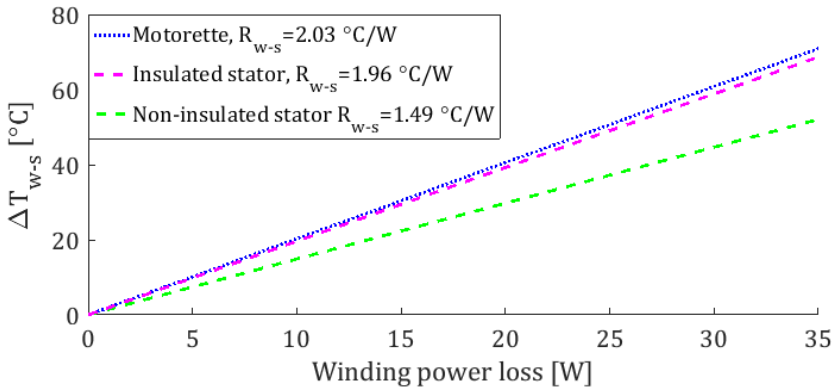

Fig. 6.5 Motorette, insulated and non-insulated stator – ME III and SE-III

A series of tests has been completed where the thermal insulation material has been removed to illustrate the importance of isolating a particular heat transfer path. The set-up comprising thermal insulation material is referred to as "insulated stator", while the set-up without thermal insulation material is referred to as "non-insulated stator". Fig. 6.5 shows the R_{w-s} values obtained from the motorette, "insulated stator" and "non-insulated stator" hardware. On the one hand, the winding-to-stator thermal contact resistances obtained for the motorette and the "insulated stator" correlate well. On the other hand, that of the "non-insulated stator", is significantly lower than of the 'insulated stator', which confirms that a non-negligible amount of heat is dissipated from the stator end-windings and through the air gap.

Table 6.2 lists the measured winding-to-stator thermal contact resistances for the analysed baseline SEs and MEs, referred to as $R_{w-s,SE}$ and $R_{w-s,\ ME}$, respectively. When the stator testing conditions are well-defined, e.g. 'insulated stator' (SE-III) or liquid cooled housing (SE-IV), the motorette and stator derived data correlate well. The minor difference between

ME-IV and SE-IV derived data can be justified by manufacturing variations: the epoxy resin has been warmed up before impregnation when manufacturing SE-IV, unlike ME-IV manufacturing. Heating epoxy resin reduces its viscosity, which can facilitate the air extraction during the vacuum impregnation procedure, and therefore can improve the impregnation goodness and thermal contact. When less defined testing conditions are adopted, e.g. 'non-insulated' stator (SE-I), a larger discrepancy is observed between SE and ME derived data. The use of motorette or 'insulated' stator assemblies is therefore recommended for the derivation of the winding-to-stator thermal contact resistances R_{w-s}.

Table 6.2 Measured winding-to-stator thermal contact resistances for all analysed baseline SEs and MEs

SE	I	II	III	IV
$R_{w-s,\ SE}$ [°C/W]	0.028	-	0.163	0.017
$R_{w-s,\ ME}$ [°C/W]	0.036	0.11	0.168	0.019

Winding thermal capacitance

A number of theoretical and empirical methods are available to estimate the winding capacitance [156], [164]. An analytical formula based on the mass *m* and specific heat capacity c_s for the constituent winding materials is defined as follows,

$$C_w = m_c c_{s,c} + m_{ci} c_{s,ci} + m_i c_{s,i} \qquad (6.8)$$

where the subscripts *c*, *ci* and *i* correspond to the conductor, conductor insulation and impregnation, respectively. The mass of conductors and electrical insulation can be estimated based on manufacturer data and electrical resistance measurements. To assess the amount of impregnating material within the stator slots, the equivalent winding sample should be weighted before and after impregnation.

In Chapter 4, a method for the estimation of the equivalent winding heat capacitance $c_{s,w}$ has been presented. If $c_{s,w}$ is available, then the winding heat capacitance C_w can be calculated using the following formula:

$$C_w = m_w c_{s,w} \quad (6.9)$$

where m_w is the total weight of the winding amalgam. Table 6.4 summarises basic data for the SE-III's winding amalgam materials. Basic data associated with epoxy resin are also included, for completeness. Reference [231] specifies values of varnish specific heat capacity between 1200 and 1900 J/(kg.°C). A sensitivity analysis has been completed,

showing that a change of $c_{s,i}$ from 1200 to 1900 J/(kg.°C) would result in less than 2% difference in C_w. Therefore, $c_{s,i}$ is assumed to be 1400 J/(kg.°C) in this analysis. The winding thermal capacitances estimated using (6.9) and measured data from material sample WS-III is referred to $C_{w,WS}$, while the one using (6.8) and material data from Table 6.3 is designated as $C_{w,cal}$. These parameters show good correlation, with $C_{w,WS}$=2014 J/(kg.°C) and $C_{w,cal}$=2084 J/(kg.°C), respectively.

Table 6.3 Basic data for winding amalgam materials

Property	Copper conductor	Enamel	Varnish [231]	Epoxy resin
c_s [J/(kg.°C)]	386	1000	1200-1900	1700
m (ME III-a) [g]	384	0.04	10	-

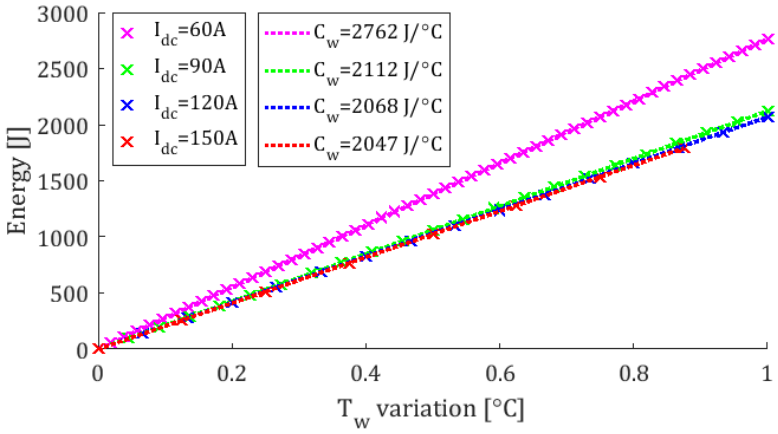

Fig. 6.6 Thermal energy vs. averaged winding temperature increase for SE-III

The existing 'short-transient' method has been used to calculate C_w. Fig. 6.6 presents measured and interpolated values for the winding thermal energy against averaged winding temperature increase data for SE-III. The slope of the individual plots, dW/dT_w, represents the equivalent C_w, as expressed in (6.7). The C_w values calculated from the data obtained at different I_{dc} correlate well with $C_{w,WS}$ and $C_{w,cal}$, apart from the calculated values at I_{dc}=60 A. This may seem slightly counter-intuitive: more time is needed for T_w to increase by 1°C at lower current amplitude than at higher current amplitude, so more measured points are available and thus the prediction of the winding capacitance was expected to be more accurate in this case. It has also been observed that if a constraint of 0.5°C or 2°C instead of 1°C was imposed on the winding temperature rise, values of C_w would be significantly dissimilar to those presented in Fig. 6.7, for all current excitation levels. This would be particularly prominent at lower current amplitudes. These observations can be explained considering the discrete expression of the winding thermal capacitance C_w, derived in Appendix E, (6.10).

$$C_w = \frac{(P_{w,k+1} - \frac{(\Delta T_{w-s})_k}{R_{w-s}})\Delta t_{k+1}}{T_{w,k+1} - T_{w,k}} \qquad (6.10)$$

where,

$$(\Delta T_{w-s})_k = T_{w,k} - T_{s,k} \qquad (6.11)$$

and Δt is the time step. Analysing (6.10), it is clear that the error made by assuming that $(\Delta T_{w-s})_k \approx 0$ will have more impact for lower $P_{w,k+1}$, i.e. lower excitation current, than for higher $P_{w,k+1}$. This explains the discrepancy between values at 'high' (I_{dc} ≥90A) and 'low' (I_{dc} =60A) current excitations observed in Fig. 6.6, and highlights the limitation of the existing short-transient method. In comparison, the proposed approach accounts for the difference between core and winding temperatures, and consequently represents a more reliable alternative.

Table 6.4 shows the measured winding heat capacitances for the analysed baseline material samples (MSs) and SEs. For the baseline machine M-I, M-III and M-IV, the winding thermal capacitance data obtained from SE and MS test data are referred to as $C_{w,\ SE}$ and $C_{w,\ MS}$, respectively. The derived C_w data from SE-III and SE-IV correlate well with data obtained from their associated MSs, while data obtained from SE-I are slightly higher than the ones derived from MS I. An explanation is that, unlike the stator assembly, the winding sample has been impregnated twice. If not, the winding sample would tend to disintegrate due to the lack of varnish, as the solvent part of the material evaporates during sample curing. This illustrates a potential limitation of the applicability of MS derived data due to manufacturing constraints. Winding capacitance values have been estimated for ME II and ME II* using WS-II and WS-IV data. Aluminium has a larger specific heat capacity but lower density than copper, and therefore the better alternative in terms of winding heat capacitance is not evident. Here, aluminium conductors provide slightly lower C_w than copper ones.

Table 6.4 Measured winding heat capacitances for all analysed SEs.

SE	I	II	III	IV
$C_{w,\ SE}$ [J/°C]	7622	-	2047	4648
$C_{w,\ MS}$ [J/°C]	8235	2144 (1823 for ME II*)	2084	4383

Comparison of methods

The derived winding-to-stator thermal contact resistance R_{w-s} and winding heat capacitance C_w are compared here for the existing 'short-transient' and the proposed

'steady-state' approach. To ensure a fair comparison, the same measured data have been used by each method: temperature and power measurements from tests until an increase in T_s by 1°C. Figs. 6.7a) and 6.7b) present the estimated R_{w-s} and C_w, respectively, for the investigated methods from stator and motorette test data.

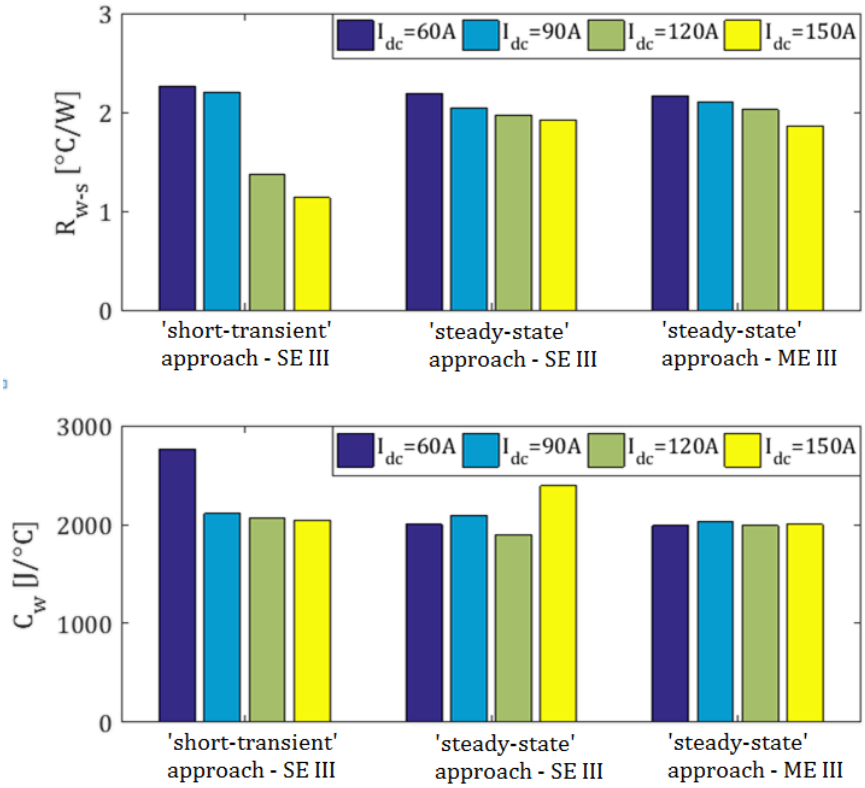

Fig. 6.7 Estimated parameters for both investigated methods from stator (SE-III) and motorette (ME III) test data, a) R_{w-s} b) C_w

From Fig. 6.7a), the existing 'short-transient' method fails to accurately predict R_{w-s}, demonstrated by the large variation in the estimated parameters at different current levels. A better correlation is observed between the motorette and stator data for the proposed 'steady-state' method. A slight decrease in R_{w-s} predictions is observed for the latter, which may be explained by the thermal expansion of the winding and core pack assemblies at higher temperature or by the fact that the thermal insulation of the set-up is not perfect, which may lead to increased heat dissipation at elevated temperatures.

From Fig. 6.7b), it is observed that estimated parameters obtained from measurements at a dc excitation current of 150A show limited applicability for the 'steady-state' method. An explanation may be that at I_{dc}=150 A, it only takes a few seconds for T_s to increase by 1ºC. This may not be sufficient to acquire a representative amount of data for curve-fitting. The parameter estimated from motorette analysis correlates well with the alternative values,

which validates the previous explanation: the motorette core pack is cooled by the cold plate, and therefore it takes a longer time for T_s to increase by 1ºC at I_{dc}=150 A. The minimum testing time required to acquire a representative amount of data has been discussed in [231] according to the system time constant. It is important to note that if steady-state data had been used for the proposed method, the obtained value for C_w would correlate well with the alternative values.

The restricted applicability of 'low' excitation current, e.g. I_{dc}=60A, for the 'short-transient' method has been previously justified by the limits of the assumption 'ΔT_{w-s}≈0'. Data from Fig. 6.7b) support this justification: for the proposed 'steady-state' method, the variation of T_s is accounted for and the winding thermal capacitance is more accurately predicted.

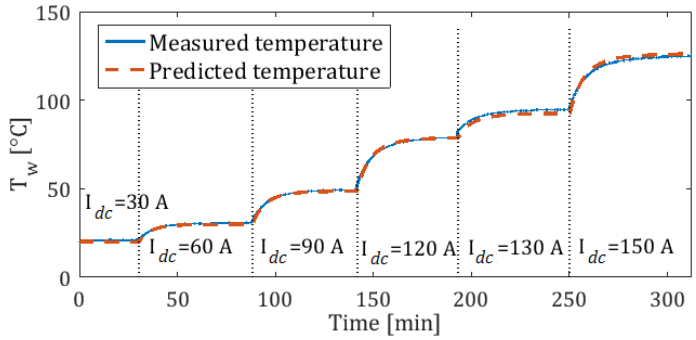

Fig. 6.8 Calculated and measured averaged winding temperature for M-I

The thermal parameters obtained from ME III using the proposed 'steady-state' method have been input in the reduced-order TEC to predict the winding temperature at different levels of excitation current at both transient and steady-state operations. The winding power loss has been iteratively updated with T_w. The thermal contact resistance between the motorette back iron and the cold plate, $R_{IP-CP,}$ was found equal to 0.07 ºC/W, and the fixed cold plate temperature has been set to 11 ºC, as in the experiments. Fig. 6.8 presents the estimated and measured averaged winding temperature, showing excellent correlation. Despite its reduced-order, the thermal model is capable of predicting accurately both the transient and steady-state behaviour of the stator-winding assembly.

Stator-to-housing thermal contact resistance

Table 6.5 shows measured stator-to-housing and housing-to-ambient thermal resistances for all analysed SEs. Thermal conductance parameters have been derived using (5.6) to account for the difference in heat transfer area. SE-IV appears to have the best stator-to-housing thermal contact interface, while SE-III is the worst alternative. However, as for the

winding-to-stator analysis, SE-I end windings were not thermally insulated during the dc tests. This may have led to a slight underestimation of R_{s-h}. Thermal conductance parameters should be used in order to compare SE-I's and SE-III's stator core-to-housing heat extraction capabilities. This would require the outer surface of the housing, including fins. The difference in testing approaches for SE-I and SE-III, where SE-III is covered with thermally insulating material, while SE-I is not, makes the comparison between derived data irrelevant. Therefore, the thermal conductance parameters have not compared here.

Table 6.5 Measured stator-to-housing and housing-to-ambient thermal contact resistances and heat conductances for all analysed SEs.

SE	I	II	III	IV
R_{s-h} [°C/W]	0.0087	-	0.013	0.002
$h_{e,\ s-h}$ [W/(m^2.°C)]	0.04	-	0.26	0.01
R_{h-a} [°C/W]	0.129	-	0.25	-

6.4 Power loss analysis

6.4.1 Experimental set-up

A series of tests with ac excitation of the stator assembly including direct power loss measurements and impedance analyses have been carried out.

Direct power loss tests have been completed with single- and three-phase ac excitations. Fig. 6.9 summarises the different direct power loss testing configurations. The single-phase direct power loss testing process is similar to the one of a motorette assembly, Fig. 6.9c). Three-phase direct power loss testing has been completed with each phase excited with a 2π/3 phase angle offset from each other, as for the normal three-phase machine operation, Fig. 6.9a). A third testing configuration, referred to as single-phase "series-parallel", has been analysed, Fig. 6.9b). This set-up consists of conducting a single-phase test, with phases two and three connected in parallel together and in series with the first phase. This set-up has been investigated as an alternative to three-phase tests for machines where the winding is configured with no access to the individual phases, e.g. no star point available, or in the context of limited availability of three-phase testing equipment. As for motorette testing, the stator under test is connected to the ac current-source and placed into an environmental chamber for pre-heating at a designated temperature. Measurements are conducted with different levels of excitation current magnitudes, frequencies and temperatures.

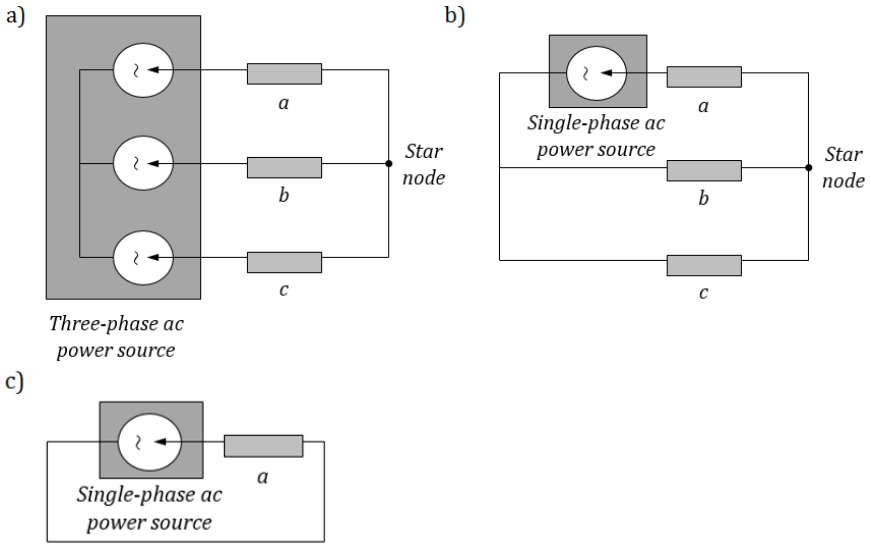

Fig. 6.9 Schematic of the different testing configurations used for direct power tests, a) three-phase excitation, b) single-phase "series-parallel" excitation, c) single-phase excitation

The impedance analyser has been used for single-phase tests, following the same procedure as the one presented for motorette testing in section 5.4.1. Here, the impedance analysis measurements have been performed at a room temperature of ~20 ºC.

6.4.2 Mathematical models

2D and 3D FE electromagnetic models have been employed to evaluate all power loss components generated within the analysed SE assemblies. The software Infolytica Magnet has been used for this analysis [248]. Each winding conductor has been represented as a solid conductor associated with an external circuit defining the electrical connections between the coils, or phases when applicable. The simulated MEs were driven by one- or three-phase sinusoidal waveform, reproducing the experimental set-ups. As for the motorette FEA model, an air region has been drawn around the motorette, with a zero vector potential condition assigned to its outer boundary, and the simulations are completed for a single electrical period, with one hundred steps. The derivation of winding and core power loss models are similar to the ones presented in section 5.4.2 in the context of motorette analysis. In addition, and depending on the slot arrangement and on the current excitation approach adopted for the tests (single- or three-phase), stator analysis allows the investigation of effects due to the interaction between neighbouring coils.

A comparison between complete stator and motorette assembly has been completed to provide some insight into the impact of neighbouring coils on the ac winding power loss, with SE-II and ME II selected for illustration. Figs. 6.10a), 6.10b) and 6.10c) present the

2D FE representations of SE-II, ME II and a theoretical representation of ME II with only one coil, respectively, with active regions highlighted.

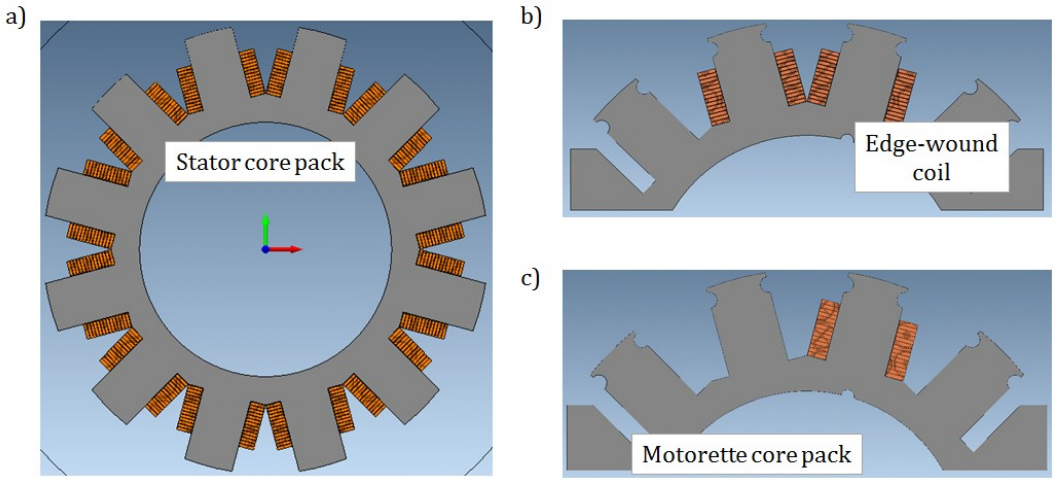

Fig. 6.10 2D mathematical model representation of investigated SE and MEs, a) SE-II, b) ME II, c) Theoretical representation of ME II with one coil removed

ME II comprises a group of two coils, which allowed the evaluation of issues related to the wedge design together with a representative thermal testing. Due to M-II specific design, the two coils of ME II, connected in series, correspond to a unique machine phase. Therefore, the effects of neighbouring coils can be evaluated by comparing ME II and its theoretical representation with only one coil, while the ac loss effects with and without neighbouring phases can be analysed from comparison between SE-II and ME II models with one phase.

6.4.3 Estimation of power loss parameters

The fundamentals for the derivation of the power loss coefficients and the calibration of electromagnetic FE model are similar for stator and motorette assemblies.

Hysteresis and eddy-current core loss coefficients

The absence of the rotor PM array results in lower flux levels within ME and SE core than within the complete machine assembly. Therefore, the measured core loss for a motorette or stator assembly will not be representative of the one of a complete machine. However, if the same manufacturing technique has been used for the core pack, the hysteresis and eddy-current power loss coefficients ε_h and ε_e should be similar for motorette, stator, and complete machine assemblies. The derivation of these parameters therefore contributes to the calibration of the complete machine electromagnetic model.

The comparison between power loss data from tests on a stator assembly and predicted power loss components from electromagnetic FE analysis, where the model parameters have been derived from motorette analysis, can provide some insight into the applicability of motorette derived loss parameters for stator or complete machine model. In Chapter 5, parameters from ME IV's FE electromagnetic model, including the hysteresis and core loss coefficients ε_h and ε_e, have been calibrated using data from tests on ME IV. These adjusted parameters have been input in SE-IV's FE model. The stator winding and core power loss have then been calculated at a fixed winding current magnitude of 50 A_{RMS} and at a frequency varying from 200 Hz to 1000 Hz. Three-phase direct power loss tests have been conducted on SE-IV for the same winding current magnitude and frequency range.

Fig. 6.11 presents the measured and predicted data for SE-IV power loss. The data correlate very well, with less than 5% difference between the predicted and the measured total losses at all analysed excitation frequencies. This confirms the applicability of motorette derived data for stator FE electromagnetic model calibration. If only the iron losses were compared, the difference between predicted and measured results would be slightly more significant, with a 12% difference observed at f=1000 Hz, Fig. 6.11. The iron loss coefficients have been adjusted to provide better correlations between predicted and measured data. The updated coefficients are detailed in Table 6.6. This difference can be explained by manufacturing nuances. Moreover, unlike ME IV, SE-IV's core pack may have been exposed to a temperature higher than 250 ºC during shrink fit, which could have altered ε_h. Indeed, the mechanical stress associated with a high heat shrink pressure could also have led to increased hysteresis loss [158].

Table 6.6 Iron loss parameters estimation following SE test

Core parameters	ε_h [$\times 10^{-4}$ W.Hz^{-a}.T^{-b}]	ε_e [$\times 10^{-5}$ W.Hz^{-2}.T^{-2}]
Model default parameters	90	3.24
Calibrated from ME measurements	178	7.14
Calibrated from SE measurements	190	7.14

Estimation of ac-to-dc ratio

The ac excitation-to-dc ratio $(R_{ac}/R_{dc})_e$ can be derived from SE tests, using the approach discussed in Chapter 5 in the context of motorette analysis. As for ME analysis, the winding power at ac operation only includes P_{dc} and $P_{ac,e}$ due to the absence of the rotor assembly during SE testing.

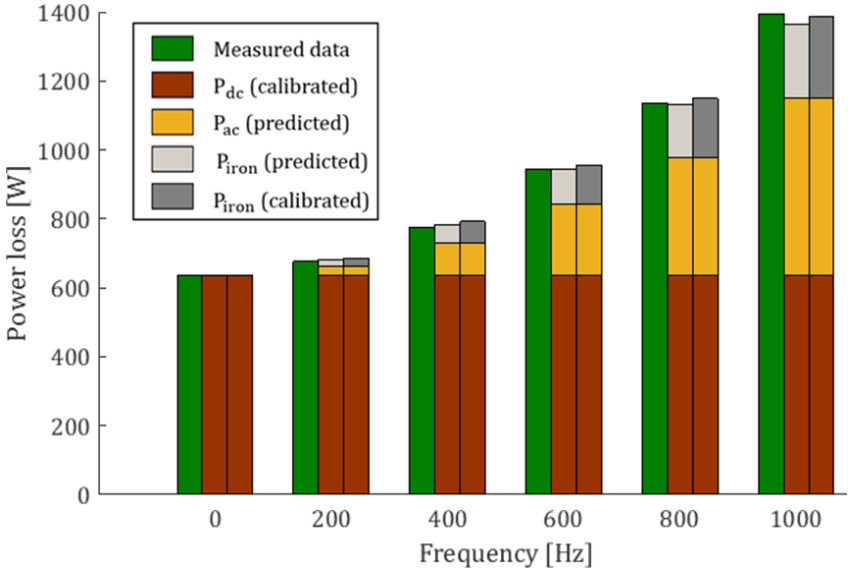

Fig. 6.11 Predicted SE-IV power loss using FE model calibrated using ME IV data for winding and core temperature of 20°C and ac current excitation of 50 A_{RMS}

The magnetic and thermal isolation between phases of single-layer modular windings, such as SE-I and SE-IV's configurations, makes a single motorette representative of the thermal and power loss effects of the complete stator. The $(R_{ac}/R_{dc})_e$ parameter derived for a motorette assembly is therefore identical to the one from a three-phase complete stator analysis, and there is a constant ratio between motorette and stator total measured power losses. In [113], SE-IV's iron and copper loss components under balanced three-phase excitation (twelve coils) were three times that seen in stator single-phase excitation tests (four coils) and twelve times that seen in motorette single-phase excitation tests (one coil). This confirmed the electromagnetic isolation between M-IV phases, as a coupling between phases would have resulted in an increase in iron and copper loss. The temperature of neighbouring phases remained unchanged for stator single-phase excitation tests [113]. This confirmed the thermal isolation between M-IV phases, and the representativeness of motorette assembly for such stator-winding configuration.

However, the stator winding are generally not isolated and a degree of magnetic coupling exists between neighbouring phases. In this case, some effects not accounted for by MEs, such as the impact of neighbouring phases or coils, can be captured by SE testing.

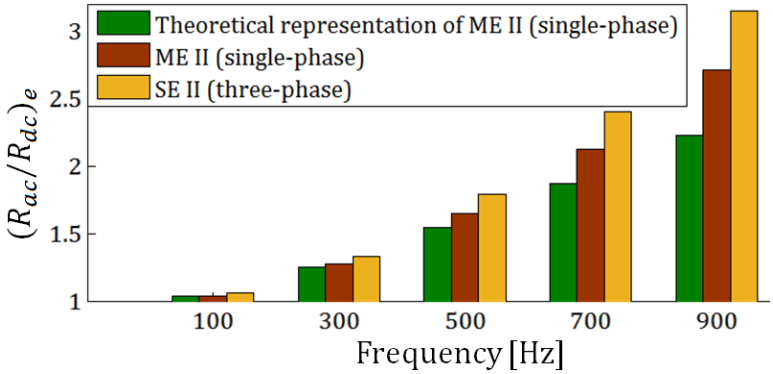

Fig. 6.12 $(R_{ac}/R_{dc})_e$ for a theoretical representation of ME II, ME II at single-phase excitation current and SE-II at three-phase ac excitation current vs. frequency for winding and core temperature of 20°C and ac current excitation of 100 A_{RMS}

A comparison between the winding power loss derived from SE-II, ME II and the theoretical representation of ME II with only one coil described in section 6.4.2, have been used to illustrate the impact of neighbouring phases and neighbouring coils on $(R_{ac}/R_{dc})_e$. Fig. 6.12 shows the calculated $(R_{ac}/R_{dc})_e$ for the three case studies for a range of excitation frequencies for a winding and core temperature of 20°C. Each model representation has been excited at a fixed winding current magnitude of 100 A_{RMS} and frequency f varying from 100 Hz to 900 Hz, with single-phase (MEs) and three-phase (SE) excitation. On the one hand, the comparison between the motorette models with one and two coils illustrates the non-negligible influence of a neighbouring coil, with a clear increase in $(R_{ac}/R_{dc})_e$ ratio in the latter case. On the other hand, the comparison of the results obtained between ME II (two coils) and SE-II highlights the significant impact of neighbouring phases. Clearly, single-phase ME testing has limited use for the direct derivation of the complete machine ac excitation-to-dc winding power loss ratio. The impact of neighbouring coils or phases should not be neglected when estimating the winding and core power losses due to current excitation, and tests on stator assembly can provide useful data in this context. Motorette testing remains a useful tool for model calibration and comparison of alternative constructions.

For some stator-winding configurations, the winding ac loss cannot be accurately predicted, due to the uncertainty associated with the exact position of the conductors within the stator slots. In this context, empirically-derived data become essential inputs for complete machine model definition. Three-phase direct power loss tests are recommended, as the measured ac excitation-to-dc winding power loss ratio $(R_{ac}/R_{dc})_e$ from stator assembly will be representative of the one of the complete machine for the same excitation. The actual machine drive may also be used in order to account for losses associated with the inverter and control, e.g. pulse width modulation (PWM) harmonic losses [238].

Single-phase direct power excitation tests can also be used for stator assemblies where the winding is configured with no access to the individual phases, e.g. no star point available. This approach is however not ideal if each stator phase is tested individually, as the impact of excited and non-excited neighbouring phases on the winding power losses is dissimilar. The single phase 'series-parallel' testing set-up described in section 6.4.1 can be used as an alternative to account for the influence of the neighbouring phases.

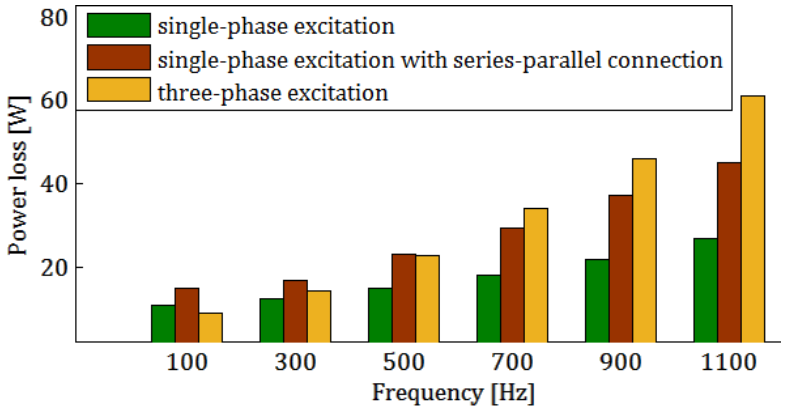

Fig. 6.13 Total power loss measured for SE-III's phase-a at single-phase, single-phase "series-parallel" and three-phase ac excitation current vs. frequency for winding and core temperature of 25°C and ac current excitation of 30 A_{RMS}

SE-III (randomly-wound round conductors) has been used to illustrate the respective outcomes of the testing approaches with single-phase excitation, single-phase excitation with series-parallel connection and three-phase excitation. For the 'series-parallel' configuration, the SE-III's phase-a was coupled in series with the parallel connection of SE-III's phase-b and phase-c, as shown in Fig. 6.9. For the three-phase tests, SE-III was connected in star configuration.

Fig. 6.13 shows the measured total power loss for SE-III's phase-a at single phase, single-phase "series-parallel", and three-phase ac excitation current for various excitation frequencies for a fixed winding and core temperature of 25°C and an ac current excitation of 30 A_{RMS}. The results comprise the total measured data, i.e. both winding and core loss components are accounted for. The total power losses per phase are significantly larger for measured data obtained from tests with three-phase excitation current than with single-phase excitation current. This suggests that most of the ac losses due to current excitation result from the presence of excited neighbouring coils. Therefore, it is highly desirable for machine designers to adopt appropriate testing set-ups to evaluate these effects, in particular when accurate and reliable mathematical predictions of ac winding loss are not feasible.

From Fig. 6.13, the single-phase "series-parallel" testing configuration is more representative of the three-phase excitation than the common single-phase testing configuration. At 'low' frequency, the single-phase "series-parallel" excitation results in slightly more losses than the three-phase test. An explanation may be associated with the influence of the amplitude of the magnetic field and of the excitation frequency on the ac power loss components. On the one hand, for the single-phase 'series-parallel' testing configuration, the amplitude of the magnetic field within a slot is higher in average than for the three-phase testing configuration, as both neighbouring coils have the same phase angle. On the other hand, the coils in the three-phase testing configuration are exposed to the magnetic field created by two currents with different phase angles, which result in a field with higher inherent frequency. For SE-III's phase-a, the frequency induced effects become dominant at $f \geq 500$ Hz.

Repeatability of the winding manufacturing process

Stator assembly testing can be used to investigate the repeatability of the winding process. A simple approach consists in measuring each phase or coil, using an Ohm meter or with dc current excitation test. The difference between stator phases might however be more significant at ac excitation current than at dc excitation current, due to the strong impact of conductor location within the slot on winding ac power loss effects. Ideally, all conductors would be arranged so that they are exposed to the same quantity of magnetic field to reduce circulating currents. However, for winding configurations such as SE-III, where a bundle is formed with many strands in parallel, arranging each strand in an allocated location would be prohibitively time-consuming to implement. Therefore, these windings are typically mushed-wound. The difference of winding power loss per slot may result in local hotspots, and therefore is it recommended to evaluate each coil or each phase, individually using tests with ac excitation to have a broader insight of the winding thermal behaviour. In particular, the inhomogeneous power loss distribution is expected to be amplified in presence of the rotor assembly.

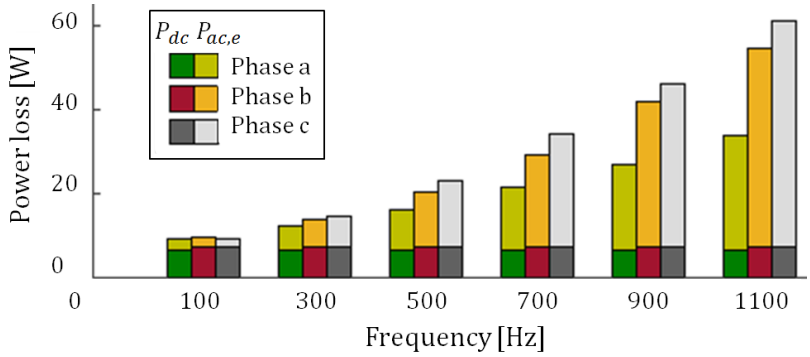

Fig. 6.14 Total power loss per phase measured for SE-III at three-phase ac excitation current vs. frequency for winding and core temperature of 25°C and ac current excitation of 30 A_{RMS}

Fig. 6.14 presents the results from three-phase tests previously described for each phase of SE-III with the dc and ac power loss separated. Clearly, the difference between stator phases is more significant at ac excitation current than at dc excitation current. These results can also be analysed in the light of the winding-to-stator thermal contact resistances R_{w-s} derived in section 6.3.3. For instance, SE-III's phase-c has a 20% higher R_{w-s} than SE-III's phase-a and a 13% higher ac power loss component at f=1100 Hz. Therefore, phase-c winding temperature should be carefully monitored, as the winding hot spot is very likely to be located within this phase.

6.5 Summary

This Chapter has presented the third building step of the proposed methodology, which utilises tests on SEs to evaluate the thermal and power loss parameters of the core pack and winding regions. Firstly, the stator assembly has been investigated in the context of thermal analysis, with focus on the estimation of the winding heat capacitance and stator-to-housing thermal contact resistances.

A procedure has been introduced for the derivation of the winding heat capacitance. This 'steady-state' method has been shown more time-efficient and reliable compared to the 'short-transient' existing approach. The comparison between motorette and stator derived data confirmed the necessity of using thermally insulating material for stator testing to ensure a well-defined heat path when deriving thermal parameters from the winding-to-housing heat extraction path.

Secondly, the stator assembly has been studied in the context of power loss analysis, with emphasis on the estimation of the ac excitation-to-dc winding power loss ratio. The representativeness of motorette assembly has also been discussed. For non-isolated winding slot, the motorette were not directly relatable to complete machines, but were

shown to be useful for the calibration of electromagnetic models, and for the comparison of alternative configurations. Initial results from the comparison of alternative stator testing approaches, including single-phase, single-phase 'series-parallel' tests or three-phase tests, have been presented. The three-phase tests were shown to be more representative of the ac winding power loss of a complete machine assembly, while single-phase 'series-parallel' tests seemed to be a good alternative if no three-phase ac power loss is available. More work is required on various stator assemblies (e.g. distributed and concentrated windings, conductor shapes, etc.) to derive more general conclusions. Additional effects, such as the impact on the PWM on the stator core loss, could also be investigated.

At the end of the design process, further information is required regarding the machine's overall electromagnetic and mechanical loss, such as the ac effects due to the rotor rotation or the PM power loss. In this case, the complete machine assembly needs to be analysed.

Chapter 7 Methodology illustration

7.1 Introduction

The final building step of the proposed methodology utilises tests on a complete machine assembly. Tests on a complete machine allow the evaluation of thermal and power loss effects associated with rotation of the rotor assembly, e.g. rotor-induced winding loss. The use beforehand of the first three building blocks greatly simplifies the thermal model validation and loss separation process, as only a reduced number of parameters are still unknown when analysing data from complete machine assembly.

A variety of approaches for the complete machine analysis are discussed in this Chapter. A focus is put on separating the power loss components generated from different sources, and on estimating thermal parameters from various machine regions. The four machine demonstrators introduced in Chapter 3 have been used for illustration. Sensitivity analyses have also been completed.

A number of case studies are presented, making use of the proposed design methodology to evaluate several concepts for the selected machine demonstrators. The use of the methodology results in a more comprehensive and truly coupled machine electromagnetic and thermal design process.

7.2 Complete machine analysis

7.2.1 Experimental set-up

A range of static and dynamic test methods can be employed during the thermal and power loss analysis and calibration of electric machines. The most common tests include conventional dynamometer, static dc excitation, open-circuit and short-circuit evaluation of a complete machine assembly. These tests have been briefly introduced in Chapter 2.

Dynamometer tests

Dynamometer tests are generally used to evaluate the machine performance and efficiency via input and output power loss measurements. During these tests, the machine under test (MUT) is mounted onto a support structure and mechanically coupled to a dynamometer load machine, referred to as prime mover. The MUT is usually inverter driven

(torque/current control mode), whereas the prime mover operates under speed control. The controlled rotational speed of the load machine is imposed to the shaft of the MUT.

The machine load and rotating speed are usually gradually increased to preserve the tested machine from electrical, mechanical or thermal damages. The electrical and mechanical powers are typically measured via an electrical power analyser (direct measurement of current and voltage) and an in-line torque transducer (measures average speed and torque). Some of the dynamometer tests account for the thermal steady-state to get some insight into the continuous behaviour of the tested machine prototype. Fig. 7.1 presents an example of the complete dynamometer set-up used for M-IV analysis. M-IV's liquid cooling set-up is visible on Fig. 7.1.

To validate the electromagnetic and thermal models, or demonstrate the specific-output capability of an electrical machine over a specific torque-speed envelope, the MUT is typically evaluated at various levels of current amplitude for maximum torque per ampere (MTPA) operation. Sometimes, torque-speed envelopes measured at a fixed reference temperature are sufficient, as compared with measurements where each test point corresponds to the thermal equilibrium of the tested machine. In this case, and in order to minimise the temperature difference between the measured points, the testing procedure can be automatised [154].

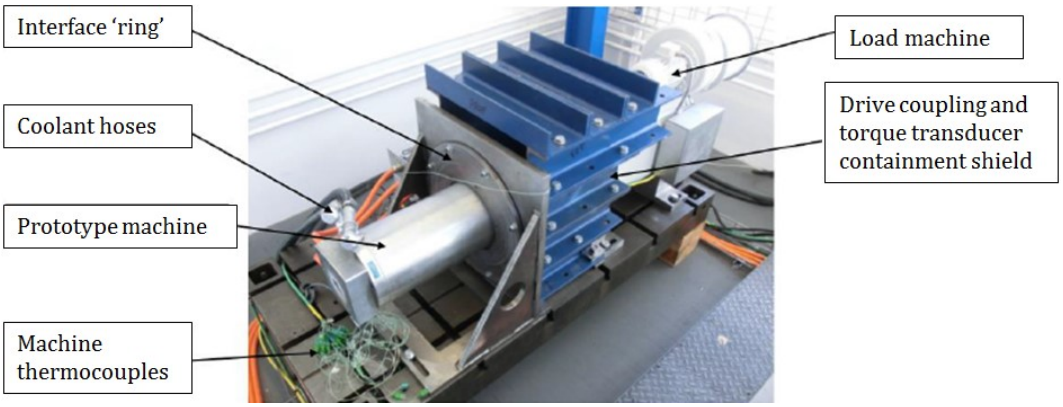

Fig. 7.1 M-IV connected to dynamometer facility

Static Thermal Tests with DC Excitation

A series of short-transient and steady-state thermal tests with dc excitation of the stator-winding assembly is generally carried out on complete machine assemblies. These tests are similar to the ones described in the context of stator testing, with the stator windings excited with controlled levels of dc current. The stator windings are typically connected in series to ensure a homogenous current distribution within the stator slots. However, for machines

where the winding is configured with no access to the individual phases, e.g. no star point available, it is not possible to have the same level of current excitation in each phase. This needs to be accounted for when analysing data from the tests. Indeed, a part of the heat produced by the phases excited with higher current amplitude may be dissipated to the phases excited with lower current amplitude. The tests are typically conducted with the machine cooling set-up in order to evaluate the impact of the latter.

Open- and Short-Circuit Tests

Open-circuit tests are typically completed to estimate the voltage induced by the winding and provide some insight into the mechanical and rotor induced power loss components, while short-circuit tests are usually used to identify magnetic parameters, such as armature and synchronous reactance values. Short-circuit tests may also be used to characterise load dependent winding and demagnetising flux path iron loss effects. These tests require the use of a prime-mover operating in speed-control and a torque-transducer, and are therefore more involved than static tests. The machine under test is spun unloaded, unconnected to the drive (open-circuit tests) or with terminals connected to form a short-circuit (short-circuit tests). In addition to the power loss, the EMF and the cogging torque (open-circuit tests), or the winding inductance (short-circuit tests) are recorded to validate the electromagnetic models. Although the main aim of open-circuit and short-circuit tests is usually not thermal calibration, these tests can provide some insight into some thermal parameters. Therefore, these tests are often completed until thermal equilibrium is reached.

Dummy Rotor Tests

Dummy rotor tests can be used to assess the machine mechanical losses, due to the difficulty of isolating these effects when testing a complete machine assembly [117]-[119]. Indeed, the rotation of a magnetised rotor assembly will induce some effects, such as PM loss, rotor induced ac winding loss, and main flux path iron loss components. The dummy rotor must be made of a non-magnetised material to ensure that the measured loss is only due to the mechanical loss components.

Ideally, the dummy rotor should be identical in terms of mass and geometry to the actual rotor with laminated core pack and PM array. The identical mass and geometry would ensure, respectively, that the bearing and windage components are representative of the actual rotor. The dummy rotor is typically inserted inside the stator of the machine, connected to a dynamometer, and spun through an in-line torque transducer. The assembly may be pre-heated using winding dc loss or suitable heating set-up to obtain representative

machine operating conditions [117], [118]. Torque and rotational speed measurements are then taken at thermal equilibrium. Fig. 7.2 presents the dummy and magnetised rotor assemblies used in [113] for the estimation of M-IV mechanical losses.

Fig.7.2 Dummy and magnetised rotor assemblies used for M-IV analysis [113]

Baseline Machine Test Data

It is often desirable to test an electric machine in a representative environment emulating the intended operating conditions. For instance, M-I's intended application is a helicopter tail rotor. This imposes the main heat extraction mechanism from the machine periphery to be forced convection. In order to reproduce this forecasted operating condition, an experimental setup comprising of an external variable speed fan has been used during tests on M-I. Similarly, M-II has been actively air-cooled using a fan arrangement, with airflow directed on the non-drive end of the machine assembly. Tests with dc current excitation have been completed on M-I and M-II with and without forced-cooling set-ups to obtain more insight into the influence of forced cooling on the machine thermal behaviour. M-II has been cooled via a shaft spiral grove cooling system, i.e. a fluid is passed down ducts in the shaft. Unfortunately, the test facility did not provide scope to install M-II's shaft spiral grove. M-II was expected to be able to generate under continuous operation a power of 33 kW when the shaft grove cooling system operates at a fixed temperature of 90 ºC. A flange plate has been coupled to M-II's shaft to act as a heat sink for initial machine evaluation. This cooling set-up had nonetheless lower heat extraction capability, and consequently tests have been completed for the output power up to 13 kW only. Further tests are therefore required to assess maximum power output capability of M-II when equipped with the intended heat extraction system.

7.2.2 Mathematical modelling

2D and 3D FE analyses have been employed to derive the machines' temperatures, electromagnetic power loss components and output power capabilities. The software Infolytica Magnet has been used to complete the 2D analyses, while ANSYS has been used

for 3D analyses according to the license available [248]. As previously, the winding regions have been homogenised or modelled as appropriate sub-regions, depending on the winding topology of the analysed machine. When available, power loss and thermal parameters derived from MS, ME and SE measurements have been used to inform the electromagnetic and thermal models.

Symmetry has been employed to analyse only a portion of each machine and reduce computation time. The number of rotor poles and stator slots have been divided by their greatest common divisor to obtain the smallest region that can be analysed using symmetry. One quarter of M-I and half of M-II, M-III and M-IV have been analysed. For all analysed machines, the ends of the machine have been joined by periodic boundary condition, as the number of rotor poles of each machine is even-numbered. If the number of rotor poles had been odd-numbered, the ends would have been joined by anti-periodic boundary conditions.

An air region has been drawn around the machine, with a zero vector potential condition assigned to its outer boundary, and the simulations are completed for a single electrical period, with one hundred steps. The rotor of the machine is defined as a fixed-speed rotating object. The airgap has been divided into two thin layers. For each step of the FE analysis, the rotor has a new position, but only the thin airgap layer in contact with the rotor need to be re-meshed and the total computation time is reduced.

Torque-Speed Envelope Predictions

Some of the electrical machines analysed here, M-III and M-IV, are designed to operate at a range of rotational speed and torque levels. In such a case, predicting the operating torque-speed envelope is required to provide complete assessment of the machine performance. Here, 2D electromagnetic model representations have been used to derive M-III's and M-IV's torque-speed envelopes. The FE analyses have been used to inform the direct-quadrature-zero (DQ0) model of the analysed machines, where the direct and quadrature flux linkage components Λ_d and Λ_q have been mapped over a range of direct and quadrature-axis currents, I_d and I_q.

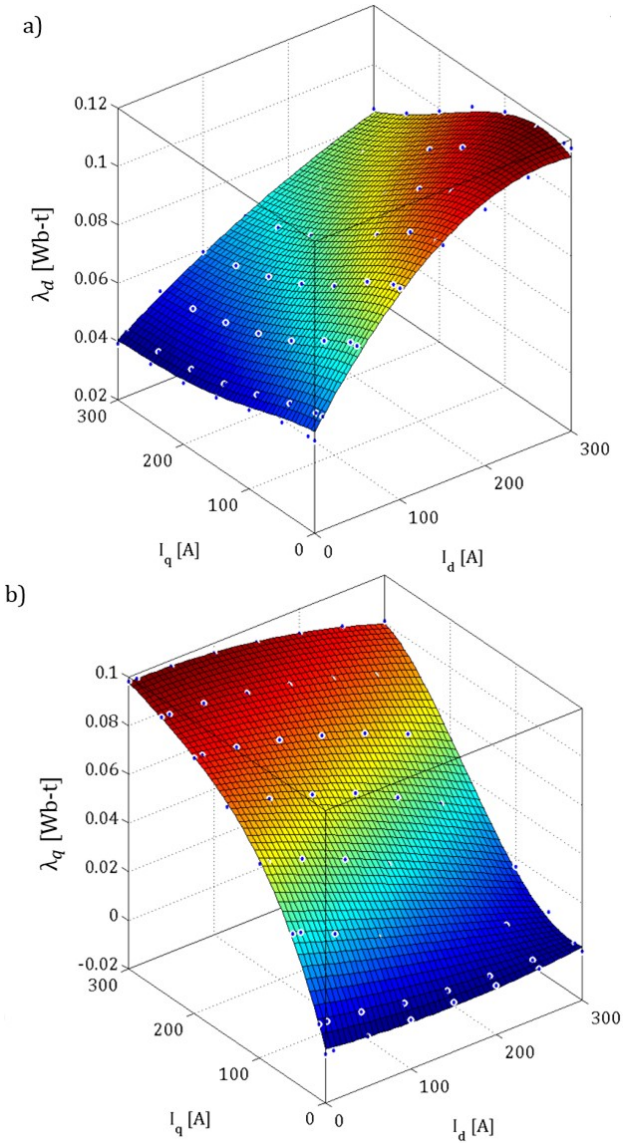

Fig. 7.3 D- and q-axis flux linkage mappings and measured values from M-IVs 2D FE model (blue circles)

Fig. 7.3 presents the flux linkage values calculated using M-IV's 2D FE model together with the associated MATLAB surface-fit. Some cross-coupling between axes can be observed from the flux linkages maps, Fig. 7.3. The obtained flux-linkage data, $\Lambda_d(I_d, I_q)$ and $\Lambda_q(I_d, I_q)$ have been used in conjunction with (7.1)-(7.3) and an optimisation routine to derive the machine's torque-speed envelope under maximum torque per ampere control [106]. This is necessary due to M-III and M-IV salient rotor structure.

$$T = \frac{m}{2} p \left(\Lambda_d \mathrm{I}_q - \Lambda_q \mathrm{I}_d\right) \qquad (7.1)$$

where m is the number of phases, here m=3, p the number of pole pairs, here p=5. The generated electromagnetic torque, (7.1) is subject to the following constraints on maximum inverter output voltage, V_{lim}, and the stator current magnitude, I_{pk},

$$V_{lim} \geq \omega_s \sqrt{{\Lambda_d}^2 + {\Lambda_q}^2} \qquad (7.2)$$

$$I_{pk} \geq \sqrt{{I_d}^2 + {I_q}^2} \qquad (7.3)$$

where ω_s the electrical rotational speed. In the analysis conducted herein, $V_{lim} = V_{dclink}/\sqrt{3}$, where V_{dclink} is the dc link voltages. The obtained torque data over a range of current vectors and rotational speeds is used to compute efficiency maps and thermal envelopes.

Electromagnetic Loss Calculation

The output power capability and electromagnetic loss have been predicted using time-stepping FE analyses, where the winding coils were driven with three-phase sinusoidal current waveforms. The complete calculated power loss data includes the winding active and end-winding regions, iron loss for the stator and rotor core packs, PM loss, and mechanical loss.

For all baseline machines, the ac and dc copper loss components have been calculated for each of the winding sub-regions to derive R_{ac}/R_{dc} ratios together with the loss temperature dependence. According to the analytical expression describing temperature dependence of the winding power loss at ac operation, (2.5), the ac winding power loss temperature dependence coefficients due to excitation β and due to the rotation of the rotor assembly γ need to be determined. The method for estimating β has been presented in the context of motorette and stator analysis (Chapters 5 and 6). The temperature coefficient γ can be derived using data from 2D FE analyses of the complete machine at open-circuit operation. The curve fitting of (7.4) at various winding temperature allows for a first estimation of the coefficient.

$$P_{ac,r|T} = P_{ac,r|T_0} \frac{1}{(1+\alpha(T-T_0))^{\gamma}} \qquad (7.4)$$

The iron losses generated over M-III's and M-IV's entire torque-speed envelope have been derived by coarsely mapping the loss as a function of I_{pk} and current angle, γ_I. The resulting 2D FE predictions have then been interpolated to provide high-resolution loss

maps at a given temperature T_0.The effect of operating frequency has been accommodated using the following formula, (7.5),

$$P_{iron}(f, I_{pk}, \gamma) = P_{hyst\,|f_0}(I_{pk}, \gamma_I)\left(\frac{f}{f_0}\right)^a + P_{eddy\,|f_0}(I_{pk}, \gamma_I)\left(\frac{f}{f_0}\right)^2 \qquad (7.5)$$

where $P_{hyst\,|f_0}$ and $P_{eddy\,|f_0}$ are respectively the hysteresis and eddy currents iron loss components calculated at a frequency f_0. The core loss has been assumed to be temperature independent in this analysis.

A set of FE simulations at open-circuit operation and under MTPA operation has been used to obtain the PM loss components. Open-circuit analyses allowed for the derivation of the PM loss component due to stator-slotting effects, while MTPA operations have been used to ascertain the PM losses from the interaction of external stator fields. In both cases, the dominant loss component was due to eddy currents resulting from cyclic variation of the magnetic flux density within the PM array [108]. The magnitude of PM power loss is described by (7.6) through the superposition of speed and current-dependent loss components.

$$P_{PM}(f, I_{pk}) = P_{slotting\,|f_0}\left(\frac{f}{f_0}\right)^2 + P_{statorinteraction\,|f_0, I_{pk0}}\left(\frac{f}{f_0}\right)^2\left(\frac{I_{pk}}{I_{pk0}}\right)^2 \qquad (7.6)$$

where $P_{slotting\,|f_0}$ is the PM loss from the slotting effect calculated at a frequency f_0 and $P_{statorinteraction\,|f_0, I_{pk0}}$ is the additional PM loss from stator field interaction calculated at a frequency f_0 and peak current I_{pk0}. The initial analysis assumed a magnet loss which is unaffected by temperature.

For all baseline machines, the mechanical losses have been estimated from measured data. The friction and winding mechanical loss coefficients can be derived by curve-fitting (7.7) with measured data.

$$P_{mechanical} = \varepsilon_{friction}.n + \varepsilon_{windage}.n^3 \qquad (7.7)$$

where

$$\varepsilon_{friction} = \pi\rho C_d R^4 L \qquad (7.8)$$

and

$$\varepsilon_{windage} = K_{fb} G \qquad (7.9)$$

If no empirical results are available, the bearing loss component can be estimated using manufacturer provided data and analytical formulae, while the aerodynamic loss components can be predicted using CFD analyses [117].

Thermal models

Lumped-parameters thermal equivalent circuit (TEC) networks have been used for the thermal analysis of the baseline machines. Similar to the approach adopted in Chapter 5 for TEC-c, the TEC models have been automatically generated based on geometry and material data using Motor-CAD software [130]. Fig. 7.4 shows the cross-section of the baseline machines, including their housing frames, obtained from the software geometric module [130]. The models account for conduction, convection and radiation heat transfer mechanisms, including 3D end-winding effects.

The TEC models can be used to evaluate the continuous operating envelopes, duty-cycle and transient operations of the analysed machines. The winding hot spot temperature limit has been set to 180 ºC.

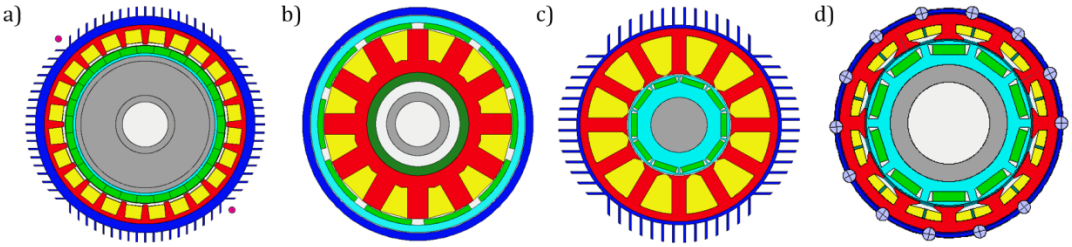

Fig. 7.4 Cross-section of machine thermal models, a) M-I, b) M-II, c) M-III, d) M-IV

The power loss predictions obtained from complete machine analysis have been used to inform the thermal models, together with the data obtained from the analysis of each of the methodology building blocks.

7.2.3 Power loss analysis

The use of the proposed methodology allows the identification of power loss parameters associated with the stator-winding region of the machine assembly. At the end of the design process, further information is required regarding the machine's overall electromagnetic and mechanical loss, such as the ac effects due to the rotor rotation or the PM power loss. In this case, the complete machine assembly needs to be analysed. Fig. 7.5 summarises the proposed approach for the derivation of the complete machine power loss in the light of the proposed methodology. The methods have been discussed and illustrated using the baseline machine assemblies.

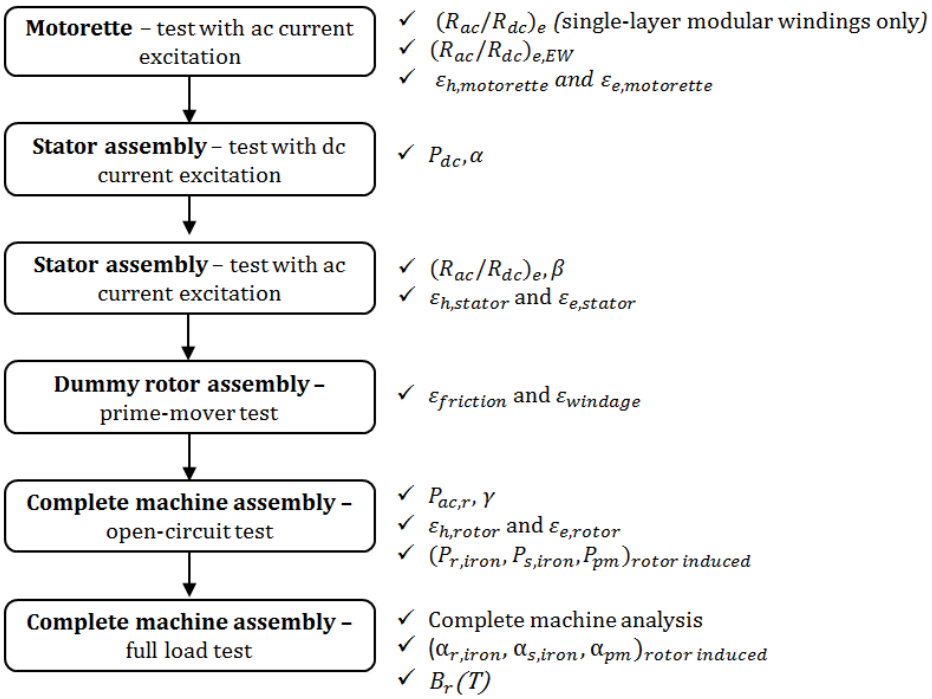

Fig. 7.5 Schematic diagram of the proposed methodology for the complete machine power loss analysis, $(R_{ac}/R_{dc})_e$: winding ac excitation to dc loss ratio, $(R_{ac}/R_{dc})_{e,EW}$ end-winding ac excitation to dc loss ratio, ε_h and ε_e: hysteresis and eddy-current core loss coefficients, P_{dc}: dc power loss, α: dc power loss temperature coefficient, β: winding ac power loss temperature coefficient, $\varepsilon_{friction}$ and $\varepsilon_{windage}$: friction and winding mechanical loss coefficients, $P_{ac,r}$: ac winding power loss due to the rotation of the rotor assembly, $(P_{r,iron}, P_{s,iron}, P_{pm})_{rotor\ induced}$: rotor induced rotor core, stator core and PM loss components, respectively, $(\alpha_{r,iron}, \alpha_{s,iron}, \alpha_{pm})_{rotor\ induced}$: temperature coefficients of the rotor induced rotor core, stator core and PM loss components, respectively.

Dummy rotor assembly – prime-mover test

Due to the difficulty of isolating the mechanical loss components from the electromagnetic ones, dummy rotors tests are recommended for an accurate evaluation of the complete machine assembly. The mechanical loss coefficients $\varepsilon_{friction}$ and $\varepsilon_{windage}$ can be evaluated by curve fitting (7.7) with the measured power loss data from dummy rotor tests. Depending on the resolution of the measured data and of the range of analysed rotational speeds, there may be several pairs of friction and windage loss coefficients $\varepsilon_{friction}$ and $\varepsilon_{windage}$ matching the experimental data. It is therefore recommended to complete the tests for a range of rotational speeds, as this may facilitate the separation between $\varepsilon_{friction}$ and $\varepsilon_{windage}$.

Completing dummy rotor tests in vacuum could also be an alternative for measuring exclusively the bearing loss effects, but with the drawback of an intricate experimental set-up. This testing method has not yet been reported in the literature.

The data derived from M-I's and M-III's dummy rotor have shown good correlation with (7.7). However, the results obtained for M-IV's dummy rotor tests were significantly higher than predicted, and did not follow (7.7)'s trend. This mismatch was initially attributed to a manufacturing issue, over simplistic formulation of (7.7) or measurement error due to common-mode noise or electrical interference. The abnormal bearing loss components were finally attributed to elevated mechanical preload of the bearings from the machine end-caps [113]. However, this conclusion has been made when examining the hardware after a failure occurred.

When no dummy rotor data is available, results from open-circuit tests can be used to estimate the mechanical loss components. At open-circuit operation, the rotation of the magnetised rotor assembly generates PM loss, rotor induced ac winding loss, and main flux path iron loss components. These power loss effects can be calculated using the electromagnetic model, and then subtracted from the total measured loss data at open-circuit operation. On the one hand, this approach is valid when the stator-winding configuration allows for an accurate model representation, e.g. well-defined conductor location within the stator slot, and the parameters of the electromagnetic model, including the hysteresis and eddy-current core loss coefficients, have been informed from tests on hardware exemplars. On the other hand, when no empirical data is available beforehand, the separation between the different loss components might appear challenging.

M-IV's mechanical loss components have been evaluated using open-circuit tests. The data obtained from motorette and stator analyses (Chapters 5 and 6) have been used to inform the FE model of the machine, and therefore the confidence in the calculated electromagnetic power loss components was high. Due to the interior permanent magnet (IPM) configuration and the semi-closed slot geometry, the variation of magnetic flux density within the magnet was expected to be small at open-circuit operation. This was confirmed by the initial FE, and therefore this loss component has been neglected. Fig. 7.6a) shows the measured, calculated and estimated loss components repartition obtained after analysis of M-IV open-circuit test data, while Fig. 7.6b) presents the deducted and curve-fitted mechanical loss data to (7.7). The mechanical loss coefficients $\varepsilon_{friction}$ and $\varepsilon_{windage}$ have been deduced from the curve fit, and are provided in Fig. 7.6b). The deducted and curve-fitted mechanical loss components show good agreement. The minor discrepancy observed for a rotational speed n=3000 RPM is attributed with measurement uncertainty.

Complete machine assembly – open circuit test

When the mechanical loss components have been obtained from dummy rotor tests, open-circuit tests can be used to estimate or validate the rotor-induced winding, core and PM power loss components.

When the proposed methodology has been applied, the stator core loss coefficients ε_h and ε_e have been identified: both the core loss components have been initially derived based on the manufacturer specific power loss data and then adjusted using experimental data from tests on motorette and stator assemblies. These core loss coefficients may be input into the model and adjusted in the light of the open-circuit test data. Moreover, the comparison between predicted and measured winding ac power loss from stator assembly will have increased the machine designer's confidence in his or her electromagnetic model. In this case, as illustrated the previous example using M-IV, the ac winding power loss due to the rotor rotation $P_{ac,r}$ can be calculated to focus on the rotor and PM loss components. However, this is only possible for winding configurations where the position of each individual conductor is well defined.

Independently of the availability of calculated $P_{ac,r}$ data, the identification and separation of each individual electromagnetic loss component should be relatively straightforward when the mechanical and core loss coefficients have been derived. It would be possible to complete a prime-mover test on the machine assembly with an unwound lamination pack, prior to coils being fitted, to specifically identify the ac winding power loss component due to the rotor rotation $P_{ac,r}$. The comparison between data measured from this prime-mover test and from open-circuit test would allowed the isolation of $P_{ac,r}$. This approach has been adopted for M-I analysis, after the removal of the stator coils due to the identification of a winding fault [187]. The time lag prior to the stator rewind offered an opportunity to complete this additional test. This may be of interest for mush-wound winding configurations, in particular when the ac winding power loss due to the rotor rotation is expected to be significant, e.g. open-slot topology. However, a combination of open-circuit and full load tests is usually sufficient for the estimation of the ac winding power loss due to the rotor rotation.

Several electromagnetic model parameters can be validated using the measured back EMF data from open-circuit or full load tests, including the magnet remanence B_r. The temperature coefficient of the magnet remanence B_r can be estimated from measurement of the output torque at various temperatures, e.g. initial and steady-state temperatures.

Inputting this parameter into the electromagnetic and thermal models is necessary for a reliable estimation of the machine output torque and power capabilities.

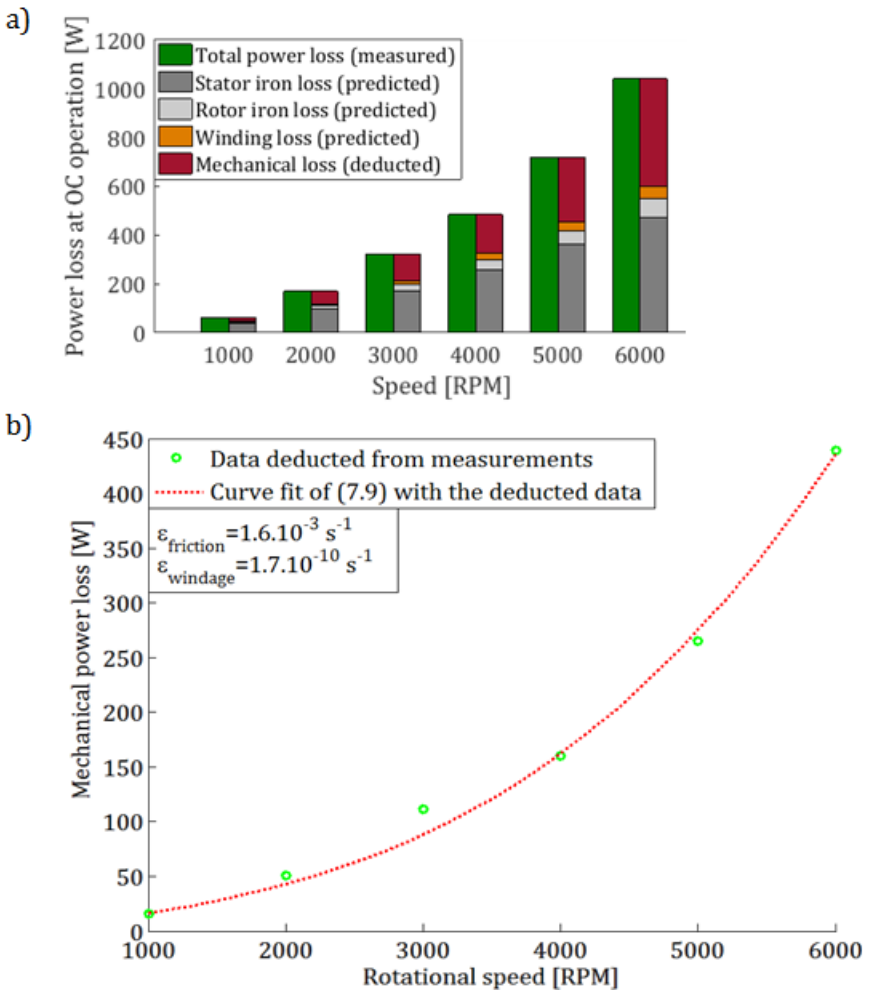

Fig. 7.6 a) Measured, predicted and deducted power loss components for open-circuit operation, b) Deducted and curve fitted power loss data for open-circuit operation – M-IV

The impact of the change in magnet remanence with temperature has been illustrated using results from load tests on M-IV. Empirical values have been measured transiently for a range of excitation currents from 20 to 95 A, increasing the machine's rotational speed in steps of 1000 RPM. Due to the reduced-time of the transient measurements, limited to a few minutes, the machine was expected to remain close to its initial temperature, T_0=80°C. Therefore, the values calculated using the 2D electromagnetic FE model have been obtained assuming a fixed winding and magnet temperature of 80°C. Fig. 7.7 presents M-IV's measured and calculated torque/speed operating points. The measured values aligned closely with calculated ones, however an offset can be observed at high-torque. This offset suggests a variation of the winding and magnet temperatures during the test. The measured winding temperature showed an increase of approximately 15 °C between test at I_{pk}=20 A

and test at I_{pk}=95A at 4000 RPM. The magnet temperature has not been monitored, but is expected to have also increased, which would lead to a decrease of B_r, hence a reduction in M-IV's output torque. This emphasises the need to account for the magnet temperature for accurate machine performance predictions. It is worth noting that the difference in measured and predicted torque may not be entirely due to magnet heating, as mechanical losses are not accounted for in the electromagnetic model. Measuring the EMF at the start and at the end of the torque-speed measurements would have provided a definitive answer. Finally, the temperature coefficient of remanence of M-IV's SmCo magnets, α_{B_r} was found to be -0.035 %/°C. The magnet remanence is then updated according to temperature as follows,

$$B_r(T) = B_{r,0}(1 + \alpha_{B_r}(T - T_0)) \qquad (7.10)$$

Where $B_{r,0}$ is the magnet remanence at temperature T_0. Equation (7.10) is similar to (2.3) used for the dc power loss components, and can be used for other loss effects, such as core loss.

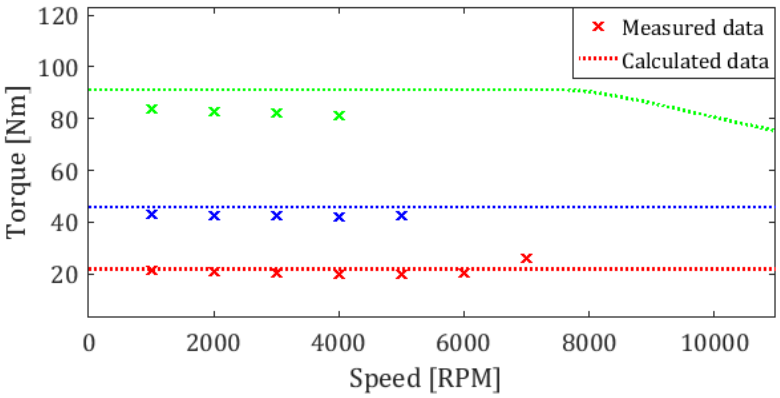

Fig. 7.7 Measured and calculated operating points – M-IV. Machine initial temperature of 80 °C

The impact of stator and rotor temperatures on the power loss parameters can be evaluated using open-circuit or full load tests completed until thermal steady-state. The increase in stator core, rotor core and PM temperature will lead to an increase in material resistivity, hence a decrease in the eddy-current induced loss components. The temperature dependence of the winding loss due to the rotor $P_{ac,r}$, referred as γ, can be estimated by curve-fitting (7.4) with data derived from the electromagnetic model or measured data. The temperature dependence of the stator core, rotor core and PM loss components is typically insignificant, hence neglected, however this assumption can be verified by analysing the measured data. If found substantial, this effect can be modelled using (7.10), as a first approximation. For instance, the temperature coefficient of the stator core pack resistivity

of M-I is 0.1%/°C, which resulted in a temperature coefficient of the eddy current loss of -0.17%/°C.

The ability of the model to account for the magnetic saturation can also be evaluated from these tests. This ability is important for machines where the rotor leakage flux highly depends on magnetic saturation, such as M-III's and M-IV's IPM designs. The number of points on the manufacturer provided B-H curves may not be sufficient to accurately model the magnetic saturation, which would impact the predicted machine capabilities. In [113] and [154], a detailed description of the empirical derivation of additional B-H curve points is described in detail for M-III and M-IV, respectively, together with the impact of an insufficient number of B-H curve points on electromagnetic performance predictions.

Once all the power loss components have been determined, a thermal analysis is required to fully comprehend the results from machine full load tests.

7.2.4 Thermal analysis

The use of the proposed methodology allows the identification of thermal parameters associated with the stator-winding region of the machine assembly. At the end of the design process, further information is required regarding the machine's overall thermal behaviour, such as the effects resulting from the rotor rotation, e.g. end-space heat transfer coefficients or rotor cooling set-up. In this case, the complete machine assembly needs to be analysed. Fig. 7.8 summarises the proposed approach for the derivation of the complete machine thermal parameters in the light of the developed methodology. Prior to machine testing, the unknown parameters of the thermal model would be selected based on data from the literature, software default data or the machine designer's own experience.

A common first step for the thermal analysis of complete machine assembly is to complete tests with dc current excitation until thermal equilibrium. Machine tests provide insight into rotor thermal parameters independent of the machine dynamic behaviour, including material thermal conductivity, specific heat capacitance, thermal contact resistance and convective heat transfer coefficient data, among others. The impact of the testing set-up on the machine transient and steady-state temperatures, e.g. flange mount, machine feet, among others, can also be evaluated.

When the proposed methodology has been applied and if the stator assembly has been tested prior to being fitted in the housing frame, the main focus of the dc tests would be the estimation of the stator-to-housing thermal contact resistance R_{s-h}.

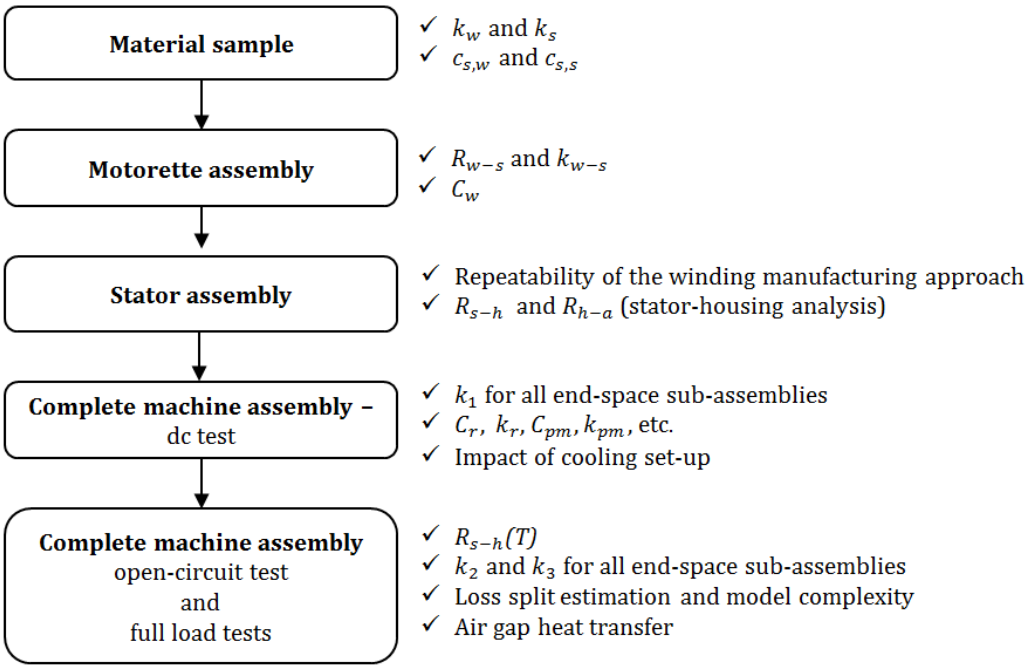

Fig. 7.8 Schematic diagram of the proposed methodology for the complete machine thermal analysis, k_w and k_s: equivalent winding and stator core thermal conductivity, $c_{s,w}$and $c_{s,s}$: winding and stator core specific heat capacitance, R_{w-s} and k_{w-s} : equivalent winding-to-stator thermal contact resistance and thermal conductivity, respectively, C_w: winding heat capacitance, k_1, k_2 and k_3: end-space heat transfer coefficients, C_r and C_{pm}: rotor and PM heat capacitance, k_r and k_{pm}: equivalent rotor core and PM thermal conductivity

This is particularly important for machine assemblies where the heat produced within the winding region is extracted via the housing frame. The impact of the core and housing temperatures on the stator-to-housing thermal contact resistance may also need to be investigated. At elevated temperatures, the higher coefficient of thermal expansion of aluminium compared to the laminated core pack may result in a worse thermal contact resistance between the two regions. This worsened contact will reduce the pressure fit between the two assemblies, which may lead to a reduction in the hysteresis loss associated with mechanical stress. Therefore, the resulting impact of elevated stator core and housing frame temperatures on the complete machine thermal behaviour cannot be straightforwardly predicted. Note that if the machine is equipped with a housing water jacket, the thermal expansion is limited due to the aluminium housing fixed temperature.

A reverse phenomenon may occur for the rotor-to-shaft thermal contact resistance R_{r-sh}, as in this case the thermal expansion of the shaft will improve the contact between both assemblies, but also lead to an increase in rotor iron loss. A good estimation of the contact between the shaft and the rotor is crucial for machines where a large part of the rotor heat is extracted within the shaft, e.g. shaft spiral grove. Investigating the temperature

dependence of R_{s-h} and R_{r-sh} using data from dynamic full load tests allows a more accurate representation of the machine thermal behaviour.

Heat transfer to the machine outer environment

The convective and radiative heat transfer from the machine periphery to its external environment may be evaluated. These two phenomena appear simultaneously and are therefore difficult to separate using measurement data. A dominant heat transfer mechanism may emerge, e.g. radiative heat transfer is usually negligible compared to forced convective cooling [99]. In this case, a single equivalent thermal resistance R_{h-a} may be used to represent both phenomena. The approach discussed in Chapter 6 based on dc test data can be used to estimate R_{h-a}. Equations (2.14)-(2.18), and (2.19), can be used in parallel to evaluate the individual contribution of the convective and radiative heat transfer mechanisms, respectively [112].

In cases where the heat management relies on multiple cooling methods, superposition testing may be use to isolate the contribution of each individual heat transfer effect. For instance, each cooling method can be tested individually, and if more information is required, tests can be completed with all cooling set-ups working and with no cooling. For each configuration, several operating points should be evaluated, e.g. tests with a range of cooling liquid temperatures and heat flow rates in the case of liquid-cooling, or with various air flow velocities in the case of air-cooling.

End-space heat transfer coefficients

Additional thermal parameters of interest include the heat transfer coefficients associated with the end-space region. The end-windings are typically the expected machine hot spot location for machines cooled via their housing frame, which makes the estimation of the end-space heat transfer crucial for machine designers. This machine area is usually very challenging to account for in thermal analysis, as the fluid flow in this region depends on parameters such as rotational speed of the rotor assembly, or shape and length of the end-windings. CFD analysis is required to get an accurate and comprehensive insight of the heat flow behaviour [185]. Depending on the model resolution and complexity, the use of this numerical method might be computationally expensive with time intensive model set-up. Several authors have proposed correlations to estimate the end-space behaviour, with the main form expressed as follows,

$$h = k_1(1 + k_2 n^{k_3}) \qquad (7.11)$$

where k_1 accounts for the natural convection when the rotor is stationary, and k_2 and k_3 account for the forced convection due to the rotation of the rotor assembly and n is averaged air velocity [238]-[240]. Table 7.1 lists some examples of published end-space coefficients used in (7.11). Additionally, a series of coefficients are provided for various end-windings geometry in [240]. An individual calibration is usually completed for each sub-assembly of the machine end-space region for k_1, k_2 and k_3.

Table 7.1 Published end-space coefficients

Machine configuration	k_1 [W.m^{-2}.°C^{-1}]	k_2 [m^{-1}.s]	k_3 [-]	Reference
TEFC IM	15.5	0.39	1	experimental data obtained for n<7.5 m.s^{-1} [164]
IM	15	0.4	0.9	[238]
IM	10	0.54	2	[239]

The heat transfer coefficient k_1 does not depend on the machine rotational speed, and can therefore be derived from dc tests on a complete machine, or stator assembly. No method is available in the literature for the specific derivation of this parameter. The method described in Chapter 6 where the stator periphery is entirely insulated apart from the assembly of interest (here the end-windings) could be adopted for the derivation of the parameter k_1 associated with the end-windings. This was however out of the scope of this thesis and will be discussed in the context of future work. Machine open-circuit or full load tests are required for the estimation of k_2 and k_3. As discussed previously, a series of tests with different rotational speeds is usually recommended. This is to account for the effects associated with change of fluid flow on the thermal parameters.

The derivation of k_1, k_2 and k_3 is crucial for machines where most of the heat is extracted via the end-windings, e.g. end-winding oil spray cooling. In [129], a fluid is passed down a duct in the shaft and then sprayed at the end-space thanks to centrifugal effects, while a measured amount of oil remains in the air gap and is splashed around by the rotor rotation. In this case, distinct k_1, k_2 and k_3 parameters may be required for different sub-regions of the same assembly. For instance, inner and outer end-winding regions are not exposed to the same amount of oil, and therefore require individual calibration in this case.

Air gap heat transfer

Another heat transfer path of interest is the heat transfer through the machine air gap. As the heat spontaneously flows from hot to cold, an amount of the heat produced within the winding assembly is usually transferred to the rotor via the machine air gap [121]. The dimensionless convection relationships developed from tests on concentric cylinders are

commonly used to estimate the heat transfer across the air gap [241]. These tests have been briefly discussed in Chapter 2 in the context of custom-designed experiments. The Nusselt number *Nu* can be derived as follows,

$$Nu = \varepsilon_1 . Ta^{\varepsilon_2} . Pr^{0.27} \qquad (7.12)$$

where *Ta,* ε_1 and ε_2 are the Taylor number and dimensionless coefficients, respectively, and *Pr* is the Prandtl number, which can be calculated using (2.16). The Taylor number must be first derived using (7.13) to determine if the flow in the air gap is laminar, vortex or turbulent,

$$Ta = Re . \sqrt{t_g / r_r} \qquad (7.13)$$

where t_s, r_r, and *Re* are the air gap radial thickness, rotor outer radius and Reynolds number, respectively. The Reynolds number can be derived from (2.18). The appropriate correlation is then selected for the calculation of the air gap heat transfer coefficient [121]. Table 7.2 lists some examples of published air gap coefficients used in (7.12).

Table 7.2 Published air gap coefficients

Flow type	*Ta*	*Nu*	ε_1	ε_2
Laminar	*<41*	2	-	-
Vortex	∈ [41, 100]	Equation (7.12)	0.202	0.63
Turbulent	>100	Equation (7.12)	0.386	0.5

The consequence of stator and rotor slotting on the air gap heat transfer has been investigated in [242], showing significant heat transfer increase for turbulent flow. However, no formula has yet been proposed to account for this effect.

7.3 Sensitivity analysis

Sensitivity analyses have been conducted to illustrate the impact of the winding thermal conductivities in the circumferential and radial directions (here x- and y-axes, respectively), $k_{w,x}$ and $k_{w,y}$ and the equivalent winding-to-stator air cavity thickness $t_{air,w-s}$. The thermal models presented in section 7.2.2 have been used. Each machine has been analysed at its base speed and the power losses, derived in section 7.2.3, have been input in to the models. For the sensitivity analysis of the winding thermal conductivities $k_{w,x}$ and $k_{w,y}$, a perfect winding-to-stator interface has been assumed, i.e. $t_{air,w-s}$=0. The range of parameters $k_{w,x}$ and $k_{w,y}$ has been obtained from the winding samples investigated in Chapter 4 and corresponds to different levels of winding impregnation 'goodness'. For the sensitivity analysis of the equivalent winding-to-stator air cavity thickness, the measured

winding thermal conductivities $k_{w,x}$ and $k_{w,y}$ of each investigated machine were input in the thermal models. The range of equivalent winding-to-stator air cavity thickness $t_{air,w-s}$ has been found from the motorette exemplars studied in Chapter 5. The software default parameters have been selected for the rest of the machine regions [130], e.g. the equivalent stator-to-housing interface air cavity thicknesses (or equivalent stator-to-shaft interface air cavity thickness for M-II) were set to 0.01 mm, which corresponds to a good surface contact.

Fig. 7.9 presents the temperature variation of all analysed machines for various $k_{w,x}$ and $k_{w,y}$. For all analysed machines, the impregnation nuances have been shown to have a significant influence on the winding conductivity: an underestimation of the data could lead to an overestimation of the winding hotspot, hence an 'over conservative' design. For all machines $k_{w,x}$ and $k_{w,y}$ have been varied independently. In practice, these parameters should not vary too much for windings formed with round conductors. The sensitivity analysis nonetheless provides some information about the way the heat transfers from the winding to the stator core. On the one hand, M-I seems more sensitive to $k_{w,y}$ than to $k_{w,x}$, suggesting that most of the heat is transferred from the winding to the housing through the stator yoke. On the other hand, the impact of $k_{w,y}$ is as important as $k_{w,x}$ for M-II and M-IV, suggesting that a non-negligible amount of heat is extracted via the stator teeth.

A similar sensitivity analysis has been completed for M-II for the core thermal conductivity. The range of parameters $k_{w,x}$ and $k_{w,y}$ has been obtained from a variation of the lamination stacking factor using (4.5). A variation of less than 3ºC has been observed for a difference in stacking factor of approximately 15%. In practice, the stacking factor is kept high as a lower value would significantly reduce the flux carrying capacity of the region. The packing factor is expected to have more impact on the thermal conductivity across the laminations. This should be investigated when considering a machine where a non-negligible quantity of heat is expected to be extracted axially, e.g. end-winding spray cooling.

Fig. 7.10 presents predicted winding hot spot temperatures for all investigated machines for various equivalent winding-to-stator air layer thicknesses. M-II appears to have less sensitivity to the equivalent winding-to-stator air layer thicknesses than the other machines but still shows an 8ºC variation for the range of analysed $t_{air,w-s}$. This confirms the importance of getting reliable and accurate data on thermal parameters at an early stage of the machine design process. In particular, and as mentioned in Chapter 5, these parameters

are challenging to predict analytically, as parameters such as the contact pressure from the winding to the stator core are hard to evaluate prior to the construction of a motorette or stator hardware exemplar.

The following section demonstrates practical use of the proposed methodology for informing the thermal design of electrical machines. Several case studies are presented where the selected machine hardware demonstrators are thermally analysed from the very onset of the machine design process. A detailed description for each of the selected case studies is provided by appropriate literature references.

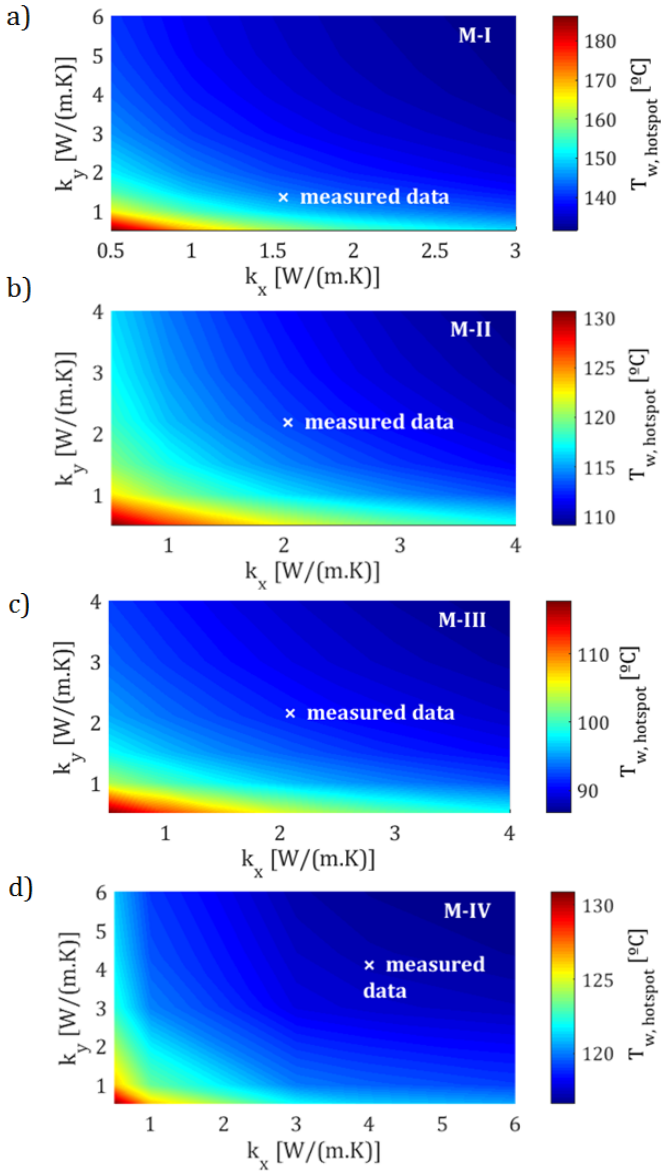

Fig. 7.9 Predicted winding hot spot temperature vs. radial and orthoradial thermal conductivity kx and ky, a) M-I, b) M-II, c) M-III, d) M-IV

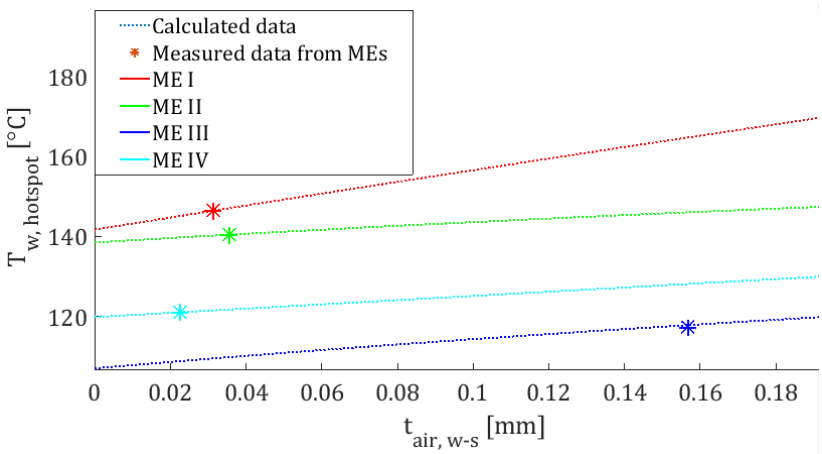

Fig. 7.10 Predicted winding hot spot temperature for all investigated machines vs equivalent winding-to-stator air gap layer thickness

7.4 Case Studies

7.3.1 Impact of slot shape geometry – Machine demonstrator I [55]

M-I comprises a parallel sided slot geometry, which should provide a superior conductor lay, and consequently improve the heat transfer from the winding to the stator core, but with the drawback of an increased stator core weight compared with a conventional trapezoidal shape [55]. The comparison of ME I (parallel slot shape) and ME I* (trapezoidal slot shape) quantifies the benefit of using parallel sided slot geometry. This comparison is the focus of a collaborative work completed in the context of this thesis, documented in [55], and has been used here for illustration.

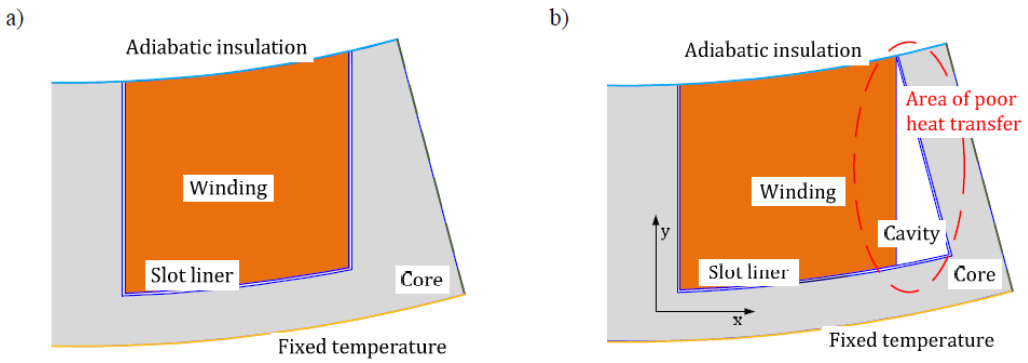

Fig. 7.11 Thermal model representation of the stator winding assembly together with boundary conditions; a) parallel sided slot geometry, b) conventional trapezoidal shape [55]

Fig. 7.11 presents a cross-section of the 3D FE models used for the estimation of the equivalent winding-to-stator thermal contact resistance. No convective heat transfer has been assumed from the end-winding regions, and the cold plate temperature has been set to 80ºC. According to the power loss analysis completed in Chapter 5, most of M-I ac winding loss effects are located in the upper layer, and therefore the winding region has

been segmented in to two layers (upper and lower) for this analysis, Fig. 7.12. The equivalent winding thermal conductivity data has been obtained from material sample WS-I.

The same coil is fitted in ME I and ME I*, however the ME I* trapezoidal slot leaves a cavity at the outer side of the coil. This cavity is assumed to be filled with an amalgam of varnish and air, depending on the 'impregnation goodness'. Figs. 7.12a) and 7.12b) show the temperature distribution within ME I* for 200 W of winding power loss, where the void within the slot is assumed to be fully occupied by impregnating varnish or air. No core loss is included, which corresponds to the testing procedure with dc excitation used for motorette thermal analysis. The impregnation 'goodness' for the cavity region has a significant impact on the outcomes of the comparative study, with more than 20 ºC difference in estimated hot spot temperature. This emphasises the need for a degree of hardware calibration in the thermal design of the stator/winding machine region.

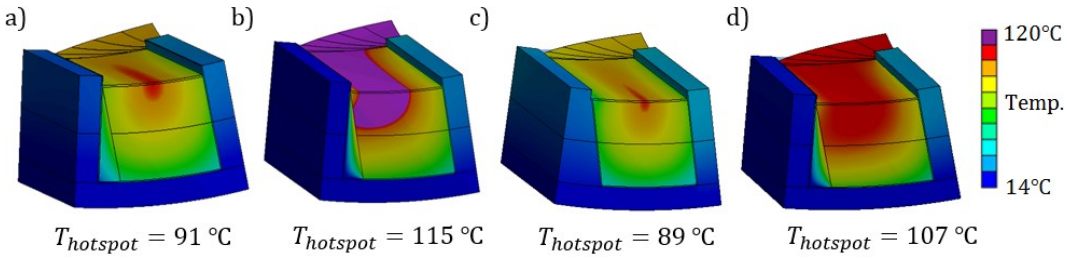

Fig. 7.12 Temperature distribution for 200W winding power loss; a) ME I* with experimentally calibrated equivalent slot liner region, b) ME I* with experimental calibrated slot liner region, c) ME I with ideal varnish impregnation, d) ME I* with empty air cavity (no varnish impregnation)

Figs. 7.12c) and 7.12d) show the temperature distribution within the stator winding assembly for MEs I and I* after model tuning based on empirical data. The equivalent slot liner regions have been calibrated using the approach described in Chapter 5. The theoretical predictions estimate an 18 ºC reduction in hot spot temperature when parallel slots are used instead of commonly adopted trapezoidal geometry. The heat distribution is also fundamentally different, with the heat from ME I* concentrated at the top winding layer. This effect is likely to be further exaggerated by the ac winding loss effects, resulting in non-homogeneous power loss distribution between the top and bottom winding layers. To provide an insight into the expected machine performance, and highlight the full benefit of the parallel and trapezoidal slot geometries, a coupled thermal and power loss analysis is therefore necessary.

Table 7.3 Assumed nodal loss breakdown at rated operation (values calculated at T_0=20ºC and for a single slot region) [55]

Node and loss type	$P_{dc,UW}$	$P_{ac,UW}$	$P_{dc,LW}$	$P_{iron,RT}$	$P_{iron,LT}$	$P_{iron,BI}$
ME I [W]	32.0	13.4	32.0	18.0	20.0	18.0
ME I* [W]	32.0	12.6	32.0	18.0	18.0	18.0

Table 7.3 lists the estimated loss components for each region at a fixed temperature T_0=20°C for the one slot. The subscripts *UW, LW, RT, LT* and *BI* refer to upper winding, lower winding, right tooth and left tooth (from Fig. 7.11), and back iron, respectively. Both the winding and core loss components are slightly larger for ME I. The ac loss components from the lower layer were found insignificant, and are therefore neglected. $P_{ac,r}$ has been evaluated using complete machine FE model, so that the MEs comparison would be more representative. The temperatures are predicted from input of the averaged losses occurring in the lumped regions. Here, the iron losses are assumed to be temperature independent, while (2.4) has been used to iteratively update the winding losses.

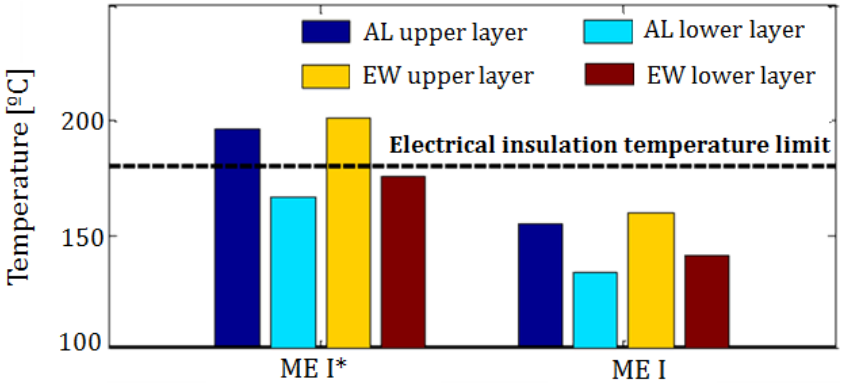

Fig. 7.13 Averaged winding temperature predictions from the coupled loss and thermal models of MEs I and I* [55]

Fig. 7.13 shows MEs I and I* predicted temperatures, with ME I parallel slots resulting in approximately 40°C lower hot spot winding temperature. Moreover, ME I* hot spot temperature would exceed the class H conductor electrical insulation temperature rating. Ensuring a similar operating temperature to ME I would lead to an 11% reduction in the torque output of ME I* at rated speed. In total, the parallel slot design of ME I allows for 35% improvement in dissipative heat transfer from the winding body into the stator core pack.

In [55], the net benefit of using a parallel slot shape has been evaluated. Taking into account the 12% increase in the mass of the stator core pack due to the iron surplus in the tapered parallel tooth, an 8% total improvement in the power output per active weight of the machine was found when changing the slot geometry from trapezoidal (ME I*) to parallel

(ME I). The coupled thermal and power loss ME analysis has provided crucial information for the thermal design of M-I, and the benefits in using unusual slot shape geometry.

7.3.2 Impact of conductor material and thickness – Machine demonstrator II [89]

Data from measurements on winding samples (Chapter 4) and motorettes (Chapter 5) have provided some insight into the thermal behaviour of M-II (copper conductors) and M-II* (aluminium conductors). Here, the focus is on the reduction of M-II's winding power loss.

M-II comprises an open-slot stator geometry, which encourages elevated winding loss from the PM rotor, and leads to strong non-homogeneous power loss distribution within the different winding conductors. A solution to reducing the magnitude of frequency-dependent winding loss is to replace copper conductors with a material of higher electrical resistivity, such as aluminium. The final machine performance and overall winding-loss is a fine balance between dc and ac loss components; hence, careful consideration of the winding design is essential to exploit the full benefits of a particular conductor material. Copper conductors with large cross-sectional area provide a good design solution when the dc loss component dominates the overall winding loss, whereas the use of aluminium conductors might be advantageous for applications where ac winding losses are otherwise severe. The comparison of M-II and M-II* quantifies the benefit of using alternative conductor material.

Data from power loss measurement on ME II and ME II* have been used to calibrate M-II and M-II* electromagnetic FE models. Each individual conductor has been represented in M-II (copper conductor) and M-II* (aluminium conductor) thermal model, based on initial FE analyses. Fig. 7.14 presents the FE prediction of the power loss component per individual conductor at MTPA operation of M-II and M-II*, for an excitation current of 400 Hz. The results endorse the importance of deriving the R_{ac}/R_{dc} ratio for each individual conductor, in particular for the conductor at the top of the slot where $P_{ac,r}$ is significant. Clearly, the common approach of averaging this coefficient over the entire winding region or volume would lead to significant discrepancies in estimations of M-II and M-II* power output capability.

Due to its high resistivity, the dc power loss component is more important in the case of aluminium conductors than copper conductors. For the conductors at the bottom of the slot, where the $P_{ac,r}$ components are insignificant, the total power loss component is more important for aluminium than copper.

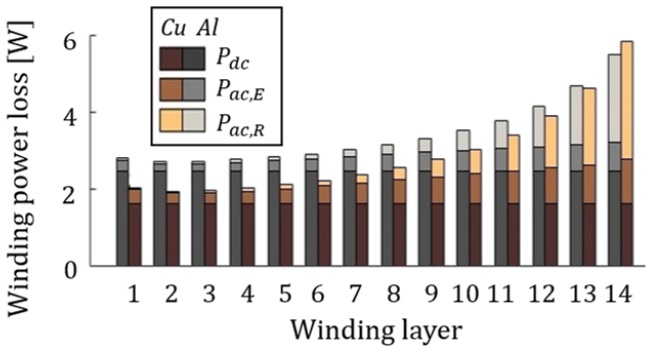

Fig. 7.14 Power loss per individual coil versus conductor layer for M-II and M-II* at rated operating point, I = 200 A_{RMS}, f=400 Hz and fixed winding temperature T = 20°C

Conversely, for the conductors located at the top of the slot, the high resistivity of aluminium leads to smaller eddy current reaction voltage from ac effects and therefore lower ac winding loss compared with copper conductors. For the studied operating point, copper is overall still a better alternative than aluminium, however depending of the frequency this trend could be reversed. The analyses have been completed here for a fixed winding temperature of T=20°C. However, in practice, M-II and M-II* would operate at higher temperatures. This would suggest copper conductors to be the most promising alternative in this case, as an increase in temperature would lead to a decrease in ac winding power loss effects, but an increase in dc power loss effects.

Because of the significant difference between the winding power loss at the top and bottom of the slot, the use of thinner conductors, with a resulting increased distance to the air gap, is worth considering. This has been investigated in [89] for copper conductors. Five conductor thicknesses were analysed starting from 2.0 mm to 1.2 mm with a conductor thickness step of 0.20 mm between neighbouring variants. Here, the same approach has been adopted for aluminium conductor. Fig. 7.15 presents the two limits of the winding alternatives considered.

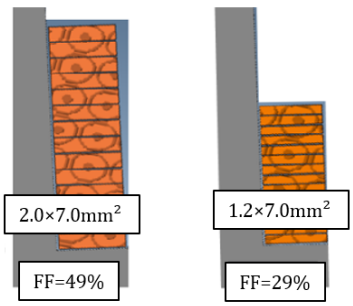

Fig. 7.15 Winding designs for several conductor thicknesses together with the winding fill factor *FF* – M-II and M-II* [89]

This investigation might seem abnormal for a designer used to the more common dc winding resistance or winding fill factor design criteria. However, the increase in dc winding loss might be lower than the reduction of ac winding loss, hence a reduction of total winding loss components.

Fig. 7.16 compares the FE prediction of the power loss component for several conductor thicknesses at MTPA operation of M-II and M-II*, at rated operating point, I = 200 A_{RMS}, f = 400 Hz and winding temperature T = 200°C. As expected, the reduced conductor thickness, which leads to reduced winding loss from the PM rotor, provides lower winding ac power loss than counterparts with relatively high winding fill factor. From Fig. 7.16, there is an optimal conductor thickness which has a minimum total winding loss component: 1.4 mm for copper conductors and 1.6 mm for aluminium conductors. The difference in optimum thickness for both conductor materials can be explained by their different resistivity. Comparison between aluminium and copper shows that aluminium is better when the ac power losses are dominant, i.e. for the elevated thickness conductor. However, aluminium never appears as the optimal option, and the copper intermediate conductor thickness design alternative seem to be the more promising option, and confirm the design choice made in [89] for M-II.

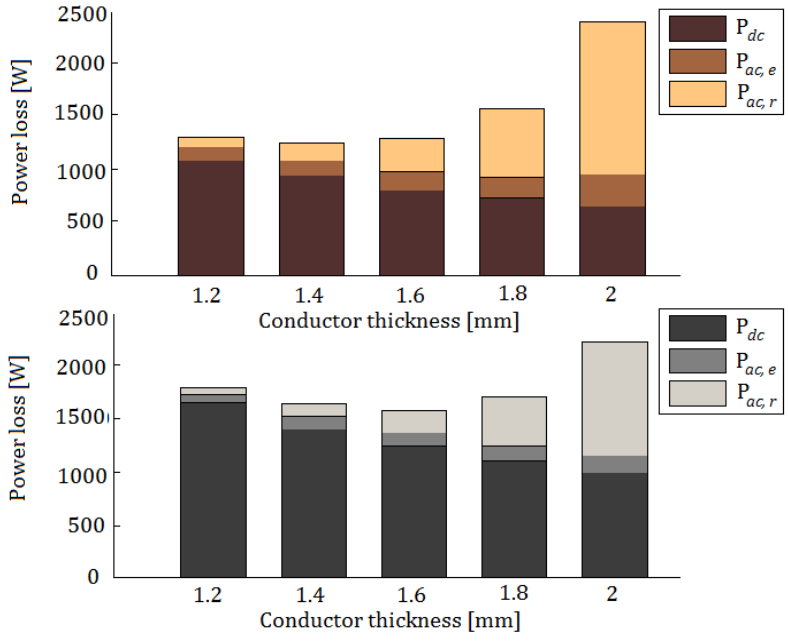

Fig. 7.16 Power loss versus conductor thickness for the generator assembly at rated operating point, I = 200 A_{RMS}, f= 400 Hz and winding temperature T = 200°C with copper (top) and aluminium (bottom) conductors.

The intended fixed speed operation of M-II makes it suitable for fine tuning. However, in most of modern applications requiring variable-frequency operation, the choice of

conductor material is further complicated. Indeed, a trade-off between dc and ac winding loss together with other machine loss components over a complete torque-speed envelope and operating cycle is necessary to make a fully informed decision regarding overall performance. This is investigated in the next section by comparing copper and aluminium conductors for M-IV over a complete operating cycle.

7.3.3 Impact of conductor material and thickness – Machine demonstrator IV [59], [113], [244]

Initial predictions from M-IV's FE analyses have shown that the ac winding power losses are significant if the stator slot window is fully utilised, i.e. high conductor fill factor is achieved. Both stator flux leakage and rotor field effects are high in the slot-opening region resulting in a localised and elevated ac loss component. To reduce the winding loss at ac operation, the conductors have been placed in the stator slot in such a manner that the area with high magnetic flux leakage is avoided, and a non-magnetic wedge is inserted in the stator slot [113]. In Chapter 5, it has been highlighted that the use of a slot wedge ensures 'good' heat transfer from the winding body into the stator core pack [113]. As previously done for M-II, it is intended to investigate the impact of conductor materials and the aspect-ratio/dimensions of the conductor cross-section on overall performance.

Table 7.4 Selected geometric data of studied winding variants for M-IV

WV	Conductor aspect ratio	Conductor cross section	Fill factor
I	0.36	4.2 mm²	43%
II	0.53	4.8 mm²	50%
III	0.6	5.4 mm²	56%

Table 7.4 presents basic geometric data relating to three winding variants (WV) analysed for both aluminium and copper. Throughout this section, winding variant I with aluminium (*Al*) conductors is referred to as WV I-*Al*, while winding variant I with copper (*Cu*) conductors is referred to as WV I-*Cu*. Note that WV I-*Cu* is the winding variant adopted for M-IV final design. In the comparative study presented here, the conductor width w is fixed and set by the slot depth (see Fig. 7.17); therefore, only the conductor thickness h is modified to accommodate the different winding variants. The windings consist of two layers per slot, which respectively comprise 14 and 10 turns for WVs I and II. For WV III, due to the limited slot width, the winding consists of two layers per slot with 12 turns each. Increasing the conductor cross-sectional area in turn increases conductor fill-factor within the slot, as seen in Table 7.4.

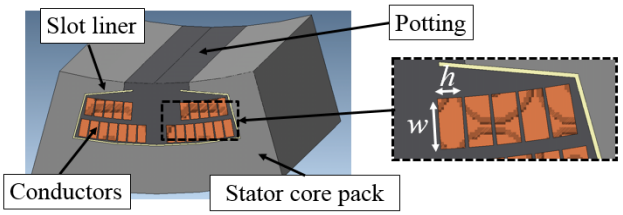

Fig. 7.17 Outline of M-IV's winding assembly [244]

Table 7.5 Winding equivalent thermal conductivity data

	Cu		*Al*	
WV	k_x [W/mK]	k_y [W/mK]	k_x [W/mK]	k_y [W/mK]
I	4.0	4.3	4	4.2
II	4.4	4.4	4.4	4.3
II	4.9	4.4	4.8	4.3

The thermal conductivity values for all WVs have been derived using (4.24). Table 7.5 presents the values obtained for these studied winding configurations. The change in thermal conductivity is higher for k_x than for k_y. This can be explained by the fact that only the conductor thickness is varied for this study. Moreover, despite the difference in thermal conductivity for copper and aluminium, the impact on thermal conductivity is limited. This is due to the low thermal conductivity of the conductor electrical insulation being the limiting factor which dominates the winding equivalent thermal conductivity.

The thermal model presented in section 7.2.2 makes use of (2.5) to account for the temperature dependence of the winding power loss. For this analysis, the influence of the current angle on R_{ac}/R_{dc} ratios has been investigated. This effect has not yet been researched in the literature, however was worth investigating for the comparison of winding variants over a complete duty cycle, including field weakening operation. When accounting for the current angle, the functional representation of the ac winding power loss temperature dependence may be expressed as follows,

$$P_{\substack{ac \\ T}} = P_{\substack{dc \\ T_0}}\big(1+\alpha(T-T_0)\big) + P_{\substack{dc \\ T_0}} \frac{\left(\frac{R_{ac}}{R_{dc}}(I_{pk},\gamma_I)\right)_{\substack{e \\ T_0}} - 1}{\big(1+\alpha(T-T_0)\big)^{\beta}} + P_{ac,r|T_0} \frac{1}{(1+\alpha(T-T_0))^{\gamma}} \quad (7.12)$$

where,

$$\left(\frac{R_{ac}}{R_{dc}}\right)_{e\,|T,I_{pk}} = \left(\frac{P_{ac}(\gamma_I)-P_{ac,r}}{P_{dc}}\right)_{e\,|T,I_{pk}} \quad (7.13)$$

The $(\frac{R_{ac}}{R_{dc}})_{|T_0}$ ratios have been derived by coarsely mapping the winding power loss at T_0 for I_{pk} and γ_I using 2D FE analyses and interpolating between the derived data points.

Figs. 7.18a) and 7.18b) present calculated $(R_{ac}/R_{dc})|_{T_0}$ for M-IV for a fixed winding temperature of 20˚C, f=400 Hz versus current amplitude I_{pk} and current angle γ_I, respectively. The impact of I_{pk} is noticeable at lower currents, where the impact of $P_{ac,r}$ becomes prominent in comparison to other winding loss component. The effect of current angle γ_I on $(R_{ac}/R_{dc})|_{T_0}$ ratio seems limited, however it follows a trend of a reduction in the magnitude of slot leakage due to the flux weakening operation. This observation may appear counter intuitive when considering the conductor at the top of the slot. An elevated I_{pk} would be expected to lead to a raise in slot leakage. Similarly, at field weakening operation, the rotor flux is shunted across the slot opening, which should result in an increase in slot leakage.

After further investigation, it appears that the results shown at Figs. 7.18a) and 7.18b) account for some averaging effects among the conductors. Fig. 7.18c) presents the results where only the ac effects due to current excitation are accounted for when evaluating the influence of γ_I. As expected, the ac effects are increasing for conductors located near the slot opening. For conductors remote from the slot opening, the overall reduction in stator flux at field weakening operation leads to a reduction in ac loss effects.

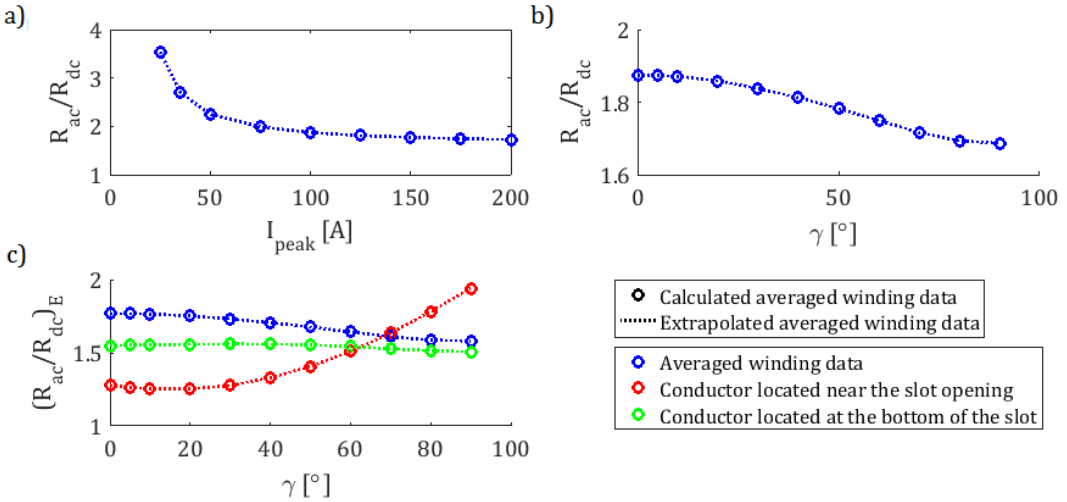

Fig. 7.18 Calculated $(R_{ac}/R_{dc})|_{T_0}$ for M-IV for winding temperature T_0 = 20˚C, a) Averaged winding data derived for current amplitude, γ_I=5˚, b) Averaged winding data derived for current angle, $I_{peak} = 100\ A$, c) Individual conductor data derived for current angle, $I_{peak} = 100\ A$

An illustration of the influence on R_{ac}/R_{dc} ratio caused by current angle and magnetic saturation is shown in Fig. 7.19, which is calculated for the winding variant adopted in M-IV, WV I-*Cu*. Fig. 7.19a) presents the target torque-speed envelope and calculated efficiency map using a simplified $R_{ac}/R_{dc}(f)$ variation, which is derived from analysis for rated current under MTPA control. In contrast, Fig. 7.19b) presents the required torque-

speed envelope with efficiency map using $R_{ac}/R_{dc}\,(f, I_{pk}, \gamma_I)$ accounting for current angle γ variation under field-weakening. A dashed-border square box has been placed in Fig. 7.19 to highlight the impact of these individual approaches. For efficiency analyses, it has been assumed that all the machine active components are at a fixed temperature of 100°C.

When analysing the efficiency maps, it appears that accounting for the change in current angle γ and current magnitude in field weakening operation results in a narrower window of "high" efficiency operation. The influence for this particular machine is small, with limited change outside of the "high" efficiency window. However, the variation of current angle γ and current magnitude is expected to have more impact for WVs where ac effects are more prominent, e.g. WV III, which has the largest conductor cross-section.

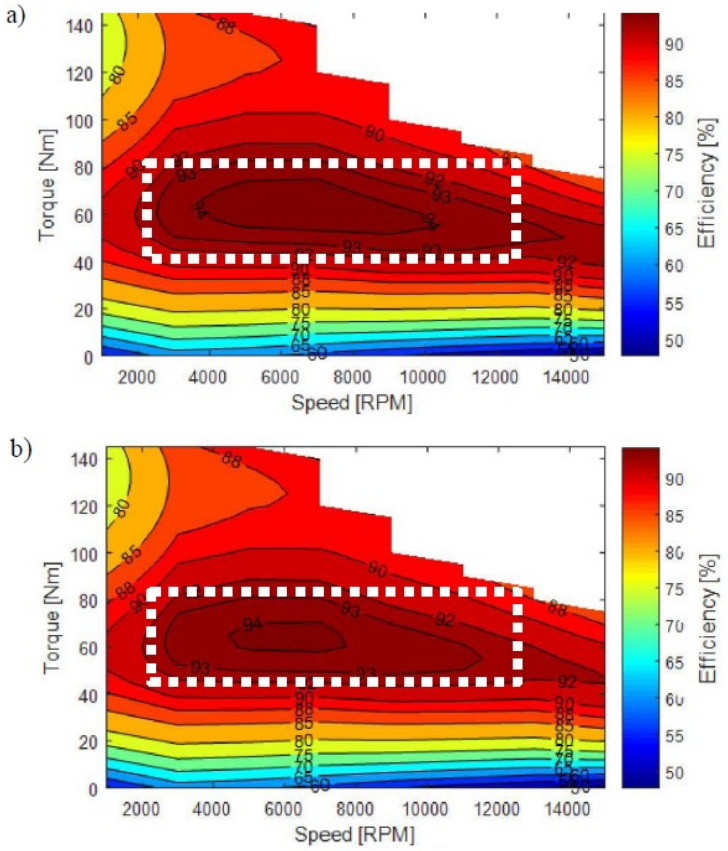

Fig.7.19 Targeted torque-speed envelope together with efficiency map calculated for WV I-*Cu*, a) $R_{ac}/R_{dc}\,(f)$ calculated at maximum torque/ampere, b) $R_{ac}/R_{dc}\,(f, I_{pk}, \gamma_I)$ accounting for flux weakening and magnetic saturation – M-IV [244]

Fig. 7.20 presents target torque–speed envelopes together with efficiency maps for all winding variants studied for M-IV. As previously, it has been assumed for the analysis that all the machine active components are at a fixed temperature of 100°C. When analysing the efficiency maps, it is clear that WV I-*Cu*, Fig. 7.20a), exhibits the largest "high" efficiency operation region, set between 3000 rpm and 12000 rpm. In comparison WV I-

Al, Fig. 7.20d), has its high efficiency operation set between 12000 rpm and 15000 rpm, respectively. This confirms that aluminium offers an interesting alternative to copper when the ac effects are dominant at high operating frequencies. This effect would be exaggerated if the stator was of an 'open-slot' design where the conductors would suffer increased losses due to slot-leakage and rotor field interactions. Likewise, it can be noted that WV II-*Cu* and WV II-*Al* offer very similar efficiency for rotational speeds higher than 4000 rpm.

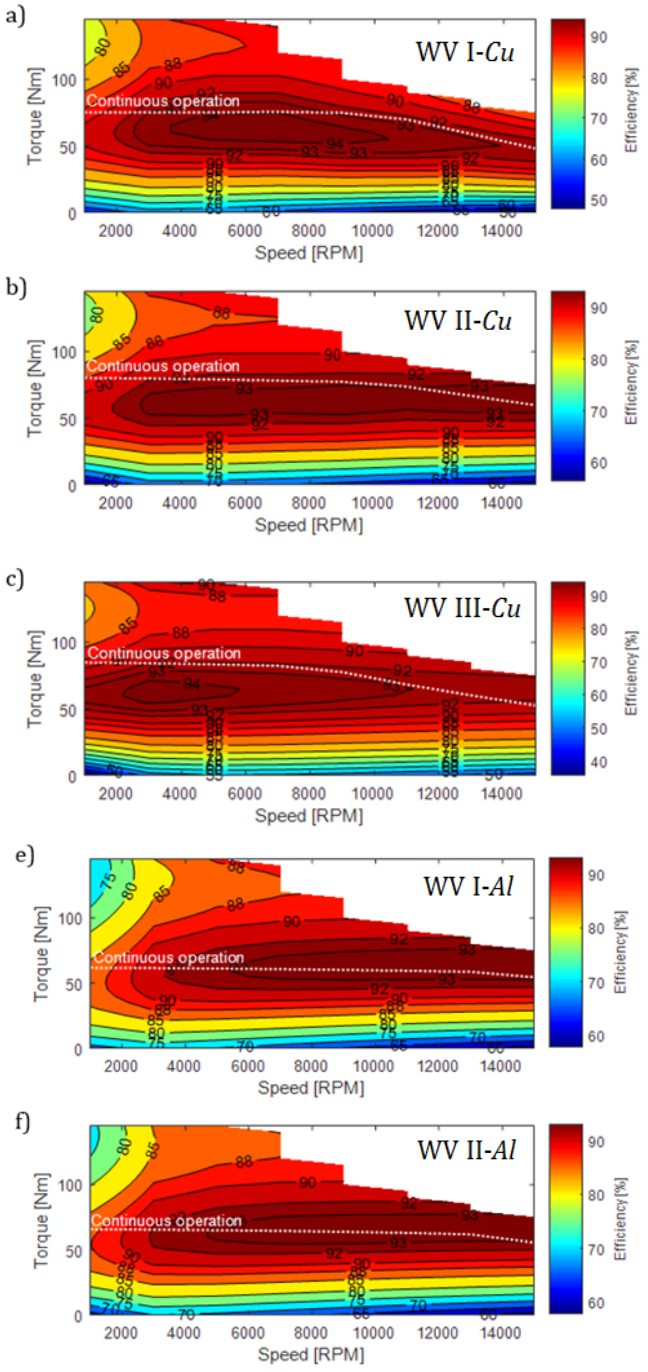

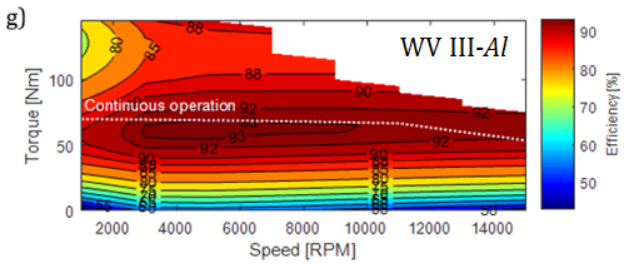

Fig.7.20 Target torque–speed envelope together with efficiency map for WVs, a) WV I-*Cu*, b) WV II-*Cu*, c) WV III-*Cu,* d) WV I-*Al*, e) WV II-*Al*, f) WV III-*Al* [244]

The continuous operating envelope is also presented in Fig. 7.20 with a dashed line. Here, the winding hot spot temperature limit has been set to 180 °C with machine housing at 80 °C and 20 l/min coolant flow for the water jacket. It is clear that WVs III, in particular with copper conductors, provide higher torque at 'low' rotational speed. However, the trend is inverted at 'high' rotational speed, where WVs I, in particular with aluminium conductors, are less affected by the ac effects.

The efficiency maps presented at Fig. 7.20 provides comprehensive insight into the machine performance with alternative conductor materials and aspect ratios. However, the intended duty cycle is a combination of continuous and transient operations, and therefore the analysis of the machine performance for a representative operating cycle would offer complete information concerning the design choice. Fig. 7.21 presents a representative operating cycle assumed in the analysis and reveals the transient nature of operation intended for the machine.

The duty cycle is based on the Extra-Urban driving cycle (EUDC) with a gear ratio of 1:3. The basic data from the vehicle model assumed to derive the required torque from the driving cycle is listed in Table 7.6.

Table 7.6 Basic data from the vehicle model used in torque derivation

Mass [kg]	Frontal Area [m^2]	Wheel Radius [m^3]	Rolling Resistance Coefficient	Drag Coefficient	Air Density [$kg.m^{-3}$]
1360	1.746	0.3	0.0054	0.26	1.225

Table 7.7 lists the averaged performance of M-IV for all winding variants calculated over the operating cycle shown in Fig. 7.21. The calculated results show that WVs with copper conductors provide the greatest average efficiency and continuous torque for the envisioned operating duty cycle.

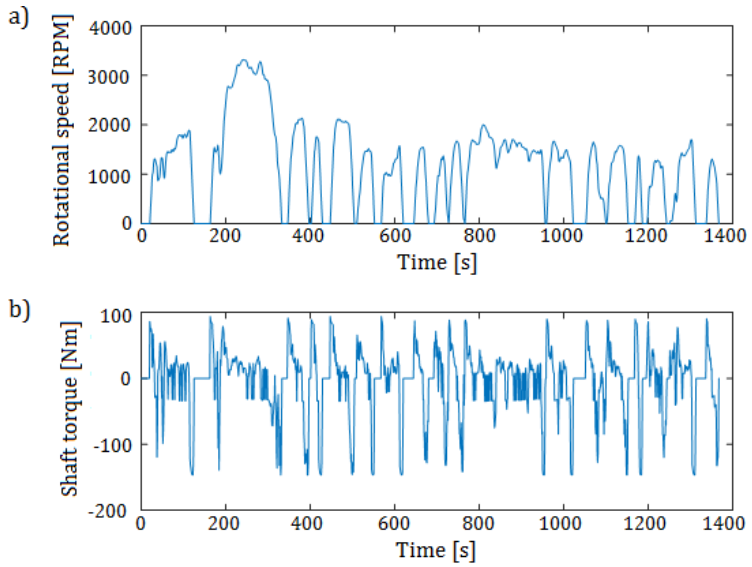

Fig. 7.21 Operating cycle assumed in the analysis; a) Rotational speed vs. time, b) Shaft torque vs. time [244]

On the other hand, WVs with aluminium have significantly lower weights and prices as compared with copper counterparts. Depending on the intended machine use, e.g. automotive application, it might be preferable to have only a small reduction in efficiency, 2%, over a driving cycle and have an overall mass saving of 3 kg. Therefore, the designer's choice could vary between WV I-*Cu* and WVII-*Al* depending on the most important design paradigms to be satisfied, e.g. "design for cost", "design for manufacturability" and/or optimizing overall vehicle efficiency.

Table 7.7 M-IV averaged performance measures over the operating cycle for different winding variants

	Cu			*Al*		
WV	I	II	III	I	II	III
Avg. efficiency [%]	85.7	86.3	85.9	83.4	84.4	83.9
Avg. power loss [W]	23.6	22.9	23.7	28.7	26.7	27.70.
Price [$] [243]	21.1	24.0	27.5	2.1	2.3	2.7
Winding weight [kg]	3.6	4.1	4.7	1.1	1.2	1.4
Machine weight [kg]	33.3	33.8	34.4	30.8	31.0	31.1

7.4 Summary

This Chapter has presented the final building step of the proposed methodology, which utilises tests on complete machine assembly. Several approaches available for the complete machine analysis and in particular for loss separation, have been discussed. The baseline machines have been used for illustration on the estimation of power loss and thermal parameters. Three case studies have illustrated how the proposed methodology can be used early in the design process for the comparison of various alternatives:

- The first case study made use of the methodology to compare alternative slot shape geometries associated with M-I. Tests on a winding sample and motorette exemplars have been used to inform the thermal and electromagnetic model. In particular, results from motorette tests have highlighted the improved heat transfer from the winding to the stator core of the parallel sided slot geometry (ME I) when compared to the trapezoidal one (ME I*). Data from motorette ac power loss measurements were used to compare the two alternative slot shape geometries, showing insignificant differences between parallel and trapezoidal. Finally, an 8% total improvement in the power output per active weight of the machine was found when changing the slot geometry from trapezoidal to parallel.

- The second case made use of the methodology to compare alternative conductor materials associated with M-II (fixed speed application). Tests on winding samples confirmed that the use of aluminium conductor instead of copper has limited impact on the equivalent winding thermal conductivity, but plays a significant role on the specific heat capacity. The comparison between the motorettes with copper (ME II) and aluminium (ME II*) conductors did not reach a conclusion on the best alternative, as different tooling had been used to manufacture the coils. This resulted in different conductor lays, which impacted the winding-to-stator heat extraction capability. The impact of different manufacturing techniques on the heat transfer was nonetheless useful to have at an early design stage, as the difference of heat extraction capability provided by both windings would influence the thermal designer in the coil manufacturing tooling to adopt in the final machine design. Results from motorette power loss tests have shown significantly lower $(R_{ac}/R_{dc})_e$ in the case of the windings formed with aluminium conductor. Measurement data have also been used to inform FE electromagnetic models, which were used to find the optimal thickness for M-II's windings formed with copper or aluminium conductor. The results shown that the optimum differs for both conductors' materials. The intended fixed speed operation of M-II made it suitable for a fine tuning.

- The third case made use of the methodology to compare alternative conductor materials and cross-sections associated with M-IV (variable speed application). Tests on winding samples and results from Chapter 4 about variation of equivalent winding thermal conductivity have been used to predict the thermal behaviour of the analysed design variants for both aluminium and copper. The motorette has

been used to evaluate the winding power loss due to excitation. In particular, M-IV's single-layer modular winding configuration made a single motorette representative of the complete stator assembly. The FE electromagnetic models have been calibrated using this data. The comparison of efficiency maps and machine power loss for complete duty cycles allowed the most promising design variants to be identified depending on the most important design criteria to be satisfied.

The case studies confirmed that by providing essential information about the analysed machines' stator-winding heat extraction capability, each building step of the methodology allows one to incorporate accurate thermal analysis from the onset of the machine design process. The use beforehand of the three first building blocks greatly simplified the thermal model validation and loss separation process, as only a reduced number of parameters are still unknown when analysing data from a complete machine assembly. By improving the thermal designer's understanding of the machine electromagnetic and thermal behaviour, and allowing for a well-informed design process, the methodology should contribute to pushing forward the boundaries of machine design, with fully optimised machine prototypes.

Chapter 8
Conclusions and future work

8.1 Rationale of Presented Work

The main objective of this thesis has been the development and validation of a systematic and reliable experiment-informed methodology for high-fidelity thermal design of electrical machines. Three machine sub-assemblies have been selected based on their capability to incrementally inform the machine thermal design as a basis for the proposed methodology.

A thorough literature review has been completed in Chapter 2, providing an overview of the main themes associated with thermal management of electric machines. The deficiencies and uncertainties associated with the traditional machine testing techniques have been identified, along with the benefits of machine sub-assembly testing solutions.

The selected building blocks of the developed methodology have been presented in Chapter 3, with emphasis placed on the thermal and power loss parameters to be estimated. The baseline machines selected for illustration have been introduced, together with reflections on how to enhance the robustness of the methodology.

The first building block of the methodology, material sample, has been investigated in Chapter 4. A repeatable procedure, making use of theoretical and empirical analyses for the estimation of equivalent thermal properties of impregnated windings, has been presented. A number of hardware winding samples have been used to demonstrate the proposed approaches, establishing a library of thermal conductivity and specific heat capacity data for thermal designers.

The second building block of the methodology, motorette assembly, has been presented in Chapter 5. A systematic procedure has been proposed for the estimation of the winding-to-stator thermal contact resistance, taking into account the thermal sensors quantity and location, and three-dimensional effects. The use of motorette assembly for the derivation of selected winding and core loss parameters has also been discussed, emphasising the benefit of power loss separation for an accurate and consistent power loss analysis.

The third building block of the methodology, stator assembly, has been investigated in Chapter 6. A procedure has been presented for the estimation of the winding heat capacitance in a reliable and time-efficient manner. The proposed method has also been applied to motorette exemplars, showing good correlation with the complete stator-winding assembly. The interactions between neighbouring stator phases and their impact on winding power loss characterisation have been discussed through alternative testing approaches.

Finally, the final building block of the methodology, complete machine assembly, has been presented in Chapter 7. Several complete machine testing approaches available for the estimation of power loss and thermal parameters for complete machine analysis have been examined. The proposed methodology has been illustrated in the context of alternative machine design comparisons. The use of each building step of the proposed methodology has provided crucial information about the thermal and power loss behaviour of the analysed electrical machines, and allowed for well-informed electromagnetic and thermal machine design.

8.2 Contribution to knowledge

The presented research objectives have delivered several contributions, which are summarised as follows.

- Two sets of formulae, associated with round and rectangular conductor types, have been provided in order to facilitate the estimation of the equivalent winding thermal conductivity. The approach accounts for the conductors' shape and placement within the winding assembly, which leads to more accurate predictions of the equivalent thermal conductivity when compared to existing techniques based on volumetric components. The large number of tested winding samples has been used to derive some guidelines into the transferability of measured data from one winding sample to the other. This allows for time effective and accurate derivation of thermal properties for composite materials, including the material thermal anisotropy.

- A technique for the estimation of the winding heat capacitance based on the winding temperature measurements has been developed, and has been applied using both motorette and stator assemblies. The proposed technique has shown improved accuracy compared to the existing approaches, without any drawback in

terms of testing time or hardware exemplars. The comparison between data obtained from motorette and stator assemblies, and data obtained from winding sample, has confirmed the validity of material sample data for first estimation of the winding heat capacitance.

- A systematic procedure has been presented for the estimation of the winding-to-stator thermal contact resistance. A library of winding-to-stator thermal contact resistance data from all investigated configurations was also established. The impact of the measured data from alternative thermal sensor locations and quantity on the quality of the model calibration; and consequently temperature predictions, has been thoroughly analysed using motorette testing. In particular, the ambiguity associated with the use of 3D data (e.g. from end-wining measurements) for the calibration of 2D thermal model has been highlighted. The analysis of the experimental data has shown that the resolution used to calibrate a particular thermal model should match or exceed the model fidelity.

- Various effects associated with the winding and core power loss have been highlighted using motorette and stator testing, with emphasis on the estimation of the ac excitation-to-dc winding power loss ratio. Different procedures have been introduced and compared for the estimation of these effects, depending on previously available data or testing equipment, and confidence in the electromagnetic models. The testing procedures include single-phase, single-phase 'series-parallel' tests or three-phase tests. The latter were shown to be more representative of the ac winding power loss of a complete machine assembly. The representativeness of motorette assembly has also been discussed in this context. For non-isolated winding slot, the motorette were not directly relatable to complete machine, but shown useful for the calibration of electromagnetic models, and for the comparison of alternative configurations.

- A comparative study upon the performance of an IPM machine fitted with alternative winding conductor materials has been completed, contrasting the impacts of aluminium as an alternative to copper for high-speed/high-frequency applications where ac effects are elevated. Due to its high electric resistivity, aluminium is less prone to ac effects, which allows for an increased conductor fill factor as compared with the copper counterpart. The improved conductor fill factor

for aluminium windings permits compensation for elevated levels of dc loss, which is higher than that for the copper equivalent. The results suggested changes in averaged efficiency over the desired duty cycle and efficiency maps appears to be relatively limited. When accounting for the significantly reduced price and weight of aluminium as compared with copper, a design choice might be made depending on the most important design paradigms to be satisfied, e.g. “design for cost” or “design for manufacturability”.

- Finally, the building steps of the proposed methodology have been used for complete machine analysis to showcase how the selected sub-assemblies can incrementally inform the machine thermal design. Appropriate, incremental machine tests focused on selected power loss parameters allow for an improved power loss separation. The case studies confirmed that by providing essential information about the analysed machines’ stator-winding heat extraction capability, each building step of the methodology allows one to incorporate accurate thermal analysis from the onset of the machine design process. The use beforehand of the three first building blocks greatly simplified the thermal model validation and loss separation process, as only a reduced number of parameters are still unknown when analysing data from complete machine assembly. By allowing a more accurate and reliable thermal design approach, the proposed methodology should enable thermal designers to move forward the boundaries of machine designs, and develop the high-performance and compact machines required for the raising ‘more electric’ technologies.

8.3 Future work

Further work is focused on possible improvements for the developed methodology.

Recent methods make use of pre-pressed windings or pre-compressed coils in order to increase the conductor fill factor [145], [191], [225], [226]. Further work is required to investigate the applicability of the method proposed in Chapter 4 to compressed coils and to get a broader understanding of the potential of compressed coils in terms of enhanced winding thermal conductivity. One of the key challenges associated with the development of a method for estimating the equivalent thermal conductivity for windings with high conductor fill factor, is to understand how the individual conductors deform when compressed in a coil forming fixture [145], [191], [225], [226]. The high conductor fill factor leads to plastic deformation of the conductors’ profile from round to polygonal as

shown in Figs. 8.1a) and 8.1b). Also, Fig. 8.1c) shows an example of a complete preformed coil with a high conductor fill factor (80%) for a high specific output machine design [216]. The winding technique employed in [216] enables geometrically accurate coil fabrication. It is expected that the manner, in which the individual conductors deform depends on the overall coil geometry and the winding compression technique.

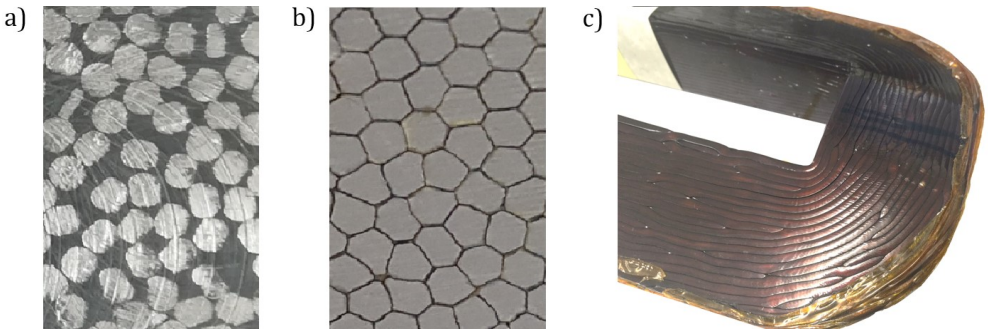

Fig. 8.1 Impregnated winding samples, a) Close-up view on a conventional winding (*FF*=55%), b) Close-up view on a compressed winding (*FF*=80%) [216], c) A pre-compressed coil exemplar [216]

The baseline machines studied in this thesis comprise concentrated winding topologies. Further work would be required to adapt the proposed methodology to electric machines with distributed windings. Initial results on this topic have been presented in [170], where the thermal behaviour of a machine with distributed windings has been predicted using tests on motorette assemblies. Distributed windings typically have significantly longer end-windings compared to concentrated topologies. To ensure the representativeness of the motorette assembly, the length of its end-windings should be adjusted to be equal to the ones present in the complete machine [170]. Fig. 8.2 shows a comparison between a motorette and a stator section of the same shape presented in [170]. The rapid-prototyped stator section is wound with three phases in the correct winding pattern required for the complete machine. The motorettes were wound with end-winding lengths that approximate those expected in the complete machine wound stator assembly. In this case, the dc winding power losses in a defined number of slots of the motorette should be equal to the ones in the same number of slots of the complete machine. However, the ac winding power losses have not been investigated in [170]. Further efforts would therefore also be required to evaluate the use of the proposed methodology for winding and core power loss analysis of electric machines with distributed winding topologies.

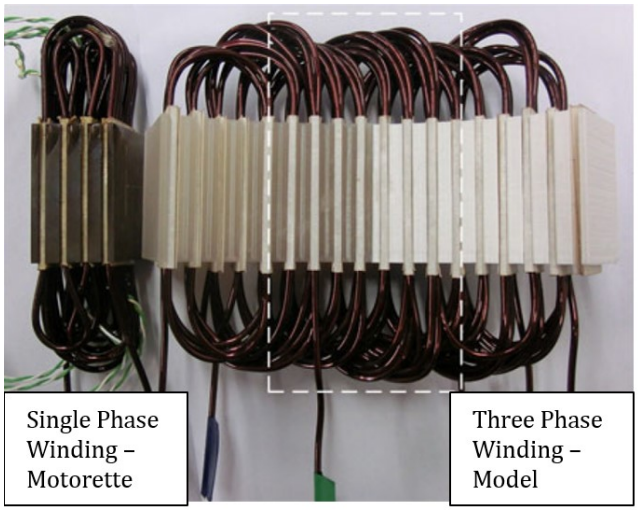

Fig. 8.2 Motorette (left) with rapid-prototyped stator section model (right) [170]

This thesis has focused on the characterisation of thermal parameters associated with conductive heat transfer effects. The use of motorette and stator assemblies for the estimation of thermal parameters associated with convective heat transfer effects would broaden the applicability of the proposed methodology. There have been some developments in using motorette assemblies to provide some insight into heat extraction directly from the winding body by passing liquid [125]. In order to simplify the hardware construction, heated pole pieces with identical shapes as the coils have been used in [125] to replace the complete winding assembly, and the study mainly focuses on the effects of the flow distribution and inlet temperature. Further work could include coupled analyses accounting for the conductive and convective heat transfer within the stator-winding assembly.

The approach mentioned in Chapter 6 for the characterisation of the housing-to-ambient heat transfer coefficient thermally insulate all peripheral regions of the stator under test apart from the housing frame. Future work could include the adaptation of the approach to other peripheral regions of the electric machines, such as the end-windings, and the end-windings-to-ambient heat transfer coefficient could be derived.

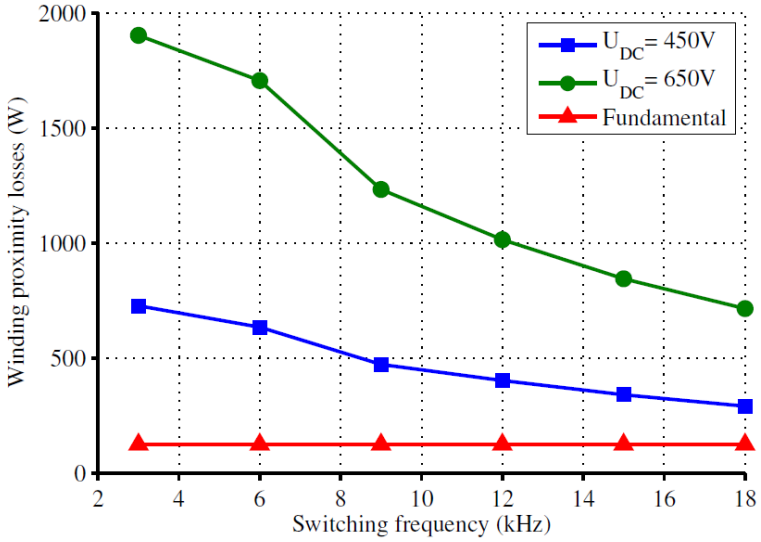

Fig. 8.3 Additional copper losses due to the proximity effect

Finally, all the ac tests presented in this thesis have been completed using an ac power source with sinusoidal excitation. In practice, the current or voltage supplied to a machine may contain high-frequency components due to the power electronics used to drive them. In [233], the influence of PWM switching frequency on the losses in PM machines has been investigated theoretically. The winding proximity losses and unequal current sharing between parallel strands effects have been analysed separately. Fig. 8.3 shows the winding proximity losses versus switching frequency. The winding proximity losses were shown to be more strongly influenced by the dc-link voltage than by the switching frequency. Further work on the experimental characterisation of these high-frequency effects on the winding and core power loss would be extremely valuable. Tests on motorettes, stator assemblies or custom-made cylindrical lamination stacks would constitute a time-efficient and accurate approach in this context.

References

[1] B. Knopf, Y.-H. H. Chen, E. De Cian, H. Forster, A. Kanudia, I. Karkatsouli, I. Keppo, T. Koljonen, K. Schumacher, and D. P. Van Vuuren, "Beyond 2020 Strategies and Costs for Transforming the European Energy System", *Climate Change Economics*, vol. 04, 2013.

[2] E. Vasconcellos, "Urban Transport, Environment and Equity: The Case for Developing Countries", *London: Earthscan*, 2001.

[3] World Energy Council, "World energy resources: 2016 survey", 2016.

[4] R. Werle, C. Brunner, S. Nielsen, S. Hatch, H. Falkner, K. Kulterer and R. Klerck, "Global effort for efficient motor systems: EMSA", *EEMODs'11 Energy efficiency in motors driven systems*, Alexandia, VA (USA), 2011.

[5] Transparency Market Research, "Electric vehicles market (on-road) (hybrid, plug-in, and battery) - global industry analysis, size, share, growth, trends and forecast, 2013 -2019," 2014.

[6] E. V. I. International Energy Agency, "Global EV outlook 2016: Beyond one million electric cars", *Clean Energy Ministerial*, 2016.

[7] J. A. Rosero, J. A. Ortega, E. Aldabas, and L. Romeral, "Moving towards a more electric aircraft", *IEEE Aerospace and Electronic Systems Magazine*, vol. 22, no. 3, pp. 3-9, March 2007.

[8] P. Wheeler and S. Bozhko, "The more electric aircraft: Technology and challenges", *IEEE Electrification Magazine*, vol. 2, no. 4, pp. 612, Dec 2014.

[9] T. J. McCoy, "Electric ships past, present, and future [technology leaders]", *IEEE Electrification Magazine*, vol. 3, no. 2, pp. 4-11, June 2015.

[10] G. Sulligoi, A. Vicenzutti, and R. Menis, "All-electric ship design: From electrical propulsion to integrated electrical and electronic power systems," *IEEE Transactions on Transportation Electrification*, vol. 2, no. 4, pp. 507-521, Dec 2016.

[11] I. Krastev, P. Tricoli, S. Hillmansen, and M. Chen, "Future of electric railways: Advanced electrification systems with static converters for ac railways," *IEEE Electrification Magazine*, vol. 4, no. 3, pp. 6-14, Sept 2016.

[12] B. Sarlioglu and C. T. Morris, "More electric aircraft: Review, challenges, and opportunities for commercial transport aircraft," *IEEE Transactions on Transportation Electrification*, vol. 1, no. 1, pp. 54-64, June 2015.

[13] A. Stefanskyi, A. Dziechciarz, F. Chauvicourt, G. E. Sfakianakis, K. Ramakrishnan, K. Niyomsatian, M. Curti, N. Djukic, P. Romanazzi, S. Ayat, S. Wiedemann, W. Peng, and S. Stipetic, "Researchers within the EU funded Marie Curie ITN project ADEPT, grant number 607361", 2013-2017.

[14] https://www.theguardian.com/politics/2017/jul/25/britain-to-ban-sale-of-all-diesel-and-petrol-cars-and-vans-from-2040 (visited on 21/08/2017)

[15] V. Honsinger, "Sizing equations for electrical machinery", *IEEE transactions on Energy Conversion*, (1), pp. 116-121, 1987

[16] X. Alabern, E. Valero,"Optimized design of an induction motor using Fuzzy logic as a calculus and decision tool", *IEEE International Electric Machines and Drives Conference (IEMDC'03)*, vol. 1, pp. 83-87, June 2003

[17] G. Sooriyakumar, R. Perryman, S. Dodds, "Design optimisation for permanent magnet synchronous motors using genetic algorithm", *Universities Power Engineering Conference (UPEC),* pp. 1-6, August 2010

[18] Z. Li, A. Miotto, "Concentrated-winding fractional-slot synchronous surface PM motor design based on efficiency map for in-wheel application of electric vehicle", *IEEE Vehicle Power and Propulsion Conference (VPPC),* pp. 1-8, Sept 2011

[19] J. Ojeda, M. Liu, E. Sedrine, M. Gabsi, "Comparison of 3-phase and 5-phase flux switching machine using a stochastic approach", *7th IET International Conference on Power Electronics, Machines and Drives (PEMD 2014)*, Manchester, June 2014

[20] D. Kim, H. Hwang, S. Bae, C. Lee, "Analysis and design of a double-stator flux-switching permanent magnet machine using ferrite magnet in hybrid electric vehicles", *IEEE Transactions on Magnetics*, *52*(7), pp. 1-4, 2016

[21] A. Damiano, A. Floris, G. Fois, I. Marongiu, M. Porru, A. Serpi, "Design of a High-Speed ferrite-based Brushless DC Machine for electric vehicles", *IEEE Transactions on Industry Applications,* 53 (5), pp.4279-4287, 2017

[22] E. Kazmin, E. Lomonova, J. Paulides, "Brushless traction PM machines using commercial drive technology, Part II: Comparative study of the motor configurations", *IEEE Electrical Machines and Systems (ICEMS 2008),* pp. 3772-3780, Oct. 2008

[23] H. C. M. Mai, R. Bernard, P. Bigot, F. Dubas, D. Chamagne, C. Espanet, "Optimal design of a PMSM using concentrated winding for application urban hybrid vehicle", *IEEE Vehicle Power and Propulsion Conference (VPPC 2010),* pp.1-6, Sept. 2010

[24] R. Bojoi, A. Cavagnino, A. Tenconi, S. Vaschetto, "Multiphase PM machine for more electric aircraft applications: Prototype for design validation" *38th Annual Conference on IEEE Industrial Electronics Society (IECON 2012),* pp. 3628-3634, 2012

[25] T. Reichert, T. Nussbaumer, J. Kolar, "Split ratio optimization for high-torque PM motors considering global and local thermal limitations", *IEEE Transactions on Energy Conversion*, *28*(3), pp.493-501, 2013

[26] C. H. Lee, K. T. Chau, C. Liu, "Design and analysis of an electronic-geared magnetless machine for electric vehicles", *IEEE Transactions on Industrial Electronics*, *63*(11), 6705-6714, 2016

[27] A. Athavale, A. Sasaki, K. Gagas, B. S. Kato, T. Lorenz, "Variable Flux Permanent Magnet Synchronous Machine (VF-PMSM) Design Methodologies to Meet Electric Vehicle Traction Requirements with Reduced Losses" *IEEE Transactions on Industry Applications*, *63*(11), 6705-6714, 2017

[28] Y. Honda, Y. Higaki, T. Morimoto, S. Takeda, "Rotor design optimisation of a multi-layer interior permanent-magnet synchronous motor" *IEE Proceedings-Electric Power Applications*, *145*(2), 119-124, 1998

[29] R. Wrobel, P. H. Mellor, "Design considerations of a direct drive brushless machine with concentrated windings", *IEEE Transactions on energy conversion*, *23*(1), 1-8, 2013

[30] A. Dianov, A. Lee, "Novel IPMSM drive for compact washing machine", *Telecommunications Energy Conference (INTELEC 2009),* pp. 1-7, Oct. 2009

[31] Y. Wang, Y. Niu, S. Fu, "Sensitivity Analysis and Optimal Design of a Dual Mechanical Port Bidirectional Flux-modulated Machine" *IEEE Transactions on Industrial Electronics*, *63*(11), 6705-6714, 2017

[32] Liu, Y., Zhang, Z., & Zhang, X. (2017). Design and Optimization of Hybrid Excitation Synchronous Machines with Magnetic Shunting Rotor for Electric Vehicle Traction Applications. *IEEE Transactions on Industry Applications*, *63*(11), 6705-6714, 2017

[33] F. Messine, F. Nogarede, B. Lagouanelle, "Optimal design of electromechanical actuators: a new method based on global optimization" *IEEE transactions on magnetics*, *34*(1), 299-308, 1998

[34] S. Huang, S. Luo, J. Leonardi, T. A. Lipo, "A general approach to sizing and power density equations for comparison of electrical machines" *IEEE Transactions on Industry Applications*, *34*(1), 92-97, 1998

[35] G. J. Atkinson, B. Mecrow, A.G. Jack, D. J. Atkinson, P. Sangha, M. Benarous, "The analysis of losses in high-power fault-tolerant machines for aerospace applications", *IEEE Transactions on Industry Applications*, *42*(5), pp.1162-1170, 2006

[36] W. Han, W. Tran, T. T. Kim, J. W. Kim, Y. J. Jung, "Mass ionized particle optimization algorithm applied to optimal FEA-based design of electric machine" *IEEE Transactions on Magnetics*, *52*(3), pp. 1-4, 2016

[37] W. Hua, G. Zhang, M. Cheng, "Investigation and design of a high-power flux-switching permanent magnet machine for hybrid electric vehicles", *IEEE Transactions on Magnetics*, *51*(3), pp. 1-5, 2015

[38] G. De Donato, G. Capponi, F. G. Rivellini, G. Caricchi, "Integral-slot versus fractional-slot concentrated-winding axial-flux permanent-magnet machines: Comparative design, FEA, and experimental tests", *IEEE Transactions on Industry Applications*, *48*(5), 1487-1495, 2012

[39] X. Chen, J. Wang, A. Griffo, "A high-fidelity and computationally efficient electrothermally coupled model for interior permanent-magnet machines in electric vehicle traction applications", *IEEE Transactions on Transportation Electrification*, *1*(4), pp.336-347, 2015

[40] X. Huang, X. Goodman, C. Gerada, Y. Fang, Q. Lu, "Design of a five-phase brushless DC motor for a safety critical aerospace application", *IEEE transactions on industrial electronics*, *59*(9), pp.3532-3541, 2012

[41] Y. Chen, X. Zhu, L. Quan, L. Wang, "Performance analysis of a double-salient permanent-magnet double-rotor motor using electromagnetic–thermal coupling method", *IEEE Transactions on Applied Superconductivity*, *26*(4), pp.1-5, 2016

[42] G. Gilson, T. Raminosoa, T. Pickering, C. Gerada, D. Hann, "A combined electromagnetic and thermal optimisation of an aerospace electric motor" *XIXth International Conference on Electrical Machines (ICEM 2010)*, pp. 1-7, Sept. 2010

[43] D. Gerada, A. Mebarki, C. Gerada,"Optimal design of a high speed concentrated wound PMSM", *International Conference on Electrical Machines and Systems (ICEMS 2009),* pp. 1-6, Nov. 2009

[44] P. Ragot, P. Markovic, M. Perriard, "Optimization of electric motor for a solar airplane application", *IEEE transactions on industry applications*, *42*(4), pp.1053-1061, 2006

[45] D. G. Dorrell, D. Staton, M. McGilp, "Design of brushless permanent magnet motors-A combined electromagnetic and thermal approach to high performance specification", *32nd Annual Conference on Industrial Electronics (IECON 2006),* pp. 4853-4858, Nov. 2006

[46] E. Kazmin, E. Lomonova, J. Paulides, "Brushless traction PM machines using commercial drive technology, Part I: Design methodology and motor design", *International Conference on Electrical Machines and Systems (ICEMS 2008),* pp. 3801-3809, Oct. 2008

[47] L. Chen, L. Chen, X. Wang, J. Lazari, "A computationally efficient multi-physics optimization technique for permanent magnet machines in electric vehicle traction applications" *IEEE International Electric Machines & Drives Conference (IEMDC 2015),* pp. 1644-1650, May 2015

[48] T. Hamiti, C. Gerada, M. Rottach, "Weight optimisation of a surface mount permanent magnet synchronous motor using genetic algorithms and a combined electromagnetic-thermal co-simulation environment", *Energy Conversion Congress and Exposition (ECCE 2011),* pp. 1536-1540, Sept. 2011

[49] R. Wrobel, J. Goss, A. Mlot, P. Mellor, "Design considerations of a brushless open-slot radial-flux PM hub motor", *IEEE Transactions on Industry Applications*, *50*(3), 1757-1767, 2014

[50] W. Jiang, W. Jahns, "Development of efficient electromagnetic-thermal coupled model of electric machines based on finite element analysis", *IEEE International Electric Machines & Drives Conference (IEMDC 2013),*pp. 816-823, May 2013

[51] N. Simpson, R. Wrobel and P. H. Mellor, "A Multi-Physics Design Methodology Applied to a High-Force-Density Short-Duty Linear Actuator"', *7th IET International Conference on Power Electronics, Machines and Drives (PEMD 2014)*, pp. 16-21, April 2014,

[52] S. Nategh, S. Huang, Z. Krings, A. Wallmark, O. Leksell, "Thermal modeling of directly cooled electric machines using lumped parameter and limited CFD analysis", *IEEE Transactions on Energy Conversion*, *28*(4), pp.979-990, 2013

[53] R. Wrobel, P. Mellor, "A general cuboidal element for three-dimensional thermal modelling," *IEEE Trans. on Magnetics*, vol. 46, no. 8, pp. 3197–3200, 2010.

[54] K. Tangudu, T.M. Jahns, "Comparison of interior PM machines with concentrated and distributed stator windings for traction", *IEEE Vehicle Power and Propulsion Conference*, pp.1-8, 2011.

[55] R. Wrobel, S. Williamson, J. Booker, P. H. Mellor, "Characterising the performance of selected electrical machine insulation systems", *Energy Conversion Congress and Exposition, ECCE2015*, pp.4857-4864, Sept. 2015

[56] R. Wrobel, A. Mlot, P. H. Mellor, "Contribution of end-winding proximity losses to temperature variation in electromagnetic devices," *IEEE Trans. Ind. Electron*., vol. 59, no. 2, pp. 848–857, Feb. 2012

[57] R. Wrobel, P. H. Mellor, "Thermal design of high-energy-density wound components," *IEEE Trans. Ind. Electron*., vol. 58, no. 9, pp. 4096– 4104, Sep. 2011.

[58] R. Wrobel, S.J. Williamson, N. Simpson, S. Ayat, J. Yon, P.H. Mellor, "Impact of slot shape on loss and thermal behaviour of open-slot modular stator windings", *Energy Conversion Congress and Exposition (ECCE 2015)*, pp. 4433-4440, Sept. 2015

[59] J. Baker, R. Wrobel, D. Drury. P. Mellor, "A Methodology for Predicting the Thermal Behaviour of Modular-Wound Electrical Machines", *IEEE Energy Conversion and Exposition (ECCE 2014)*, pp. 5176 – 5183, Sept. 2014

[60] R. Wrobel, D. Salt, N. Simpson, and P. H. Mellor, "Comparative study of copper and aluminium conductors - future cost effective PM machines", *7th IET International Conference on Power Electronics, Machines and Drives (PEMD 2014)*, pp. 16-21, April 2014

[61] L. Siesing, A. Reinap, M. Andersson, "Thermal properties on high fill factor electrical windings: Infiltrated vs non infiltrated," *Int. conf. in Electrical Machines (ICEM 2014)*, pp. 2218–2223, Sept. 2014

[62] D. A. Howey, P. R. N. Childs, A. S. Holmes, "Air-Gap Convection in Rotating Machines," *IEEE Transactions on Industrial Electronics*, vol. 59, no. 3, pp. 1367 – 1375, March 2012

[63] R. Camillieri, D. A. Howey, M. D. McCulloch, "Thermal Limitations in Air-Cooled Axial Flux In-Wheel Motors for Urban Mobility Vehicles: a Preliminary Analysis," *Conference on Electrical Systems for Aircraft, Railway and Ship Propulsion (ESARS 2012)*, pp. 1 – 8, October 2012

[64] D. A. Howey, A. S. Holmes, K. R. Pullen, "Measurement of Stator Heat Transfer in Air-Cooled Axial Flux Permanent Magnet Machines," *35th IEEE Industrial Electronics Annual Conference (IECON 2009)*, pp. 1197 – 1202, November 2009

[65] D. A. Howey, A. S. Holmes, K. R. Pullen, "Measurement and CFD Prediction of Heat Transfer in Air-Cooled Disc-Type Electrical Machines," *IEEE Transactions on Industry Applications*, vol. 47, no. 4, pp. 1716 – 1723, August 2011

[66] D. Howey, A. Holmes, K. Pullen, "Radially resolved measurement of stator heat transfer in a rotor-stator disc system", *International Journal of Heat and Mass Transfer*, vol. 53, no. 1-3, pp. 493-501, 2010

[67] D. Howey, A. Holmes, K. Pullen, “Prediction and measurement of heat transfer in air-cooled disc-type electrical machines”, *5th lET International Conference on Power Electronics, Machines and Drives (PEMD 2010)*, pp. 1-6, April 2010

[68] J. R. Hendershot and T. J. E. Miller, Design of Brushless Permanent Magnet Motors. Oxford, U.K.: Clarendon, 1994

[69] B.G. Lamme, “Temperature Distributions in Electrical Machinery”, *A.I.E.E*, 1916

[70] J. Fechheimer, “Longitudinal and Transverse Heat Flow in Slot-Wound Armuature Coils”, *A.I.E.E*, 1921

[71] I. Langmuir, “Laws of Heat Transmission in Electrical Machinery”, *A.I.E.E*, 1913

[72] H.D. Symons, M. Walker, “The Heat Paths in Electrical Machinery”, *A.I.E.E*, 1911

[73] G. E. Luke, “The Cooling of Electric Machines”, *Transactions of the American Institute of Electrical Engineers*, vol. XLII, pp. 636652, 1923

[74] R. E. Steven, Electrical Machines and Power Electronics, New York: Van Nostrand-Reinhold, 1983

[75] D. O'Kelly, Performance and Control of Electical Machines, New York: McGraw-Hill, 1991

[76] N. Simpson, R. Wrobel and P. H. Mellor, “A Multi-Physics Design Methodology Applied to a High-Force-Density Short-Duty Linear Actuator”, *7th IET International Conference on Power Electronics*, *Machines and Drives (PEMD 2014)*, pp. 16-21, April 2014

[77] W. Jiang and T. Jahns, “Development of efficient electromagnetic- thermal coupled model of electric machines based on finite element analysis”, *IEEE International Electric Machines Drives Conference (IEMDC 2013),* pp. 816823, 2013

[78] Y. Duan, R.G. Harley, T.G. Habetler, “A useful multi-objective optimization design method for PM motors considering nonlinear material properties”*, IEEE Energy Conversion Congress and Exposition*, San Jose, pp. 187-19, 2009

[79] W. Jiang, T.M. Jahns, T.A. Lipo, W. Taylor, Y. Suzuki, “Machine design optimization based on _nite element analysis in a high-throughput computing environment”, *IEEE Energy Conversion Congress and Exposition (ECCE 12),* pp. 869-876, Raleigh, NC, Sept. 2012

[80] P. Dowell, “Effects of eddy currents in transformer windings”, *Proc. Inst. Elect. Eng*., vol. 113, no. 8, pp. 1387-1394, Aug. 1966

[81] P. Reddy, T. Jahns, “Analysis of bundle losses in high speed machines”, *International Power Electronics Conference (IPEC 2010)*, pp. 2181-2188, June 2010

[82] P. Reddy, T. Jahns, T. Bohn, “Modeling and analysis of proximity losses in high-speed surface permanent magnet machines with concentrated windings”, *Energy Conversion Congress and Exposition (ECCE 2010)*, pp. 996-1003, Sept. 2010

[83] P. H. Mellor, R. Wrobel, N. Simpson, “AC losses in high frequency electrical machine windings formed from large section conductors,” *IEEE Energy Conversion and Exposition (ECCE 2014)*, pp. 1806-1813, Sept. 2014

[84] P. B. Reddy, Z. Q. Zhu, S. H. Han, T. M. Jahns, “Stranded-level proximity losses in PM machines designed for high-speed operation”, *Proc. Int. Conf. on Elec. Machines (ICEM 2008)*, Vilamoura, Portugal, Sept. 2008

[85] M. van der Geest, H. Polinder, J. A. Ferreira, D. Zeilstra, “Current Sharing Analysis of Parallel Strands in Low Voltage High Speed Machines”, *IEEE Transactions on Industrial Electronics*, vol. 61, no. 6, pp. 3064-3070, June 2014

[86] P. Reddy, T. Jahns, T. Bohn, “Transposition effects on bundle proximity losses in high-speed PM machines,” *IEEE Energy Convers. Congr. Expo*., pp. 19191926, Sep. 2009

[87] M. Vetuschi, F. Cupertino, “Minimization of proximity losses in electrical machines with tooth- wound coils”, *IEEE Energy Conversion and Exposition (ECCE 2014)*, pp. 5555 – 5562, Sept. 2014

[88] D. C. Hanselman and W. H. Peake, “Eddy-currents effects in slot-bound conductors,” *Proc. Inst. Elect. Eng.—Electr. Power Appl*., vol. 142, no. 2, pp. 131–136, Mar. 1995

[89] R. Wrobel, D. Staton, R. Lock, J. Booker, D. Drury, “Winding design for minimum power loss and low-cost manufacture in application to fixed-speed PM generator,” *IEEE Energy Conversion and Exposition* (*ECCE 2014)*, pp. 5563-5570, Sept. 2014

[90] H. Hamalainen, J. Pyrhonen, J. Nerg, J. Talvitie, “AC Resistance Factor of Litz-Wire Winding Used in Low-Voltage High-Power Generators”, *IEEE Transactions on Industrial Electronics*, vol. 61, no. 2, pp. 693-700, February 2014.

[91] C. Sullivan, J. McCurdy, R.A. Jensen, “Analysis of Minimum Cost in Shape-Optimized Litz-Wire Inductor Windings”, *32nd IEEE Pow. Elecs. Spec. Conf.,* vol. 3, pgs. 1473-1478, June 2001

[92] H. Hamalainen, J. Pyrhonen, J. Nerg, “AC Resistance Factor in One-Layer Form-Wound Winding Used in Rotating Electrical Machines,” *IEEE Transactions on Magnetics*, vol. 49, no. 6, pp. 2967-2973, June 2013

[93] T. Dordea, T. Torac, I. Madescu, G. Proca, V. Mot, M. Ocolisan, "The current distribution on the elementary conductors of the Roebel bar", *XIXth International Conference on Electrical Machines (ICEM 2010),* pp. 1-5, Sept. 2010

[94] P. Mellor, R. Wrobel, D. Salt, A. Griffo, "Experimental and analytical determination of proximity losses in a high-speed PM machine", *IEEE Energy Cony. Congress and Exposition (ECCE 2013)*, p.354-351, Sept. 2013

[95] R. Wrobel, D. Salt, A. Griffo, N. Simpson, P. Mellor, "Derivation and scaling of AC copper loss in thermal modelling of electrical machines," *IEEE Trans. Ind. Electron.,* vol. 61, no. 8, pp. 4412-4420, Aug. 2014

[96] R. Wrobel, N. Simpson, "Winding Loss Separation in Thermal Analysis of Electromagnetic Devices", *International Conference in Electrical Machines (ICEM16)*, pp. 2218–2223, Sept. 2016

[97] P. H. Mellor, R.Wrobel, and N. McNeill, "Investigation of proximity losses in a high speed brushless permanent magnet motor," *Conf. Rec. 41st IEEE IAS Annu. Meeting*, vol. 3, pp. 1514-1518, Oct. 2006

[98] S. Nategh, A. Krings, O. Wallmark, M. Leksell, "Evaluation of impregnation materials for thermal management of liquid-cooled electric machines", *IEEE Trans. Ind. Electron*., vol. 61, pp. 5956-5965, 2014

[99] A. Boglietti, A. Cavagnino, D. Staton, "Determination of critical parameters in electrical machine thermal models," *Conf. Rec. IEEE IAS Annu. Meeting*, pp. 73–90, New Orleans, LA, Sep. 2007

[100] J. Chen, J. Wang, D. Cheng, S. Wang, Y. Zhu, Y. Liu, "Modeling of temperature effects on magnetic property of nonoriented silicon steel lamination", *IEEE Transactions on Magnetics*, *51*(11), 1-4, 2015

[101] G. Bertotti, "General properties of power losses in soft ferromagnetic materials", *IEEE Transactions on magnetics*, *24*(1), pp.621-630, 1988

[102] S. Han, T. Jahns, Z.Q. Zhu, "Analysis of rotor core eddy-current losses in interior permanent magnet synchronous machines", *Industry Applications Society Annual Meeting*, Edmonton, Alta, October 2008

[103] P. H. Mellor, R. Wrobel, D. Holliday, "A computationally efficient iron loss model for brushless AC machines that caters for rated flux and field weakened operation," *IEEE International Electric Machines and Drives Conference* (*IEMDC 2009)*, pp. 490-494, 2009

[104] J. Goss, M. Popescu, D. Staton, R. Wrobel, J. Yon, P. H. Mellor,"A comparison between maximum torque/ampere and maximum efficiency control strategies in IPM synchronous machines," *IEEE Energy Conversion and Exposition* (*ECCE 2014)*, pp. 2403-2410, Sept. 2014

[105] T.L. Mthombeni, P. Pillay, "Physical basis for the variation of lamination core loss coefficients as a function of frequency and flux density" *IEEE 32nd Annual Conference on Industrial Electronics (IECON 2006),*pp. 1381-1387, November 2006

[106] J. Goss, P. H. Mellor, R. Wrobel, D. A. Staton, M. Popescu, "The design of AC permanent magnet motors for electric vehicles: A computationally efficient model of the operational envelope," *6th IET Int. Conference on Power Electronics, Machines and Drives* (*PEMD 2012)*, pp. 1-6, April. 2012

[107] J. Pyrhonen, S. Ruoho, J. Nerg, M. Paju, S. Tuominen, H. Kankaanpaa, R. Stern, A. Boglietti and N. Uzhegov, "Hysteresis Losses in Sintered NdFeB Permanent Magnets in Rotating Electrical Machines," *IEEE Trans. Ind. Electron.*, vol. 62, no. 2, pp. 857--865, Feb. 2015

[108] X. Wu, R. Wrobel, P.H. Mellor and C. Zhang, "A Computationally Efficient PM Power Loss Derivation for Surface-Mounted Brushless AC PM Machines", *IEEE International Conference on Electric Machine (ICEM 2014)*, pp. 17-23, Sept. 2014

[109] S. Ruoho, M. Haavisto, E. Takala, T. Santa-Nokki, M. Paju, "Temperature Dependence of Resistivity of Sintered Rare-Earth Permanent-Magnet Materials", *IEEE Trans. Magn*.,vol. 46, no. 1, pp. 15-20, January 2010

[110] H. Polinder, M.J. Hoeijmakers, "Eddy-current losses in the segmented surface-mounted magnets of a PM machine", *IEE Proceedings-Electric Power Applications*, 146(3), pp.261-266, 1999

[111] K.J. Meessen, J. Paulides, E. Lomonova, "Analysis of 3-D effects in segmented cylindrical quasi-Halbach magnet arrays", *IEEE Transactions on Magnetics*, *47*(4), pp.727-733, 2011

[112] S.M. Jang, H.J. Park, H.J. Choi, J.H. Han, "Analysis on the magnetic force characteristics of segmented magnet used in large permanent-magnet wind power generator", *IEEE Transactions on Magnetics*, 49(7), pp.3981-3984, 2013

[113] J. Baker, "A Design Methodology for Permanent-Magnet Electrical Machines with Concentrated Modular Windings", University of Bristol, July 2015

[114] B. Scheerlinck, H. De Gersem, P. Sergeant, "3-D eddy current and fringing-flux distribution in an axial-flux permanent-magnet synchronous machine with stator in laminated iron or SMC", *IEEE Transactions on Magnetics*, 51(11), pp.1-4, 2015

[115] J.F. Gieras and M. Wing*, "*Permanent Magnet Motor Technology - Design and Applications"*, Marcel Dekker,* New York, 2002

[116] http://www.skf.com (visited on 12/12/2017)

[117] R. Wrobel, G. Vainel, C. Copeland, T. Duda, D. Staton, and P. Mellor, "Investigation of mechanical loss components and heat transfer in an axial-flux pm machine," *IEEE Transactions on Industry Applications*, vol. 51, no. 4, pp. 3000–3011, July 2015

[118] H. Hofmann, S. R. Sanders, "High-Speed Synchronous Reluctance Machine with Minimized Rotor Losses," *IEEE Transactions on Industry Applications*, vol. 36, no. 2, pp. 531–539, March/April 2000

[119] M. Calasan, M. Ostojic, D. Petrovic, "The retardation Method for Bearing Loss determination," *International Symposium on Power Electronics, Electrical Drives, Automation and Motion, (SPEEDAM 2012)*, pp. 25–29, June 2012

[120] Y. Yang *et al.*, "Thermal management of electric machines," *IET Electr. Syst. Transp.*, pp. 1–13, 2016

[121] D. A. Staton and A. Cavagnino, "Convection heat transfer and flow calculations suitable for electric machines thermal models," *IEEE Trans. Ind. Electron.,* vol. 55, no. 10, pp. 3509–3516, Oct. 2008

[122] M. Popescu, D. Staton, A. Boglietti, A. Cavagnino, D. Hawkins, and J. Goss, "Modern heat extraction systems for power traction machines - a review," *IEEE Transactions on Industry Applications*, vol. PP, no. 99, pp. 1–1, 2016

[123] A. Valenzuela and J. A. Tapia, "Heat transfer and thermal design of finned frames for TEFC variable speed motors," *IEEE IECON*, pp. 4835–4840, Paris, France, Nov. 2006

[124] E. Driesen, "The submerged double jet impingement (SDJI) method for thermal testing of packages," *Electron. Cool.*, May 2001

[125] R. Camilleri, D. Howey, M. McCulloch, "Predicting the Temperature and Flow Distribution in a Direct Oil-Cooled Electrical Machine With Segmented Stator", *IEEE Trans. on Ind. Electronics*, pp.82-91, 2016

[126] F. P. Incropera and D. P. Dewitt, Fundamentals of Heat and Mass Transfer (Wiley, New York, 1996).

[127] A. Boglietti, A. Cavagnino, and D. Staton, "TEFC induction thermal models: A parameters sensitivity analysis", *IEEE Trans. Ind. App*, vol. 41, no. 3, pp. 756-763, May/Jun. 2005

[128] A. Lindner, H. Ingo, "Practical evaluation of a passive stator cooling concept without thermal stacking", *IEEE Workshop on Electrical Machines Design, Control and Diagnosis (WEMDCD 2017)*, pp. 132-139, 2017

[129] L. Fedoseyev and E. M. Pearce, Jr., "Rotor assembly with heat pipe cooling system," *U.S. Patent Application 2014/0368064 A1*, 2014

[130] Motor CAD V.10 Manual, Motor Design Ltd., 2017

[131] Zhou, Peng, Nicholas Robert Kalayjian, Grant Dufresne Cutler, and Peteris Koch Augenbergs, "Liquid cooled rotor assembly", *U.S. Patent 7,489,057*, issued February 10, 2009

[132] C. Paar and A. Muetze, "Discussion of machine placement and integration on the thermal design of HEV IPM machines," *IEEE Transp. Electrific. Conf. Expo.,* pp. 1–6, Jun. 2016

[133] D. Staton, A. Boglietti, and A. Cavagnino, "Solving the more difficult aspects of electric motor thermal analysis in small and medium size industrial induction motors," *IEEE Trans. Energy Convers.*, vol. 20, no. 3, pp. 620–628, Sep. 2005.

[134] S. Mezani, N. Takorabet, and B. Laporte, "A combined electromagnetic and thermal analysis of induction motors," *IEEE Trans. Magn*., vol. 41, no. 5, pp. 1572–1575, May 2005

[135] D. G. Dorrrell, D. A. Staton, J. Hahout, D. Hawkins, and M. I. Mc Gilp, "Linked electromagnetic and thermal modelling of a permanent magnet motor," *IEEE PEMD*, Dublin, Ireland, pp. 536–540, Apr. 2006

[136] A. Di Gioia, A. Brown, I.P. Nie, Y. Knippel, R. Ludois, D.C. Dai, J. Hagen, S. Alteheld, "Design of a wound field synchronous machine for electric vehicle traction with brushless capacitive field excitation", *Energy Conversion Congress and Exposition (ECCE 2016),*pp. 1-8, Sept. 2016

[137] Z. Li, J. Guo, J. Fu, D. Gu, G. Xiong, "Research on heat transfer of spraying evaporative cooling technique for large electrical machine", *International Conference on Electrical Machines and Systems (ICEMS 2009)*, pp. 1-4, Nov. 2009

[138] M. Polikarpova, P. Ponomarev, P.1. Roytta, "Direct liquid cooling for an outer-rotor direct-drive permanent-magnet synchronous generator for wind farm Application", *IET Electric Power Application*, pp.523-532, 2015

[139] A. Boglietti, A. Cavagnino, M. Pervis, and A. Vallan "Evaluation of radiation thermal resistances in industrial motors," *IEEE Trans. Ind. Appl.*, vol. 42, no. 3, pp. 688–693, May/Jun. 2006

[140] http://www.porsche.com/uk/models/panamera/panamera-s-e-hybrid/ (visited on 18/07/2017)

[141] http://www.yasamotors.com/products/yasa-750/ (visited on 18/07/2017)

[142] M. Galea, C. Gerada, C. Raminosoa, T. Wheeler, P., "A thermal improvement technique for the phase windings of electrical machines", *IEEE Transactions on Industry Applications*, *48*(1), pp.79-87, 2012

[143] C. R. Sullivan, "Aluminium Windings and Other Strategies for High-Frequency Magnetic Design in an Era of High Copper and Energy Costs," *IEEE Transactions on Power Electronics*, vol. 23, no. 4, pp. 2044 -2051, 2008

[144] R. Wrobel, P. H. Mellor, "Thermal Design of a High Energy Density Wound Components*", IEEE Trans. on Ind. Electronics,* vol. 58, no. 9, pp. 4096-4104, Sept. 2011

[145] J. D. Widmer, R. Martin, B.C .Mecrow, "Pre-Compressed and Stranded Aluminium Motor Windings for Traction Motors", *IEEE International Machine and Drives Conference (IEMDC 2015)*, pp.1851,1857, May 2015

[146] M. Kimiabeigi, J. D. Widmer, "On Winding Design of a High Performance Ferrite Motor for Traction Application", *International conference on electrical machines (ICEM 2016)*, Lausanne, pp.16

[147] L. Del Ferraro, F. G. Capponi, "Aluminium Multi-Wire for High- Frequency Electric Machines," *42nd IEEE Industry Applications Annual Meeting, IAS 2007*, pp. 89 – 93, 2007

[148] "Motors and Generators", *NEMA Standard MG-1*, 2017

[149] "Electrical Insulation—Thermal Evaluation and Designation", *3rd ed., IEC Standard 60085*, 2004

[150] https://www.zeusinc.com/ (visited on: 18/07/2017)

[151] https://www.kaptontape.com/ (visited on: 18/07/2017)

[152] http://www.alconex.com/products/alconex-gold-products/ (visited on: 18/07/2017)

[153] G.C. Mechler, "Manufacturing and cost analysis for aluminium and copper die cast induction motors for GM's powertrain and R&D divisions", *M.S. thesis, Department of Materials Science and Engineering*, Massachusetts Institute of Technology, Cambridge, MA, 2010

[154] J. Goss, "The Design of AC Brushless Permanent Magnet Motors for Electric Vehicle Traction Applications", *PhD thesis*, University of Bristol, March 2015

[155] J. Cousineau, K. Bennion, M. Mihalic, S. Narumanchi, "Characterization of Contact and Bulk Thermal Resistance of Laminations for Electric Machines", *Nat. Renewable Energy Lab. report*, 2015

[156] N. Simpson, R. Wrobel, P. H. Mellor, "Estimation of Equivalent Thermal Parameters of Impregnated Electrical Windings," *IEEE Trans. on Industry Applications*, vol. 49, no. 6, pp. 25052515, Nov. 2013

[157] D. P. Kulkarni, G. Rupertus, and E. Chen, "Experimental investigation of contact resistance for water cooled jacket for electric motors and generators," *IEEE Trans. Energy. Convers.,* vol. 27, no. 1, pp. 204–210, Mar. 2012

[158] N. Simpson, R. Wrobel, J.D. Booker, P. Mellor, "Multi-physics experimental investigation into stator-housing contact interface", *8th IET International Conference on Power Electronics, Machines and Drives (PEMD16)*, Glasgow, April 2016

[159] A. Boglietti, M. Cossale, S. Vaschetto, T. Dutra, "Thermal Conductivity Evaluation of Fractional-Slot Concentrated-Winding Machines", *IEEE Transactions on Industry Applications*, *53*(3), pp.2059-2065, 2017

[160] Y. P. Shlykov and Y. A. Ganin, "Thermal resistance of metalic contacts*", Int. J. Heat and Mass Transfer*, Vol. 7, pp. 921-929, 1964

[161] M. Cooper, B. B. Mikic and M. M. Yovanovich, "Thermal Contact Conductance"*, Journal of Heat and Mass Transfer*, vol. 12, pp. 279-300, 1969

[162] T. F. Lemczk and M. M. Yovanovich, "New models and methodology for predicting thermal contact resistance in compound cylinders and fintubes*", Thermal/Mechanical Heat Exchanger Design - Karl Gardner Memorial Session*, pp. 59-70, 1987

[163] C. V. Madhusudana, "Thermal conductance of cylindrical joints"*, International Journal of Heat and Mass Transfer*, vol. 42, pp. 1273-1278, 1998

[164] P. H. Mellor, D. Roberts, D. R. Turner. "Lumped parameter thermal model for electrical machines of TEFC design", *IEE Electric Power Applications*, vol. 138, No.5, pp.205-218, 1991

[165] R. Camilleri, D. A. Howey, M. D. McCulloch, "Experimental investigation of the thermal contact resistance in shrink fit assemblies with relevance to electrical machines", *7th IET International Conference on Power Electronics, Machines and Drives (PEMD 2014)*, pp. 2.11.04–2.11.04, 2014

[166] D. Meeker. (2013) Finite element method magnetics (version: 4.2)

[167] C.J. Carpenter, "Magnetic equivalent circuits", *Institution of Electrical Engineers*, vol. 115, no. 10, pp. 1503-1511, Oct. 1968

[168] V. Ostovic, V., "A simplified approach to magnetic equivalent-circuit modeling of induction machines", *IEEE Transactions on Industry Applications*, *24*(2), pp.308-316, 1988

[169] F.Bosenuik, B. Ponick, "Parametrization of Transient Thermal Models for Permanent Magnet Synchronous Machine Exclusively Based on Measurements", *Conf. Rec IEEE SPEEDAM*, pp. 295-301, 2014

[170] J. Godbehere, R. Wrobel, D. Drury, P. H. Mellor, "Experimentally Calibrated Thermal Stator Modelling of AC Machines for Short-Duty Transient Operation", *International Conference on Electrical Machine (ICEM)*, pp. 1-6, Lausanne, Sept. 2016

[171] F. Tao, S. Wei, W. Xuhui, "A simplified thermal circuit model of permanent magnet machine part I: Model and parameters", *IEEE Conference and Expo Transportation Electrification Asia-Pacific (ITEC Asia-Pacific 14),* pp. 1-4, Aug. 2014

[172] U. San Andres, U. Almandoz, G. Poza, J. Escalada, "Thermal test procedure and analytical model calibration method for electrical machines", *IEEE Workshop on Electrical Machines Design Control and Diagnosis (WEMDCD13),* pp. 95-103, March 2013

[173] B. Assaad, K. El kadri Benkara, S. Vivier, G. Friedrich, A. Michon, "Thermal design optimization of electric machines using a global sensitivity analysis", *International Conference on Electrical Machines (ICEM 16),* pp. 2099-2105, Sept. 2016

[174] I. J. Perez, J. G. Kassakian, "A Stationary Thermal Model for Smooth Air-Gap Rotating Electric Machines", *Electric Machines & Power Systems*, vol. 3, no. 3-4, pp. 285303, Apr. 1979

[175] N. Simpson, R. Wrobel, P. H. Mellor, "A General Arc-Segment Element for Three-Dimensional Thermal Modeling," *IEEE Transactions on Magnetics*, vol. 50, no. 2, pp. 265–268, Feb. 2014

[176] https://www.adamsmagnetic.com/sites/default/files/Adams-Materials-Catalog.pdf (visited on: 18/07/2017)

[177] F. Qi, M. Schenk, R. De Doncker, "Discussing details of lumped parameter thermal modeling in electrical machines," *7th IET International Conference on Power Electronics, Machines and Drives (PEMD 2014)*, pp. 2.11.04–2.11.04, 2014

[178] A. Boglietti, A. Cavagnino, D. Staton, M. Shanel, M. Mueller, C. Mejuto, "Evolution and modern approaches for thermal analysis of electrical machines," *IEEE Trans. Ind. Electron.*, vol. 56, no. 3, pp. 871– 882, Mar. 2009

[179] F. Qi, A. Stippich, M. Guettler, M. Neubert, and R. W. D. Doncker, "Methodical Considerations for Setting Up Space-Resolved Lumped-Parameter Thermal Models for Electrical Machines," *17th International Conference on Electrical Machines and Systems (ICEMS14)*, Hangzhou, China Methodical, pp. 651–657, 2014

[180] A. Boglietti, E. Carpaneto, M. Cossale, S. Vaschetto, M. Popescu, D. Staton, "Stator winding thermal conductivity evaluation: An industrial production assessment", *Energy Conversion Congress and Exposition (ECCE15)*, pp. 4865-4871, Sept. 2015

[181] A. Boglietti, A. Cavagnino, M. Lazzari, M. Pastorelli, "A simplified thermal model for variable speed self-cooled industrial induction motor", *IEEE Transactions on Industry Applications*, vol. 39, no. 4, pp. 945-952, August 2003

[182] A. Boglietti, E. Carpaneto, M. Cossale, A. Lucco Borlera, D. Staton, M. Popescu, "Electrical Machine First Order Short-Time Thermal Transient Model: Measurements and Parameters Evaluation", *IEEE Industrial Electronics Conference (IECON14)*, pp. 555-561, 2014

[183] R. Wrobel, P. H. Mellor, D. Holliday, "Thermal modelling of a segmented stator winding design*," IEEE Trans. Ind. Appl.*, vol. 47, no. 5, pp. 2023–2030, Sep./Oct. 2011

[184] G. Guemo, P. Chantrenne, J. Jac, "Parameter identification of a lumped parameter thermal model for a permanent magnet synchronous machine" *IEEE International Electric Machines & Drives Conference (IEMDC 13*), pp. 1316 – 1320, May 2013

[185] C. Kral, A. Haumer, M. Haigis, H. Lang, and H. Kapeller, "Comparison of a CFD analysis and a thermal equivalent circuit model of a TEFC induction machine with measurements," *IEEE Transactions on Energy Conv.*, vol. 24, no. 4, pp. 809–818, Dec. 2009

[186] Camilleri, R., Beard, P., Howey, D.A., McCulloch, M.D., "Measuring the Heat Transfer Coefficient in a Direct Oil-Cooled Electrical Machine using Thin Film Heat Flux Gauge"s, *14th UK Heat Transfer Conference (UKHTC2015)*, Edinburgh, Scotland, 7-8 September 2015

[187] J. Yon, J. L. Baker, P.H. Mellor, S. J. Williamson, R.Wrobel, "Test Characterization of a High Performance Fault Tolerant Permanent Magnet Machine", *IEEE International Machines and Drives Conference (IEMDC17)*, Miami, May 2017

[188] U. San Andres, G. Almandoz, G. Poza, J. Escalada, "Thermal test procedure and analytical model calibration method for electrical machines", *Workshop on Electrical Machines Design Control and Diagnosis (WEMDCD13),* pp. 95-103, March 2013

[189] N. Simpson, P.H Mellor, R. Wrobel, G. Iordanidis "Coupled thermalelectromagnetic design of a short-duty, high-specific force linear actuator," *International Conference on Power Electronics, Machines and Drives (PEMD12)*, pp. 1-5, April 2012

[190] M. Jaritz, J. Biela, "Analytical model for the thermal resistance of windings consisting of solid or Litz wire", *15th European Conference on Power Electronics and Applications (EPE13*), pp. 1-5, 2013

[191] A. G. Jack, B. C. Mecrow, P. G. Dickinson, D. Stephenson, J. S. Burdess, N. Fawcett, and 1. T. Evans,, "Permanent magnet machines with powdered iron cores and pressed windings," *IEEE Trans. Ind. Appl.*, vol. 36, no. 4, pp. 1077–1084, Jul./Aug. 2000

[192] Z. Tang, P. Pillay, A. Omekanda, C. Li, C. Cetinkaya, "Young's modulus for laminated machine structures with particular reference to switched reluctance motor vibrations", *IEEE Trans. Ind. Appl.,* vol. 40, pp. 748-754, May/Jun. 2004

[193] D. Andessner, J. Passenbrunner, R. Kobler, W. Amrhein, "Measurement of the magnetic characteristics of soft magnetic materials with the use of an iterative learning control algorithm*", IEEE Vehicle Power and Propulsion Conference*, pp.1-8, Sept. 2011

[194] K. Tangudu, T.M. Jahns, "Comparison of interior PM machines with concentrated and distributed stator windings for traction application*", IEEE Vehicle Power and Propulsion Conference*, pp.1-8, Sept. 2011

[195] E.L. Brancato, "Insulation Aging a Historical and Critical Review", *IEEE Trans. on Electrical Insulation*, vol.12 , no.4, pp.308-317, Aug. 1978

[196] M. Galea, C. Gerada, T. Raminosoa, P. Wheeler, "Design of a High Force Density Tubular Permanent Magnet Motor", *IEEE Trans. on Ind. Application*., vol. 49, no. 5, pp. 79 - 87, 2012

[197] D. Simmers, L. Coney, "A Reynolds analogy solution for the heat transfer characteristics of combined Taylor vortex and axial flows", *International Journal of Heat and Mass Transfer*, vol. 22, pp. 679-689, 1979

[198] F. Tachibana, S. Fukui, "Convective heat transfer of the rotational and axial flow between two concentric cylinders", *Bulletin of Japan Society of Mechanical Engineers*, pp.385-391, 1964

[199] J. Owen, C. Haynes, F. Bayley, "Heat Transfer from an Air-Cooled Rotating Disk", *Procs. of the Royal Society of London. Series A, Math. and Physical Sciences*, vol. 336, no. 1607, pp. 453-473, 1974

[200] Y. Liu, Y. Ho, S. L. Fu, W. N. Zhang, "Design optimization of a novel doubly fed dual-rotor flux-modulated machine for hybrid electric vehicles", *IEEE Transactions on Magnetics*, *51*(3), pp. 1-4, 2015

[201] Assaad, B., El kadri Benkara, K., Vivier, S., Friedrich, G. and Michon, A., "Thermal design optimization of electric machines using a global sensitivity analysis", *International Conference on Electrical Machines (ICEM 16),*pp. 2099-2105, Sept. 2016

[202] S. Y. Goh, J. Wale, J. Greenwood, "Thermal analysis for stator slot of permanent magnet machine", *International Conference on Electrical Machines (ICEM 16),*pp. 2099-2105, Sept. 2016

[203] A. Krings, A. Mousavi, S. A. Wallmark, O. Soulard, "Temperature influence of NiFe steel laminations on the characteristics of small slotless permanent magnet machines", *IEEE transactions on magnetics*, *49*(7), pp. 4064-4067, 2013

[204] R. Vlach, R. Grepl, R. Krejci, "Control of Stator Winding Slot Cooling by Water Prediction of Heating*", IEEE International Conference on Mechatronics and Automation (ICMA07)*, pp. 1-5 ,2007

[205] S. Iwasaki, R. Deodhar, Y. Liu, A. Pride, Z. Zhu 1. Bremner, "Influence of PWM on the proximity loss in permanent-magnet brush less ac machines", *IEEE Trans. on Ind. Appl*., vol. 45, pp. 1359-1367, 2009

[206] X. Fang, B. Liu, B. Han, K. Wang, "Analysis of circulating current loss for high speed permanent magnet motor", *IEEE Trans. on Magnetics*, vol. 11, no. 99, pp. 11-18, 2014

[207] P. Arumugam, T. Hamiti, C. Gerada, "Modeling of Different Winding Configurations for Fault-Tolerant Permanent Magnet Machines to Restrain Interturn Short-Circuit Current", *IEEE Trans. on Energy Conv*., vol. 27, no. 2, pp. 351 - 361, 2012

[208] P. Werynski, D. Roger, R. Corton, 1. F Brudny, "Proposition of a new method for in-service monitoring of the aging of stator winding insulation in AC motors", *IEEE Trans. on Energy Conv.,* vo1.21, no.3, pp.673-681, 2006

[209] V.T. Buyukdegirmenci, M. P. Magill, S. Nategh, P. T. Krein, "Development of closed-form solutions for fast thermal modeling of rotating electric machinery", *IEEE International Machines and Drives Conference (IEMDC13)*, pp. 832-838, May 2013

[210] J. Richnow, P. Stenzel, A. Renner, D. Gerling, C. Endisch, "Influence of Different Impregnation Methods and Resins on Thermal Behaviour and Lifetime of Electrical Stators", *Electric Drives Production Conference (EDPC14)*, pp. 1-7. Sept. 2014

[211] W. Boughamni, J.-P. Manata, S. Ait-Amar, D. Roger, "Electrical Machines Insulation: Towards Low Environmental Impact Solutions", *IEEE International Conference on Solid Dielectrics (ICSD13)*, pp. 557 - 560, 2013

[212] H. P. Liu and J. J. Hahne, "High-speed compulsator stator thermal management", *IEEE Trans. Magn.*, vol. 39, no. I, pp. 357-361, 2003

[213] Q. Wang, Z. Li, 1. Wu, and Y. Yin, "The thermal conductivity and electrical strength of epoxy resin with different filler content of micro and nano alumina", *IEEE International Conference Condition Monitoring and Diagnosis (CMD12)*, pp. 1110-1113, 2012

[214] H. Hamalainen, J. Pyrhonen, J. Nerg, J. Talvitie, "Ac resistance factor of Litz-wire windings used in low-voltage high-power generators", *IEEE Trans. on Ind. Electronics*, vol. 61, no. 2, pp. 693- 700, Feb. 2014

[215] P.B. Reddy, T.M. Jahns, P.J. McCleer, T.P. Bohn, T.P., "Design, analysis and fabrication of a high-performance fractional-slot concentrated winding surface PM machine", *Energy Conversion Congress and Exposition (ECCE10),* pp. 1074-1081, Sept. 2010

[216] R. Wrobel, N. Simpson, P. Mellor, 1. Goss, D. Staton, "Design of a brush less PM starter-generator for low-cost manufacture and a high aspect-ratio mechanical space envelope", *IEEE Energy Conv. And Exposition (ECCE15)*, pp. 813-820, Sept. 2015

[217] N. Bianchi, E. Fornasiero, S. Bolognani, "Thermal analysis of a five-phase motor under faulty operations", *IEEE Transactions on Industry Applications*, *49*(4), pp.1531-1538, 2013

[218] A. El-Refaie, "Fractional-Slot Concentrated-Windings Synchronous Permanent Magnet Machines: Opportunities and Challenges", *IEEE Transactions on Industrial Electronics*, vol. 57, no. 1, pp. 107-121, Jan. 2010

[219] M. Popescu, D. Dorrell, D. Ionel, C. Cossar, "Single and double layer windings in fractional slot-per-pole PM machines effects on motor performance," *34th Annual Conference of IEEE Industrial Electronics*, pp. 2055-2060, Nov. 2008

[220] S. Nategh, O. Wallmark, M. Leksell, Z. Shuang, "Thermal analysis of a PMaSRM using partial FEA and lumped parameter modeling," *IEEE Trans. Energy Convers.*, vol. 27, no. 2, pp. 477–488, Jun. 2012

[221] L.J. Wu, Z.Q. Zhu, "Simplified Analytical Model and Investigation of Open-Circuit AC Winding Loss of Permanent Magnet machines," *IEEE Transactions on Industrial Electronics*, vol. 61, no. 9, pp.4990-4999, Sept. 2014

[222] L. Idoughi, X. Mininger, F. Bouillault, L. Bernard och a. E. Hoang, "Thermal model with winding homogenization and fit discretization for stator slot," *IEEE Trans. Magn.*, vol. 47, no. 12, pp. 4822-4826, 2011

[223] R. Wrobel, S. Ayat, J. Baker, "Analytical Methods for Estimating Equivalent Thermal Conductivity in Impregnated Electrical Windings Formed Using Litz Wire", *IEEE International Machines and Drives Conference (IEMDC17)*, Miami, May 2017

[224] Z. Hashin and S. Shtrikman, "A variational approach to the theory of the effective magnetic permeability of multiphase materials," *J. Appl. Phys.*, vol. 33, no. 10, pp. 3125–3131, Oct. 1962

[225] M. C. Kulan, N. J. Baker, and J. D. Widmer, "Design of a high fill factor permanent magnet integrated starter generator with compressed stator windings," *IEEE Transactions on industry applications.*, vol. 53, no. 4, pp. 3371–3378, July/August 2017

[226] J. D. Widmer, C. M. Spargo, G. J. Atkinson, and B. C. Mecrow, "Solar plane propulsion motors with precompressed aluminum stator windings," *IEEE Trans. Energy Convers.*, vol. 29, no. 3, pp. 681–688, Sep. 2014

[227] G. W. Milton, "Bounds on the transport and optical properties of a two- component composite material," *Journal of Applied. Physique.*, vol. 52, pp. 5294–5304, 1981

[228] S. Torquato and F. Lado, "Bounds on the conductivity of a random array of cylinders*," Proc. R. Soc. Lond A 417*, pp. 59–80, 1988

[229] B. J. Chalmers, J. Richardson, "Investigation of high-frequency no-load losses in induction motors with open stator slots", *Proceedings of the Institution of Electrical Engineers*, vol. 113, no. 10, pp. 1597–1605, 1966

[230] S. Ayat, R. Wrobel, J. Goss, D. Drury, "Experimental Calibration in Thermal Analysis of Electrical Machines", *IEEE Energy Conversion Congress nd Exposition (ECCE16),* Milwaukee, Sept. 2016

[231] S. Ayat, L. Haipeng, F. Chauvicourt, R. Wrobel, "Experimental Derivation of Thermal Parameters of the Stator-Winding Region in Thermal Analysis of PM Electrical Machines", *44th Annual Conference of the IEEE Industrial Electronics Society (IECON 2018),* Washington, 2018, , (*in press*).

[232] K D Jayasuriya, A M Stewart and S J Campbell, "The specific heat capacity of GE varnish (200-400K), *Journal of Physics E: Scientific Instruments*, vol. 15, no. 9, 1998

[233] M. van der Geest, H. Polinder , J. A. Ferreira, "Influence of PWM switching frequency on the losses in PM machines", *21th International conference on electrical machines (ICEM 2014)*, pp. 16, Berlin, 2014

[234] Heiles, F. "Design and Arrangement of Cooling Fins", *Elecktrotecknik und Maschinenbay*, Vol. 69, No. 14, July 1952

[235] R. Wrobel, S. Ayat, J. Godbehere, "A Systematic Experimental Approach Deriving Stator-Winding Heat Transfer", *IEEE International Machines and Drives Conference (IEMDC)*, Miami, May 2017.

[236] J. D. Booker, C. E. Truman, "Measuring the Coefficient of Friction for Use in Shrink-fit Calculations", *Experimental Techniques*, vol. 35, no. 2, pp. 7-13, 2011

[237] http://www.zotefoams.com/product/zotek/zotek-n/ (Date viewed: 29/10/2017)

[238] A. DiGerlando, I. Vistoili, "Thermal Networks of Induction Motors for Steady State and Transient Operation Analysis", *International conference on electrical machines (ICEM 94)*, Paris, 1994

[239] E. Schubert, "Heat transfer coefficients at end winding and bearing covers of enclosed asynchronous machines, *Elektrie*, vol. 22, 1968

[240] S.J. Pickering, D.Lampard, N. Hay, T.F. Roylance, "Heat transfer from end-windings of a low voltage concentric-wound induction motor", *IEE EMD 1995*, UK, Sept. 1995

[241] G. I. Taylor, "Distribution of velocity and temperature between concentric cylinders," *Proceedings of the Royal Society*, vol. 159, pp. 546–578, 1935

[242] C. Gazley, "Heat transfer characteristics of rotating and axial flow between concentric cylinders," *Trans. ASME*, pp. 79–89, Jan. 1958

[243] https://www.lme.com/Metals/Non-ferrous/ (Date viewed: 29/04/2017)

[244] S. Ayat, R. Wrobel, J. Baker, D. Drury, "A Comparative Study Between Aluminium and Copper Windings for a Modular-Wound IPM Electric Machine", *IEEE International Machines and Drives Conference (IEMDC)*, Miami, May 2017.

[245] M. Farkas, "Differential equations", *North-Holland Publishing Co,* Amsterdam, (1977)

[246] A. Clifford, *"*Multivariate error analysis: a handbook of error propagation and calculation in many-parameter systems*", John Wiley & Sons, 1973.*

[247] ANSYS Mechanical 18.2, *User Manual*, 2017

Appendix A
Paper abstracts

Experimental Derivation of Thermal Parameters of the Stator-Winding Region in Thermal Analysis of PM Electrical Machines [231]

44th Annual Conference of the IEEE Industrial Electronics Society (IECON 2018)

The majority of heat generated in a permanent magnet (PM) electrical machine is usually attributed to the stator-winding assembly. Here, the main dissipative heat flow from the winding body is typically through the stator core pack to the machine housing. A good understanding of the machine dominant heat transfer mechanisms is therefore crucial in thermal design-analysis. There are two main experimental techniques available in the literature to inform the stator-winding heat transfer, the short-transient and steady-state DC thermal tests. Both tests allow deriving thermal parameters of the stator-winding region, including the winding-to-stator thermal resistance. The short-transient technique has been developed specifically for rapid thermal evaluation of complete machine assembly, e.g. in-production machine quality assessment. In contrast, the steady-state method is frequently time intensive, requiring for the tested hardware to reach thermal equilibrium. This drawback of the considerable testing time is particularly prominent for large machines with high thermal time constant. Both techniques can be applied to the complete machine as well as to variety of the stator-winding sub-assemblies (motorette testing). Motorette testing enables a more controlled and repeatable testing environment with reduced time and resources required. This paper aims to connect both experimental techniques by comparing thermal parameters obtained from both complete stator and motorette thermal testing. The experimental work has been supplemented with theoretical analyses to identify the applicability and limitations of the experimental methods.

Coupled Electromagnetic and Thermal Design-Optimization of a Traction IPM machine with High-Torque Overload Capability

23th International conference on electrical machines (ICEM 2018)

This paper presents a design exercise of an interior permanent magnet (IPM) machine with high-torque overload capability. The machine is intended for traction applications, where the intermediate transient operation is one of the key design requirements, alongside with

the more common specification for the continuous operating duty. The design approach frequently adopted, when considering the transient overload, focuses solely on the continuous operation with appropriate design margins. Consequently, such method is often unreliable and requires a degree of experience or multiple design iterations need to be performed. In contrast, this work proposes a technique accommodating for the transient overload form the onset of the design process. The initial machine sizing is based on a coupled electromagnetic and thermal analysis combined with an optimization routine. The developed design-optimisation system employs computationally efficient and accurate models informed from tests on representative hardware subassemblies. Further to the design challenges associated with the specific operating duty, the materials and processes used in fabrication of the machine should assure here a cost-effective design solution. The theoretical findings show that proposed method is effective for designing machines for more demanding transient overload events, where both transient specific output and its duration are simultaneously considered.

Comparative Study of Thermal Properties of Electrical Windings Impregnated with Alternative Varnish Materials

9th IET International Conference on Power Electronics, Machines and Drives (PEMD)

The thermal design-analysis of devices with electrical windings impregnated using varnish materials is frequently challenging. This is due to difficulties in predicting theoretically the equivalent thermal properties for the composite materials, such as impregnated windings, in a reliable manner. The existing approach makes use of the impregnation ‘goodness’ factor, which allows for imperfections associated with the winding impregnation to be accounted for. This however, requires experimentally derived data from appropriate material samples or machine assemblies. Considering relatively large range of commercially available varnishes, such data is often limited and is not readily accessible. In this investigation, a set of three alternative varnish materials commonly used in impregnation of low voltage electrical windings has been evaluated. To provide better understanding of the material impregnating properties, data from multiple impregnations is also provided. The experimental findings have been supplemented with theoretical analysis on the impregnation ‘goodness’ and stator-winding contact thermal resistance for a selected winding construction. To highlight the importance of appropriate input thermal material data, a case study machine design is thermally analysed.

Comparative Study of Thermal Properties of Electrical Windings Impregnated with Alternative Varnish Materials

9th International Conference on Power Electronics, Machines and Drives (PEMD18)

The thermal design-analysis of devices with electrical windings impregnated using varnish materials is frequently challenging. This is due to difficulties in predicting theoretically the equivalent thermal properties for the composite materials, such as impregnated windings, in a reliable manner. The existing approach makes use of the impregnation 'goodness' factor, which allows for imperfections associated with the winding impregnation to be accounted for. This however, requires experimentally derived data from appropriate material samples or machine assemblies. Considering relatively large range of commercially available varnishes, such data is often limited and is not readily accessible. In this investigation, a set of three alternative varnish materials commonly used in impregnation of low voltage electrical windings has been evaluated. To provide better understanding of the material impregnating properties, data from multiple impregnations is also provided. The experimental findings have been supplemented with theoretical analysis on the impregnation 'goodness' and stator-winding contact thermal resistance for a selected winding construction. To highlight the importance of appropriate input thermal material data, a case study machine design is thermally analysed.

3D Homogenisation of concentrated windings with rectangular conductors

10th IEEE International Machines and Drives Conference (IEMDC 2017)

Design optimisation of electromagnetic devices is strongly affected by thermal behaviour. In order to check whether thermal limitations are exceeded, one has to accurately evaluate the loss generated for each working condition using an electromagnetic model, and feed it to a thermal model. Using the two models in a sequential manner, however, can lead to an error in the loss estimation. Moreover, a proper loss distribution calculation allows for a more precise temperature field computation, allowing for an accurate prediction of the hotspot temperature. When AC effects are significant, this process becomes more computationally expensive since every single wire should be included in the model and this inevitably slows the design procedure. In this work a method is presented for model order reduction of coupled 3D electromagnetic-thermal finite element analysis via homogenisation. The method, applied to a hardware exemplar representative of an open-slot modular stator-winding assembly, is demonstrated to provide very accurate results compared to a fine model where every single conductor is taken into account, but with a

factor 30 reduction in simulation time. Extensive experimental validation is also provided. Due to the reduction in computational effort, the method is suitable for improving the design process and reducing the time to market of many electromagnetic devices, including electrical machines, inductors and transformers.

Analytical Methods for Estimating Equivalent Thermal Conductivity in Impregnated Electrical Windings Formed Using Litz Wire [223]

10th IEEE International Machines and Drives Conference (IEMDC 2017)

This paper discusses two analytical methods used in estimating the equivalent thermal conductivity of impregnated electrical windings constructed with Litz wire. Both methods are based on a double-homogenisation approach consecutively employing the individual winding conductors and wire bundles. The first method is suitable for Litz wire with round-profiled enamel-coated conductors and round-shaped bundles; whereas the second method is tailored for compacted Litz wires with conductors and/or bundles having square or rectangular profiles. The work conducted herein expands upon established methods for cylindrical conductor forms, and develops an equivalent lumped-parameter thermal network for rectangular forms. This network derives analytical formulae which represents the winding's equivalent thermal conductivity and directly accounts for any thermal anisotropy. The estimates of equivalent thermal conductivity from theoretical, analytical and finite element (FE) methods have been supplemented with experimental data using impregnated winding samples and are shown to have good correlation.

A Systematic Experimental Approach Deriving Stator-Winding Heat Transfer

10th IEEE International Machines and Drives Conference (IEMDC 2017)

This work is devoted to providing a more systematic approach to thermal design and analysis of electrical machines with the research focused on heat transfer from the winding body to the stator core pack/machine periphery. The heat transfer from the winding body is notoriously difficult to predict theoretically due to the multi-material composite structure of the stator-winding assembly. Together with numerous manufacture and assembly factors, the heat transfer is usually informed empirically. Further to this, the stator-winding assembly frequently constitutes the main source of power loss within a machine assembly. Both the heat transfer and power loss effects have a significant impact on the machine's overall power output capability. A common approach when quantifying the heat transfer across the stator-winding is based on an equivalent thermal resistance. This method

provides reliable information regarding the capability of the dissipative heat transfer. However, as the thermal resistance data is related to a particular machine and stator-winding assembly, the results are difficult to transfer and compare across different machine designs. Especially if no supplementary stator-winding construction data is available. Here, a method utilising an equivalent thermal conductance has been proposed to enable data transfer for the alternative machine builds and topologies. This allows for a relatively simple comparison among alternative stator-winding assemblies. Both the experimental and theoretical findings are presented in the paper to illustrate the proposed approach.

A Comparative Study Between Aluminium and Copper Windings for a Modular-Wound IPM Electric Machine [244]

10th IEEE International Machines and Drives Conference (IEMDC 2017)

This paper conducts a comparative study upon the performance of an electrical machine fitted with alternative winding conductor materials. The study focusses on an existing interior-mount PM machine (IPM), which is wound with copper (*Cu*) conductors in a single-layer "modular" topology. An analysis exercise is performed to investigate the impact of using alternative conductor materials, such as Aluminium (*Al*). The studied machine employs profiled rectangular conductors, which can offer many performance and manufacturing benefits. It is however acknowledged that windings formed from large section conductors frequently suffer from elevated ac losses, e.g. from high-speed and/or high frequency operation. In this context, replacing commonly used *Cu* windings with a material of higher electrical resistivity, such as *Al*, is an interesting alternative. The immediate impact would be an increase of dc winding resistance and therefore elevated dc losses. However, under high-frequency operation, the increased material resistance helps to abate the effects of ac loss. A more detailed approach for the loss and efficiency derivation is provided herein, accounting for magnetic saturation and stator current vector in field weakening operation. Theoretical predictions suggest that the use of *Al* conductors offer benefits to performance under certain operating conditions and are a viable alternative to the commonly used *Cu* counterpart. In the analysed case, only a moderate reduction in machine performance is experienced at lower speed ranges. The mathematical models used in this work were informed from tests on a hardware prototype to provide more reliable machine performance predictions.

Experimental Calibration in Thermal Analysis of Electrical Machines [230]

8th IEEE Energy Conversion Congress and Exposition (ECCE 2016)

Thermal design of electric machines frequently involves tests on a fully constructed prototype to calibrate various build factors associated with the manufacture, assembly and materials used in the hardware construction. The prototype machine is usually instrumented with multiple temperature sensors providing a detailed insight into the temperature distribution. The resolution of the experimentally gathered data is usually limited by the number of temperature sensors, and therefore the quality of model calibration is highly affected by the input data. This paper investigates the issue of thermal model calibration in the context of available machine hardware and measured data resolution. Also, the research evaluates the most suitable thermocouple location with reference to the model complexity, from reduced-order lumped-parameters circuit to high-fidelity finite element method (FEM). The investigation is focused on the stator-winding assembly, which is frequently associated with the main source of power loss within a PM machine body. A prototype of a PM generator has been selected to illustrate the effects associated with the model calibration. Tests on a representative stator-winding sub-assembly (motorette) have been used in the analysis. The results suggest that the measured data from alternative sensor locations for a given machine region has a significant impact on the quality of the model calibration and consequently temperature predictions.

Estimation of Equivalent Thermal Conductivity for Impregnated Electrical Windings Formed from Profiled Rectangular Conductors

8th IET International Conference on Power Electronics, Machines and Drives (PEMD 2016)

In order to improve accuracy and reduce model setting-up and solving time in thermal analysis of electrical machines, transformers and wound passive components, the multi-material winding region is frequently homogenised. The existing winding homogenization techniques are predominantly focused on winding constructions with round conductors, where thermal conductivity across conductors is usually assumed to be isotropic. However, for the profiled rectangular conductors that assumption is no longer valid, and anisotropy of the winding equivalent thermal conductivity needs to be considered. This paper presents analytical methods for deriving equivalent thermal properties of impregnated windings with profiled rectangular conductors. The techniques allow for computationally efficient and accurate derivation of the composite thermal conductivity accounting for the material thermal anisotropy. Efficacy of the methods has been demonstrated on a number of

hardware winding samples commonly used in low-voltage applications. The theoretical analysis has been supplemented with experimentally derived data showing close correlation.

Experiment Informed Methodology for Thermal Design of PM Machines

11th International Conference on Ecological Vehicles and Renewable Energies (EVER 2016)

The common approach used in the thermal design of electrical machines is calibrating thermal models based on the designer's previous experience, or hardware tests on a prototype machine. This allows for various manufacture and assembly nuances to be accounted for in the design process, assuring accurate and computationally efficient predictions of the machine thermal behaviour. The post-manufacture calibration of thermal models from tests on a complete machine has limited use in development of machine topologies, where no previous experience or machine hardware exist. In this context, an experiment informed design technique that makes use of reduced order machine sub-assemblies presents an attractive alternative. In particular, the hardware manufacture cost and time is significantly reduced compared to the prototyping of the complete machine assembly. This allows for numerous hardware samples to be constructed and tested, to inform the machine design process. The use of the machine sub-assembly testing is focused, but not limited to identifying and quantifying various power loss and heat transfer phenomena. This paper reviews the applicability of the sub-assembly testing in a broader context of the machine design. The aim of the research focuses on formulating a basis for sub-assembly based, experiment informed methodology for the thermal design of electrical machines.

Impact of slot shape on loss and thermal behaviour of open-slot modular stator windings [58]

7th IEEE Energy Conversion Congress and Exposition (ECCE 2015)

This paper presents results from an investigation into the optimal design of an open-slot, modular stator winding. The impact of the stator slot shape on the winding temperature rise is explored, taking account the distribution of loss that occurs in the open slot winding, including ac effects, and the heat transfer characteristics from the winding assembly into the stator core pack. The application focus is a single-layer, concentrated wound brushless PM machine, however the work is applicable to other machine formats. Alternative stator lamination profiles are compared; the commonly used parallel sided tooth with a trapezoidal slot, and a parallel sided slot with a trapezoidal tooth. The investigation includes

the development of a reduced order thermal model representation of the stator. This model is employed to undertake coupled loss and thermal analyses to provide more accurate comparisons of the designs accounting for ac and temperature effects. The experimental and theoretical findings indicate the parallel sided slot design will result in a 37ºC lower winding temperature or an 11% increase in torque at the intended machine operation point.

Appendix B
Propagation of uncertainty

B.1 Uncertainty of thermal conductivity measurements

A necessary step when working with empirical data is to evaluate the uncertainty *u* associated with the measured values. The uncertainty *u(y)* of a function *y* of measured independent parameters $x_1, x_2, \ldots, x_n$, each of which has an independent uncertainty $\Delta x_1, \Delta x_2, \ldots, \Delta x_n$ can be expressed as follows [246],

$$u(y) = \sqrt{\sum_{i=1}^{n} \left(\frac{\partial y}{\partial x_i}\Delta x_i\right)^2} \qquad \text{(B.1)}$$

where $\delta y/\delta x_i$ is the partial derivative of *y* with respect to x_i and Δx_i is the independent uncertainty of x_i.

The uncertainty *u(k)* of the thermal conductivity *k* measured using the heat flux meter experimental set-up described in section 4.4.2 can be calculated using (4.8) and (B.1),

$$u(k) = \sqrt{\left(\frac{\partial k}{\partial l}u(l)\right)^2 + \left(\frac{\partial k}{\partial A}u(A)\right)^2 + \left(\frac{\partial k}{\partial U}u(U)\right)^2 + \left(\frac{\partial k}{\partial T_1}u(T_1)\right)^2 + \left(\frac{\partial k}{\partial T_2}u(T_2)\right)^2} \qquad \text{(B.2)}$$

where *u(l)*, *u(A), u(U) and U(T)* are the measurement uncertainties of the length, area, voltage and temperature, respectively. It may be noted that the accuracy of the current is not considered, as a high-accuracy dc current source has been utilised for the tests, *u(I)*<< 10^{-3}A, and therefore the current has been assumed constant. The partial derivative of *k* according to the different parameters subject to measurement uncertainties are expressed as follows:

$$\frac{\partial k}{\partial l} = \frac{UI}{(T_1 - T_2)A} \qquad \text{(B.3)}$$

$$\frac{\partial k}{\partial A} = -\frac{UIl}{(T_1 - T_2)A^2} \qquad \text{(B.4)}$$

$$\frac{\partial k}{\partial U} = -\frac{Il}{(T_1 - T_2)A} \qquad \text{(B.5)}$$

$$\frac{\partial k}{\partial T_1} = -\frac{UIl}{(T_1-T_2)^2 A} \qquad \text{(B.6)}$$

$$\frac{\partial k}{\partial T_2} = \frac{UIl}{(T_1-T_2)^2 A} \qquad \text{(B.7)}$$

Combining (B.2) and (B.3)-(B.7), the following expression is obtained:

$$u(k) = k\sqrt{\left(\frac{u(l)}{l}\right)^2 + \left(\frac{u(A)}{A}\right)^2 + \left(\frac{u(U)}{U}\right)^2 + 2\left(\frac{u(T)}{(T_1-T_2)}\right)^2} \qquad \text{(B.8)}$$

The material sample cross-section area is obtained from measurements of the cross-section sides, and therefore *u(A)* is obtained from *u(l)* using (B.1):

$$u(A) = \frac{\sqrt{2.l_A.u(l)^2}}{2} \qquad \text{(B.9)}$$

The measurements are completed on four faces of the cuboidal sample during the tests, and the obtained results are then averaged. The final value of the obtained thermal conductivity, $k_{average}$, is shown below:

$$u\left(k_{average}\right) = \sqrt{4\left(\frac{u(k)}{4}\right)^2} = \frac{u(k)}{2} \qquad \text{(B.10)}$$

Formulas (B.3)-(B.10) are used to calculate the values of the uncertainties for the thermal conductivity measurements, which are provided in Table 4.4 in section 4.3.3.

B.2 Uncertainty of specific heat capacity measurements

Using (4.9) and (B.1), the uncertainty of the specific heat capacity measured using the calorimetric method described in section 4.4.2 can be expressed as follows:

$$u(c_s) = \sqrt{\left(\frac{\partial c_s}{\partial m_f}u(m_f)\right)^2 + 2\left(\frac{\partial c_s}{\partial \Delta T_f}u(\Delta T_f)\right)^2 + \left(\frac{\partial c_s}{\partial m_s}u(m_s)\right)^2 + 2\left(\frac{\partial k}{\partial \Delta T_s}u(\Delta T_s)\right)^2} \qquad \text{(B.11)}$$

where $u(m_f), u(\Delta T_f), u(m_s)$ and $u(\Delta T_s)$ are the measurement uncertainties of the fluid mass, fluid temperature change, solid mass and solid temperature change, respectively. After deriving the partial derivatives associated with each parameter subject to measurement uncertainties using (B.3)-(B.7), the following expression is obtained:

$$u(c_s) = c_s\sqrt{\left(\frac{u(m_f)}{m_f}\right)^2 + 2\left(\frac{u(\Delta T_f)}{\Delta T_f}\right)^2 + \left(\frac{u(m_s)}{m_s}\right)^2 + 2\left(\frac{u(\Delta T_s)}{\Delta T_s}\right)^2} \qquad \text{(B.12)}$$

The measurements are completed on four faces of the cuboidal sample during the tests, and the obtained results are then averaged. The final value of the specific heat capacity $c_{s,average}$ is shown below:

$$u\left(c_{s,average}\right) = \sqrt{4\left(\frac{u(c_s)}{4}\right)^2} = \frac{u(c_s)}{2} \qquad \text{(B.13)}$$

B.3 Uncertainty of winding-to-stator thermal contact resistance measurements

Using (5.3) and (B.1), the uncertainty of the winding-to-stator thermal contact resistance $u(R_{w-s})$ measured using the experimental set-up described in section 5.3.1 for motorette testing, can be expressed as follows:

$$u(R_{w-s}) = R_{w-s}\sqrt{2\left(\frac{u(T)}{(T_w - T_s)}\right)^2 + \left(\frac{u(U)}{U}\right)^2} \qquad \text{(B.14)}$$

where T_w, T_s, U, *u(T)* and *u(U)* represent the winding average temperature, stator average temperature, voltage, measurement uncertainty of temperature and measurement uncertainty of voltage. The measurements are completed on both sides of the motorette assembly (e.g. core pack and end-winding regions) during the tests, and the obtained results are then averaged. The final value of thermal conductivity obtained, $R_{w-s,\ average}$, is shown below:

$$u\left(R_{w-s,average}\right) = \sqrt{2\left(\frac{u(R_{w-s})}{2}\right)^2} = \frac{u(R_{w-s})}{\sqrt{2}} \qquad \text{(B.15)}$$

Appendix C
Derivation of analytical formulas for the estimation of the equivalent winding thermal conductivity

C.1 Round conductors

According to observations made from Fig. 4.9, the heat fluxes across the electrical insulation and impregnation have a radial direction, while the heat flux across the conductor flows along y-axis. The radial thermal resistance in a hollow cylinder, $R_{r,hollow}$, and half hollow cylinder, $R_{r,hollow,half}$ are obtained from the well-known solution of the heat conduction equation with zero heat generation and expressed as follows, respectively [126]:

$$R_{r,hollow} = \frac{\ln\frac{r_2}{r_1}}{2\pi kL} \qquad \text{(C.1)}$$

$$R_{r,hollow,half} = \frac{\ln\frac{r_2}{r_1}}{\pi kL} \qquad \text{(C.2)}$$

where L, r_1 and r_2 are the hollow cylinder height, inner and outer radius. The thermal resistances R_{ci} and R_i, are derived from (C.2),

$$R_i = \frac{\ln\frac{r_i}{r_{ci}}}{\pi k_i L} \qquad \text{(C.3)}$$

$$R_{ci} = \frac{\ln\frac{r_{ci}}{r_c}}{\pi k_{ci} L} \qquad \text{(C.4)}$$

The thermal resistance across a half cylinder is derived in this Appendix. Fig. C.1 presents an outline of heat transfer across conductor together with the nomenclature used from thermal resistance calculation.

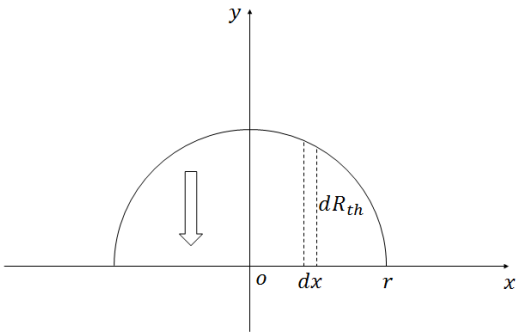

Fig. C.1. Outline of heat transfer across conductor with nomenclature used for thermal resistance calculation.

An expression of the thermal resistance corresponding to the heat transferred across the small length *dx*, so called dR, can be given as follows:

$$dR = \frac{y}{k(L \cdot dx)} \qquad \text{(C.5)}$$

$$\frac{1}{R} = \int_{-r}^{r} \frac{1}{dR} \qquad \text{(C.6)}$$

where, according to Pythagorean theorem,

$$y = \sqrt{r^2 - x^2} \qquad \text{(C.7)}$$

Thus,

$$\frac{1}{R} = kL \int_{-r}^{r} \frac{dx}{\sqrt{r^2 - x^2}} = \left[kL \cdot \tan^{-1}\left(\frac{x}{\sqrt{r^2 - x^2}}\right) \right]_{-r}^{r} \qquad \text{(C.8)}$$

$$\lim_{\theta \to +\infty} \tan^{-1}\theta = \frac{\pi}{2} \qquad \text{(C.9)}$$

$$\lim_{\theta \to -\infty} \tan^{-1}\theta = -\frac{\pi}{2} \qquad \text{(C.10)}$$

$$\frac{1}{R} = kl\pi \qquad \text{(C.11)}$$

Finally,

$$R = \frac{1}{kL\pi} \qquad \text{(C.12)}$$

The thermal resistance across the conductor R_c is obtained from (C.12),

$$R_c = \frac{1}{\pi k_c L} \qquad \text{(C.13)}$$

Finally, following the lumped-parameter TEC representation shown in Fig. 4.11c), the equivalent winding thermal resistance R_e is expressed:

$$R_e = R_i + R_{ci} + R_c = \frac{\ln\frac{r_i}{r_{ci}}}{\pi k_i L} + \frac{\ln\frac{r_{ci}}{r_c}}{\pi k_{ci} L} + \frac{1}{\pi k_c L} \qquad \text{(C.14)}$$

The equivalent winding thermal conductivity is of interest here. According to (C.12),

$$R_e = \frac{1}{\pi k_e L} \qquad \text{(C.15)}$$

Finally,

$$k_e = \frac{1}{\frac{\ln\frac{r_i}{r_{ci}}}{k_i} + \frac{\ln\frac{r_{ci}}{r_c}}{k_{ci}} + \frac{1}{k_c}} \qquad \text{(C.16)}$$

C.2 Rectangular conductors

When spacing between conductors is sufficiently small, the heat transfer can be assumed unidirectional for each axis, which is in line with the heat flux data from the 2D FE model, Fig. 4.14. The assumption of a unidirectional heat transfer for each axis allows one to derive two TECs model associated with x- and y- winding axes respectively, Figs. C.2a) and C.2b). Each TEC model comprises three parallel branches associated with the three parallel heat flux regions presented in Fig. 4.14.

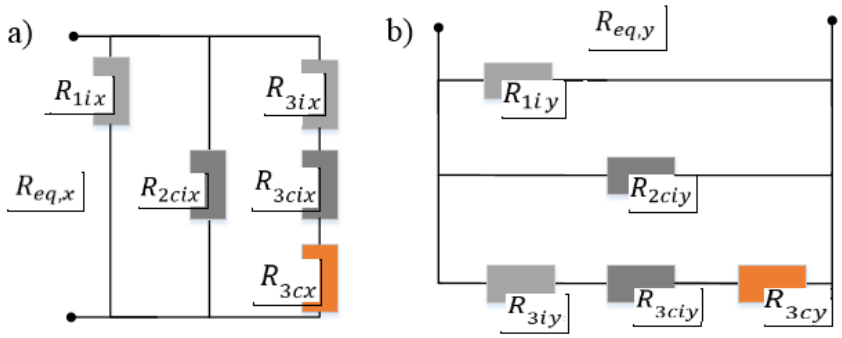

Fig. C.2 Reduced-order equivalent-circuit lumped-parameter network representation and the nomenclature used, a) Thermal resistance along x-axis, b) Thermal resistance along y-axis

The set of formulas leading to derivation of equivalent thermal conductivity along x-axis, $k_{w,x}$, is listed below (C.17) – (C.25).

$$R_{1ix} = \frac{x_{ci} + x_c}{k_{ix}\, y_i\, d_z} \qquad \text{(C.17)}$$

$$R_{3ix} = \frac{x_i}{k_{ix}\, l_y\, d_z} \quad \text{(C.18)}$$

$$R_{2cix} = \frac{x_c}{k_{ci}\, y_{ci}\, d_z} \quad \text{(C.19)}$$

$$R_{3cx} = \frac{x_c}{y_c\, k_c\, d_z} \quad \text{(C.20)}$$

$$R_{3cix} = \frac{x_{ci}}{(y_{ci}+y_c) k_{ci}\, d_z} \quad \text{(C.21)}$$

$$R_{3x} = R_{3ix} + R_{3cix} + R_{3cx} \quad \text{(C.22)}$$

According to Fig. C.2a),

$$R_{w,x} = \frac{1}{\frac{1}{R_{1ix}} + \frac{1}{R_{2cix}} + \frac{1}{R_{3x}}} \quad \text{(C.23)}$$

Finally,

$$k_{w,x} = \frac{l_x}{R_{w,x}\, A_x} \quad \text{(C.24)}$$

where

$$A_x = l_y d_z \quad \text{(C.25)}$$

and d_z is the length of the WS/individual conductors in z-axis. The equivalent thermal conductivity along y-axis, $k_{w,y}$, can be derived by replacing the subscript *x* with *y* and vice-versa in the previous set of formulas.

C.3 Litz wires

Fig. C.3 illustrates schematically, two stages of the homogenisation process, Figs. C.3a) and C.3b), together with the equivalent thermal circuits, Figs. C.3c) and C.3d). Equation subscripts *1* and *2* correspond with model region numbers in Fig. C.3. Due to symmetry, only half of a single conductor/bundle of conductors is used in the analytical derivation. Each of the thermal resistances is derived based on geometrical and material data for a specific model region. For the conductor level homogenization, Method III-rectangular has

been used. and $k_{w,x}$ is the equivalent thermal conductivity of the impregnated square profiled copper conductors in the x-axis, a_x and a_y are the Litz bundle dimension in *x* and *y* axis, respectively, d_x and d_y is the spacing between conductors in *x* and *y* axis. The equivalent thermal conductivity along x-axis $k_{w,x}$ can be derived by replacing the subscript *x* with *y* and vice-versa in the previous set of formulas. More details about the method efficacy is available in [223]. The following set of equations then provides the equivalent thermal conductivity for complete winding with impregnated Litz wire, i.e. bundle level homogenisation, (C.26) – (C.35).

$$R_{1e} = \frac{\frac{a_x}{2}}{k_{w,x} a_y d_z} \tag{C.26}$$

$$R_{1i} = \frac{\frac{a_x}{2}}{2k_i \frac{d_y}{2} d_z} \tag{C.27}$$

$$R_{2i} = \frac{\frac{d_x}{2}}{k_i d_z \left(a_y + 2\frac{d_y}{2}\right)} \tag{C.28}$$

$$R_1 = R_{1e} + R_{2i} \tag{C.29}$$

$$R_2 = \frac{1}{\frac{1}{R_1} + \frac{1}{R_{1i}}} \tag{C.30}$$

$$R_{w,x} = R_2 \tag{C.31}$$

$$k_{w,x} = \frac{l_{Litz}}{A_{Litz} R_{Litz}} \tag{C.32}$$

Where,

$$l_x = \frac{a_x}{2} + \frac{d_x}{2} \tag{C.33}$$

$$A_x = \left(a_y + 2\frac{d_y}{2}\right) d_z \tag{C.34}$$

Finally,

$$k_{w,x} = \frac{a_x + d_x}{a_y + d_y} \left(\frac{a_y k_{e,x} k_i (a_y + d_y)}{a_x k_i (a_y + d_y) + a_y k_{e,x} d_x} + \frac{k_i d_y}{a_x} \right) \tag{C.35}$$

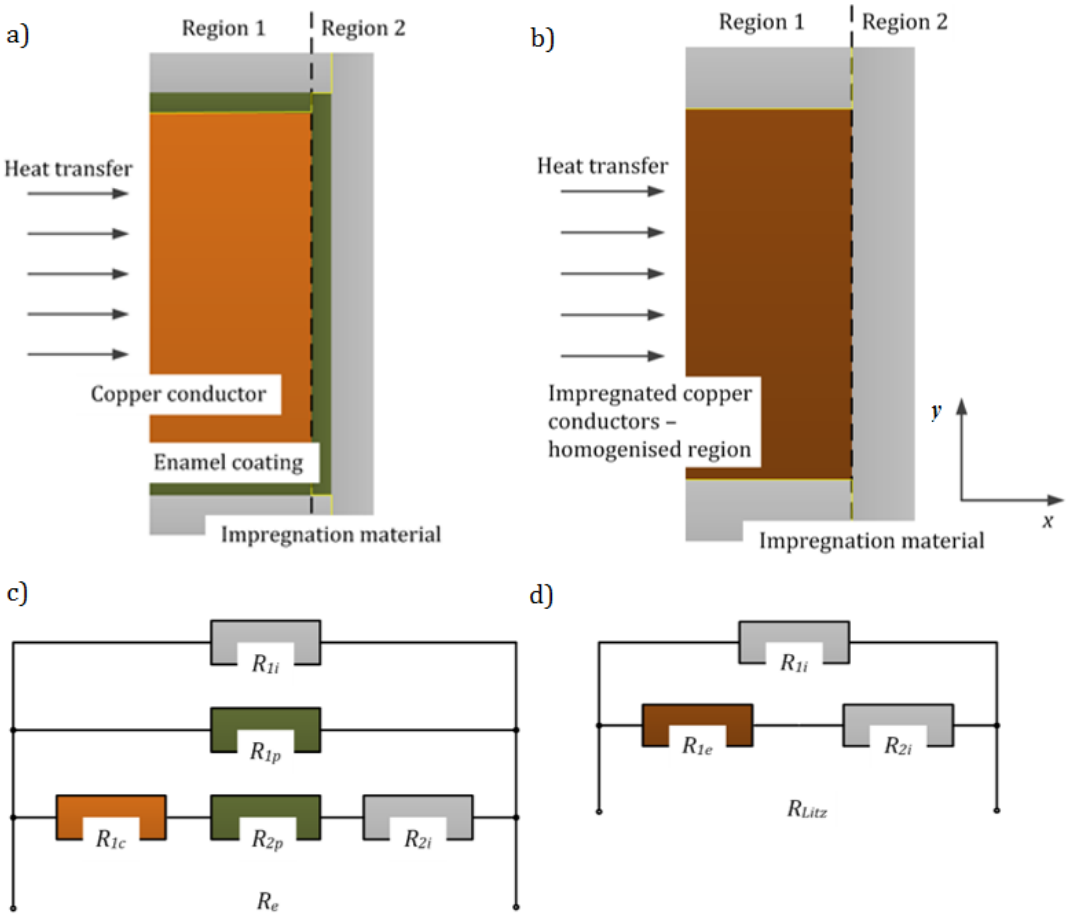

Fig.C.3 Schematic model representation of the compacted Litz wire together with lumped parameter equivalent network. The heat transfer/thermal conductivity along *x* axis is considered.

Appendix D
Slot geometry and end-windings correction functions

D.1 Slot geometry correction functions

Two slot geometrical factors, the slot shape w/h and cross-section area S_{ca}, need to be accounted for when comparing the heat extraction capability from the winding body into the stator core of several stator-winding assemblies. Ideally, both the shape and size of stator slots would need to be the same to make a valid comparison. Clearly, this requirement is difficult to satisfy in the majority of practical cases, including the selected MEs. Two correcting functions, the shape and size functions C_{f1} and C_{f2}, have been developed to enable an unconstrained comparison [235]. These functions have been derived theoretically from the FE analyses and are used to adjust the measured data from the thermal tests. The stator-winding slot is represented here as a homogenised region with equivalent winding conductivity, and the dc power loss generated within the winding region is assumed to be homogenously distributed. This analysis only considers functional trends, which are independent on boundary and material settings. The stator core pack assembly is represented by a fixed temperature boundary condition, while the heat transfer from the stator slot opening is assumed to be negligible. Fig. D.1 shows the simplified 2D FE thermal model representation, together with the boundary conditions, used for the analysis of slot geometrical factors influence.

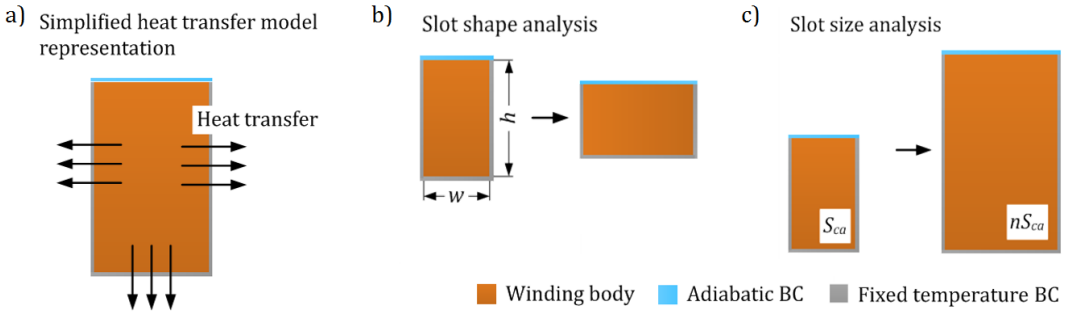

Fig D.1 a) Simplified FE 2D thermal model representation for derivation of correcting function, b) Slot shape analysis, c) slot size analysis [235]

Both correcting functions have been individually obtained and were derived for the stator-to-winding thermal conductance h_e, defined in (5.6). By accounting for A_{w-s}, h_e already introduces a geometrical factor into the heat extraction capability evaluation. For the shape

C_{f1} derivation, the *w*/*h* ratio has been adjusted, such that the slot contour, (2*w*+*h*), through which the heat is dissipated, remained unchanged. This is to ensure that only the influence of the slot shape is accounted for. Similarly, a fixed *w*/*h* ratio has been assumed while deriving the size function C_{f2} to ensure that only the slot cross-sections S_{ca} influence is evaluated. For each function, the maximum value of the thermal conductance obtained has been used to normalise the data. This ensures that C_{f1} and C_{f2} are independent of the slot size and slot shape initially assumed in the thermal analysis. Figs. D.2a) and D.2b) present the correcting functions for C_{f1} and C_{f2}, respectively. From Fig. D.2a), it is observed that C_{fl} is symmetrical, with the symmetry point for *w*/*h* = 2. This corresponds with the largest slot cross-section area among analysed *w*/*h* ratios for a fixed length of the winding-to-slot contour. 'Narrow-deep' and 'wide-shallow' slot geometries have similar capabilities of conducting heat from the winding body. This conclusion is valid only when the heat transfer from the slot opening region is negligible, Fig D.1, which is the case for the baseline machines investigated in this thesis.

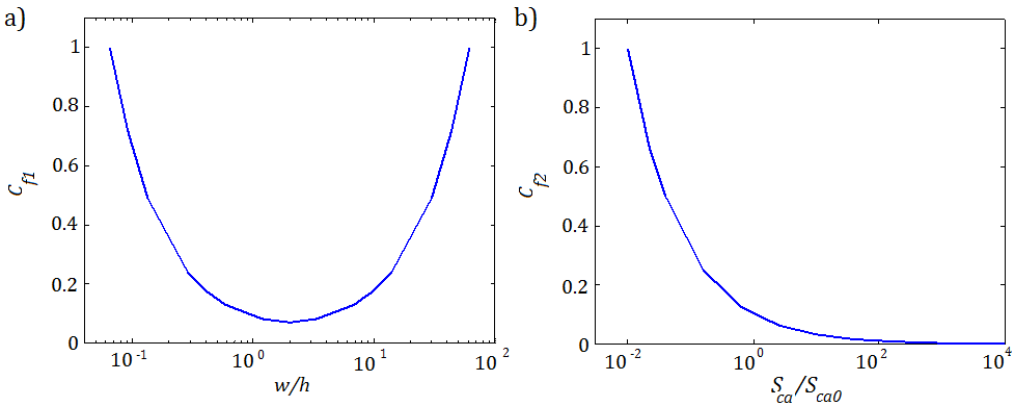

Fig D.2 Correcting functions for a) slot shape C_{fl} vs. *w*/*h*, b) slot size C_{f2} vs. S_{ca}/S_{ca0} [235]

The mathematical description of C_{fl} was found by interpolating the FE derived data (D.1).

$$C_{f1}(x) = p_{11}x^4 + p_{12}x^3 + p_{13}x^2 + p_{14}x + p_{15} \qquad \text{(D.1)}$$

where,

$$x = log_{10}(w/h) \qquad \text{(D.2)}$$

and p_{11}=0.1255, p_{12}=-0.1514, p_{13}=0.2007, p_{14}=-0.09264 and p_{15}=0.09307. From Fig. D.2b), it is observed that larger slots have poorer dissipative heat transfer capabilities as compared with the smaller slots. This is due to the fact that l_{slot} and S_{ca} do not increase in the same rate for a fixed slot shape. Indeed, when multiplying *w* and *h* by a factor *N*, l_{slot} is multiplied by *N*, while S_{ca} is multiplied by N^2. Therefore, if the heats flux through l_{slot} is

fixed, a larger slot would extract a lower ratio of heat compared to a smaller configuration. The mathematical description of C_{f2} was found by interpolating the FE derived data (D.3).

$$C_{f2}(x) = p_{21}e^{(p_{22}x)} \quad \text{(D.3)}$$

where,

$$x = log_{10}(S_{ca}/S_{ca0}) \quad \text{(D.4)}$$

and p_{21}=0.09925 and p_{22}=-1.154. Here, S_{ca0} is a chosen reference value. The measured values of thermal conductance are adjusted for slot shape and slot size using the following formulas,

$$h_{e1}(w/h)_i = h_e(w/h)_m \frac{C_{f1}((w/h)_i)}{C_{f1}((w/h)_m)} \quad \text{(D.5)}$$

$$h_{e2}(S_{ca}/S_{ca0})_i = h_e(S_{ca}/S_{ca0})_m \frac{C_{f2}((S_{ca}/S_{ca0})_i)}{C_{f2}((S_{ca}/S_{ca0})_m)} \quad \text{(D.6)}$$

where the subscripts *i* and *m* refer to adjusted and measured at *w*/*h* or S_{ca}/S_{ca0} factors respectively. In order to take into account both the slot shape and slot size, (D.5) and (D.6) are often applied successively. The value obtained after applying (D.5) and (D.6) is referred to as h_{e12}. The order of application of (D.5) and (D.6) has no influence on the result, i.e. h_{e12}= h_{e21}. This will enable the comparison of slot configuration with various shape and size.

D.2 End-winding correction functions

The employed correction factor C_{f3} for the end-winding has been developed based on M-III, and therefore might not be applicable for other stator-winding configurations. In [235], it was assumed that C_{f3} applies for all the analysed stator-winding exemplars. Equations (D.7) and (D.9) provide mathematical description for the adjustment with relative length of the end-winding.

$$C_{f3}(x) = p_{31}x^3 + p_{32}x^2 + p_{33}x + p_{34} \quad \text{(D.7)}$$

Where,

$$x = l_a/(l_a + l_e) \quad \text{(D.8)}$$

And p_{31}=1.4827, p_{32}=-2.5250, p_{33}=0.4939 and p_{34}=0.9951. The nomenclature used in (D.8) and (D.9) is equivalent to that described in Chapter 5, i.e. l_a and l_e refer to the winding active length and end-winding length, respectively.

$$h_e(l_a/(l_a+l_e)) = h_e(l_a/(l_a+l_e))_m \frac{C_{f3}(l_a/(l_a+l_e))}{C_{f3}(l_a/(l_a+l_e))_m} \quad \text{(D.9)}$$

Appendix E
Solution of a first order differential equation describing the temperature evolution within the stator winding region of an electrical machine

Applying the energy conservation law to the selected part of circuit in Fig. 6.3 in Chapter 6, the following equation is obtained (referred to as (6.2) in Chapter 6),

$$P_w(t) = C_w \frac{dT_w}{dt} + \frac{T_w(t) - T_s(t)}{R_{w-s}} \qquad \text{(E.1)}$$

Several methods can be used to find the solution of a first order differential equation, such as the forward Euler method [245]. A discrete form of (E.1) is given as follows,

$$P_{w,k+1} = C_w \frac{T_{w,k+1} - T_{w,k}}{t_{k+1} - t_k} + \frac{T_{w,k} - T_{s,k}}{R_{w-s}} \qquad \text{(E.2)}$$

which may be re-written as,

$$T_{w,k+1} = T_{w,k} + \frac{1}{1 + \frac{R_{w-s} C_w}{t_{k+1} - t_k}} (T_{s,k} + R_{w-s} P_{w,k} - T_{w,k}) \qquad \text{(E.3)}$$

And,

$$\frac{1}{1 + \frac{R_{w-s} C_w}{t_{k+1} - t_k}} = \frac{t_{k+1} - t_k}{t_{k+1} - t_k + R_{w-s} C_w} \qquad \text{(E.4)}$$

If $(t_{k+1} - t_k) = o(R_{w-s} C_w)$ then,

$$\frac{t_{k+1} - t_k}{t_{k+1} - t_k + R_{w-s} C_w} \cong \frac{t_{k+1} - t_k}{R_{w-s} C_w} \qquad \text{(E.6)}$$

Knowing that the power series of the exponential function,

$$e^x = \sum_0^\infty \frac{x^n}{n!} \qquad \text{(E.7)}$$

Then,

$$1-(1-\frac{t_{k+1}-t_k}{R_{w-s}\,C_w})\cong 1-e^{-\frac{t_{k+1}-t_k}{R_{w-s}C_w}} \tag{E.8}$$

By combining (E.3) and (E.8), the expression presented is obtained:

$$T_{w,k+1}=T_{w,k}+(T_{s,k}+R_{w-s}P_{w,k}-T_{w,k})(1-e^{-\frac{t_{k+1}-t_k}{R_{w-s}C_w}}) \tag{E.9}$$